Photoluminescence and Raman Spectroscopy of Highly Ordered Organic Semiconductor Structures

Artur Mannanov

2019

**Photoluminescence and Raman Spectroscopy of
Highly Ordered Organic Semiconductor Structures**

Photoluminescence and Raman Spectroscopy of Highly Ordered Organic Semiconductor Structures

Proefschrift

ter verkrijging van de graad van doctor aan de
Rijksuniversiteit Groningen
op gezag van de
rector magnificus prof. dr. E. Sterken,
en volgens besluit van het College voor Promoties.

De openbare verdediging zal plaatsvinden op

vrijdag 12 juli 2019 om 9.00 uur
door

Artur Mannanov

geboren op 29 juni 1990
te Chelyabinsk, Sovjet-Unie

Promotores

Prof. dr. J. C. Hummelen

Prof. dr. D. Y. Paraschuk

Prof. dr. M. S. Pchenitchnikov

Beoordelingscommissie

Prof. dr. L. J. A. Koster

Prof. dr. K. Vandewal

Prof. dr. J. Gierschner

Table of Content

Thesis Abbreviations

AC5-TMS	1,4-*bis*{5-[4-(trimethylsilyl)phenyl]thiophen-2-yl}benzene oligomer
AIM8	1-Tetradecyl-3-(3-cyclopropane[1,9](C_{60}-Ih)[5,6]fullerene-3-yl)-indolin-2-one fullerene derivative
BHJ	bulk heterojunction
bisPC$_{61}$BM	[6,6]-diphenyl-C62-bis(butyric acid methyl ester) fullerene derivative
CB	chlorobenzene solvent
CC	cold crystallization
CF	chloroform solvent
CH_2Cl_2	dichloromethane solvent
CP	conjugated polymers
D2-Und-P2TP-TMS	1,3-*bis*[11-(4-{5'-[4-(trimethylsilyl)phenyl]-2,2'-bithien-5-yl}phenyl)undecyl]-1,1,3,3-tetramethyldisiloxane dimer
DCB	orthodichlorobenzene solvent
EQE	external quantum efficiency
FP5	1,4-*bis*(5-phenylfuran-2-yl)benzene oligomer
FP8	5,5'-bis(4-(5-phenylfuran-2-yl)phenyl)-2,2'-bifuran oligomer
FRET	Förster resonance energy transfer
HBIM	1-(3,5-di-tret-butyl-4-hydroxybenzyl)-3-(3-cyclopropane[1,9](C_{60}-Ih)[5,6]fullerene-3-yl)-indolin-2-one fullerene derivative
Hex-TTPTT-Hex	1,4-*bis*(5′-hexyl-2,2′-bithiene-5-yl)benzene oligomer
HOMO	the highest occupied molecular orbital
IPC	index of polymer crystallinity
IrC$_{60}$	(η_2-C_{60})IrH(CO)[(+)-2,3-O-isopropylidene-2,3-dihydroxy-1,4-bis(diphenylphosphino)butane] fullerene derivative
LB	Langmuir-Blodgett
LCD	liquid crystal display
LS	Langmuir-Schaefer
LUMO	the lowest unoccupied molecular orbital
MC	Monte-Carlo
MD	molecular dynamics
ODMS	octyldimethylchlorosilane for dielectric surface passivation
OFET	organic field-effect transistors
OLED	organic light-emitting diode
OLET	organic light-emitting transistor
OPD	organic photovoltaic device
OSC	organic solar cell
P3HT	poly(3-hexylthiophene) polymer
PC$_{61/71}$BM	[6,6]-phenyl C61/71 butyric acid methyl ester fullerene derivative
PCE	power conversion efficiency
PDS	photothermal deflection spectroscopy
PL	photoluminescence
PVT	physical vapor transport technique for crystal growth

x

QY   quantum yield
SSM   self-assembled semiconductor monolayer
THF   tetrahydrofuran solvent
TMS-4P-TMS   4,4‴-*bis*(trimethylsilyl)-1,1′:4′,1″:4″,1‴-quaterphenyl oligomer
TMS-P2TP-TMS,   5,5′-*bis*[4-(trimethylsilyl)phenyl]-2,2′-bithiophene oligomer
TMS-P4TP-TMS   5,5‴-*bis*[4-(trimethylsilyl)phenyl]-2,2′:5′,2″:5″,2‴-quaterthiophene
                            oligomer
TPCO   thiophene-phenylene co-oligomer
WLED   white light-emitting diode

Chapter 1. General Introduction
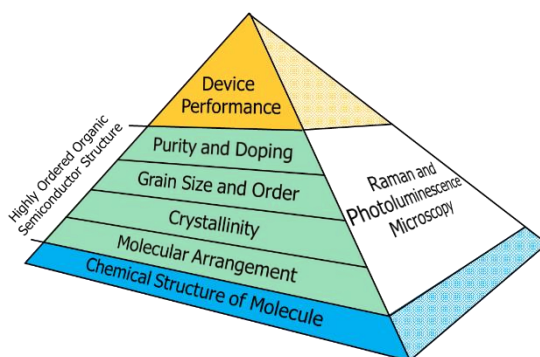
Organic electronics is a branch of electronics in which the devices are based on organic semiconductor materials. Organic semiconductors have conductive properties due to π-electron conjugation in the materials. The main advantage of organic semiconductors over their inorganic counterparts is the variability of the chemical structure of conjugated molecules and hence their semiconductor properties. Apart from the chemical structure of the molecules, their shape and arrangement, crystallinity, short- and long-range order, impurities and doping govern electrophysical and photophysical processes in an organic semiconductor. Molecular packing is one of the key features that allows for fine-tuning the architecture of the organic semiconductor to gain new material properties. Control of the molecular packing in organic semiconductors can improve their (opto)electronic performance and extend their applicability for electronics.

In this Chapter, the fundamental concepts of organic optoelectronic devices are reviewed. The Chapter introduces highly ordered organic semiconductor structures and shows that their advantages are beneficial for emerging organic electronic devices. Spectroscopic approaches for tracking the photophysical and structural dynamics in the organic semiconductor materials are introduced. Finally, the research goals, objectives, and the key findings of this Thesis are formulated.

1.1. Basics of Organic Electronics

Developments in semiconductor technologies are the driving force for progress in science and technology. Following the discovery of semiconductor properties in the middle of the nineteenth century, and the subsequent construction of a semiconductor transistor in 1947 by U. Brattain, J. Bardeen, and W. Shockley,[1-2] acoustoelectronics, optoelectronics, and digital electronics, i.e., the key branches of solid-state electronics, emerged. This led to a consequent breakthrough in radiophysics and telecommunication technologies, along with a significant reduction in computer size. The first computer prototype, ENIAC, built in 1946, was modernized to the transistorized counterpart, TX-0, which was demonstrated at the Massachusetts Institute of Technology in 1956. The first transistor was made with silicon and germanium, i.e., the Group IV elements – still the most widely used elemental semiconductors. Binary semiconductors based on Group III-V elements (gallium arsenide) were later found useful for high-speed electronic devices. In addition to conventional inorganic semiconductors, common organic insulators become semiconducting when charge carriers are injected from the electrode(s), as was discovered by H. Kallmann and M. Pope in the 1960s.[3]

One decade later, the first organic semiconductor device was invented and currently known as organic solar cell (OSC).[4] Due to the contribution by A. Heeger, A. MacDiarmid, and H. Shirakawa in the field of conducting polymers in the late 1970s,[5] the polymer semiconductor research started to expand rapidly. Soon after, in 1983, the concept of an organic thin-film transistor was proposed,[6] and in 1987 an organic light-emitting diode (OLED) was made.[7] All these discoveries led to rapid developments in an interdisciplinary field of science combining semiconductor physics, materials science, and organic chemistry, the so-called organic electronics. Nowadays, solid organic semiconductors are applied as active elements of numerous electronic devices such as OLEDs, OSCs, organic field-effect transistors (OFETs), and memory cells.[8–9]

Organic electronics is a modern field of applied and basic research in which the developments are based on organic semiconductor materials. Organic electronics might be flexible, transparent, stretchable, and lightweight, and its production and utilization can be ecofriendly processes,[10–12] which is not the case with silicon or composite inorganic semiconductors. These advantages make organic semiconductors attractive to many research groups around the world.

2

In the last decades, organic electronics has been significantly renovated: the power conversion efficiency (PCE) of solar energy in organic solar cells has been improved a hundredfold and reached the impressive level of 17.3%.[4, 13] OFETs exhibit charge carrier mobilities up to 20 cm²/(V·s),[14] which is one order of magnitude higher than in devices based on amorphous silicon. OLEDs for more than a decade were produced for a particular market in which they were known for their high color-rendering index, excellent contrast ratio, and low power consumption, compared to their inorganic analogues, liquid crystal displays (LCDs).

Organic semiconductors have conductivity properties due to the presence of π-electron conjugation in the molecule, i.e., overlapping of p-orbitals along the molecular backbone. Each unit in the molecular backbone is a carbon atom, and each has three equivalent sp^2-hybridized orbitals and one p_z-orbital directed perpendicularly to the plane formed by sp^2-hybridized orbitals (Figure 1.1). The sp^2-orbitals are directed along the lines connecting neighboring atoms, forming a covalent σ-bond. Each sp^2-hybridized electron (σ-electron) belongs only to a specific pair of atoms. Several sp^2-hybridized carbon atoms represent a chain so that each p_z-orbital overlaps with a pair (sometimes three) of neighbors, and therefore the corresponding electron (π-electron) might not be attributed to a single pair (see Figure 1.1). Such an effect is called *conjugation* (or π-conjugation), and the corresponding electrons are delocalized electrons.[15]
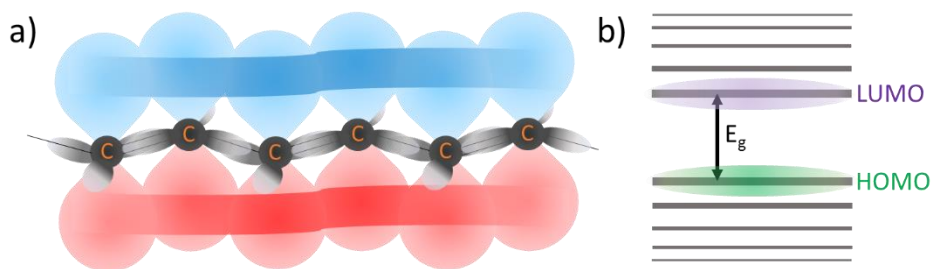
Figure 1.1. (a) A schematic fragment of the chemically simplest semiconductor polymer, polyacetylene. The blue and red lanes show schematically the formed π-electron delocalization of the conjugated chain as a result of overlapping of p_z-orbitals (shown as blue-and-red figure-of-eight shapes) of the carbon atoms. The gray ovals illustrate equivalent sp^2-hybridized orbitals (three for each carbon); (b) energy diagram of an organic semiconductor. The black arrow indicates the energy gap between energies of the HOMO and the LUMO as an analogue of the band gap in inorganic semiconductors E_g.

Due to electron delocalization along the molecular backbone, the electronic properties of the conjugated molecule significantly depend on the length of the

conjugated chain: for example, the energy of the lowest electronic transition decreases with increasing the conjugation length.[16] In some specific cases, physical quantities attributed to conjugated molecules were found to be nonlinearly dependent on the conjugation length, as well as the energy of the lowest electronic transition or, for example, optical susceptibility.[17] The presence of π-electron conjugation in a polymer is usually necessary to obtain a high mobility of charges and hence, electrical conductivity.

The energy states of the π-electrons consist of the levels of electronically occupied and unoccupied molecular orbitals (see Figure 1.1b). The energies of the Highest Occupied Molecular Orbital (HOMO) and the Lowest Unoccupied Molecular Orbital (LUMO) are separated by an energy band gap. The width of the energy band gap in organic semiconductors typically lies in the range from 1 to 4 eV. In conjugated materials, the π-electron system is responsible for the processes of light absorption and luminescence, and charge carrier generation and their transport. To construct a model of these processes, organic semiconductors might be considered as inorganic, so that HOMO might be assigned to the top of the valence band (Ev), and that LUMO might be assigned to the bottom of the conduction band (Ec).[18]

Nonetheless, despite conventional consideration of an organic semiconductor as an inorganic one, there exists an essential difference between organic and inorganic semiconductors in their dielectric constant. The dielectric constant is much lower in the organic semiconductors.[19–20] For lower dielectric constant materials, the Coulomb interaction between the holes and electrons is stronger, which enhances attraction between them, compared to materials with a high dielectric constant. That is why in an organic semiconductor, photon absorption leads to the formation of bound states between an electron and a hole, or *excitons*,[21] with a binding energy ranging from 50 meV to > 1000 meV.[22] At room temperature, the thermal energy kT is 25.7 meV; therefore, thermal dissociation of excitons in organic semiconductors is unlikely. In contrast, excitons in inorganic semiconductors have a binding energy of kT or lower, which makes free electron and hole formation after photoexcitation highly probable.

The main advantage of organic over inorganic semiconductors is the chemical (and structural) variability, which allows for creating semiconductor materials with specified properties. The most important parameters of organic semiconductor materials include the energy band gap, the values of HOMO and LUMO energy levels, the absorption spectrum, the extinction coefficient, the mobility of free

charges, and the stability in a device; all these parameters might be controlled at the stages of chemical synthesis and film fabrication.[12] Variation of molecular conjugated building blocks (such as phenyl, thiophene, furan, and carbazole) can be organized very differently in the molecular structure, which ultimately leads to countless possible structures with unique properties.[23]

The organic semiconductor structures are usually based on the following types of molecules: conjugated polymers (CPs) and small molecules. The latter also include conjugated oligomers that consist of an alternating sequence of double and single bonds (often including aromatic rings), so that the π-π conjugation extends over the whole molecule.[24]

CPs, or semiconducting polymers, are polymers with π-electron conjugation – in the ideal case, along all repeating monomer units. CPs have been among the most studied organic semiconductors for solar power conversion to electrical energy in organic photovoltaic devices (OPDs) for the last two decades.[23, 25–26] Moreover, as discovered in 1990[27], CPs might demonstrate electroluminescence (EL), i.e., CP-based film luminesce in response to an applied electric current. CPs attract high interest to the semiconductor structures in the development of solid-state light-emitting devices.

In addition to CPs, small π-conjugated molecules might be used as the basis for organic semiconductor devices. For example, organic semiconductors in light-emitting devices[28] are commonly small, π-conjugated molecules. Unlike polymers that contain long chain molecules with repeating elementary (monomer) units, small molecules have fixed sizes. Optical, electrical, and physicochemical properties of various small molecules depend on conjugated moieties (e.g., phenyl, thiophene, and furan), the length and morphology of the molecular backbone, and substituents. Conjugated oligomers, as a broad class of small conjugated molecules, can form highly ordered structures, acquiring important optoelectronic properties such as efficient charge transport,[14] long-range exciton diffusion,[29] and strongly polarized luminescence.[30]

All-in-all, CP and conjugated small molecules represent the basis for emerging organic optoelectronic devices such as solar cells, light-emitting diodes and, on the longer term, light-emitting transistors and injection lasers.[11, 31–36]

1.2. Bulk Heterojunction

A typical OPD consists of an active layer placed between two electrodes with different values of work function (Figure 1.2a). The most studied active layer for photovoltaic applications is a bulk heterojunction (BHJ) film that, in the simplest case, is a nanoscale mixture of two components: the donor and acceptor. It is known [25, 37] that the BHJ architecture allows achieving high absorption required for catching as much of the incoming light as possible, while warranting the excitons to reach the interface between the two materials where the charge separation occurs, despite the limited diffusion lengths of the excitons.

Light absorption in a BHJ active layer creates an excited state located at a conjugated molecule or a molecular segment (Figure 1.2b).[25, 37] The excited state is considered to be an exciton, or an electron-hole pair bound together by Coulombic interaction. In OPDs, the excitons can be separated into free charges, i.e., an electron and a hole, by an effective field, which arises at the donor-acceptor interface of the BHJ. In a BHJ, excitons are broken up at the material's interface, and the electron acquires energetically favorable pathway from the conduction band of the donor to the conduction band of the acceptor (Figure 1.2b). The electric field caused by the difference in work functions of the electrodes (the anode and cathode) drives the free charges towards the electrodes.[25]
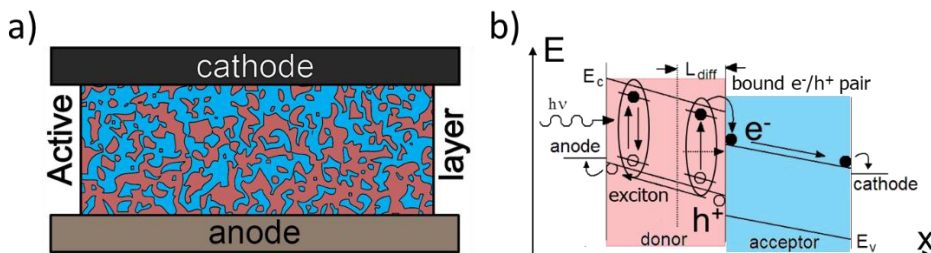
Figure 1.2. OPD based on the BHJ. (a) The active layer is a mixture of a donor and an acceptor placed between two electrodes (cathode and anode); BHJ morphology is schematically represented as a mesh of red and blue regions that correspond to the donor and acceptor materials, respectively. (b) A simplified energy diagram of an OPD (adapted from Ref. 48). E- and x- axes in the graph are energies and spatial coordinates from anode to cathode, respectively. Ec and Ev indicate the energy levels of the conduction and valence bands, respectively, of each material. A photon (the curved arrow) with hv energy is absorbed in the donor and generates an electron-hole pair (an exciton). The exciton diffuses (L_D is diffusion length) to the donor-acceptor interface where the exciton splits to free charges: an electron (e⁻, dot) and a hole (h⁺, circle).

To efficiently transport the free charges to the outer circuit, most of the charges must find their pathways to the corresponding electrode through the BHJ (as schematically represented in Figure 1.2a). The BHJ morphology, i.e., the three-dimensional structure of the donor-acceptor mixture, often requires optimization to enhance the donor and acceptor phase order and to prolong continuous pathways for free charges within the phases, and as a result, to improve the PCE of BHJ in an OPD. Such an important optimization could be performed by thermal or solvent annealing of the BHJs.[38–41] Polymer-fullerene BHJs have been the focus of organic photovoltaic research for more than twenty years.[25, 37, 42–45] In particular, poly(3-hexylthiophene) (P3HT) with [6,6]-phenyl C_{61} butyric acid methyl ester ($PC_{61}BM$) blends as an active layer are the most studied in the research field on OPDs. The $P3HT:PC_{61}BM$ blends development led to significant boost power conversion efficiency of OPDs from ~1% up to ~6%.[18, 46–47]

1.3. Light-Emitting Materials

Organic highly luminescent semiconductor materials are the basis for modern electroluminescent devices, such as light-emitting diodes in high-definition TV screens, advanced smartphones, portable media players, and digital cameras. The tuning capability of organic semiconductor properties through molecular design has attracted intensive interest and inspired development of many intriguing features such as low-temperature processability, flexibility, and diverse colors, as well as cost-effective applications.[12] As mentioned above, OLED displays have inherent advantages over conventional LCD screens: true black state and a fast response time, an ultra-thin profile for flexibility, and a wide color gamut using a white light-emitting diode (WLED) as the backlight.[49] Moreover, OLEDs are energy-saving products, which warrants their prominence in the future.

A current priority in organic optoelectronics is to create a perspective class of versatile semiconductors that possess the light-generation capability of OLEDs and the electrical switching capacity (for light generation) of OFETs. An organic light-emitting transistor (OLET)[50–54] combines these features in a single device, for which the operating principle might be simply represented as an OFET with an EL active layer (Figure 1.3). An electron and a hole are injected from the device electrodes, and then they are transported within a conductive channel towards each other under suitable bias conditions. Electron-hole pair (exciton) formation likely occurs as the electron and hole face each other in the channel. Radiative relaxations of excitons

generate a photon, i.e., electroluminescence. In addition to radiative exciton decay, excitons can diffuse within the semiconductor and may be annihilated by other excitons and get trapped by an impurity. The last two unwanted processes compromise the efficiency of devices.
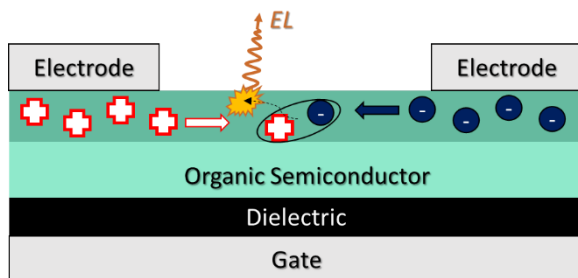
Figure 1.3. A schematic concept of the electroluminescence process in a single-layer OLET. Electrons (shown as the blue dots), and holes (as the red crosses) move in the organic semiconductor layer with a high-charge carrier density (a conductive channel marked as the darkened lane). The black oval shows an electron-hole pair formation (exciton), which, after its diffusion (dash line), radiatively decays (the orange arrow).

To design emerging light-emitting devices such as OLETs and electrically pumped lasers, the materials which combine efficient charge transport and high luminescence are considered the most promising.

Charge carrier mobility is a key characteristic of organic semiconductors,[55] and π-electron overlapping (Figure 1.1), electron-phonon coupling, and shallow or deep trap concentration are essential parameters, which determine the charge carrier transport efficiency in an organic semiconductor.[56–57] To achieve efficient charge transport, highly ordered organic semiconductors such as single crystals and self-assembled monolayers, are promising due to tight molecular packing (which ensures strong intermolecular coupling) and the low density of defects in these structures.

The internal quantum photoluminescence (PL) efficiency, or quantum yield (QY) of a material is defined as:[34] $QY = \frac{N_r}{N_{abs}} = \frac{\tau_n}{\tau_r + \tau_n}$, where N_{abs} is the number of absorbed photons by the material, and N_r is the number of emitted photons following the absorption; τ_n and τ_r are the excited state non-radiative and radiative lifetimes, respectively (see Figure 1.7b). The power conversion efficiency from electrical power to optical power of an optoelectronic device is fundamentally based on the external quantum efficiency (EQE)[58–59] of luminescence. The EQE of fluorescence that is a type of photoluminescence (PL) is typically limited at the level of 25% (at

least 75% of exciton formations are triplets, which do not provide fluorescence[34]) in organic semiconductor materials. However, there are many successful efforts based on delayed fluorescence and phosphorescence to boost the limits of organic semiconductors' luminescence and therefore to provide further enhancement of the optoelectronic device performance.[58, 60–61] A rational device design, selection of excellent materials with high luminescence quantum yield, molecular doping of the materials, careful manipulation of charge and exciton distributions, and optimization of outcoupling techniques are the crucial for the commercialization of organic light-emitting devices.[62–65]

1.4. Exciton Diffusion

Exciton diffusion controls the performance of organic photovoltaic and light-emitting devices. In BHJ photovoltaic devices, photogenerated excitons diffuse to a heterojunction interface, to dissociate into a free charge carriers, electrons, and holes, and it is essential to match the exciton diffusion length and the phase separation scale.[66–69] In the light-emitting devices based on complex tandem or doped structures, the long-range exciton diffusion facilitates energy transport between the functional segments.[70]

Exciton diffusion as the mechanism of a random hopping between molecules or conjugated segments occurs by either dipole–dipole interactions or Dexter energy transfer.[68, 71–72] The exciton diffusion length is characterized by the following parameters: the (average) distance of each exciton hop, l_0, the mean time of between the hops (exciton hopping time), τ_{hop}, and the exciton lifetime, τ_1. Thus, the commonly used relation for the exciton diffusion length is $L_D = l_0\sqrt{\tau_1/\tau_{\text{hop}}}$.[68, 71–73]

In the pioneering study by O. Simpson,[74] singlet exciton diffusion across a thin layer of anthracene was traced by the neighboring tetracene-doped (0.33%) anthracene layer evaporated at the top of the anthracene film and used as a quencher. Assuming an isotropic medium, the diffusion length of singlet excitons was estimated as 46 nm. Presumably, the diffusion length is overestimated due to a contribution from triplet excitons (whose diffusion length is much longer)[72], which are generated as a result of ultrafast singlet-to-triplet conversion and subsequent delayed triplet-to-singlet conversion.[75–76]

Fluorescence quenching-based techniques are among the most common spectroscopic methods to evaluate the exciton diffusion length.[68, 71–72] In the volume quenching technique, fluorescence is measured for various concentrations of

quenching molecules. For accurate exciton diffusion length measurements, quenchers ought to be homogeneously distributed over the material volume, and therefore the quencher concentration should be low to avoid quencher aggregation. In the case of luminescent quenchers, e.g., quantum dots[77] or molecular self-dopants,[78] time-resolved and spectrally-resolved PL data are collected, allowing distinguishing between host and quencher PL in the doped structures. The dynamics of individual excitons are typically simulated by kinetic Monte Carlo (MC) modeling[77–79] (Figure 1.4a) of an exciton random walk in a 3D cubic crystal grid (for more details, see Chapter 3).

The model presented above has a number of built-in assumptions. First, the exciton hopping time, τ_{hop}, is considered isotropic while for tight molecular packing in a molecular crystal it should be in general anisotropic.[72, 77, 79] Second, the model considers exciton hopping to the nearest neighbor only thereby neglecting the long-range interactions.[72, 77] Third, the exciton is assumed to be localized at a single site, i.e. the coherence of the possible excitonic wavefunction is ignored.[77, 79]
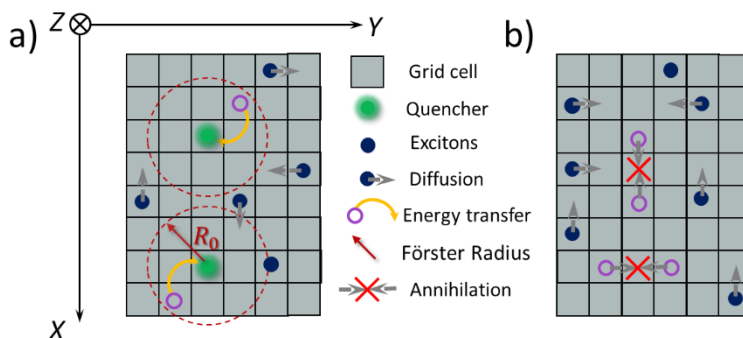
Figure 1.4. Schematics of Monte Carlo simulations of exciton diffusion for the volume quenching technique (a) and the exciton-exciton annihilation method (b). Each gray matrix represents a 2D projection of the 3D material grid. The notations of all symbols are shown between of the panels. Purple circles indicate the removed excitons from the grid resulting in exciton PL quenching.

An alternative method to study exciton diffusion is exciton-exciton annihilation.[66, 80–81] This technique is also based on PL quenching, where a moving exciton meets another exciton, which results in their mutual destruction (annihilation). The probability of the exciton annihilation is sharply enhanced by the increase of exciton density in the system due to the bi-particle origin of the process.

By increasing the excitation flux, i.e., increasing the exciton density, the acceleration of PL decay is observed. The exciton diffusion length is then derived either directly from the exciton density or more accurately from the Monte Carlo simulations (Figure 1.4b). Despite the simplicity of the method, the exciton-exciton annihilation method requires carefully determined exciton density (i.e., incident light power, excitation profile and material absorbance), which is generally complicated to measure.

Other, less conventional but nonetheless powerful methods of exciton diffusion length estimations exist,[68, 71–72] such as microwave conductivity measurements[82] or real-time tracking of exciton harvesting with ultrafast transient absorption.[83–84] Exciton diffusion in molecularly self-doped crystals is investigated in Chapters 3 and 4 of this Thesis.

1.5. Highly Ordered Semiconductor Structures

1.5.1. Polymer Films

In general, conjugated polymers form disorder or polycrystalline films, which are less ordered than the films prepared from good-crystallizing small molecules.[85] That is why lower mobilities of free charge carriers are normally observed in the semiconductors based on polymers with respect to those based on good-crystallizing small molecules.[85] However, post-deposition processing applied to polymer films significantly improves the polymer crystallinity making the films attractive especially for OPDs.[45, 86] In addition, in the polymer-based BHJs the polymer crystallinity in the as-cast films might be largely disturbed by acceptor molecules but further restored by post-deposition treatments under controlled conditions, obtaining the desired BHJ morphology.[87]
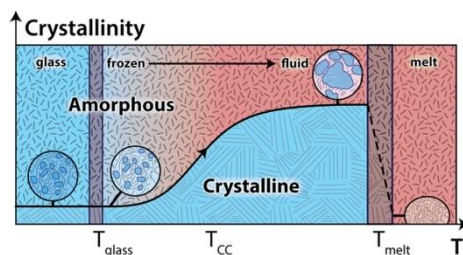
Figure 1.5. Polymer crystallization scheme (adapted from Ref. 102) from the amorphous polymer phase corresponding to thermal annealing of the polymer-fullerene blend. T_g is the glass transition temperature, T_{CC} is a temperature range at which cold crystallization operates, and T_m is the melting point of the polymer phase. The polymer crystallinity dynamics is represented by the black curve, which is continued as the dash line after the melting point.

For instance, as-cast blends of P3HT with $PC_{61}BM$ initially possess a non-optimal morphology that results in their poor photovoltaic performance, specifically in low PCE.[88] The performance of the polymer-based OPDs improves after thermal annealing, which is usually applied as a post-deposition treatment.[89–91] As shown in Ref. 92, the OPD's PCE shows a steep increase right after the thermal annealing begins. The highest PCE of the P3HT:$PC_{61}BM$ blend was obtained after annealing at 110 °C.[92] Further temperature increase might cause polymer melting, which disturbs the BHJ morphology, and, hence, the OPD's performance decreases. Thus, the optimal temperature of BHJ post-deposition treatment has to be determined with separate experimental runs before device fabrication. The post-deposition protocol optimizations in the polymer-fullerene blends have been reported in many experimental studies: in-situ atomic force microscopy,[93] UV–vis spectroscopy,[38] X-ray diffraction,[38, 86] ellipsometry,[94–95] scanning electron microscopy,[96] and ultrafast spectroscopy.[69, 97–98]

In polymer-based BHJs, polymer chains become more ordered (i.e., the polymer crystallinity enhances) during thermal annealing. The polymer phase crystallization operates in the temperature region from the glass transition temperature T_g,[99] (the lower limit) to the melting temperature of the crystalline phase T_m (the upper limit), and, therefore, is called "cold." Cold crystallization (CC)[100–102] (Figure 1.5) is a thermally activated process, during which the polymer chains acquire mobility, and the polymer phase partially crystallizes. CC is one of the crucial processes that determine the BHJ morphology and, hence, the BHJ photovoltaic properties.[88, 103–104] Thus, tracking polymer CC during annealing of BHJ film provides significant

information for an optimal annealing protocol. Polymer CC during thermal annealing of various BHJs is considered in detail in Chapter 2 of this Thesis.

1.5.2. Single Crystals

More than 60 years ago, organic semiconductor single crystals such as naphthalene and anthracene single crystals,[105–106] have been reported. Nowadays, well-ordered packing of conjugated molecules commonly provides efficient charge transport and long-range exciton diffusion.[29, 72] For instance, single crystal rubrene field-effect transistors exhibit the record charge carrier mobility of 20 $cm^2 \cdot V^{-1} \cdot s^{-1}$ competing with their inorganic counterparts.[14, 107] Due to the low density of defects in organic single crystals, there are very few PL quenching centers and few charge carrier traps in them. Moreover, organic single crystals have precise alignment of their molecules and the transition dipole moments, commonly resulting in strongly polarized PL,[30] which might enhance PL-outcoupling through the material-air interface.[30, 108–109]

The packing of organic small molecules in the crystal determines its semiconducting and luminescent properties, such as the mobility of free charges and PL anisotropy. Crystal packing variations (Figure 1.6) could be achieved by using the molecules of the same conjugation core but with various substituent groups. In contrast to the simplest crystal packing motif with one molecule per unit cell (Z = 1) shown in Figure 1.6a, the "zig-zag" arrangement of two layers (Figure 1.6 b and d) might originate from "head-to-tail" interactions between these layers. Note that the PL of the zig-zag arrangement crystals is isotropic. For Z > 1, the molecular arrangement in crystal structure might represent "herringbone packing" (Figure 1.6c-d), i.e., the face-to-edge alignment of the molecules.[110] The herringbone packing usually demonstrates diminished π-electron coupling as compared to face-to-face arrangement.

The molecular backbone can be inclined by an angle φ with respect to the molecular layer plane, and the inclination quantified as the angle φ can also be controlled by the functional molecular substituents.[110] Molecular aggregations with the various angle φ can demonstrate variety PL features[111] and, in some cases of the angle close to 0°, strongly polarized PL originated from the thin crystal surface.[30, 112] In this Thesis, different crystal arrangements are investigated: Chapter 3 explores crystals with zig-zag and herringbone packing (Figure 1.6d); Chapter 4 explores crystals with herringbone packing (Figure 1.6c); and Chapter 5 explores crystals with a face-on orientation of the molecules with respect to the to the largest crystal face (Figure 1.6c with φ of about 0°).
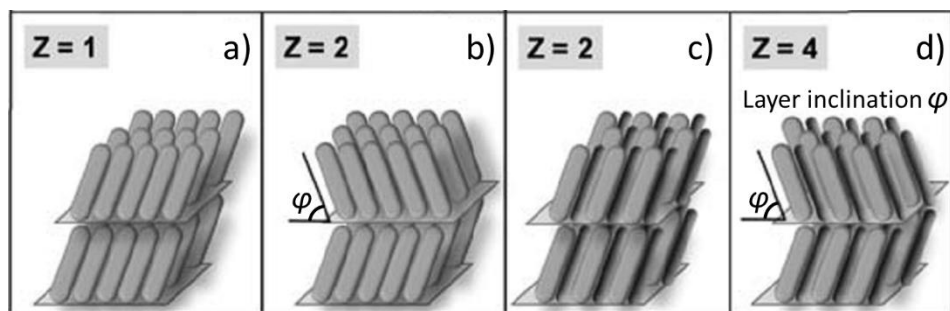
Figure 1.6. Schematic illustrations of 3D-intermolecular arrangements in organic single crystals based on conjugated oligomers (adapted from Ref. 110).

In the last 70 years, doping of organic single crystals with highly luminescent molecules has been successfully applied as one of the promising approaches to study, control, and enhance PL of the crystals.[63, 113–114] Organic crystal doping could be achieved by using the mixture of source material with dopants (similar sublimation temperatures and crystal lattices are necessary) in a suitable ratio to the source material before the crystal growth or by placing source and dopant material in two separated zones of a furnace with the specific temperatures.[115]

Figure 1.7a plots a schematic illustration of PL in crystals doped by luminescent dopants, where an exciton first diffuses in the crystal matrix (host), and then the exciton energy is transferred to a dopant. In general, the overlap of the absorption spectrum of the dopants (energy acceptor) and the PL spectrum of the host (energy donor) allows for Förster resonant energy transfer (FRET) from the donor to the acceptor (Figure 1.7b).[116] The simplest FRET model is based on the point dipole approximation (PDA) so that FRET occurs with the Förster rate:[117] $K = 1/\tau \cdot (R_0/r)^6$, where τ is the lifetime of the donor excitons, R_0 is the Förster radius of the pair of the donor and acceptor molecules, and r is the distance between them. The Förster radius depends on the PL quantum yield and the refractive index of the host, the orientational factor of the donor and acceptor molecules, and the spectral overlap of donor PL and acceptor absorption.[116] Calculations of the orientational factor in molecular crystals need to consider the long-range surrounding of the given dipole as FRET is intrinsically a long-range process. As a first approximation, in Chapter 3, the orientational factor was assumed to be 2/3 as donor and acceptor molecules in a crystal unit cell were cross-cross oriented.[116] In Chapter 4, we used a more realistic approach that takes into account the real crystal structure and

calculated the dipole-dipole interaction energy between the acceptor and two nearest shells of donor molecules.

Förster resonant energy transfer in the doped organic single crystals controls the crystal PL properties,[118–119] and the enhancement of PL efficiency will directly depend on the Förster rate – in particular, on the lifetime of the donor excitons (usually on a nanosecond scale).[116] In this Thesis, the PDA is used despite it can overestimate or underestimate the FRET rate in dependence on the packing motif of the extended dipoles.[110] However, FRET between the extended dipoles calls for much more complicated (atomistic) models,[79, 110, 119] which are beyond the scope of the current Thesis.
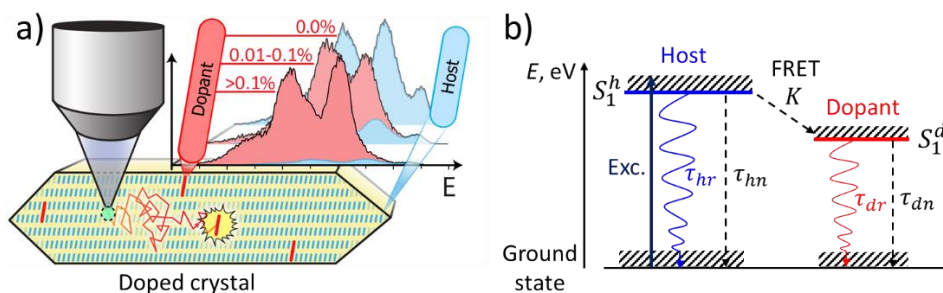
Figure 1.7. (a) The concept of PL of a molecularly doped crystal. (b) Jablonski diagram illustrating FRET from the host (energy donor) to the dopants (energy acceptors) with the following processes (the details are given in Section 3.5.6): photoexcitation of the host (the straight navy arrow); host PL (the curved blue arrow) with the radiatively lifetime τ_{hr} and the nonradiative decay (the dash black arrow) with the non-radiatively lifetime τ_{hn}; FRET (the dash black arrow) with the Förster rate K; dopant PL (the curved red arrow) with the radiative lifetime τ_{dr}, and dopant nonradiative decay (the dash black arrow) with the non-radiative lifetime τ_{dn}. S_1^h and S_1^d are the lowest singlet excited states of the host and dopant, respectively.

1.5.3. Monolayers

OLETs are a promising class of optoelectronic devices combining the OFET operating principle (Figure 1.3) and the light-emission potential of OLEDs.[50–54] In conventional OFETs (and in OLETs as well), the current flows within an ultrathin layer, with a thickness less than 10 nm contacting the gate dielectric (Figure 1.3).[120] This geometry motivates the fabrication of semiconductor monolayer films, i.e., whose thickness corresponds to the size of one or a few molecules.[121–123] The concept of self-assembled monolayers (SAMs) was proposed in 1946,[124] and a well-ordered monolayer on the basis of organic compounds was obtained in the 1970s.[125–126] To

form a semiconductor SAM, a reactive group responsible for chemical bonding to the substrate, a conjugated molecular core, and an aliphatic spacer for compensating substrate roughness and facilitating self-alignment of the conjugated cores should be present in the molecular structure (Figure 1.8a).[125–128] This allows individual molecules to form a crystalline layer.
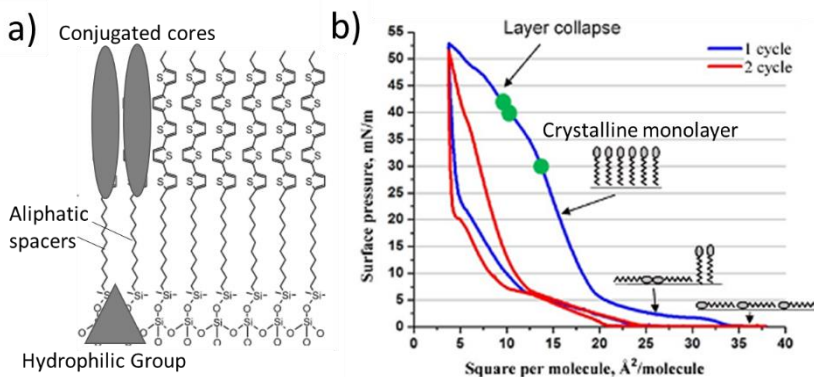
Figure 1.8. (a) Schematic representation of a self-assembled monolayer structure; (b) Langmuir isotherms and cartoons showing the most probable SAM molecular structures at different compression stages for the first compression cycle. The figure is adapted from Ref. 128.

It is known that organic compounds for SAM are also capable of forming ordered monolayers with the Langmuir method,[127–128] one of the most robust and fast techniques for producing monolayers with a well-controlled structure. Following self-assembly at the air-water interface, a Langmuir monolayer might be transferred to a solid substrate by two methods. In the Langmuir-Blodgett (LB) technique,[129] a substrate moves upwards vertically from the water below the surface, and in the Langmuir-Schaefer (LS) technique, the substrate is placed parallel to the water surface, touching the water surface, and then the substrate is lifted.[130] The strongest advantage of the Langmuir methods is that they allow complete covering of a substrate by a monolayer with low defect concentration. To form a monolayer in the Langmuir method, the surface layer of SAM-type molecules with a hydrophilic anchor group and a hydrophobic conjugated fragment (Figure 1.8a), is compressed on the water surface using barriers.[127] The sequential isothermal compression controls the monolayer film structure (Figure 1.8b), which can be crystalline. The attractive molecules for light-emitting Langmuir semiconductor layers are chlorosilyl and disiloxane derivatives of thiophene-phenylene co-oligomers (TPCOs)

because, in solid phase, they combine decent charge carrier transport and bright PL.[128, 131–135]

Thus, Langmuir films of such molecules are prospective materials for producing highly luminescent semiconductor monolayers for optoelectronic applications. PL properties of organic semiconductor monolayers are considered in Chapter 6 of this Thesis.

1.6. Goals and Objectives of the Thesis

This Thesis concerns the understanding of photophysics and morphology dynamics in highly ordered organic semiconductor systems. It also provides the essential connections between fast photophysics and structural properties in such systems.

The Thesis aims to answer the following questions: How could the polymer crystallinity essential for efficient functioning of the organic photovoltaic devices be efficiently restored in the as-cast bulk heterojunction? What are the fundamental dynamic processes that determine exciton dynamics and energy transfer efficiency in doped organic single crystals? What are the differences in luminescent dynamics of the highly ordered semiconductor monolayers and single crystals?

To answer these questions, the following objectives are posed:

1) To follow the polymer cold crystallization in real time in a series of polymer-based bulk heterojunction films and to optimize their post-deposition treatment protocols;

2) To explain and control the PL quantum yield in molecular doped semiconductor single crystals;

3) To reveal the energy transport processes in doped single crystals;

4) To understand anisotropic properties of PL in doped single crystals;

5) To elucidate the ultrafast PL dynamics in semiconductor monolayers.

To fulfill the objectives, in-situ Raman spectroscopy and ultrafast polarization-resolved PL spectroscopy were used. These techniques will be briefly described in the following section.

1.7. Photoluminescence and Raman Microscopy

1.7.1. In-situ Raman Spectroscopy

Raman spectroscopy is a unique and effective tool to study the vibrational transitions of π-conjugated (polymer) chains in the ground state. Raman scattering originating from the organics with long π-conjugation length (i.e., π-electron delocalization) is of high intensity due to the large Raman cross section.[136–138] As a result, the signal of π-conjugated species dominates in the Raman spectrum of the material, and the frequency, shape, and intensity of specific vibrational Raman bands become strongly sensitive to the π-conjugation length and its interruption due to various defects.[136–137, 139] Thus, Raman spectroscopy can be also effectively used to probe the order of π-conjugated species, e.g. in such a complicated system as BHJ, and follow its morphology features during their post-deposition treatment processing.[140] This is important to enhance photovoltaic properties of the BHJ.
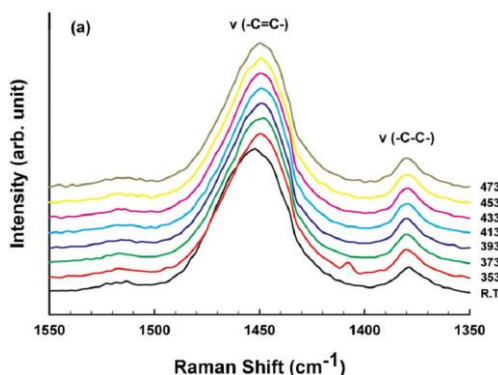
Figure 1.9. Raman band shift of the 1350 (C-C intraring stretch) and 1560 cm^{-1} (symmetric C=C stretch) modes for the P3HT:PC$_{61}$BM BHJ as a function of the thermal annealing temperature (adapted from Ref. 141). The numbers on the right side of the panel represent temperatures of the BHJ in Kelvin scale.

Already the first Raman studies[141–143] of the OPD's active layers based on BHJ with P3HT as the donor component showed that the polymer in-plane ring vibrations (see Figure 1.9) provide qualitative and quantitative information related to the device performance. It was shown that the shape and position of the corresponding Raman bands are related to the polymer crystallinity in BHJs. [141] It is believed that the thermal annealing of P3HT-based films leads to the optimal morphology of the polymer phase with the enhanced order of the polymer chains, which results in

18

increased π-electron delocalization along the polymer chain (i.e., longer conjugation length).[141] The Raman band of the P3HT vibrational C=C stretching mode (Figure 1.9) might be decomposed to a sum of the ordered (crystalline) and disordered (amorphous) P3HT phase contributions,[140, 144] thereby providing information about the share of crystalline polymer phase in the BHJ. Raman spectroscopy was successfully used to study the polymer crystallinity of the P3HT:PC$_{61}$BM films before and after thermal annealing.[140]

1.7.2. Ultrafast Photoluminescence Spectroscopy

Ultrafast PL spectroscopy is a powerful tool for comprehensive study of transient processes in organic semiconductors, such as exciton relaxations, annihilations, energy transport, and transformations. Ultrafast PL spectroscopy provides multidimensional information with picosecond time resolution. The latter might be easily realized with the use of a streak camera (Figure 1.10). In a simplified picture of the streak-camera operation, the input photons are first spatially dispersed in one direction (horizontal in Figure 1.10) by a spectrometer (not shown). To obtain the time delay between photons of different colors, the photons are initially converted into the electrons. Then the electric field applied to deflection electrodes sweeps electron distribution into another direction (vertical in Figure 1.10), providing the time axis.
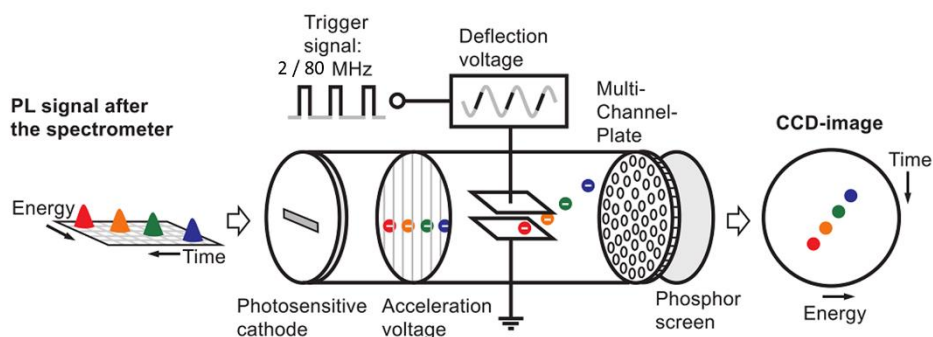
Figure 1.10. Conventional operation principle of a streak camera. The figure is adapted from Ref. 145.
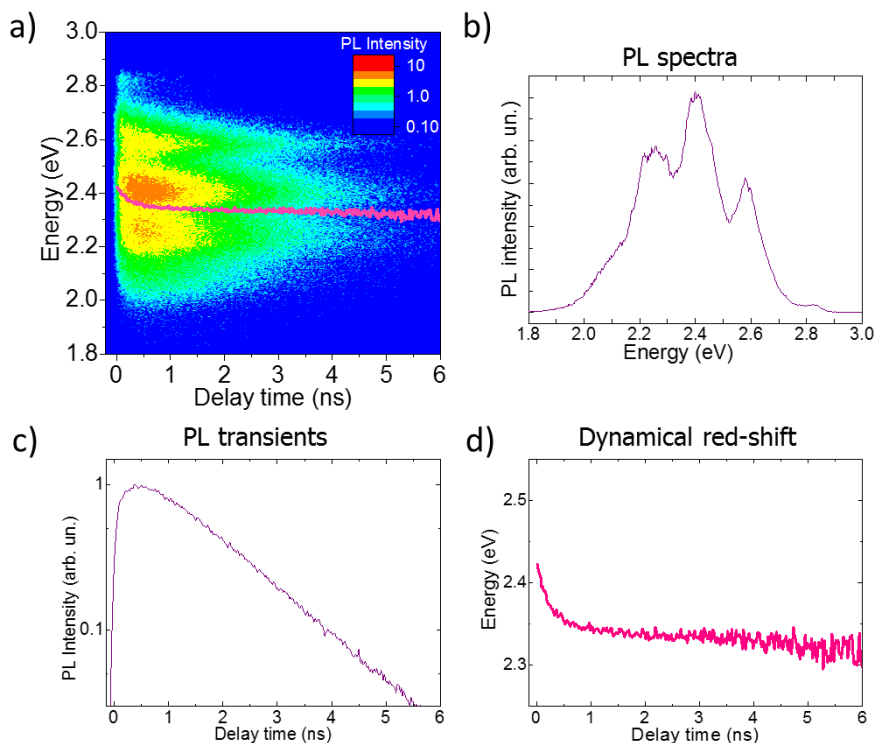
Figure 1.11. Two-dimensional PL map (a) with spectral and temporal axes, which was obtained by ultrafast PL spectroscopy. The PL mean energy values for each time are shown with a pink line in panels (a) and (d). Examples of the PL data (b–d) are extracted from the PL map.

Optical properties resulting from tight molecular packing in organic semiconductors could be comprehensively studied by PL spectroscopy because the molecular packing is usually anisotropic, affecting the PL polarization.[146–149] As a result, the effects of crystal packing, and moreover luminescent dopants (specifically, their arrangement in and interaction with the crystal matrix) could be identified by analyzing polarization-resolved PL, i.e., at the different polarization patterns using polarized excitation and PL detection. The polarization patterns are usually achieved using two polarizers in the excitation and PL detection channels. The microscope configuration allows us to investigate time-resolved PL from single crystal domains extracting distinct PL data. Moreover, PL collected in the confocal microscope configuration and from the excitation volume just underneath the sample surface is minimally affected by PL reabsorption (i.e., absorption of already-emitted PL due to

the overlap between the absorption and PL spectra). The confocality is realized with two orthogonally oriented slits at the entrances of the spectrometer and the streak camera instead of a more traditional pinhole in the focal conjugated plane. This provides efficient blocking of the extrafocal PL and therefore filtering PL within the depth of focus.

The result of the ultrafast PL spectroscopy with the streak camera detection is a two-dimensional map (Figure 1.11a) of PL intensity as a function of time and energy (wavelength). By integrating of the PL map over the time window, the PL spectrum (panel b) is obtained for a given time interval. Integration of the PL map over the spectral region provides the PL transient attributed to the given spectral region (panel c). The PL transients represent the convolution of the actual PL signal and the apparatus response function of typically 5–20 ps. Tracking the PL mean energy with time, a transient red-shift of PL (panel d) is revealed, which is useful to observe energy transfer processes such as FRET or exciton downhill migration.

1.8. Findings and Overview of the Thesis

The current Thesis concerns the optically detected dynamics in ordered organic semiconductor structures: polycrystalline polymer films, single crystals, and monolayers. These dynamics are linked to structural features such as the chemical structure of the molecules, and their arrangements, crystallinity, molecular doping, and impurities. Experimentally, the optically sensitive dynamics are probed by Raman and ultrafast photoluminescence spectroscopies. Such an extensive study in various highly ordered organic structures aims to develop new approaches for improving the performance of organic optoelectronic devices.

The main findings of this Thesis are the following:

1) In polymer-based bulk heterojunction films, the correlation between polymer cold crystallization dynamics and preparation conditions has been revealed, providing valuable information for development of polymer bulk-heterojunction fabrication protocols;

2) The advanced concept of molecular self-doping, i.e. emerging of a highly luminescent dopant as a minute amount byproduct of the source material synthesis, has been confirmed by ultrafast PL spectroscopy in organic semiconductor crystals, and used to control and improve their PL properties;

3) Exciton diffusion length of 24 nm in organic semiconductor crystals based on furan-containing oligomers has warranted the high PL quantum yield in the crystals doped by highly luminescent molecules at 10s of ppm concentrations;

4) Strong PL anisotropy in the single crystals of thiophene phenylene co-oligomers with the face-on geometry was explained as originated from gray and dark states in the crystal structure;

5) Langmuir monolayers' 2D structure has reduced PL quenching efficiency compared to their bulk counterpart.

The Thesis consists of six chapters, including this general introduction (Chapter 1).

In Chapter 2, Raman spectroscopy was applied to track the polymer crystallinity in real time in BHJs upon thermal annealing. The polymer crystallinity was calculated from the share of the quasicrystalline polymer phase in the Raman spectrum of the carbon-carbon stretch modes. Cold crystallization of the polymer phase was suggested for BHJ films, based on different fullerene derivatives and cast from different solvents. This allowed us to better understand BHJ preparation conditions and post-deposition treatment protocols for optimizing organic photovoltaic devices.

In Chapter 3, the concept of molecular self-doping with by-products of the host material synthesis was studied in various organic single crystals. To demonstrate the effect of self-doping on PL properties, time- and spectrally resolved PL were measured in the variously doped crystals. The PL data were fitted with the outcome of the Monte Carlo modelling to disentangle the exciton diffusion and Förster resonant energy transfer (FRET). We concluded that molecular self-doping combined with improved excitonic transport and FRET is an efficient approach to control PL of organic single crystals.

Chapter 4 is devoted to the investigation of exciton diffusion in highly luminescent single crystals, based on furan-containing co-oligomers. To realize the volume-quenching method of exciton diffusion length measurement, smooth embedding of the dopants into the host crystal lattice was confirmed by molecular dynamics simulations. Using ultrafast PL spectroscopy combined with Monte Carlo simulations, an exciton diffusion of 24 nm was obtained. The exciton-exciton annihilation experiments independently verified the obtained exciton diffusion length. Due to the long-range exciton diffusion, high PL and efficient charge transport, the doped furan-phenylene single crystals are promising candidates for organic optoelectronic devices.

In Chapter 5, time-resolved PL anisotropy of single crystals with a face-on orientation of thiophene phenylene co-oligomers was studied. According to the polarization-resolved PL measurements, PL is mainly polarized along the molecule backbones, regardless of the excitation polarization. However, PL induced by the excitation orthogonally polarized with respect to the molecular backbones, unexpectedly exhibits much higher efficiency as compared to the parallel one. Blue and red flanks of time-resolved PL clearly show the biexponential behavior, which was assigned to the presence of gray and dark states in the optical bandgap of the AC5-TMS crystal. We hypothesize that such states might originate from the self-dopants and/or the near-surface defects; further analysis is clearly required to establish their exact origin. Understanding anisotropic PL features is the key factor to achieve better performance of the molecular crystals in optoelectronic devices.

Chapter 6 is devoted to ultrafast photophysics in the monolayer structures deposited using Langmuir-Blodgett and Langmuir-Shaffer methods, which lead to different monolayer morphologies. PL properties significantly depend on the monolayer film morphologies; for example, the Langmuir-Blodgett deposition method results in higher PL intensity and longer PL lifetime. It was also shown that the PL quantum yield is higher for monolayers as compared to bulk polycrystalline 3D structures. This result was explained by the higher structural order in the monolayers. Thus, Langmuir films are promising for optoelectronic monolayer devices.

Overall, the Thesis considers dynamic processes in the highly ordered organic systems with various structural features, and it proposes possible improvements to their photovoltaic and luminescence performances for optimal functionality in organic optoelectronic devices.

1.9. Personal contribution

The current thesis is a result of close collaboration between several groups from different institutions. While individual contributions are acknowledged at the end of each chapter, here the author would like to factorize his own contributions into the research projects. The author was directly involved in the formulation of tasks, developing experiments, and scientific discussions on the experimental results. The author carried out all experiments described in the thesis, including Raman spectroscopy, time-resolved photoluminescence spectroscopy, the polarization-resolved PL measurements, exciton annihilation experiments, atomic force microscopy, and implementation of the Monte-Carlo modelling and molecular

dynamics simulations. The author also prepared polymer:fullerene films and implemented the real-time Raman protocol.

1.10. References

1. Bardeen, J.; Brattain, W. H., The Transistor, a Semi-Conductor Triode. *Phys. Rev.* **1948**, *74*, 230-231.
2. Nobel Prize in Physics for 1956: Dr. W. Shockley, Prof. J. Bardeen and Dr. W. H. Brattain. *Nature* **1956**, *178*, 1149.
3. Kallmann, H.; Pope, M., Bulk Conductivity in Organic Crystals. *Nature* **1960**, *186*, 31–33.
4. Chamberlain, G. A., Organic Solar Cells: A Review. *Solar Cells* **1983**, *8*, 47-83.
5. Shirakawa, H.; Louis, E. J.; MacDiarmid, A. G.; Chiang, C. K.; Heeger, A. J., Synthesis of Electrically Conducting Organic Polymers: Halogen Derivatives of Polyacetylene, (Ch). *J. Chem. Soc., Chem. Commun.* **1977**, 578-580.
6. Ebisawa, F.; Kurokawa, T.; Nara, S., Electrical Properties of Polyacetylene/Polysiloxane Interface. *J. Appl. Phys.* **1983**, *54*, 3255-3259.
7. Tang, C. W.; VanSlyke, S. A., Organic Electroluminescent Diodes. *Appl. Phys. Lett.* **1987**, *51*, 913-915.
8. Puniredd, S. R.; Pisula, W.; Müllen, K., 2 - Influence of Film Morphology on Optical and Electronic Properties of Organic Materials. In *Handbook of Organic Materials for Optical and (Opto)Electronic Devices*, Ostroverkhova, O., Ed. Woodhead Publishing: 2013; pp 83-101.
9. Ji, Y.; Zeigler, D. F.; Lee, D. S.; Choi, H.; Jen, A. K. Y.; Ko, H. C.; Kim, T.-W., Flexible and Twistable Non-Volatile Memory Cell Array with All-Organic One Diode–One Resistor Architecture. *Nat. Commun.* **2013**, *4*, 2707(7).
10. Moliton, A.; Hiorns, R. C., Review of Electronic and Optical Properties of Semiconducting Π-Conjugated Polymers: Applications in Optoelectronics. *Polym. Int.* **2004**, *53*, 1397-1412.
11. Forrest, S. R.; Thompson, M. E., Introduction: Organic Electronics and Optoelectronics. *Chem. Rev.* **2007**, *107*, 923-925.
12. Wang, C.; Dong, H.; Hu, W.; Liu, Y.; Zhu, D., Semiconducting Π-Conjugated Systems in Field-Effect Transistors: A Material Odyssey of Organic Electronics. *Chem. Rev.* **2012**, *112*, 2208-2267.
13. Meng, L., *et al.*, Organic and Solution-Processed Tandem Solar Cells with 17.3% Efficiency. *Science* **2018**, *361*, 1094-1098.
14. Podzorov, V.; Menard, E.; Borissov, A.; Kiryukhin, V.; Rogers, J. A.; Gershenson, M. E., Intrinsic Charge Transport on the Surface of Organic Semiconductors. *Phys. Rev. Lett.* **2004**, *93*, 086602.
15. Heeger, A. J., Nobel Lecture: Semiconducting and Metallic Polymers: The Fourth Generation of Polymeric Materials. *Rev. Mod. Phys.* **2001**, *73*, 681-700.
16. Schott, M.; Nechtschein, M., *Organic Conductors: Fundamentals and Applications*; CRC Press: New York, 1994; Introduction to conjugated and conducting polymers.
17. Zhu, X.; Chen, Y. M.; Li, L.; Jeng, R. J.; Mandal, B. K.; Kumar, J.; Tripathy, S. K., Photocrosslinkable Polymers with Stable Second-Order Optical Nonlinearity. *Opt. Commun.* **1992**, *88*, 77-80.

18.   Brabec, C. J.; Sariciftci, N. S.; Hummelen, J. C., Plastic Solar Cells. *Adv. Funct. Mater.* **2001**, *11*, 15-26.

19.   Torabi, S., *et al.*, Strategy for Enhancing the Dielectric Constant of Organic Semiconductors without Sacrificing Charge Carrier Mobility and Solubility. *Adv. Funct. Mater.* **2015**, *25*, 150-157.

20.   Dunlap, W. C.; Watters, R. L., Direct Measurement of the Dielectric Constants of Silicon and Germanium. *Phys. Rev.* **1953**, *92*, 1396-1397.

21.   Frenkel, J., On the Transformation of Light into Heat in Solids. I. *Phys. Rev.* **1931**, *37*, 17-44.

22.   Knupfer, M., Exciton Binding Energies in Organic Semiconductors. *Appl. Phys. A* **2003**, *77*, 623-626.

23.   Duan, C.; Huang, F.; Cao, Y., Recent Development of Push-Pull Conjugated Polymers for Bulk-Heterojunction Photovoltaics: Rational Design and Fine Tailoring of Molecular Structures. *J. Mater. Chem.* **2012**, *22*, 10416-10434.

24.   Müllen, K., *Electronic Materials: The Oligomer Approach*; WILEY-VCH Verlag GmbH, 1998.

25.   Spanggaard, H.; Krebs, F. C., A Brief History of the Development of Organic and Polymeric Photovoltaics. *Sol. Energy Mater. Sol. Cells* **2004**, *83*, 125-146.

26.   Wang, T.; Pearson, A. J.; Lidzey, D. G.; Jones, R. A. L., Evolution of Structure, Optoelectronic Properties, and Device Performance of Polythiophene:Fullerene Solar Cells During Thermal Annealing. *Adv. Funct. Mater.* **2011**, *21*, 1383-1390.

27.   Burroughes, J. H.; Bradley, D. D. C.; Brown, A. R.; Marks, R. N.; Mackay, K.; Friend, R. H.; Burns, P. L.; Holmes, A. B., Light-Emitting Diodes Based on Conjugated Polymers. *Nature* **1990**, *347*, 539–541.

28.   Schwab, T.; Lüssem, B.; Furno, M.; Gather, M. C.; Leo, K., 18 - Organic Light-Emitting Diodes (OLEDs). In *Handbook of Organic Materials for Optical and (Opto)Electronic Devices*, Ostroverkhova, O., Ed. Woodhead Publishing: 2013; pp 508-534.

29.   Lunt Richard, R.; Benziger Jay, B.; Forrest Stephen, R., Relationship between Crystalline Order and Exciton Diffusion Length in Molecular Organic Semiconductors. *Adv. Mater.* **2009**, *22*, 1233-1236.

30.   Yomogida, Y.; Sakai, H.; Sawabe, K.; Gocho, S.; Bisri, S. Z.; Nakanotani, H.; Adachi, C.; Hasobe, T.; Iwasa, Y.; Takenobu, T., Multi-Color Light-Emitting Transistors Composed of Organic Single Crystals. *Org. Electron.* **2013**, *14*, 2737-2742.

31.   Yu, G.; Gao, J.; Hummelen, J. C.; Wudl, F.; Heeger, A. J., Polymer Photovoltaic Cells: Enhanced Efficiencies via a Network of Internal Donor-Acceptor Heterojunctions. *Science* **1995**, *270*, 1789-1791.

32.   Hoppe, H.; Sariciftci, N. S., Morphology of Polymer/Fullerene Bulk Heterojunction Solar Cells. *J. Mater. Chem.* **2006**, *16*, 45-61.

33.   Kido, J.; Kimura, M.; Nagai, K., Multilayer White Light-Emitting Organic Electroluminescent Device. *Science* **1995**, *267*, 1332-1334.

34.   Friend, R. H., *et al.*, Electroluminescence in Conjugated Polymers. *Nature* **1999**, *397*, 121-128.

35.   Forrest, S. R., The Path to Ubiquitous and Low-Cost Organic Electronic Appliances on Plastic. *Nature* **2004**, *428*, 911-918.

36.   Miller, R. D.; Chandross, E. A., Introduction: Materials for Electronics. *Chem. Rev.* **2010**, *110*, 1-2.

37.   Günes, S.; Neugebauer, H.; Sariciftci, N. S., Conjugated Polymer-Based Organic Solar Cells. *Chem. Rev.* **2007**, *107*, 1324-1338.

38.   Chen, F.-C.; Ko, C.-J.; Wu, J.-L.; Chen, W.-C., Morphological Study of P3HT:PCBM Blend Films Prepared through Solvent Annealing for Solar Cell Applications. *Sol. Energy Mater. Sol. Cells* **2010**, *94*, 2426-2430.

39.   Sirringhaus, H., *et al.*, Two-Dimensional Charge Transport in Self-Organized, High-Mobility Conjugated Polymers. *Nature* **1999**, *401*, 685–688.

40.   Li, G.; Yao, Y.; Yang, H.; Shrotriya, V.; Yang, G.; Yang, Y., "Solvent Annealing" Effect in Polymer Solar Cells Based on Poly(3-Hexylthiophene) and Methanofullerenes. *Adv. Funct. Mater.* **2007**, *17*, 1636-1644.

41.   Janssen, G.; Aguirre, A.; Goovaerts, E.; Vanlaeke, P.; Poortmans, J.; Manca, J., Optimization of Morphology of P3HT/PCBM Films for Organic Solar Cells: Effects of Thermal Treatments and Spin Coating Solvents. *Eur. Phys. J.: Appl. Phys.* **2007**, *37*, 287-290.

42.   Kim, Y., *et al.*, A Strong Regioregularity Effect in Self-Organizing Conjugated Polymer Films and High-Efficiency Polythiophene:Fullerene Solar Cells. *Nat. Mater.* **2006**, *5*, 197–203.

43.   Nelson, J., Polymer:Fullerene Bulk Heterojunction Solar Cells. *Mater. Today* **2011**, *14*, 462-470.

44.   Veldman, D.; İpek, Ö.; Meskers, S. C. J.; Sweelssen, J.; Koetse, M. M.; Veenstra, S. C.; Kroon, J. M.; Bavel, S. S. van; Loos, J.; Janssen, R. A. J., Compositional and Electric Field Dependence of the Dissociation of Charge Transfer Excitons in Alternating Polyfluorene Copolymer/Fullerene Blends. *J. Am. Chem. Soc.* **2008**, *130*, 7721-7735.

45.   Keivanidis, P. E.; Clarke, T. M.; Lilliu, S.; Agostinelli, T.; Macdonald, J. E.; Durrant, J. R.; Bradley, D. D. C.; Nelson, J., Dependence of Charge Separation Efficiency on Film Microstructure in Poly(3-Hexylthiophene-2,5-Diyl):[6,6]-Phenyl-C61 Butyric Acid Methyl Ester Blend Films. *J. Phys. Chem. Lett.* **2010**, *1*, 734-738.

46.   Li, G.; Shrotriya, V.; Huang, J.; Yao, Y.; Moriarty, T.; Emery, K.; Yang, Y., High-Efficiency Solution Processable Polymer Photovoltaic Cells by Self-Organization of Polymer Blends. *Nat. Mater.* **2005**, *4*, 864–868.

47.   Dennler, G.; Scharber Markus, C.; Brabec Christoph, J., Polymer-Fullerene Bulk-Heterojunction Solar Cells. *Adv. Mater.* **2009**, *21*, 1323-1338.

48.   Trukhanov, V. A.; Bruevich, V. V.; Paraschuk, D. Y., Effect of Doping on Performance of Organic Solar Cells. *Phys. Rev. B* **2011**, *84*, 205318.

49.   Chen, H.-W.; Lee, J.-H.; Lin, B.-Y.; Chen, S.; Wu, S.-T., Liquid Crystal Display and Organic Light-Emitting Diode Display: Present Status and Future Perspectives. *Light: Sci. Appl.* **2018**, *7*, 17168(13).

50.   Hepp, A.; Heil, H.; Weise, W.; Ahles, M.; Schmechel, R.; von Seggern, H., Light-Emitting Field-Effect Transistor Based on a Tetracene Thin Film. *Phys. Rev. Lett.* **2003**, *91*, 157406.

51.   Muccini, M., A Bright Future for Organic Field-Effect Transistors. *Nat. Mater.* **2006**, *5*, 605-613.

52.   Zaumseil, J.; Sirringhaus, H., Electron and Ambipolar Transport in Organic Field-Effect Transistors. *Chem. Rev.* **2007**, *107*, 1296-1323.

53.   Cicoira, F.; Santato, C., Organic Light Emitting Field Effect Transistors: Advances and Perspectives. *Adv. Funct. Mater.* **2007**, *17*, 3421-3434.

54. Hotta, S.; Yamao, T.; Bisri, S. Z.; Takenobu, T.; Iwasa, Y., Organic Single-Crystal Light-Emitting Field-Effect Transistors. *J. Mater. Chem. C* **2014**, *2*, 965-980.

55. Karl, N., Charge Carrier Transport in Organic Semiconductors. *Synth. Met.* **2003**, *133-134*, 649-657.

56. Podzorov, V., Organic Single Crystals: Addressing the Fundamentals of Organic Electronics. *MRS Bull.* **2013**, *38*, 15-24.

57. Wang, C.; Dong, H.; Jiang, L.; Hu, W., Organic Semiconductor Crystals. *Chem. Soc. Rev.* **2018**, *47*, 422-500.

58. Ohno, Y. In *Color Rendering and Luminous Efficacy of White LED Spectra*, Optical Science and Technology, the SPIE 49th Annual Meeting, SPIE: 2004; p 11.

59. Reinhard, E.; Khan, E. A.; Akyuz, A. O.; Johnson, G., *Color Imaging: Fundamentals and Applications*; A K Peters/CRC Press 2008.

60. Baleizão, C.; Berberan-Santos, M. N., Thermally Activated Delayed Fluorescence in Fullerenes. *Ann. N.Y. Acad. Sci.* **2008**, *1130*, 224-234.

61. Jou, J.-H.; Kumar, S.; Agrawal, A.; Li, T.-H.; Sahoo, S., Approaches for Fabricating High Efficiency Organic Light Emitting Diodes. *J. Mater. Chem. C* **2015**, *3*, 2974-3002.

62. Smith, L. H.; Wasey, J. A. E.; Samuel, I. D. W.; Barnes, W. L., Light out-Coupling Efficiencies of Organic Light-Emitting Diode Structures and the Effect of Photoluminescence Quantum Yield. *Adv. Funct. Mater.* **2005**, *15*, 1839-1844.

63. Wang, H., *et al.*, Doped Organic Crystals with High Efficiency, Color-Tunable Emission toward Laser Application. *Cryst. Growth Des.* **2009**, *9*, 4945-4950.

64. Koh, T.-W.; Spechler, J. A.; Lee, K. M.; Arnold, C. B.; Rand, B. P., Enhanced Outcoupling in Organic Light-Emitting Diodes via a High-Index Contrast Scattering Layer. *ACS Photonics* **2015**, *2*, 1366-1372.

65. Preinfalk, J. B.; Eiselt, T.; Wehlus, T.; Rohnacher, V.; Hanemann, T.; Gomard, G.; Lemmer, U., Large-Area Screen-Printed Internal Extraction Layers for Organic Light-Emitting Diodes. *ACS Photonics* **2017**, *4*, 928-933.

66. Lanzani, G., *The Photophysics Behind Photovoltaics and Photonics*; Wiley-VCH: Weinheim, Germany, 2012.

67. Brabec, C.; Scherf, U.; Dyakonov, V., *Organic Photovoltaics: Materials, Device Physics, and Manufacturing Technologies*; Wiley-VCH Verlag GmbH & Co. KGaA: Weinheim, Germany, 2011.

68. Hedley, G. J.; Ruseckas, A.; Samuel, I. D. W., Light Harvesting for Organic Photovoltaics. *Chem. Rev.* **2017**, *117*, 796-837.

69. Serbenta, A.; Kozlov, O. V.; Portale, G.; van Loosdrecht, P. H. M.; Pshenichnikov, M. S., Bulk Heterojunction Morphology of Polymer:Fullerene Blends Revealed by Ultrafast Spectroscopy. *Sci. Rep.* **2016**, *6*, 36236.

70. Kamtekar Kiran, T.; Monkman Andrew, P.; Bryce Martin, R., Recent Advances in White Organic Light-Emitting Materials and Devices (WOLEDs). *Adv. Mater.* **2009**, *22*, 572-582.

71. Menke, S. M.; Holmes, R. J., Exciton Diffusion in Organic Photovoltaic Cells. *Energy Environ. Sci.* **2014**, *7*, 499-512.

72. Mikhnenko, O. V.; Blom, P. W. M.; Nguyen, T.-Q., Exciton Diffusion in Organic Semiconductors. *Energy Environ. Sci.* **2015**, *8*, 1867-1888.

73. Scholes, G. D., Long-Range Resonance Energy Transfer in Molecular Systems. *Annu. Rev. Phys. Chem.* **2003**, *54*, 57-87.

74. Simpson, O., Electronic Properties of Aromatic Hydrocarbons. III. Diffusion of Excitons. *Proc. R. Soc. London, Ser. A* **1957**, *238*, 402-411.

75. Michel-Beyerle, M. E.; Haberkorn, R.; Kinder, J.; Seidlitz, H., Direct Evidence for the Singlet-Triplet Exciton Annihilation in Anthracene Crystals. *Phys. Status Solidi (b)* **1978**, *85*, 45-49.

76. Kalinowski, J.; Stampor, W.; Di Marco, P.; Garnier, F., Photogeneration of Charge in Solid Films of A-Sexithiophene. *Chem. Phys.* **1998**, *237*, 233-243.

77. Akselrod, G. M.; Prins, F.; Poulikakos, L. V.; Lee, E. M. Y.; Weidman, M. C.; Mork, A. J.; Willard, A. P.; Bulović, V.; Tisdale, W. A., Subdiffusive Exciton Transport in Quantum Dot Solids. *Nano Lett.* **2014**, *14*, 3556-3562.

78. Parashchuk, O. D.; Mannanov, A. A.; Konstantinov, V. G.; Dominskiy, D. I.; Surin, N. M.; Borshchev, O. V.; Ponomarenko, S. A.; Pshenichnikov, M. S.; Paraschuk, D. Y., Molecular Self-Doping Controls Luminescence of Pure Organic Single Crystals. *Adv. Funct. Mater.* **2018**, *28*, 1800116.

79. Poulsen, L., *et al.*, Three-Dimensional Energy Transport in Highly Luminescent Host−Guest Crystals: A Quantitative Experimental and Theoretical Study. *J. Am. Chem. Soc.* **2007**, *129*, 8585-8593.

80. Suna, A., Kinematics of Exciton-Exciton Annihilation in Molecular Crystals. *Phys. Rev. B* **1970**, *1*, 1716-1739.

81. Lewis, A. J.; Ruseckas, A.; Gaudin, O. P. M.; Webster, G. R.; Burn, P. L.; Samuel, I. D. W., Singlet Exciton Diffusion in Meh-PPV Films Studied by Exciton–Exciton Annihilation. *Org. Electron.* **2006**, *7*, 452-456.

82. Fravventura, M. C.; Hwang, J.; Suijkerbuijk, J. W. A.; Erk, P.; Siebbeles, L. D. A.; Savenije, T. J., Determination of Singlet Exciton Diffusion Length in Thin Evaporated C60 Films for Photovoltaics. *J. Phys. Chem. Lett.* **2012**, *3*, 2367-2373.

83. Kozlov, O. V.; de Haan, F.; Kerner, R. A.; Rand, B. P.; Cheyns, D.; Pshenichnikov, M. S., Real-Time Tracking of Singlet Exciton Diffusion in Organic Semiconductors. *Phys. Rev. Lett.* **2016**, *116*, 057402.

84. Dowgiallo, A.-M.; Mistry, K. S.; Johnson, J. C.; Reid, O. G.; Blackburn, J. L., Probing Exciton Diffusion and Dissociation in Single-Walled Carbon Nanotube–C60 Heterojunctions. *J. Phys. Chem. Lett.* **2016**, *7*, 1794-1799.

85. Hiszpanski, A. M.; Loo, Y.-L., Directing the Film Structure of Organic Semiconductors via Post-Deposition Processing for Transistor and Solar Cell Applications. *Energy Environ. Sci.* **2014**, *7*, 592-608.

86. Agostinelli, T., *et al.*, Real-Time Investigation of Crystallization and Phase-Segregation Dynamics in P3HT:PCBM Solar Cells During Thermal Annealing. *Adv. Funct. Mater.* **2011**, *21*, 1701-1708.

87. Collins, B. A.; Tumbleston, J. R.; Ade, H., Miscibility, Crystallinity, and Phase Development in P3HT/PCBM Solar Cells: Toward an Enlightened Understanding of Device Morphology and Stability. *J. Phys. Chem. Lett.* **2011**, *2*, 3135-3145.

88. Padinger, F.; Rittberger, R. S.; Sariciftci, N. S., Effects of Postproduction Treatment on Plastic Solar Cells. *Adv. Funct. Mater.* **2003**, *13*, 85-88.

89. Riedel, I.; Parisi, J.; Dyakonov, V.; Lutsen, L.; Vanderzande, D.; Hummelen, J. C., Effect of Temperature and Illumination on the Electrical Characteristics of Polymer–Fullerene Bulk-Heterojunction Solar Cells. *Adv. Funct. Mater.* **2004**, *14*, 38-44.

90.   Ma, W.; Yang, C.; Gong, X.; Lee, K.; Heeger, A. J., Thermally Stable, Efficient Polymer Solar Cells with Nanoscale Control of the Interpenetrating Network Morphology. *Adv. Funct. Mater.* **2005**, *15*, 1617-1622.

91.   Peet, J.; Kim, J. Y.; Coates, N. E.; Ma, W. L.; Moses, D.; Heeger, A. J.; Bazan, G. C., Efficiency Enhancement in Low-Bandgap Polymer Solar Cells by Processing with Alkane Dithiols. *Nat. Mater.* **2007**, *6*, 497-500.

92.   Li, G.; Shrotriya, V.; Yao, Y.; Yang, Y., Investigation of Annealing Effects and Film Thickness Dependence of Polymer Solar Cells Based on poly(3-Hexylthiophene). *J. Appl. Phys.* **2005**, *98*, 043704.

93.   Roige, A.; Campoy-Quiles, M.; Osso, J. O.; Alonso, M. I.; Vega, L. F.; Garriga, M., Surface Vs Bulk Phase Transitions in Semiconducting Polymer Films for OPV and OLED Applications. *Synth. Met.* **2012**, *161*, 2570-2574.

94.   Wang, T., *et al.*, The Development of Nanoscale Morphology in Polymer: Fullerene Photovoltaic Blends During Solvent Casting. *Soft Matter* **2010**, *6*, 4128-4134.

95.   Leman, D.; Kelly, M. A.; Ness, S.; Engmann, S.; Herzing, A.; Snyder, C.; Ro, H. W.; Kline, R. J.; DeLongchamp, D. M.; Richter, L. J., In Situ Characterization of Polymer–Fullerene Bilayer Stability. *Macromol.* **2015**, *48*, 383-392.

96.   Treat, N. D.; Brady, M. A.; Smith, G.; Toney, M. F.; Kramer, E. J.; Hawker, C. J.; Chabinyc, M. L., Interdiffusion of PCBM and P3HT Reveals Miscibility in a Photovoltaically Active Blend. *Adv. Energy Mater.* **2011**, *1*, 82-89.

97.   Grancini, G.; Polli, D.; Fazzi, D.; Cabanillas-Gonzalez, J.; Cerullo, G.; Lanzani, G., Transient Absorption Imaging of P3HT:PCBM Photovoltaic Blend: Evidence for Interfacial Charge Transfer State. *J. Phys. Chem. Lett.* **2011**, *2*, 1099-1105.

98.   Westenhoff, S.; Howard, I. A.; Friend, R. H., Probing the Morphology and Energy Landscape of Blends of Conjugated Polymers with Sub-10 Nm Resolution. *Phys. Rev. Lett.* **2008**, *101*, 016102.

99.   Demir, F.; Van den Brande, N.; Van Mele, B.; Bertho, S.; Vanderzande, D.; Manca, J.; Van Assche, G., Isothermal Crystallization of P3HT:PCBM Blends Studied by Rhc. *J. Therm. Anal. Calorim.* **2011**, *105*, 845-849.

100.   Wunderlich, B., Theory of Cold Crystallization of High Polymers. *J. Chem. Phys.* **1958**, *29*, 1395-1404.

101.   Ke, B., Differential Thermal Analysis of High Polymers. IV. Saturated Linear Polyesters. *J. Appl. Polym. Sci.* **1962**, *6*, 624-628.

102.   Mannanov, A. A.; Bruevich, V. V.; Feldman, E. V.; Trukhanov, V. A.; Pshenichnikov, M. S.; Paraschuk, D. Y., Real-Time Tracking of Polymer Crystallization Dynamics in Organic Bulk Heterojunctions by Raman Microscopy. *J. Phys. Chem. C* **2018**.

103.   Chirvase, D.; Parisi, J.; Hummelen, J. C.; Dyakonov, V., Influence of Nanomorphology on the Photovoltaic Action of Polymer–Fullerene Composites. *Nanotechnology* **2004**, *15*, 1317-1323.

104.   Gluecker, M.; Foertig, A.; Dyakonov, V.; Deibel, C., Impact of Nongeminate Recombination on the Performance of Pristine and Annealed P3HT:PCBM Solar Cells. *Phys. Status Solidi RRL* **2012**, *6*, 337-339.

105.   Carswell, D. J.; Ferguson, J.; Lyons, L. E., Photo- and Semi-Conductance in Molecular Single Crystals. *Nature* **1954**, *173*, 736.

106.   Sangster, R. C.; Irvine, J. W., Study of Organic Scintillators. *J. Chem. Phys.* **1956**, *24*, 670-715.

107.   Choi, H. H.; Cho, K.; Frisbie, C. D.; Sirringhaus, H.; Podzorov, V., Critical Assessment of Charge Mobility Extraction in Fets. *Nat. Mater.* **2017**, *17*, 2-7.

108.   Kim, J.-S.; Ho, P. K. H.; Greenham, N. C.; Friend, R. H., Electroluminescence Emission Pattern of Organic Light-Emitting Diodes: Implications for Device Efficiency Calculations. *J. Appl. Phys.* **2000**, *88*, 1073-1081.

109.   Mayr, C.; Schmidt, T. D.; Brütting, W., High-Efficiency Fluorescent Organic Light-Emitting Diodes Enabled by Triplet-Triplet Annihilation and Horizontal Emitter Orientation. *Appl. Phys. Lett.* **2014**, *105*, 183304.

110.   Gierschner, J.; Park, S. Y., Luminescent Distyrylbenzenes: Tailoring Molecular Structure and Crystalline Morphology. *J. Mater. Chem. C* **2013**, *1*, 5818-5832.

111.   Gierschner, J.; Lüer, L.; Milián-Medina, B.; Oelkrug, D.; Egelhaaf, H.-J., Highly Emissive H-Aggregates or Aggregation-Induced Emission Quenching? The Photophysics of All-Trans Para-Distyrylbenzene. *J. Phys. Chem. Lett.* **2013**, *4*, 2686-2697

112.   Takeshi, Y.; Yuki, T.; Kazunori, Y.; Tomoharu, M.; Takayuki, O.; Shu, H., Polarized Emissions from Single Crystals of Thiophene/Phenylene Co-Oligomers Measured by Microspectroscopy. *Jpn. J. Appl. Phys.* **2008**, *47*, 4719.

113.   Northrop, D. C.; Simpson, O., Electronic Properties of Aromatic Hydrocarbons II. Fluorescence Transfer in Solid Solutions. *Proc. R. Soc. London, Ser. A* **1956**, *234*, 136.

114.   Powell, R. C.; Soos, Z. G., Singlet Exciton Energy Transfer in Organic Solids. *J. Lumin.* **1975**, *11*, 1-45.

115.   Hu, P.; Du, K.; Wei, F.; Jiang, H.; Kloc, C., Crystal Growth, Homo–Lumo Engineering, and Charge Transfer Degree in Perylene-Fxtcnq (X = 1, 2, 4) Organic Charge Transfer Binary Compounds. *Cryst. Growth Des.* **2016**, *16*, 3019-3027.

116.   Lakowicz, J. R., Energy Transfer. In *Principles of Fluorescence Spectroscopy*, Lakowicz, J. R., Ed. Springer US: Boston, MA, 2006; pp 443-475.

117.   Förster, T., Transfer Mechanisms of Electronic Excitation Energy. *Radiat. Res., Suppl.* **1960**, *2*, 326-339.

118.   Lei, Y.-L.; Jin, Y.; Zhou, D.-Y.; Gu, W.; Shi, X.-B.; Liao, L.-S.; Lee, S.-T., White-Light Emitting Microtubes of Mixed Organic Charge-Transfer Complexes. *Adv. Mater.* **2012**, *24*, 5345-5351.

119.   Gierschner, J.; Varghese, S.; Park, S. Y., Organic Single Crystal Lasers: A Materials View. *Adv. Opt. Mater.* **2016**, *4*, 348-364.

120.   Muccini, M.; Koopman, W.; Toffanin, S., The Photonic Perspective of Organic Light-Emitting Transistors. *Laser Photonics Rev.* **2011**, *6*, 258-275.

121.   Smits, E. C. P., *et al.*, Bottom-up Organic Integrated Circuits. *Nature* **2008**, *455*, 956.

122.   Novak, M., *et al.*, Low-Voltage P- and N-Type Organic Self-Assembled Monolayer Field Effect Transistors. *Nano Lett.* **2011**, *11*, 156-159.

123.   Ringk, A., *et al.*, N-Type Self-Assembled Monolayer Field-Effect Transistors and Complementary Inverters. *Adv. Funct. Mater.* **2012**, *23*, 2016-2023.

124.   Bigelow, W. C.; Pickett, D. L.; Zisman, W. A., Oleophobic Monolayers: I. Films Adsorbed from Solution in Non-Polar Liquids. *J. Colloid Sci.* **1946**, *1*, 513-538.

125.   Polymeropoulos, E. E.; Sagiv, J., Electrical Conduction through Adsorbed Monolayers. *J. Chem. Phys.* **1978**, *69*, 1836-1847.

126. Sagiv, J., Organized Monolayers by Adsorption. II. Molecular Orientation in Mixed Dye Monolayers Built on Anisotropic Polymeric Surfaces. *Isr. J. Chem.* **1979**, *18*, 339-345.

127. Chen, X.; Lenhert, S.; Hirtz, M.; Lu, N.; Fuchs, H.; Chi, L., Langmuir–Blodgett Patterning: A Bottom–up Way to Build Mesostructures over Large Areas. *Acc. Chem. Res.* **2007**, *40*, 393-401.

128. Agina, E. V., *et al.*, Formation of Self-Assembled Organosilicon-Functionalized Quinquethiophene Monolayers by Fast Processing Techniques. *Langmuir* **2012**, *28*, 16186-16195.

129. Kotov, N. A.; Meldrum, F. C.; Wu, C.; Fendler, J. H., Monoparticulate Layer and Langmuir-Blodgett-Type Multiparticulate Layers of Size-Quantized Cadmium Sulfide Clusters: A Colloid-Chemical Approach to Superlattice Construction. *J. Phys. Chem.* **1994**, *98*, 2735-2738.

130. Santhanam, V.; Andres, R. P., Microcontact Printing of Uniform Nanoparticle Arrays. *Nano Lett.* **2004**, *4*, 41-44.

131. Bisri, S. Z.; Takenobu, T.; Yomogida, Y.; Shimotani, H.; Yamao, T.; Hotta, S.; Iwasa, Y., High Mobility and Luminescent Efficiency in Organic Single-Crystal Light-Emitting Transistors. *Adv. Funct. Mater.* **2009**, *19*, 1728-1735.

132. Hotta, S.; Yamao, T., The Thiophene/Phenylene Co-Oligomers: Exotic Molecular Semiconductors Integrating High-Performance Electronic and Optical Functionalities. *J. Mater. Chem.* **2011**, *21*, 1295-1304.

133. Sizov, A. S.; Agina, E. V.; Gholamrezaie, F.; Bruevich, V. V.; Borshchev, O. V.; Paraschuk, D. Y.; de Leeuw, D. M.; Ponomarenko, S. A., Oligothiophene-Based Monolayer Field-Effect Transistors Prepared by Langmuir-Blodgett Technique. *Appl. Phys. Lett.* **2013**, *103*, 043310.

134. Borshchev, O. V.; Sizov, A. S.; Agina, E. V.; Bessonov, A. A.; Ponomarenko, S. A., Synthesis of Organosilicon Derivatives of [1]Benzothieno[3,2-B][1]-Benzothiophene for Efficient Monolayer Langmuir–Blodgett Organic Field Effect Transistors. *Chem. Commun.* **2017**, *53*, 885-888.

135. Agina, E. V., *et al.*, Luminescent Organic Semiconducting Langmuir Monolayers. *ACS Appl. Mater. Interfaces* **2017**, *9*, 18078-18086.

136. Lefrant, S.; Perrin, E.; Buisson, J. P.; Eckhardt, H.; Han, C. C., Vibrational Studies of Polyparaphenylene-Vinylene (PPV). *Synth. Met.* **1989**, *29*, 91-96.

137. Sakamoto, A.; Furukawa, Y.; Tasumi, M., Infrared and Raman Studies of poly(P-Phenylenevinylene) and Its Model Compounds. *J. Phys. Chem.* **1992**, *96*, 1490-1494.

138. Rumi, M.; Zerbi, G.; Müllen, K.; Müller, G.; Rehahn, M., Nonlinear Optical and Vibrational Properties of Conjugated Polyaromatic Molecules. *J. Chem. Phys.* **1997**, *106*, 24-34.

139. Shorygin, P. P., Raman Scattering and Conjugation. *Russ. Chem. Rev.* **1971**, *40*, 367-392.

140. Tsoi, W. C.; James, D. T.; Kim, J. S.; Nicholson, P. G.; Murphy, C. E.; Bradley, D. D. C.; Nelson, J.; Kim, J. S., The Nature of in-Plane Skeleton Raman Modes of P3HT and Their Correlation to the Degree of Molecular Order in P3HT:PCBM Blend Thin Films. *J. Am. Chem. Soc.* **2011**, *133*, 9834-9843.

141. Yun, J.-J.; Peet, J.; Cho, N.-S.; Bazan, G. C.; Lee, S. J.; Moskovits, M., Insight into the Raman Shifts and Optical Absorption Changes Upon Annealing Polymer/Fullerene Solar Cells. *Appl. Phys. Lett.* **2008**, *92*, 251912.

142.   Gao, Y. Q.; Grey, J. K., Resonance Chemical Imaging of Polythiophene/Fullerene Photovoltaic Thin Films: Mapping Morphology-Dependent Aggregated and Unaggregated C=C Species. *J. Am. Chem. Soc.* **2009**, *131*, 9654-9662.

143.   Gao, Y.; Martin, T. P.; Niles, E. T.; Wise, A. J.; Thomas, A. K.; Grey, J. K., Understanding Morphology-Dependent Polymer Aggregation Properties and Photocurrent Generation in Polythiophene/Fullerene Solar Cells of Variable Compositions. *J. Phys. Chem. C* **2010**, *114*, 15121-15128.

144.   Gao, Y.; Grey, J. K., Resonance Chemical Imaging of Polythiophene/Fullerene Photovoltaic Thin Films: Mapping Morphology-Dependent Aggregated and Unaggregated C═C Species. *J. Am. Chem. Soc.* **2009**, *131*, 9654-9662.

145.   Terzić, M.; Marinković, B. P.; Šević, D.; Jureta, J.; Milosavljević, A. R., Development of Time-Resolved Laser-Induced Fluorescence Spectroscopic Technique for the Analysis of Biomolecules. *Facta Univ., Ser.: Phys., Chem. Technol.* **2008**, *6*, 105-117.

146.   Cehelnik, E. D.; Mielenz, K. D.; Cundall, R. B., *A Study of the Polarization of Fluorescence of Ordered Systems with Application to Ordered Liquid Crystals*, 1976; Vol. 80A.

147.   Chamarro, M.; Gourdon, C.; Lavallard, P., Photoluminescence Polarization of Semiconductor Nanocrystals. *J. Lumin.* **1996**, *70*, 222-237.

148.   Prutskij, T.; Percino, M. J.; Perova, T. S., Polarization Anisotropy of Photoluminescence from Triphenylamine-Based Molecular Single Crystals. *Cryst. Res. Technol.* **2013**, *48*, 1039-1043.

149.   Lu, H.; Wu, S.; Zhang, C.; Qiu, L.; Wang, X.; Zhang, G.; Hu, J.; Yang, J., Photoluminescence Intensity and Polarization Modulation of a Light Emitting Liquid Crystal via Reversible Isomerization of an A-Cyanostilbenic Derivative. *Dyes Pigm.* **2016**, *128*, 289-295.

Chapter 2. Real-Time Tracking of Polymer Crystallization Dynamics in Bulk Heterojunctions by Raman Microscopy
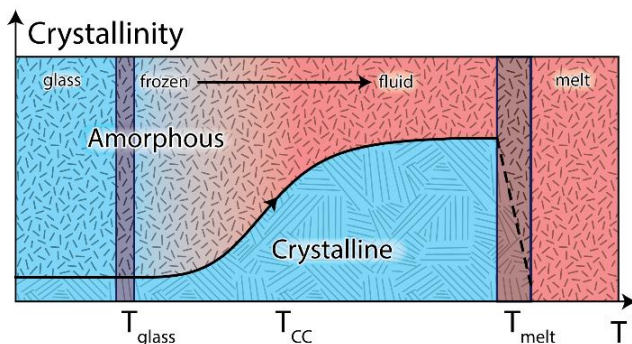
State-of-the-art organic photovoltaic active layers typically undergo post-treatment such as thermal or solvent vapor annealing to increase their performance by tuning the bulk heterojunction morphology. The molecular crystallinity is one of the key factors that determine the morphology. Real-time tracking of the crystallinity during the post-treatment is strongly desired for understanding the physics of the crystallization process and for optimizing the post treatment protocol. Here, we report on cold crystallization dynamics of the polymer in the temperature range of 50–150 °C in polymer:fullerene blends based on poly(3-hexylthiophene) with various fullerene-based acceptors (C_{60}, $PC_{61}BM$, $PC_{71}BM$, $bisPC_{61}BM$, HBIM, AIM8, and IrC_{60}) in real-time by Raman microscopy. We also reveal how different solvents, fullerene acceptors, and temperatures affect cold crystallization during thermal annealing. We further demonstrate a correlation between the fullerene derivative weight and the polymer crystallinity for the as-cast films, and also a correlation of the polymer crystallinity before and after annealing. Our findings are essential for developing efficient strategies of morphology optimization in emerging organic photovoltaic devices with the real-time Raman microscopy tracking as a valuable tool.

2.1. Introduction

The most efficient organic photovoltaic devices (OPDs), e.g., solar cells and photodetectors, are based on bulk heterojunctions (BHJs)[1-2] that are phase separated blends of donor and acceptor semiconductor materials.[3-6] For efficient OPDs, the organic BHJs should have a specific morphology of the donor and acceptor separated phases to provide efficient exciton dissociation, separation of free charges, and their transport to the device electrodes.[5, 7]

Polymer:fullerene blends, as the most studied BHJs, have been in the focus of research for the last two decades.[4-5, 8] In many cases, the charge generation and transport in such blends are affected by polymer crystallization,[8-9] which can be largely disturbed by fullerene acceptor molecules.[10] The polymer:fullerene blend morphology changes upon annealing have been probed by a number of experimental techniques: in-situ atomic force microscopy,[11] UV–vis spectroscopy,[12] X-ray diffraction,[9, 12] ellipsometry,[13-14] scanning electron microscopy,[15] and ultrafast spectroscopy.[16-18] For instance, as-cast poly(3-hexylthiophene) (P3HT) with [6,6]-phenyl C61 butyric acid methyl ester ($PC_{61}BM$) blends usually show a non-optimal morphology that results in their poor photovoltaic performance, specifically in low power conversion efficiency (*PCE*).[19]

Thermal or solvent annealing are commonly used to optimize the BHJ morphology.[12, 20-22] For annealing the polymer, the following two temperatures define the operational window: the glass transition temperature T_g,[23-24] (the lower limit) and the melting temperature of the crystalline phase T_m (the upper limit). Between these two temperatures the polymer chains acquire mobility, partially crystallize and hence become more ordered — the process known as cold crystallization (CC).[25-26] In the $P3HT:PC_{61}BM$ blends, CC results in an increase in the optical absorption at the longer wavelengths, the charge separation efficiency and carrier mobility; these all lead to a significant boost in the *PCE*.[19, 24, 27-28] For instance, differential scanning calorimetry (DSC) studies[29] revealed that the morphology of $P3HT:PC_{61}BM$ blend films results from a dual crystallization as the crystallization of both donor and acceptor phases is hindered by the other one during thermal annealing.

Raman microscopy possesses a unique ability to distinguish crystalline and amorphous domains in the BHJ.[30-31] This ability is based on the fact that the frequency of delocalized carbon-carbon stretching modes is changed upon crystallization due to interchain interactions. This approach was developed by Kim

and coworkers[32] who demonstrated that the contributions of amorphous and quasi-crystalline polymer phases to the Raman spectra of P3HT:PC$_{61}$BM blends can be factorized.[32-33] In particular, they showed that the shifts of the frequency of the Raman carbon-carbon band can be attributed to crystallization of the polymer phase in the blend films during annealing.[34] Here we refine the Raman method developed in Ref. 32 to track the polymer crystallinity *in real-time* during CC of the polymer phase and apply this technique to study thermal annealing in various P3HT:fullerene blends.

Apart from the commonly-used PC$_{61}$BM acceptor, other fullerene-based acceptors are actively studied to increase the OPD performance via increase of the acceptor optical absorption, reduction of the acceptor electron affinity (to increase the operating voltage of OPD), and to optimize the donor:acceptor miscibility in blend.[35-39] Although it is known that the acceptor molecules in the BHJ disturbs the ordered polymer phase,[10] there is still a lack of understanding how strong its effect is on the polymer phase crystallinity in the BHJ with non-PCBM fullerene acceptors. This understanding is important for optimization of the post-deposition treatment protocols of such blends used as the OPD active layers.

In this Chapter, we report the polymer crystallization dynamics tracked by the real-time Raman microscopy technique during thermal annealing in the BHJ blends cast from different solvents and in the blends with various fullerene-based acceptors, with P3HT as an archetypical example. Casting blends from the higher-boiling-point solvent results in a larger content of the quasicrystalline phase in as-cast films. We show a correlation of the polymer crystallinity before and after the CC. We also establish how different solvents, blend compositions, and temperatures induce polymer mobility during thermal annealing. Thus, the real-time Raman microscopy technique provides an easy access to polymer crystallization dynamics of organic photovoltaic active layers during their postprocessing.

2.2. Materials and Methods

2.2.1. Materials

Regioregular P3HT (RR-P3HT) was purchased from Lumtec. The weight-average (Mw) and regioregularity are >45,000 kg/mol, >95%, respectively. Regiorandom P3HT (RRa-P3HT) was purchased from Rieke-Metals. The weight-average molecular weight (Mw) was >60,000 kg/mol. Different fullerene-based acceptors

were studied (Supplementary Information, Section 2.4.1): C_{60}, $PC_{61}BM$, $PC_{71}BM$, 1-(3,5-di-tret-butyl-4-hydroxybenzyl)-3-(3-cyclopropane[1,9](C_{60}-Ih)[5,6]fullerene-3-yl)-indolin-2-one (HBIM),[40] 1-Tetradecyl-3-(3-cyclopropane[1,9](C_{60}-Ih)[5,6]fullerene-3-yl)-indolin-2-one (AIM8),[41] exohedral metallocomplex (η_2-C_{60})IrH(CO)[(+)-2,3-O-isopropylidene-2,3-dihydroxy-1,4-bis(diphenylphosphino)butane] (IrC$_{60}$),[42] and [6,6]-Diphenyl-C62-bis(butyric acid methyl ester) (bisPC$_{61}$BM)[43]. C_{60}, $PC_{61}BM$, bisPC$_{61}$BM and $PC_{71}BM$ with purity of >99.5%; >99.5%; >99.5%; >99%, respectively, were purchased from Solenne BV. HBIM and AIM8 were obtained from Arbuzov Institute of Organic and Physical Chemistry (Russian Academy of Sciences) while IrC$_{60}$ was obtained from Nesmeyanov Institute of Organoelement Compounds (Russian Academy of Sciences). Synthesis and characterization of HBIM, AIM8, and IrC$_{60}$ were reported elsewhere.[40-42] All the materials were used without additional purification.

2.2.2. Thin Films

Solutions for active layers were prepared by dissolving P3HT and fullerene derivatives together in orthodichlorobenzene (DCB) at a weight ratio of 1:1 and a total concentration of 20 g/L. This ratio was chosen as optimal or close to optimal for solar cells based on P3HT and the studied fullerene derivatives.[27, 40-44] For the P3HT:PC$_{61}$BM and P3HT:PC$_{71}$BM blends, chlorobenzene (CB) and chloroform (CF) solvents were also used. The solutions were stirred at a magnetic stirrer for 5 hours at 75 °C and then were spin-cast at 900 rpm on a glass substrate. The resulted film thicknesses measured with an atomic force microscope (NTEGRA Spectra, NT-MDT) were in the range of 80–150 nm.

2.2.3. Raman Spectra

Raman spectra were recorded using a Renishaw inVia Raman microscope (50x, NA=0.5 Nikon large working distance objective) in the confocal configuration. The excitation laser wavelength was set at 488 nm (Ar$^+$ laser line). It has been shown that this (resonant) excitation wavelength provides high Raman sensitivity to P3HT crystallization.[32] The excitation beam power on the sample was 0.25 mW to ensure a linear excitation regime (Section 2.4.2); the acquisition time of one Raman spectrum with ~1 cm^{-1} resolution was ~1 s. To avoid laser-induced changes of the sample (e.g. photodegradation and laser heating) under long-time exposure, the Raman spectra were collected by scanning over the sample area of ~ 100x100 μm^2

and then averaged (see Section 2.4.3 for details). The sample temperature was controlled by a Linkam stage (THMS600) with nitrogen gas purging. Following Ref.[32], the Raman spectra were recorded and analyzed in the spectral region from 1350 to 1500 cm^{-1} containing the in-plane ring vibrations of P3HT: symmetric C=C stretch mode at 1450 cm^{-1} and C–C intraring stretch mode at 1380 cm^{-1} (assigned in Ref. 45), which are highly sensitive to the crystallization of polymer chains in resonant Raman conditions.

2.2.4. Annealing Protocols

Raman probing of polymer crystallization during thermal annealing was performed using two thermal annealing protocols: the fast and slow ones. In the fast protocol, annealing was performed under a constant elevated temperature to simulate common annealing protocols normally used to enhance the OPD performance.[46] The polymer:fullerene blend was first heated fast at the maximum heating rate (100 °C/min) up to a pre-set temperature (75, 90, 105, 120 °C) and then annealed at this temperature. The Raman spectra of the sample were recorded during the constant temperature phase of the experiment. This experiment was performed in real-time to obtain the crystallization rate *in situ*, i.e. during annealing. In the slow annealing protocol, the heating rate was set at a much lower value, 5 °C/min, to achieve quasi-static annealing,[34] in the temperature range of 20–170 °C.

2.2.5. Crystallinity Definition

The polymer crystallinity was calculated by fitting the Raman spectrum of the sample by a linear combination of the "amorphous" and "crystalline" reference spectra as was proposed by Tsoi *et al.*[32] (Section 2.4.2). However, important difference of this study is that the spectral decomposition was performed in real time at the current temperature of the sample (i.e., without having it cooled before the Raman measurements). This approach required to obtain reference Raman spectra at all temperatures used (see below). Raman spectra of the annealed pristine RR-P3HT and RRa-P3HT:PC$_{61}$BM (4:1 weight ratio to quench the polymer fluorescence) samples were used as the references for the quasi-crystalline and amorphous phases, respectively (Section 2.4.2). RRa-P3HT does not crystallize,[47] whereas pristine RR-P3HT shows the highest degree of crystallinity. The pristine P3HT samples were prepared as described in Ref. 32 to facilitate direct comparison of the results.

The polymer crystallinity in blend films was quantified by the "index of polymer crystallinity" (*IPC*). The *IPC* value was defined as a fraction of the RR-P3HT spectrum in the fit to the blend film spectrum, where the fit is constructed from a superposition of both reference spectra:[32]

$$IPC(T) = P_{RR}(T)\Big/\Big(P_{RRa}(T) \times \frac{\sigma_{RR}}{\sigma_{RRa}} + P_{RR}(T)\Big), \tag{2.1}$$

where P_{RR} and P_{RRa} are the fitting coefficients obtained as shares of the RR- and RRa-P3HT reference Raman spectra in the Raman spectrum of the blend (Section 2.4.2); *T* is the temperature, $\sigma_{RR}/\sigma_{RRa} = 1.2\pm0.2$ is the ratio of Raman cross-sections of the reference samples (Section 2.4.2). This ratio was obtained from Raman and Fourier-transform infrared (FTIR) absorption spectroscopy (Section 2.4.2). Unlike the approach based on comparing visible absorption spectra proposed in Ref. 32, the method applied here benefits from direct measurement of the chromophore density in the sample and hence should be more accurate for calculation of the relative Raman cross-sections. *IPC*=1 corresponds to the annealed pristine RR-P3HT film, while *IPC*=0 corresponds to the amorphous polymer.

The Raman spectra of conjugated polymers depend on temperature (Figure S2.3a).[33, 48-49] Therefore, we measured the reference Raman spectra at all temperatures with a 1°C step and used the corresponding spectra for calculation of the *IPC* according to Equation 2.1. Note that the ratio of Raman cross-sections of the reference samples does not show any temperature dependence (Figure S2.3b).

2.3. Results and Discussion

2.3.1. Real-Time Tracking of Polymer Crystallinity

Figure 2.1 shows polymer crystallization dynamics of P3HT:PC$_{61}$BM and P3HT:PC$_{71}$BM films for different annealing temperatures for the fast annealing protocol. At high temperatures (105, 120 °C), the *IPC* reaches 90% of its final value faster than in 5 min and then levels off. At low temperatures (75, 90 °C), the *IPC* dynamics exhibit different behavior: the initial crystallization rate is significantly lower, which is assigned to lower mobility of polymer chains so that the *IPC* does not reach the maximum achieved at higher temperatures. Note that *IPC*=1 does not imply that all RR-P3HT is in the crystalline state, but only the fraction that can crystallize; the share of this fraction was estimated as ~10% from the DSC data.[50]

As follows from Figure 2.1, the higher annealing temperature results in faster *IPC* rising at the initial annealing stage for both PCBMs. However, the polymer crystallization dynamics are somewhat different: the *IPC* rising amplitude during the first 2 minutes is lower for $PC_{61}BM$ (panel a) than for $PC_{71}BM$ (panel b), i.e. from ~0.43 to ~0.65 *vs*. from ~0.49 to ~0.8. This difference is explained by the effect of $PC_{61}BM$ and $PC_{71}BM$ on the polymer packing and will be discussed in detail in Section 2.3.3.
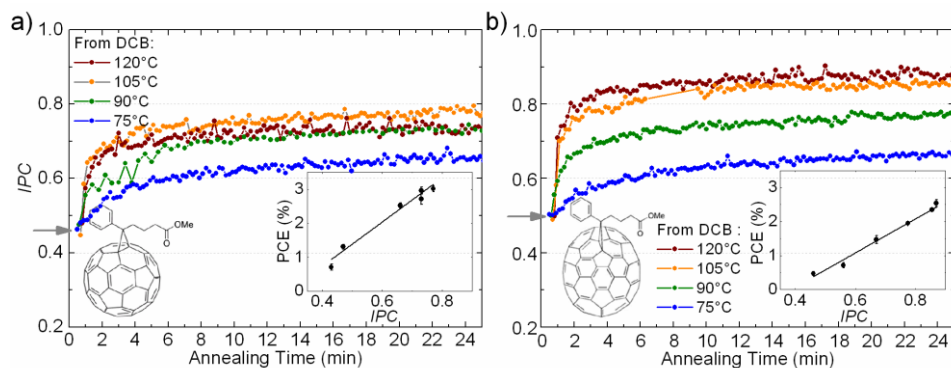
Figure 2.1. IPC dynamics in P3HT:$PC_{61}BM$ (a) and P3HT:$PC_{71}BM$ (b) blend films prepared from dichlorobenzene (DCB) for the fast annealing protocol (heating rate of 100 °C/min) at the following annealing temperatures: 75 (blue), 90 (olive), 105 (orange), 120 °C (wine). The arrows indicate the IPC values for the as-cast P3HT:$PC_{61}BM$ (~0.43) and P3HT:$PC_{71}BM$ (~0.49) blend films, respectively. At the initial stage of the heating process (0-1 minute), the sample temperature is not reliably established. The insets show the PCE vs. the final IPC in P3HT:$PC_{61}BM$ (a) and P3HT:$PC_{71}BM$ (b) solar cells. The lines in insets are linear fits.

The OPD performance based on P3HT:$PC_{61}BM$ blend depends strongly on the polymer crystallinity.[28, 51] Polymer crystallization results in the higher external quantum efficiency of the OPD and in the red shift of the absorption spectrum, which altogether lead to a significant *PCE* increase.[28] To investigate the effect of crystallinity on the *PCE*, the photovoltaic performance of the solar cell samples was examined (Section 2.4.4). The *PCE* showed excellent correlation with the *IPC* for both P3HT:$PC_{61}BM$ and P3HT:$PC_{71}BM$ blends (Figure 2.1, insets).

Thermal annealing optimizes the BHJ morphology by increasing the crystallinity of the conjugated polymer chains in the active layer. This increases charge mobility and reduces the energy of the lowest electronic state thereby broadening the absorption spectrum. All this leads to an increase in the short-circuit current and the

PCE,[52] which is fully consistent with our results. Moreover, the obtained correlation between the *IPC* and the *PCE* is in line with the previous studies probing the blend morphology and photovoltaic performance. Direct structural studies on P3HT:PC$_{61}$BM and P3HT:PC$_{71}$BM blends indicate that thermal annealing improves the polymer crystallinity resulting in a *PCE* increase.[36, 53-54]Furthermore, such a directly measured morphological parameter as the crystal domain purity, which is closely related to the *IPC*, clearly correlates with the *PCE* for a wide range of OPD including high-efficiency solar cells.[55]

2.3.2. Solvent Effect

To unravel the slow polymer crystallization dynamics, an annealing protocol with a significantly slower (quasistatic) temperature increase is required. As was established previously for the P3HT:PC$_{61}$BM blends,[34] dynamics of the C=C Raman band shift of P3HT during annealing was similar for the heating rates of 5 and 10 °C/min, indicating a quasistatic process. Therefore, for the slow annealing protocol, we chose a heating rate of 5 °C/min (Section 2.2), which allowed us to quantitatively describe the impact of solvent and various fullerene derivatives (Section 2.3.3) on the polymer crystallization.

Figure 2.2 shows *IPC* dynamics at the slow annealing protocol for P3HT:PC$_{61}$BM and P3HT:PC$_{71}$BM blend films prepared from different solvents. The data in both panels are subdivided into three areas: no evident *IPC* change at temperature below ~50°C; efficient polymer crystallization with a steep *IPC* increase in the range of 50–110°C; *IPC* levelling off at temperatures above ~110°C. According to the DSC data in Ref. 29, the glass transition temperature, T_g, in P3HT:PC$_{61}$BM 1:1 blends is about 50°C; therefore, T_g is well correlated with the beginning of the efficient annealing (*IPC* increase).

Annealing significantly increases the *IPC* of the P3HT:PC$_{61}$BM blend cast from CB, from 0.31±0.04 to 0.74±0.04. The *IPC* values before and after annealing are similar to those reported in Ref. 32: 0.42 to 0.94 (annealed at 140°C for 30 min), respectively (the *IPC* are recalculated from the crystalline molar fraction reported in Ref. 32). The difference in the *IPC* most probably originates from different approaches to evaluate the σ_{RR}/σ_{RRa} ratio, which in Ref. 32 was reported as 0.6 (see Supporting Information in Ref. 32). Using this value, we would obtain the *IPC* ranging from 0.45±0.04 to 0.88±0.04 before and after annealing, respectively, which is in better agreement with the values in Ref. 32.
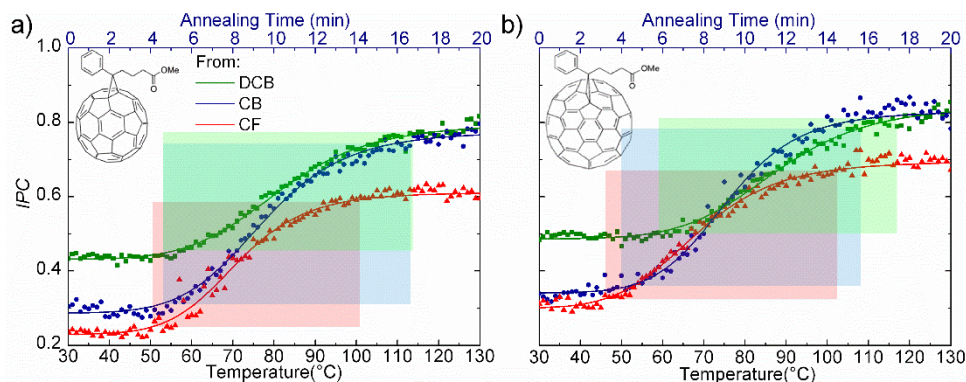
Figure 2.2. Real-time IPC dynamics at the slow (5 °C/min) annealing protocol as a function of the annealing temperature (at the bottom) and of the annealing time (at the top) for P3HT:PC$_{61}$BM (a) and P3HT:PC$_{71}$BM (b) blends films prepared from DCB (olive), CB (navy) and CF (red). The coordinates of the rectangles corners represent the parameters T_{CC}^{min}, T_{CC}^{max}, IPC$_I$, and IPC$_F$ calculated from the curves and introduced further in Section 2.3.2 (for the list of the parameters, see Table S2.2).

Figure 1.5 shows a schematic representation of the observed crystallization behavior of a polymer:fullerene blend at quasi-equilibrium heating (i.e., slow annealing protocol). The crystallization dynamics represented by the black curve is similar to the measured *IPC* dynamics for the P3HT:PC$_{61}$BM blend film shown in Figure S2.10a. According to the cold crystallization (CC) theory,[25] CC occurs above the glass transition temperature at which the amorphous phase in a polymer system can acquire mobility. In the temperature range between T_g and T_m, i.e., during the CC process, the polymer chains from the amorphous phase of the blend tend to crystallize. The polymer crystallization dynamics are irreversible in the temperature range of 50–110 °C in Figure 2.2 (Figure S2.9). This temperature range is very similar to that reported for the P3HT:PC$_{61}$BM blend by Demir *et al.*[23], who obtained T_g = 36 °C and the CC temperature region of ~70–150 °C from the rapid-scanning DSC. In our experiments, CC occurs at somewhat lower temperatures in the range 50–110 °C. The apparent difference in the CC temperatures can be assigned to different rates at which the sample was heated.[24] In the present experiments, the heating rate was a factor of 100 slower than in the rapid-scanning DSC so that the slow annealing protocol used herein is much closer to the thermodynamic equilibrium in the blend. Another reason of the mentioned difference could be assigned to the fact that the CC temperature depends on the film thickness.[56]

The real-time Raman microscopy technique allowed us to identify and quantify polymer crystallization in the form of temperature dependence similar to that recorded in a DSC scan. Indeed, the slow heating protocol is similar to the one routinely used in DSC. However, in contrast to DSC, the Raman technique benefits from chemical selectivity of the Raman spectrum. Therefore, the *IPC* curves report crystallization dynamics of the polymer chains in the blend, while the DSC curves encompass features of all components in the blend including, e.g., fullerene crystallization/melting.[14] Moreover, the real-time Raman microscopy technique can be applied directly to the OPD active layer at standard OPD post-treatment conditions — this is important as T_g and the CC temperature range depend on the film thickness.[24, 56] Finally, the data collection on thin films needs a few µg of material (i.e., the amount needed for film preparation), whereas DSC usually requires special non-equilibrium conditions and several mg of material.[23, 29]

To quantify the characteristic parameters of the blend film under annealing, we define the following quantities: (1) the *IPC* of the as-cast blend film, *IPC*$_{ac}$, that is an average value of the *IPC* below 50 °C; (2) *IPC* of the annealed blend film, *IPC*$_{an}$, that is an average value of the *IPC* within a 10-degrees window around the *IPC* maximum; (3) the initial *IPC* value which is provisionally defined as the latest value above the 5% uncertainty margin of the *IPC*$_{ac}$ value: *IPC*$_I$ = *IPC*$_{ac}$ + (*IPC*$_{an}$ − *IPC*$_{ac}$)·0.05, and a temperature corresponding to the initial *IPC*, T_{CC}^{min}, at which CC starts; (4) a temperature at which CC ends, T_{CC}^{max}, corresponding to the final *IPC*, *IPC*$_I$ = *IPC*$_{ac}$ + (*IPC*$_{an}$ – *IPC*$_{ac}$)·0.95. This temperature corresponds to the upper limit of CC: all the polymer chains that could crystallize have been crystallized. These four parameters are presented in Figure 2.2 as the coordinates of the rectangles corners (the parameter values are presented in Table S2.2). As follows from Figure 2.1, the *IPC* values before and after annealing are higher for PC$_{71}$BM, while Figure 2.2 demonstrates that the *IPC* in the P3HT:PC$_{71}$BM blend is always higher than that in the P3HT:PC$_{61}$BM blend. The difference is assigned to the larger molecule size of PC$_{71}$BM, which impedes mixing the fullerene derivative with the polymer chains and, therefore, less perturbs the polymer phase crystallinity.

As follows from Figure 2.2, the initial *IPC* values depend on the type of the solvent. Increasing the solvent boiling temperature in series of CF, CB, DCB (boiling temperatures are 61, 131, and 181°C, respectively) increases the solidification time of the liquid spin-cast films, which is determined by the solvent evaporation time, and results in longer time available for mobility of the polymer chains. This mobility fosters the initial crystallization during the film solidification and results in a clear

correlation between the IPC_I and the solvent boiling temperature (Table S2.2). Note that P3HT solubilities are very close in CF, CB, DCB (14–16 g/L), whereas $PC_{61}BM$ solubilities in these solvents are different (29, 60 and 42 g/L, respectively)[57] and do not correlate with the IPC (Figure 2.2a). This could be explained by the fact that the acceptor solubility largely affects the aggregated acceptor phase but not the mixed polymer:fullerene phase and hence the IPC.

Figure 2.2 indicates that the higher boiling solvent DCB as compared to CF results in increase of the CC temperature range (the horizontal size of the rectangles) from 50–100°C to 55–115 °C and from 45–100°C to 60–120 °C for $P3HT:PC_{61}BM$ and $P3HT:PC_{71}BM$, respectively. However, the CB-cast films show the same IPC_F as those prepared from DCB. Meanwhile, the CF-cast film exhibits the lowest IPC that does not achieve the maximum after annealing as was observed for the other solvents. Even though the initial IPC of the CF-cast and CB-cast films are very close, the IPC in the annealed CF-cast film is significantly lower (Figure 2.2). This indicates that the maximal IPC value critically depends on the solvent type, and the fullerene acceptor solubility[58] might be an essential factor. Therefore, the particular solvent used for blend preparation can increase both IPC_I and IPC_F. However, casting blends from some solvents (e.g., CF) might negatively affect the polymer phase crystallinity not allowing the highest IPC value even after thermal annealing of the blend films. As the films prepared from DCB showed the highest crystallinity, we decided to choose DCB as a solvent for the further study of blends of P3HT with different fullerene acceptors.

2.3.3. Various Fullerene-Based Acceptors

In the Raman technique, the IPC exclusively accounts for the properties of the polymer (donor) component in BHJ. As the acceptor component could affect both amorphous and crystalline phases of the blend, we studied how various fullerene derivatives influence the polymer crystallization dynamics during annealing.

Figure 2.3 shows slow annealing dynamics for P3HT:fullerene 1:1 blends spin-cast from DCB. All the blends demonstrate the three consecutive annealing phases similar to P3HT:fullerene blends (Figure 2.2; for IPC dynamics of C_{60} with all three annealing phases see Figure S2.10b).
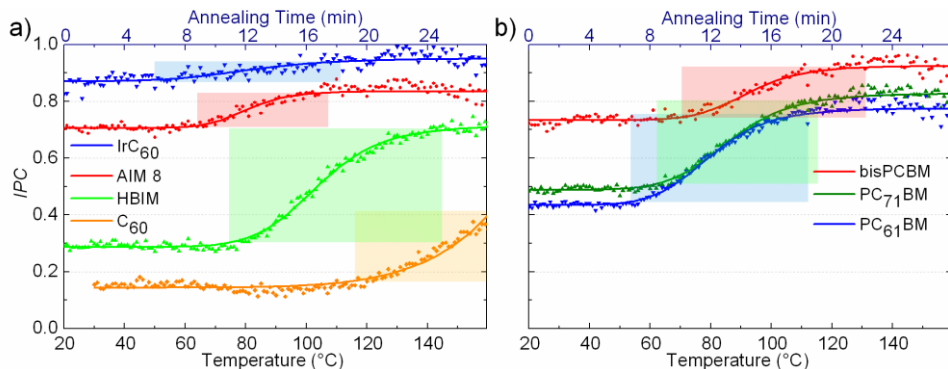
Figure 2.3. IPC for blend films of P3HT with various fullerene derivatives (in panel a: IrC_{60}, AIM8, HBIM and C_{60}; in panel b: $bisPC_{61}BM$, $PC_{71}BM$ and $PC_{61}BM$) as a function of the annealing temperature/time. The coordinates of the rectangles corners represent T_{CC}^{min}, T_{CC}^{max}, IPC_I, and IPC_F parameters calculated from the curves; for the list of the parameters see Table S2.2.

Both initial and final *IPC*s vary significantly for the different fullerene derivatives. While IrC_{60} and AIM8 do not reduce much the polymer crystallinity ($IPC_I = 0.88$ and 0.71, respectively), C_{60} makes P3HT nearly amorphous ($IPC_I = 0.17$). Furthermore, Figure 2.3 shows that all the blends exhibit different temperatures T_{CC}^{min} at which annealing starts, from 50 to 117 °C. In contrast to the data on the P3HT:$PC_{61}BM$ blends processed from various solvents (Figure 2.2), the difference in T_{CC}^{min} for the various blends is much higher.

The most important parameter in the CC theory[25] is the ratio between the weights of the polymer species that can crystallize and the other blend components that are unable to contribute in the crystalline phase. In the case of P3HT:fullerene blends, this ratio highly depends on the portion of fullerene acceptor blended with the amorphous polymer phase.[23] According to the published data,[38] $PC_{61}BM$ can intercalate into the polymer crystalline phase between the nearest polymer side-chains in poly(terthiophene):$PC_{61}BM$ and poly(2-methoxy-5-(3,7-dimethyloxy)-p-phenylene vinylene):$PC_{61}BM$. Nevertheless, there is an insufficient space between the side-chains of the ordered RR-P3HT to allow the fullerene intercalation.[38] Meanwhile, all investigated fullerene derivatives are miscible with P3HT that might result in the amorphous P3HT:fullerene phase.[38, 40-43] Above T_g, the amorphous phase gains mobility allowing CC to commence, and the *IPC* starts to grow. Therefore, the CC temperature range T_{CC}^{min} – T_{CC}^{max} is determined by the amorphous phase

composition, namely on the polymer:fullerene weight ratio[33] and the fullerene derivative type (Table S2.2).

   To understand whether the chemical composition of the fullerene addend affects the polymer phase crystallinity in the blend films, in Figure 2.4a we plot the IPC_I as a function of the fullerene acceptor molar volume (the IPC_I vs the fullerene weight is given in Figure S2.12a). The molar volumes for P3HT and C_{60}, $PC_{61}BM$, $PC_{71}BM$, bis-$PC_{61}BM$ were taken from Ref. 14, and, for the other fullerene derivatives, were calculated as a sum of the van der Waals volumes of the fullerene cage and the corresponding addend as described in Ref. 59 (Ref. 60 for an Ir atom). Approximately linear correlation between the IPC_I in the blend and the fullerene acceptor molar volume might be attributed to the P3HT:fullerene miscibility in the polymer amorphous phase, i.e. the less fullerene acceptor volume affects more the polymer phase leading to the lower IPC in as-cast blends. However, the initial IPC does not show any clear correlation with the fullerene acceptor solubility (Figure S2.11). This is in line with the data from Ref. 61, which show that the fullerene acceptor solubility albeit important, is not directly correlated with the PCE. Similarly to the fullerene acceptor solubility, the PCE generally increases with increase of the IPC upon annealing, but this trend is not universal (Table S2.2).
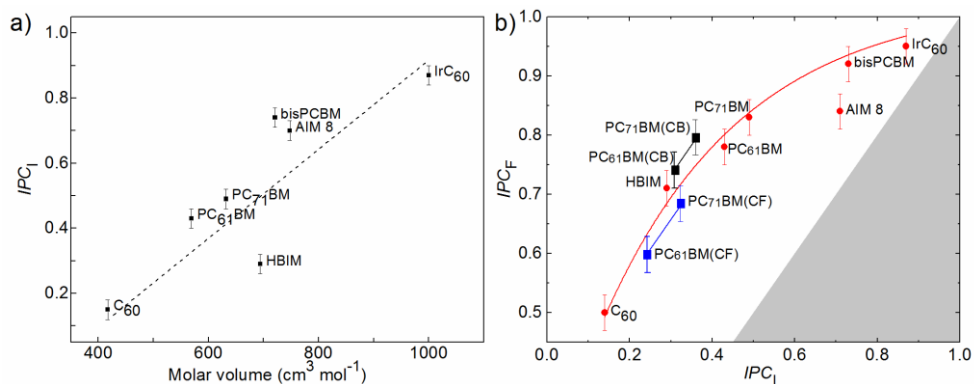
Figure 2.4. IPC charts for blends of P3HT with various fullerene derivatives. (a) Initial IPC (IPC_I) versus the molar volume of the fullerene derivatives. The dash line is a linear fit; (b) Final IPC (IPC_F) versus the initial IPC (red symbols are for DCB, black symbols for CB and blue symbols for CF). The red and black lines are guides to the eye. The gray shaded area corresponds to decrease of the IPC (i.e. $IPC_F < IPC_I$) upon annealing.

   Figure 2.4b plots the IPC_F versus the IPC_I for all P3HT:fullerene blends studied. These IPCs show a positive correlation indicating that the lower limit of the IPC_F is determined by its initial value (IPC_I). Note the apparent similarity between CC and

solid film formation from solution (e.g., by spin-casting): the mobility of polymer chains at temperatures higher than T_g is akin to the polymer fluidity in the liquid film formed upon film casting. As a result, polymer crystallization occurs both during film drying and thermal annealing the P3HT:fullerene blends. However, the room for the increase of polymer crystallinity is limited: more the fullerene acceptor disturbs the polymer crystallinity during film drying (leading to lower IPC_I), lower the IPC_F is after post processing (Figure 2.4b). This trend is in line with the CC theory of polymers,[25] Note that T_{CC}^{min} does not show any clear correlation with the fullerene acceptor volume nor its solubility nor the IPC_I (Figure S2.13).

2.4. Conclusions

In summary, we have demonstrated Raman microscopy to be a powerful tool to probe polymer cold crystallization dynamics in real time during thermal annealing. The cold crystallization of polymer chains is shown to operate within the temperature range of 50–150 °C in various P3HT:fullerene blends. The IPCs of P3HT:PC$_{61}$BM and P3HT:PC$_{71}$BM annealed blends show excellent correlation with the power conversion efficiency of organic solar cells based on the blends.

The refined Raman microscopy technique has allowed us to monitor the dynamics of cold crystallization of P3HT:fullerene blend films in real-time at subsecond timescales right during temperature annealing. This technique is similar to DSC but, in contrast, can be applied directly to the solar cells active layer and benefit from high chemical selectivity and spatial resolution. The results show that the parameters important for polymer crystallization in the bulk heterojunction are the annealing temperature, solvent, and acceptor type. Specifically, casting blend from the higher boiling solvent results in larger quasi-crystalline phase in as-cast films. Furthermore, we found a correlation between the fullerene addend weight and the polymer crystallinity for as-cast films, and also a correlation of the polymer crystallinity at the start and end of the cold crystallization. The real-time Raman microscopy technique might be easily extended to *in-situ* study of cold crystallization dynamics during another popular annealing technique, solvent vapor annealing.

As Raman microscopy is chemically selective, it has the ability to clearly distinguish the donor and acceptor species in the blend and hence a high potential to probe crystallization of either donor or acceptor component in BHJs separately. From this point of view, it will be interesting to study crystallization of the acceptor

component (be it a fullerene derivative[14] or another polymer or a small-molecule acceptor[62]), which could also contribute to charge photogeneration in organic solar cells.[63]

The spatial resolution of standard Raman microscopy as used herein does not suffice to probe the nanomorphology that of a key importance for the OPD performance.[64] Radical increase of the spatial resolution to directly distinguish donor/acceptor domains of a few tens of nm in size could be achieved with the tip-enhanced Raman microscopy.[65] Indirect morphology retrieving by time-resolved Raman microscopy[66] is also in the horizon similarly to the early-reported pump-probe approaches.[16-18] This together with the ability of Raman microscopy to distinguish crystalline and amorphous phases in vivo (as demonstrated in this Chapter) of the donor and acceptor components makes it a powerful tool for optimization of the morphology in real-time, which is hardly accessible to other structural methods.

Author Contributions

VVB conceived the project; AAM participated in its further development. AAM performed the preparation of polymer:fullerene films and their Raman microscopy study. AAM and VVB developed the real-time protocol. EVF performed the Raman study under the standard annealing protocol. VAT fabricated the solar cells and evaluated their *PCE*s. DYuP and MSP supervised the development of the project.

2.5. Supplementary Information

2.5.1. Chemical Structures of the Fullerene Derivatives Studied

To unravel the effect of various fullerene acceptors on polymer crystallization dynamics during annealing, we prepared seven poly(3-hexylthiophene):fullerene (P3HT:fullerene) blend compositions. Chemical structures of all fullerene derivatives shown in Figure S2.1 differ by molecular weights and the addends.

a) C_{60}	b) $PC_{61}BM$	c) $PC_{71}BM$	d) HBIM

e) AIM 8	f) IrC_{60}	g) $bisPC_{61}BM$
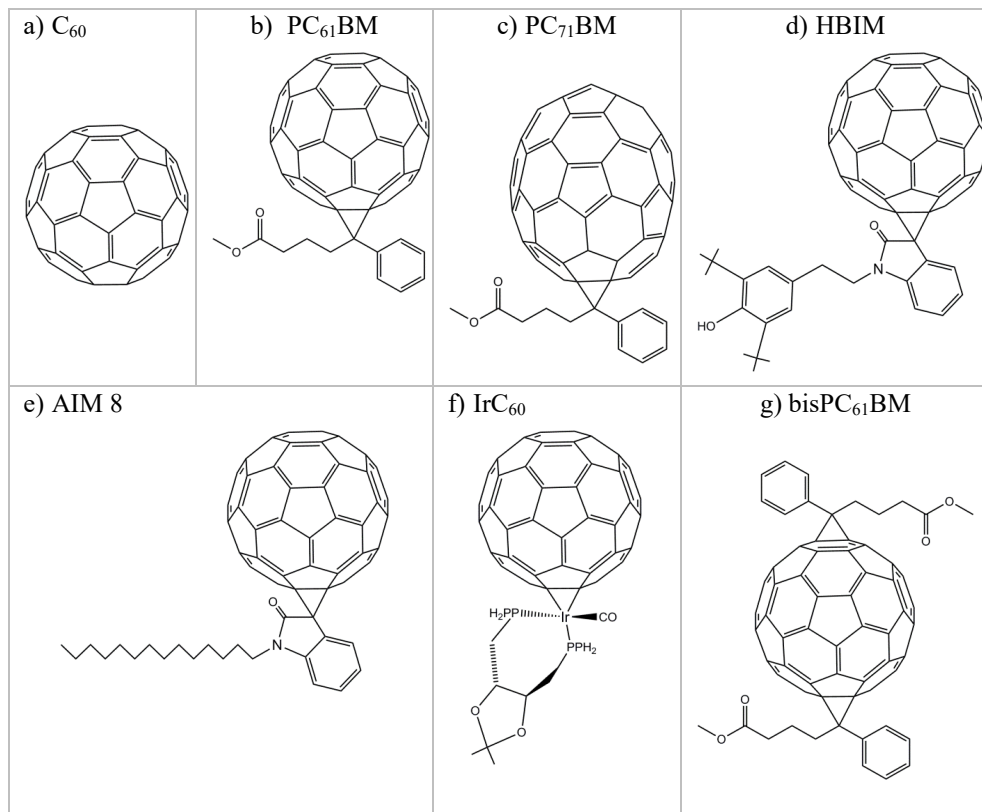
Figure S2.1. Chemical structures of the fullerene derivatives studied.

2.5.2. Tracking Polymer Crystallinity

2.5.2.1. Linearity of the Raman Signal

Figure S2.2a shows Raman spectra of a P3HT:$PC_{61}BM$ blend film at different excitation powers. For the laser power <0.5 mW, the Raman signal intensity increases linearly with the excitation power (Figure S2.2b), while at higher excitation powers it begins to saturate. Thus, the optimal laser power of 0.25 mW was set as operational for all experiments in this work.
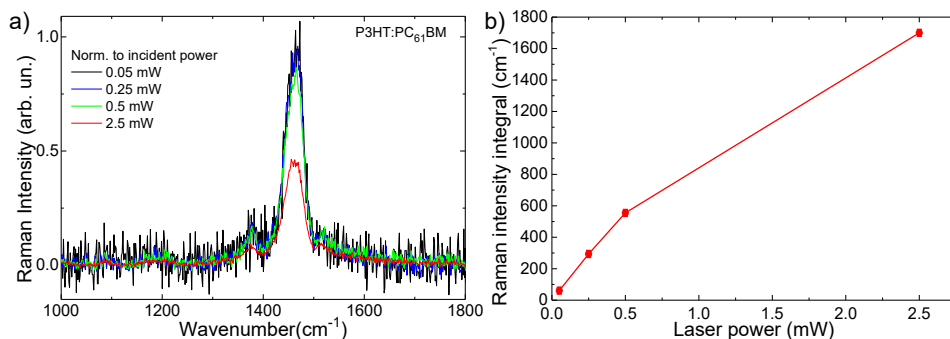
Figure S2.2. (a) The Raman spectra of 1450 cm-1 band of the P3HT:PC$_{61}$BM blend films accumulated for 1 second at different incident laser powers. The spectra are normalized to the laser power. (b) Integrated Raman signal as a function of the incident laser power. The wavelength of the excitation laser was 488 nm.

2.5.2.2. Calculation of the Ratio of the Raman Cross-sections between Crystalline and Amorphous P3HT phases

To perform decomposition of the Raman spectra of the samples onto the spectra of crystalline and amorphous phases, one needs the relative cross-sections of the two phases. Raman intensity can be expressed as $I \sim \sigma \times n_s \times d$,[67] where σ is the Raman scattering cross-section, n_s is the density of scatterers, and d is the sample thickness. Therefore, if we measure Raman spectra of two reference samples, the problem boils down to finding the respective products of scatterer density over the thickness. Unlike the approaches implemented before,[32, 68] here we evaluate the relative cross sections explicitly from the Raman intensities estimating the chromophore density from FTIR absorption spectroscopy in the regions of C–C, C=C, and C–H stretching modes. The final expression for the Raman cross sections ratio becomes:

$$\frac{\sigma_{RR}^{Ram}}{\sigma_{RRa}^{Ram}} = \frac{I_{RR} \times A_{RRa} \times N_{RR}}{I_{RRa} \times A_{RR} \times N_{RRa}} \tag{S2.1}$$

where the indices "RR" and "RRa" refer to the two reference samples, crystalline and amorphous, respectively; A_{RR} and A_{RRa} are FTIR absorptions (absorbance integral); N_{RR} and N_{RRa} are numbers of C–H or carbon-carbon bonds per one P3HT repeated unit in the RR-P3HT and RRa-P3HT samples (see below), respectively.

Pristine RR-P3HT and RRa-P3HT:PC$_{61}$BM samples were prepared on BaF$_2$ substrates (transparent in the IR spectral range) as the references for the crystalline

and amorphous polymer phases, respectively. $PC_{61}BM$ was added to quench the fluorescent background of the amorphous sample. $RRa-P3HT:PC_{61}BM$ weight ratio as low as 4:1 was chosen to avoid contaminations of the polymer Raman spectra with the $PC_{61}BM$ ones. The RR-P3HT sample was heated to 150 °C and then cooled back to the room temperature (i.e., annealed) prior the Raman/FTIR measurements.

The Raman spectra of the reference samples are shown in Figure S2.3; IR absorption spectra of the reference samples in the regions of C–H or carbon-carbon stretching modes are shown in Figure S2.4. There were no observable changes in the Raman spectra of the samples on BaF_2 and coverslip (used in all other measurements) substrates.
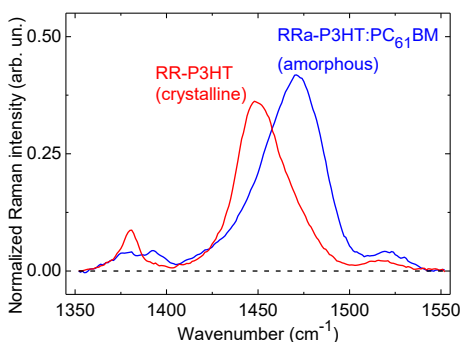
Figure S2.3. Raman spectra of the annealed RR-P3HT and $RRa-P3HT:PC_{61}BM$ samples. The wavelength of the excitation laser was 488 nm.
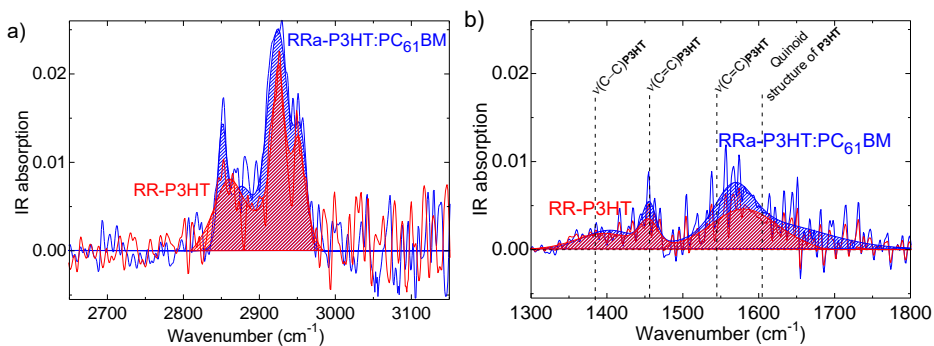

Figure S2.4. Background-corrected FTIR absorption spectra of the reference RR-P3HT and $RRa-P3HT:PC_{61}BM$ samples in the regions of C-H (a) and carbon-carbon (b) stretching modes. Integral absorptions around 1500 and 2900 cm^{-1} are listed in Table S2.1. In panel (b), the dashed lines indicate mode assignment.[69]

The parameters for calculation of the relative Raman scattering cross-sections are listed in Table S2.1. In the case of C-H modes, the ratio of the number of RR-P3HT C-H bonds (N_{RR}) to the number of RRa-P3HT:PC$_{61}$BM C-H bonds (N_{RRa}) normalized by the molar mass (M_{ω}), is given as:

$$\frac{N_{RR}^{C-H}}{N_{RRa}^{C-H}} = \frac{N^{C-H}(RR:P3HT)}{N^{C-H}(RRa:P3HT) + 0.25 \times N^{C-H}(PCBM) \times M_w(P3HT)/M_w(PCBM)} = 0.95 \quad (S2.2)$$

where N^{C-H} is the number of C-H bonds in the polymer repeat unit and M_{ω}(P3HT) is the molar mass of the polymer. The calculations according to Equation S2.1 result in $\sigma_{RR}/\sigma_{RRa} = 1.2 \pm 0.2$.

Table S2.1. Parameters for calculation of the relative Raman scattering cross-sections of the crystalline and amorphous P3HT phases. The values of uncertainties are standard deviations for 8 sets of measured data.

Ref. Sample	Raman intensity integral around 1450 cm^{-1} ($I_{RR/RRa}$), cm^{-1}	IR absorbance integral around 1500 cm^{-1} ($A_{RR/RRa}$), cm^{-1}	IR absorbance integral around 2900 cm^{-1} ($A_{RR/RRa}$), cm^{-1}	CH bonds per P3HT repeat unit (N^{CH})
RR-P3HT	15.2±0.4	0.8±0.2	0.65±0.1	14
RRa-P3HT: PC$_{61}$BM (4:1)	20.2±0.4	1.2±0.2	1.1±0.1	14.7

In the case of carbon-carbon stretch modes, PC$_{61}$BM does not contribute to the absorption due to the negligibly weak absorption of the PC$_{61}$BM fraction. This can be verified by observing the PC$_{61}$BM carbonyl mode around 1750 cm^{-1},[70] which is indistinguishable above the noise level in the experimental FTIR spectrum (Figure S2.4b); other lower-frequency modes of PCBM (CH and CC) in the range 1400-1600 cm^{-1} have even lower absorption.[70] The calculations according to Equation S2.1 yield the Raman cross-sections ratio as $\sigma_{RR}/\sigma_{RRa} = 1.1 \pm 0.4$. Therefore, the ratios of σ_{RR}/σ_{RRa} obtained by both methods are similar within experimental uncertainty; the value of 1.2 ± 0.2 will be used further on.

2.5.2.3. Real-time Tracking

The reference Raman spectra change (albeit slightly) upon heating (Figure S2.5a); therefore, it is imperative for decomposition to use the reference spectra at a given temperature. To record reference Raman spectra of the crystalline and amorphous P3HT phase at elevated temperature, the slow annealing protocol (see the experimental section in the manuscript) was engaged. 9÷12 reference Raman spectra were recorded per each temperature with an increment of 1°C, averaged and

subsequently used for decomposition. Finally, we obtained the ratio of the Raman cross sections at different temperatures (Figure S2.5b); no dependence was found.
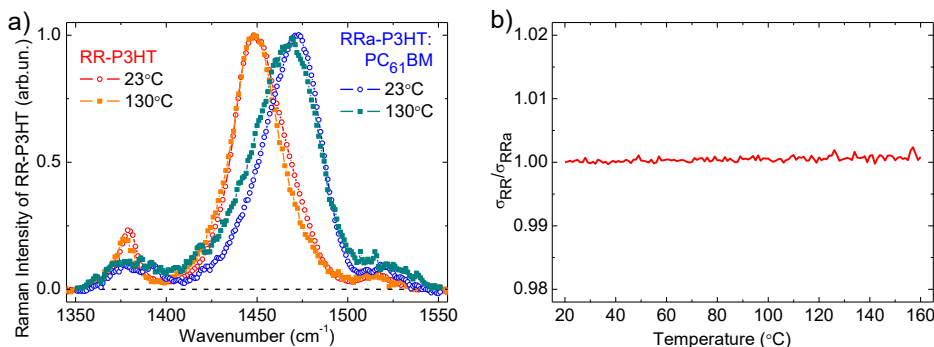
Figure S2.5. Temperature-dependent Raman measurements. (a) Raman spectra of RR-P3HT (red/orange symbols) and RRa-P3HT:PC$_{61}$BM (blue/cyan symbols) films at 23°C (open circles) and 135°C (closed squares). The spectra are normalized to the maxima for ease of comparison (b) Normalized (at 20°C) temperature dependence of the ratio of the Raman cross-sections.

2.5.3. Decomposition of Raman Spectra

Temperature-dependent Raman spectra of the investigated P3HT:fullerene samples were recorded at the rate of one spectrum per second. In the slow annealing protocol, 12 spectra were recorded per 1 °C and averaged. Each spectrum at temperature T was decomposed to a superposition of the two references spectra of RR-P3HT (crystalline phase) and RRa-P3HT:PC$_{61}$BM (amorphous phase) at the given temperature T:

$$SPC_T^{sample} = P_{RR} \times SPC_T^{RR-P3HT} + P_{RRa} \times SPC_T^{RRa-P3HT} \qquad \text{(S2.3)}$$

where P_{RR} and P_{RRa} are the least-square-deviation fit parameters (weights); $SPC_T^{RR-P3HT}, SPC_T^{RRa-P3HT}, SPC_T^{sample}$ are Raman spectra of the reference RR-P3HT, RRa-P3HT:PC$_{61}$BM samples and investigated sample, respectively. Figure S2.6 shows two representative examples of such decomposition. Finally, the *IPC* value was calculated according to Equation 2.1.[32] The uncertainty of the procedure mainly originates from the uncertainty in the Raman cross sections and amounts to ~0.04.

a)

b)
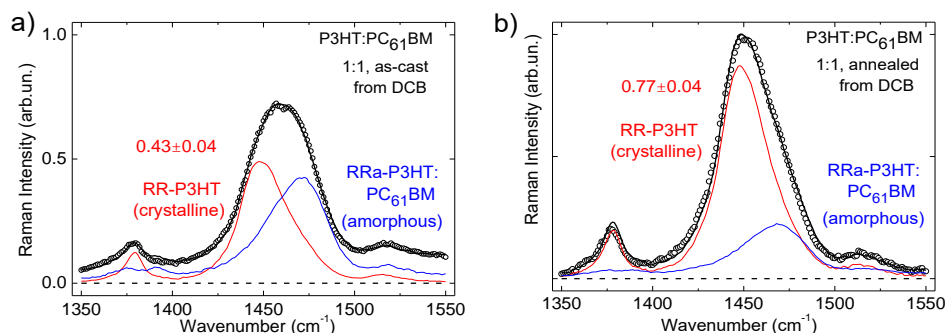
Figure S2.6. Examples of the spectral decomposition of P3HT Raman spectra for as-cast (a) and annealed at 120°C (b) P3HT:PC$_{61}$BM films. The circles show the measured data; the black lines are the superposition of the reference RR-P3HT (red) and RRa-P3HT:PC$_{61}$BM (blue) spectra according to (Equation S2.2). The corresponding *IPC* values are shown in each panel.

As mentioned in Section 2.2.5 of the Thesis, *IPC* does not quantify the percentage of aggregated polymer chains. As introduced by Tsoi *et al.*,[32] the *IPC* can be calibrated with the use of more direct techniques to evaluate the polymer crystallinity such as differential scanning calorimetry (DSC) so that *IPC*=1 corresponds to the polymer crystallinity of ∼10%.

2.5.4. Excitation Assisted Laser Annealing

Excitation laser power deposited into the focal region might affect the polymer phase crystallinity due to sample photo-degradation or simply heating. Assuming the steady-state thermal regime (i.e., thermal equilibrium with the bath of infinite heat capacity), the relative heating is estimated as ~50°C (excitation laser power of 0.25 mW, laser spot of ~10 μm, sample absorbance of ~0.5 at 488 nm, thermal conductivity[71] of ~0.07 W·m^{-1}·K^{-1}) probably resulting in thermal annealing. Therefore, care should be taken to avoid possible laser-assisted thermal annealing or sample photo-degradation.
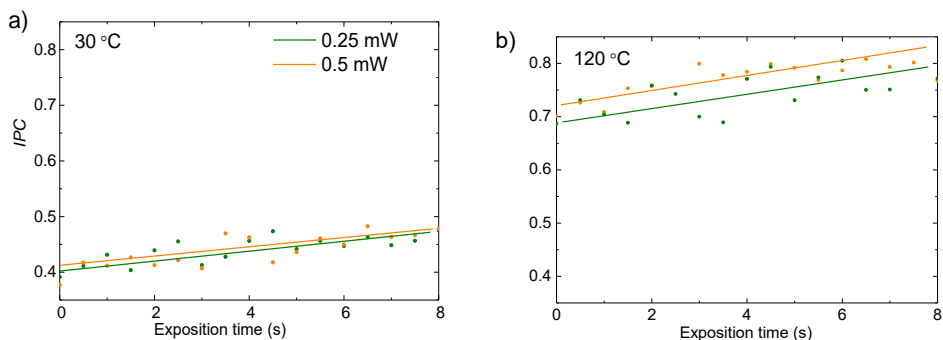
Figure S2.7. *IPC* of a P3HT:PC$_{61}$BM blend (prepared from DCB) as a function of the exposition time at different powers of the excitation laser and temperatures. The excitation spot position on the sample was fixed. The solid lines are linear fits to the experimental data; the null-slope of the lines would signify no laser-assisted annealing.

To evaluate the importance of this effect, we continuously obtained a sequence of Raman spectra from one spot in the sample without moving it, and then calculated the resulted *IPC* (Figure S2.7) as a function of the exposition time. At the excitation laser power of 0.25 mW and 0.5 mW, the slopes of the *IPC* dynamics at all temperatures are similar and do not exceed 0.02 s^{-1} which is well within the *IPC* uncertainty margins. Therefore, if the excitation spot is moved once per second, no laser-assisted annealing/degradation takes place. Such movement was embedded in the data-collection protocol.

2.5.5. Correlation between *PCE* and *IPC*

Figure S2.8 demonstrates the *PCE* (for measurement details see Ref. 72) and final (annealed) *IPC* as a function of the annealing temperature in P3HT:PC$_{61}$BM (black) and P3HT:PC$_{71}$BM (red) solar cells. The *IPC* in P3HT:PC$_{61}$BM and P3HT:PC$_{71}$BM blends is well correlated with the *PCE*; therefore, the *IPC* is a critical parameter affecting the device performance. Note that according to the previous studies, the maximum *PCE* is achieved at weight ratios of P3HT and fullerene derivatives of 1:1 for PC$_{61}$BM,[27] and 1:0.5 for PC$_{71}$BM.[44] This could explain why here the *PCE* of P3HT:PC$_{61}$BM blend is higher than the that of P3HT:PC$_{71}$BM blend.
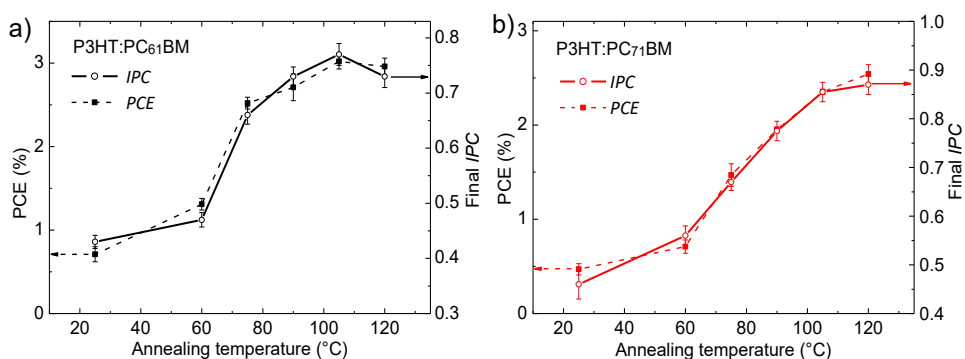
Figure S2.8. *PCE* (dash) and final *IPC* values (solid) obtained from Figure 2.1 as functions of annealing temperature in P3HT:PC$_{61}$BM (a) and P3HT:PC$_{71}$BM (b) blends.

2.5.6. Supporting Data of the Slow Annealing Protocol

2.5.6.1. Various Fullerene Derivatives

Table S2.2. Slow annealing protocol parameters (i.e. T_{CC}^{min}, T_{CC}^{max}, IPC_I, and IPC_F) for P3HT:fullerene blends cast from different solvents, and *PCEs* of the corresponded solar cells.

P3HT:fullerene (solvent)	IPC_I	T_{CC}^{min}, °C	*PCE*, %	IPC_F	T_{CC}^{sat}, °C	*PCE*, %
	As-cast film			Annealed film		
PC$_{61}$BM (DCB)	0.43	56	0.92	0.77	115	3.15
PC$_{61}$BM (CB)	0.31	52	-	0.74	114	-
PC$_{61}$BM (CF)	0.25	50	-	0.59	100	-
PC$_{71}$BM (DCB)	0.49	61	0.54	0.83	117	2.67
PC$_{71}$BM (CB)	0.35	50	-	0.80	104	-
PC$_{71}$BM (CF)	0.32	44	-	0.68	98	-
HBIM (DCB)	0.31	76	1.7[40]	0.70	147	2.0[40]
AIM 8 (DCB)	0.71	65	1.39[41]	0.83	106	1.14[41]
IrC$_{60}$ (DCB)	0.88	50	0.68[73]	0.94	112	1.15[73]
C$_{60}$ (DCB)	0.17	117	0.01[74]	0.60	175	0.05[74]
bisPC$_{61}$BM (DCB)	0.74	70	2.25[75]	0.92	132	2.4[76]

Table S2.2 lists the T_{CC}^{min}, T_{CC}^{max}, IPC_I, and IPC_F parameters for the P3HT:fullerene blends together with available *PCE*.

2.5.6.2. Irreversibility of the Annealing Process in P3HT:PC₆₁BM Blend

Figure S2.9 demonstrates irreversibility of polymer crystallization in P3HT:PC$_{61}$BM blend above T_g. The slow annealing protocol at the first stage (1) was used. During retaining the sample temperature at 130°C (stage 2) for a few minutes, *IPC* slightly increases which most probably indicates extremely slow dynamics of CC. During the cooling process (3), *IPC* also somewhat increases, which might be assigned to continuing weak CC as long as the sample temperature is higher than T_g. Therefore, the slow annealing protocol captures most of CC dynamics and therefore could be regarded as quasi-steady-state in a good approximation.
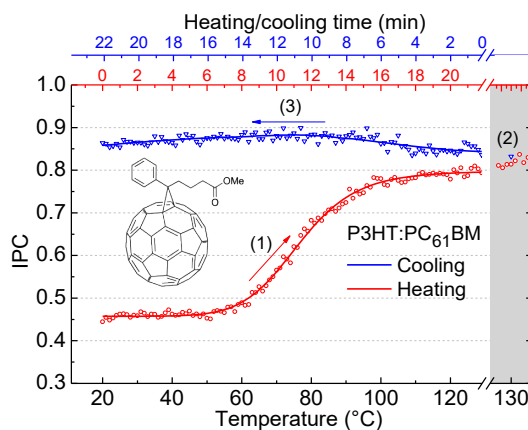
Figure S2.9. Irreversibility of the *IPC* dynamics. (1) slow annealing protocol, i.e., +5°C per min from 20 to 130°C (red curve); (2) the sample temperature is kept at 130°C for 8 minutes (shaded area); (3) slow cooling protocol, i.e., –5°C per min from 130 to 20°C (blue curve).

2.5.6.3. *IPC* Dynamics in the Extended Temperature Range

To observe the four consecutive annealing phases (three of them are described in Section 2.3.2 and the fourth one is melting) for the P3HT:fullerene blend films, *IPC* in the extended temperature range (including the melting temperature region) 20–170 °C for P3HT:PC$_{61}$BM and 30–220 °C for P3HT:C$_{60}$ was recorded (Figure S2.10). The *IPC* dynamics are well correlated with the crystallization scenario proposed (Figure 1.5 in the Thesis's introduction).
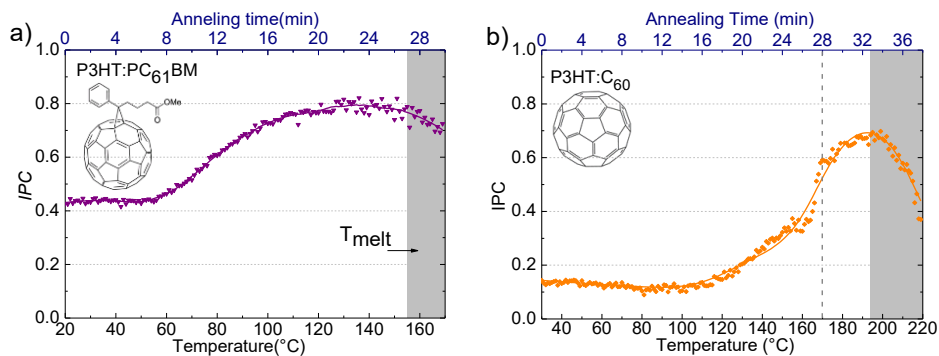
Figure S2.10. Real-time *IPC* dynamics of P3HT:PC$_{61}$BM (a) and P3HT:C$_{60}$ (b) blend film (purple and orange, respectively). The lines are guides to the eye. Shaded areas represent the sample melting region.[29]

2.5.7. *IPC* and T_{CC} Charts for P3HT Blends with Various Fullerene Acceptors
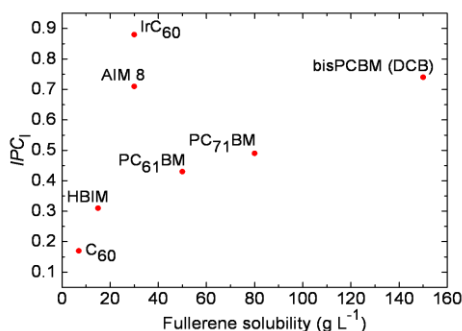
Figure S2.11. *IPC*$_I$ in P3HT:fullerene (C$_{60}$,[77] HBIM,[40] PC$_{61}$BM,[61] PC$_{71}$BM,[61] AIM 8,[41] IrC$_{60}$,[73] bisPC$_{61}$BM in DCB[78]) blends as a function of fullerene acceptor solubility in CB except bisPC$_{61}$BM, which was prepared from DCB.
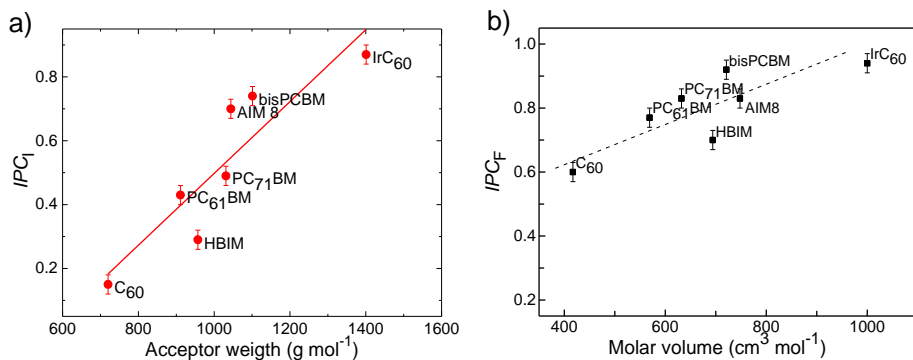
Figure S2.12. Initial *IPC* versus the fullerene derivative weight (a) and final *IPC* versus the molar volume of the fullerene derivative. The red line in panel (a) is a linear fit. The dash line in panel (b) is a guide to eye.
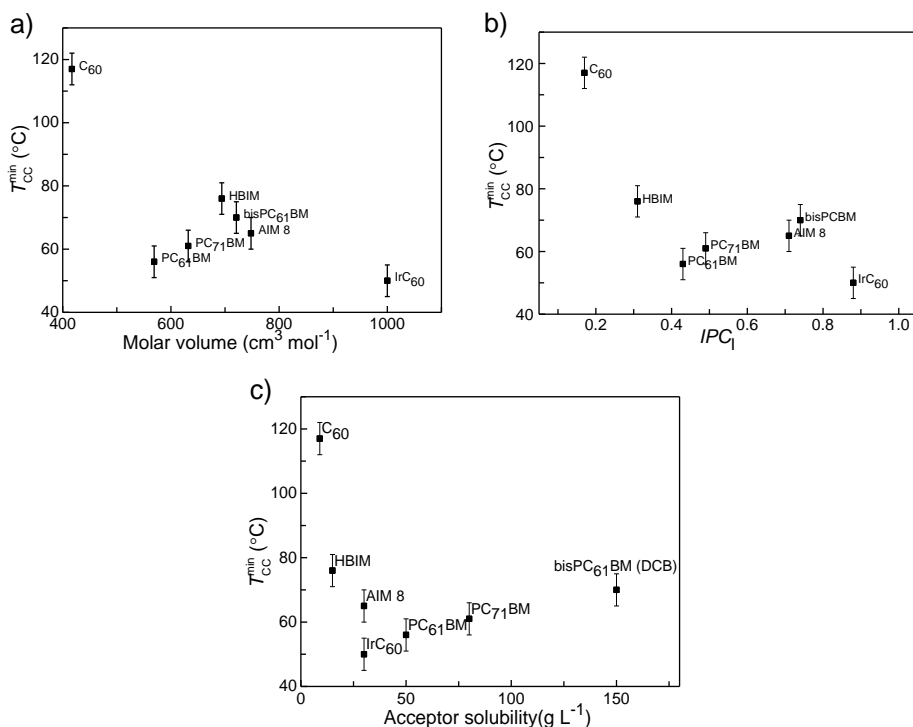
Figure S2.13. T_{CC}^{min} versus the fullerene acceptor molar volume (a), versus IPC_I (b) and versus the fullerene acceptor solubility in CB (c), the bisPC$_{61}$BM solubility in shown for DCB.

2.6. References

1.   Yu, G.; Gao, J.; Hummelen, J. C.; Wudl, F.; Heeger, A. J., Polymer Photovoltaic Cells: Enhanced Efficiencies via a Network of Internal Donor-Acceptor Heterojunctions. *Science* **1995**, *270*, 1789.

2.   Armin, A.; Jansen-van Vuuren, R. D.; Kopidakis, N.; Burn, P. L.; Meredith, P., Narrowband Light Detection via Internal Quantum Efficiency Manipulation of Organic Photodiodes. *Nat. Commun.* **2015**, *6*, 6343-6351.

3.   Hoppe, H.; Sariciftci, N. S., Morphology of Polymer/Fullerene Bulk Heterojunction Solar Cells. *J. Mater. Chem.* **2006**, *16*, 45-61.

4.   Nelson, J., Polymer:Fullerene Bulk Heterojunction Solar Cells. *Mater. Today* **2011**, *14*, 462-470.

5.   Veldman, D.; İpek, Ö.; Meskers, S. C. J.; Sweelssen, J.; Koetse, M. M.; Veenstra, S. C.; Kroon, J. M.; Bavel, S. S.; Loos, J.; Janssen, R. A. J., Compositional and Electric Field Dependence of the Dissociation of Charge Transfer Excitons in Alternating Polyfluorene Copolymer/Fullerene Blends. *J. Am. Chem. Soc.* **2008**, *130*, 7721-7735.

6.   Liao, H.-C.; Ho, C.-C.; Chang, C.-Y.; Jao, M.-H.; Darling, S. B.; Su, W.-F., Additives for Morphology Control in High-Efficiency Organic Solar Cells. *Mater. Today* **2013**, *16*, 326-336.

7.   Gunes, S.; Neugebauer, H.; Sariciftci, N. S., Conjugated Polymer-Based Organic Solar Cells. *Chem. Rev.* **2007**, *107*, 1324-1338.

8.   Keivanidis, P. E.; Clarke, T. M.; Lilliu, S.; Agostinelli, T.; Macdonald, J. E.; Durrant, J. R.; Bradley, D. D. C.; Nelson, J., Dependence of Charge Separation Efficiency on Film Microstructure in Poly(3-Hexylthiophene-2,5-Diyl):[6,6]-Phenyl-C61 Butyric Acid Methyl Ester Blend Films. *J. Phys. Chem. Lett.* **2010**, *1*, 734-738.

9.   Agostinelli, T., *et al.*, Real-Time Investigation of Crystallization and Phase-Segregation Dynamics in P3HT:PCBM Solar Cells During Thermal Annealing. *Adv. Funct. Mater.* **2011**, *21*, 1701-1708.

10. Collins, B. A.; Tumbleston, J. R.; Ade, H., Miscibility, Crystallinity, and Phase Development in P3HT/PCBM Solar Cells: Toward an Enlightened Understanding of Device Morphology and Stability. *J. Phys. Chem. Lett.* **2011**, *2*, 3135-3145.

11. Roige, A.; Campoy-Quiles, M.; Osso, J. O.; Alonso, M. I.; Vega, L. F.; Garriga, M., Surface Vs Bulk Phase Transitions in Semiconducting Polymer Films for OPV and OLED Applications. *Synth. Met.* **2012**, *161*, 2570-2574.

12. Chen, F.-C.; Ko, C.-J.; Wu, J.-L.; Chen, W.-C., Morphological Study of P3HT:PCBM Blend Films Prepared through Solvent Annealing for Solar Cell Applications. *Sol. Energy Mater. Sol. Cells* **2010**, *94*, 2426-2430.

13. Wang, T., *et al.*, The Development of Nanoscale Morphology in Polymer: Fullerene Photovoltaic Blends During Solvent Casting. *Soft Matter* **2010**, *6*, 4128-4134.

14. Leman, D.; Kelly, M. A.; Ness, S.; Engmann, S.; Herzing, A.; Snyder, C.; Ro, H. W.; Kline, R. J.; DeLongchamp, D. M.; Richter, L. J., In Situ Characterization of Polymer–Fullerene Bilayer Stability. *Macromol.* **2015**, *48*, 383-392.

15. Treat, N. D.; Brady, M. A.; Smith, G.; Toney, M. F.; Kramer, E. J.; Hawker, C. J.; Chabinyc, M. L., Interdiffusion of PCBM and P3HT Reveals Miscibility in a Photovoltaically Active Blend. *Adv. Energy Mater.* **2011**, *1*, 82-89.

16.   Serbenta, A.; Kozlov, O. V.; Portale, G.; van Loosdrecht, P. H. M.; Pshenichnikov, M. S., Bulk Heterojunction Morphology of Polymer:Fullerene Blends Revealed by Ultrafast Spectroscopy. **2016**, *6*, 36236.

17.   Grancini, G.; Polli, D.; Fazzi, D.; Cabanillas-Gonzalez, J.; Cerullo, G.; Lanzani, G., Transient Absorption Imaging of P3HT:PCBM Photovoltaic Blend: Evidence for Interfacial Charge Transfer State. *J. Phys. Chem. Lett.* **2011**, *2*, 1099-1105.

18.   Westenhoff, S.; Howard, I. A.; Friend, R. H., Probing the Morphology and Energy Landscape of Blends of Conjugated Polymers with Sub-10 Nm Resolution. *Phys. Rev. Lett.* **2008**, *101*, 016102(4).

19.   Padinger, F.; Rittberger, R. S.; Sariciftci, N. S., Effects of Postproduction Treatment on Plastic Solar Cells. *Adv. Funct. Mater.* **2003**, *13*, 85-88.

20.   Sirringhaus, H., *et al.*, Two-Dimensional Charge Transport in Self-Organized, High-Mobility Conjugated Polymers. *Nature* **1999**, *401*, 685.

21.   Li, G.; Yao, Y.; Yang, H.; Shrotriya, V.; Yang, G.; Yang, Y., "Solvent Annealing" Effect in Polymer Solar Cells Based on Poly(3-Hexylthiophene) and Methanofullerenes. *Adv. Funct. Mater.* **2007**, *17*, 1636-1644.

22.   Janssen, G.; Aguirre, A.; Goovaerts, E.; Vanlaeke, P.; Poortmans, J.; Manca, J., Optimization of Morphology of P3HT/PCBM Films for Organic Solar Cells: Effects of Thermal Treatments and Spin Coating Solvents. *Eur. Phys. J.: Appl. Phys.* **2007**, *37*, 287-290.

23.   Demir, F.; Van den Brande, N.; Van Mele, B.; Bertho, S.; Vanderzande, D.; Manca, J.; Van Assche, G., Isothermal Crystallization of P3HT:PCBM Blends Studied by Rhc. *J. Therm. Anal. Calorim.* **2011**, *105*, 845-849.

24.   Müller, C., On the Glass Transition of Polymer Semiconductors and Its Impact on Polymer Solar Cell Stability. *Chem. Mater.* **2015**, *27*, 2740-2754.

25.   Wunderlich, B., Theory of Cold Crystallization of High Polymers. *J. Chem. Phys.* **1958**, *29*, 1395-1404.

26.   Ke, B., Differential Thermal Analysis of High Polymers. IV. Saturated Linear Polyesters. *J. Appl. Polym. Sci.* **1962**, *6*, 624-628.

27.   Chirvase, D.; Parisi, J.; Hummelen, J. C.; Dyakonov, V., Influence of Nanomorphology on the Photovoltaic Action of Polymer–Fullerene Composites. *Nanotechnology* **2004**, *15*, 1317-1323.

28.   Gluecker, M.; Foertig, A.; Dyakonov, V.; Deibel, C., Impact of Nongeminate Recombination on the Performance of Pristine and Annealed P3HT:PCBM Solar Cells. *Phys. Status Solidi RRL* **2012**, *6*, 337-339.

29.   Zhao, J.; Swinnen, A.; Van Assche, G.; Manca, J.; Vanderzande, D.; Mele, B. V., Phase Diagram of P3HT/PCBM Blends and Its Implication for the Stability of Morphology. *J. Phys. Chem. B* **2009**, *113*, 1587-1591.

30.   Gao, Y.; Grey, J. K., Resonance Chemical Imaging of Polythiophene/Fullerene Photovoltaic Thin Films: Mapping Morphology-Dependent Aggregated and Unaggregated C═C Species. *J. Am. Chem. Soc.* **2009**, *131*, 9654-9662.

31.   Gao, Y.; Martin, T. P.; Niles, E. T.; Wise, A. J.; Thomas, A. K.; Grey, J. K., Understanding Morphology-Dependent Polymer Aggregation Properties and Photocurrent Generation in Polythiophene/Fullerene Solar Cells of Variable Compositions. *J. Phys. Chem. C* **2010**, *114*, 15121-15128.

32.   Tsoi, W. C.; James, D. T.; Kim, J. S.; Nicholson, P. G.; Murphy, C. E.; Bradley, D. D. C.; Nelson, J.; Kim, J. S., The Nature of in-Plane Skeleton Raman Modes of P3HT and Their

Correlation to the Degree of Molecular Order in P3HT:PCBM Blend Thin Films. *J. Am. Chem. Soc.* **2011**, *133*, 9834-9843.

33. Razzell-Hollis, J.; Limbu, S.; Kim, J.-S., Spectroscopic Investigations of Three-Phase Morphology Evolution in Polymer: Fullerene Solar Cell Blends. *J. Phys. Chem. C* **2016**, *120*, 10806-10814.

34. Razzell-Hollis, J.; Tsoi, W. C.; Kim, J.-S., Directly Probing the Molecular Order of Conjugated Polymer in OPV Blends Induced by Different Film Thicknesses, Substrates and Additives. *J. Mater. Chem. C* **2013**, *1*, 6235-6243.

35. Trukhanov, V. A.; Paraschuk, D. Y., Non-Fullerene Acceptors for Organic Solar Cells. *Polymer Science Series C* **2014**, *56*, 72-83.

36. Ma, W.; Yang, C.; Gong, X.; Lee, K.; Heeger, A. J., Thermally Stable, Efficient Polymer Solar Cells with Nanoscale Control of the Interpenetrating Network Morphology. *Adv. Funct. Mater.* **2005**, *15*, 1617-1622.

37. He, Y. J.; Li, Y. F., Fullerene Derivative Acceptors for High Performance Polymer Solar Cells. *PCCP* **2011**, *13*, 1970-1983.

38. Mayer, A. C.; Toney, M. F.; Scully, S. R.; Rivnay, J.; Brabec, C. J.; Scharber, M.; Koppe, M.; Heeney, M.; McCulloch, I.; McGehee, M. D., Bimolecular Crystals of Fullerenes in Conjugated Polymers and the Implications of Molecular Mixing for Solar Cells. *Adv. Funct. Mater.* **2009**, *19*, 1173-1179.

39. Ye, L., *et al.*, Quantitative Relations between Interaction Parameter, Miscibility and Function in Organic Solar Cells. *Nat. Mater.* **2018**, *17*, 253-260.

40. Valitov, M. I.; Romanova, I. P.; Gromchenko, A. A.; Shaikhutdinova, G. R.; Yakhvarov, D. G.; Bruevich, V. V.; Dyakov, V. A.; Sinyashin, O. G.; Paraschuk, D. Y., Indolinone-Substituted Methanofullerene—a New Acceptor for Organic Solar Cells. *Sol. Energy Mater. Sol. Cells* **2012**, *103*, 48-52.

41. Romanova, I. P., *et al.*, Novel Indolin-2-One-Substituted Methanofullerenes Bearing Long N-Alkyl Chains: Synthesis and Application in Bulk-Heterojunction Solar Cells. *Beilstein J. Org. Chem.* **2014**, *10*, 1121-1128.

42. Zapunidy S. A.; Martyanov D. S.; Nechvolodova E. M.; Tsikalova M. V.; Novikov Y. N.; Paraschuk D. Y., Approaches to Low-Bandgap Polymer Solar Cells: Using Polymer Charge-Transfer Complexes and Fullerene Metallocomplexes. *Pure Appl. Chem.* **2008**, *80*, 2151-2161.

43. Kim, C.-H.; Song, M.; Jin, S.-H.; Lee, J. W., High Open-Circuit Voltage of Organic Bulk Heterojunction Solar Cells Base on Poly(3-Hexylthiophene): Fullerene Derivatives. *Mol. Cryst. Liq. Cryst.* **2011**, *538*, 216-222.

44. Balderrama, V. S.; Estrada, M.; Viterisi, A.; Formentin, P.; Pallarés, J.; Ferré-Borrull, J.; Palomares, E.; Marsal, L. F., Correlation between P3HT Inter-Chain Structure and Jsc of P3HT:PC[70]BM Blends for Solar Cells. *Microelectron. Reliab.* **2013**, *53*, 560-564.

45. Yacoby, Y.; Ehrenfreund, E., Resonant Raman-Scattering in Conjugated Polymers. *Top. Appl. Phys.* **1991**, *68*, 73-135.

46. Inoue, K.; Ulbricht, R.; Madakasira, P. C.; Sampson, W. M.; Lee, S.; Gutierrez, J.; Ferraris, J.; Zakhidov, A. A., Temperature and Time Dependence of Heat Treatment of RR-P3HT/PCBM Solar Cell. *Synth. Met.* **2005**, *154*, 41-44.

47. Shen, X. B.; Duzhko, V. V.; Russell, T. P., A Study on the Correlation between Structure and Hole Transport in Semi-Crystalline Regioregular P3HT. *Adv. Energy Mater.* **2013**, *3*, 263-270.

48.   Paraschuk, D. Y.; Arnautov, S. A.; Shchegolikhin, A. N.; Kobryanskii, V. M., Temperature Evolution of Electronic and Lattice Configurations in Highly Ordered Trans-Polyacetylene. *JETP Lett.* **1996**, *64*, 658-663.

49.   Osotov, M. O.; Bruevich, V. V.; Paraschuk, D. Y., Thermal Vibrational Disorder of a Conjugated Polymer in Charge-Transfer Complex. *J. Chem. Phys.* **2009**, *131*, 094906(5).

50.   Malik, S.; Nandi, A. K., Crystallization Mechanism of Regioregular Poly(3-Alkyl Thiophene)S. *J. Polym. Sci., Part B: Polym. Phys.* **2002**, *40*, 2073-2085.

51.   Li, G.; Shrotriya, V.; Yao, Y.; Yang, Y., Investigation of Annealing Effects and Film Thickness Dependence of Polymer Solar Cells Based on Poly(3-Hexylthiophene). *J. Appl. Phys.* **2005**, *98*, 043704.

52.   Wang, T.; Pearson, A. J.; Lidzey, D. G.; Jones, R. A. L., Evolution of Structure, Optoelectronic Properties, and Device Performance of Polythiophene:Fullerene Solar Cells During Thermal Annealing. *Adv. Funct. Mater.* **2011**, *21*, 1383-1390.

53.   Abu-Zahra, N.; Algazzar, M., Effect of Crystallinity on the Performance of P3HT/PC70BM/N-Dodecylthiol Polymer Solar Cells. *J. Sol. Energy Eng.* **2013**, *136*, 021023(7).

54.   Chandrasekaran, N.; Gann, E.; Jain, N.; Kumar, A.; Gopinathan, S.; Sadhanala, A.; Friend, R. H.; Kumar, A.; McNeill, C. R.; Kabra, D., Correlation between Photovoltaic Performance and Interchain Ordering Induced Delocalization of Electronics States in Conjugated Polymer Blends. *ACS Appl. Mater. Interfaces* **2016**, *8*, 20243-20250.

55.   Jiao, X.; Ye, L.; Ade, H., Quantitative Morphology–Performance Correlations in Organic Solar Cells: Insights from Soft X-Ray Scattering. *Adv. Energy Mater.* **2017**, *7*, 1700084.

56.   Campoy-Quiles, M.; Sims, M.; Etchegoin, P. G.; Bradley, D. D. C., Thickness-Dependent Thermal Transition Temperatures in Thin Conjugated Polymer Films. *Macromol.* **2006**, *39*, 7673-7680.

57.   Machui, F.; Langner, S.; Zhu, X.; Abbott, S.; Brabec, C. J., Determination of the P3HT:PCBM Solubility Parameters via a Binary Solvent Gradient Method: Impact of Solubility on the Photovoltaic Performance. *Sol. Energy Mater. Sol. Cells* **2012**, *100*, 138-146.

58.   Wang, C. I.; Hua, C. C., Solubility of C60 and PCBM in Organic Solvents. *J. Phys. Chem. B* **2015**, *119*, 14496-14504.

59.   Bondi, A., Van Der Waals Volumes and Radii. *J. Phys. Chem.* **1964**, *68*, 441-451.

60.   Ping, M.; Xiubin, L.; Yuankai, W., A Formula for Calculating Atomic Radii of Metals. *J. Chem. Educ.* **1990**, *67*, 218.

61.   Troshin, P. A., *et al.*, Material Solubility-Photovoltaic Performance Relationship in the Design of Novel Fullerene Derivatives for Bulk Heterojunction Solar Cells. *Adv. Funct. Mater.* **2009**, *19*, 779-788.

62.   Cheng, P.; Li, G.; Zhan, X.; Yang, Y., Next-Generation Organic Photovoltaics Based on Non-Fullerene Acceptors. *Nat. Photonics* **2018**, *12*, 131-142.

63.   Jamieson, F. C.; Domingo, E. B.; McCarthy-Ward, T.; Heeney, M.; Stingelin, N.; Durrant, J. R., Fullerene Crystallisation as a Key Driver of Charge Separation in Polymer/Fullerene Bulk Heterojunction Solar Cells. *Chem. Sci.* **2012**, *3*, 485-492.

64.   Noriega, R.; Rivnay, J.; Vandewal, K.; Koch, F. P. V.; Stingelin, N.; Smith, P.; Toney, M. F.; Salleo, A., A General Relationship between Disorder, Aggregation and Charge Transport in Conjugated Polymers. *Nat. Mater.* **2013**, *12*, 1038-1044.

65.   Deckert-Gaudig, T.; Taguchi, A.; Kawata, S.; Deckert, V., Tip-Enhanced Raman Spectroscopy - from Early Developments to Recent Advances. *Chem. Soc. Rev.* **2017**, *46*, 4077-4110.

66. Fausti, D.; H.M. van Loosdrecht, P., Time-Resolved Raman Scattering. In *Optical Techniques for Solid-State Materials Characterization*, Prasankumar, R. P.; Taylor, A. J., Eds. 2011.

67. McCreery, R. L., Calibration and Validation. In *Raman Spectroscopy for Chemical Analysis*, John Wiley & Sons, Inc.: 2005; pp 251-291.

68. Rodriguez-Martinez, X.; Vezie, M. S.; Shi, X.; McCulloch, I.; Nelson, J.; Goni, A. R.; Campoy-Quiles, M., Quantifying Local Thickness and Composition in Thin Films of Organic Photovoltaic Blends by Raman Scattering. *J. Mater. Chem. C* **2017**, *5*, 7270-7282.

69. Baibarac, M.; Lapkowski, M.; Pron, A.; Lefrant, S.; Baltog, I., Sers Spectra of Poly(3-Hexylthiophene) in Oxidized and Unoxidized States. *J. Raman Spectrosc.* **1998**, *29*, 825-832.

70. Maibach, J., *et al.*, Impact of Processing on the Chemical and Electronic Properties of Phenyl-C61-Butyric Acid Methyl Ester. *J. Mater. Chem. C* **2014**, *2*, 7934-7942.

71. Duda, J. C.; Hopkins, P. E.; Shen, Y.; Gupta, M. C., Thermal Transport in Organic Semiconducting Polymers. *Appl. Phys. Lett.* **2013**, *102*, 251912.

72. Mannanov, A. A.; Bruevich, V. V.; Feldman, E. V.; Trukhanov, V. A.; Pshenichnikov, M. S.; Paraschuk, D. Y., Real-Time Tracking of Polymer Crystallization Dynamics in Organic Bulk Heterojunctions by Raman Microscopy. *J. Phys. Chem. C* **2018**.

73. Gromchenko, A. P3HT:IrC60 Performance Study. Lomonosov Moscow State University, Moscow, 2010.

74. Motaung, D. E.; Malgas, G. F.; Arendse, C. J., Insights into the Stability and Thermal Degradation of P3HT:C60 Blended Films for Solar Cell Applications. *J. Mater. Sci.* **2011**, *46*, 4942-4952.

75. Yun, M. H.; Kim, G.-H.; Yang, C.; Kim, J. Y., Towards Optimization of P3HT:Bispcbm Composites for Highly Efficient Polymer Solar Cells. *J. Mater. Chem.* **2010**, *20*, 7710-7714.

76. Lenes, M.; Shelton, S. W.; Sieval, A. B.; Kronholm, D. F.; Hummelen, J. C.; Blom, P. W. M., Electron Trapping in Higher Adduct Fullerene-Based Solar Cells. *Adv. Funct. Mater.* **2009**, *19*, 3002-3007.

77. Ruoff, R. S.; Tse, D. S.; Malhotra, R.; Lorents, D. C., Solubility of Fullerene (C60) in a Variety of Solvents. *J. Phys. Chem.* **1993**, *97*, 3379-3383.

78. Voroshazi, E., *et al.*, Novel bis-C60 Derivative Compared to Other Fullerene bis-Adducts in High Efficiency Polymer Photovoltaic Cells. *J. Mater. Chem.* **2011**, *21*, 17345-17352.

Chapter 3. Molecular Self-Doping Controls Luminescence of Pure Organic Single Crystals
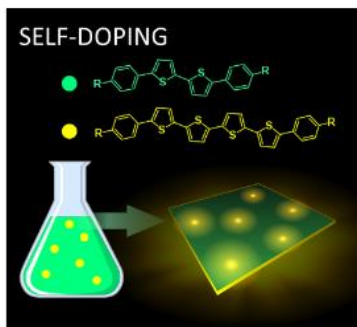
Organic optoelectronics calls for materials combining bright luminescence and efficient charge transport. The former is readily achieved in isolated molecules, while the latter requires strong molecular aggregation, which usually quenches luminescence. This hurdle is generally resolved by doping the host material with highly luminescent molecules collecting the excitation energy from the host. Here, we introduce a novel concept of molecular self-doping in which a higher luminescent dopant emerges as a minute-amount byproduct during the host material synthesis. As a one-stage process, self-doping is more advantageous than widely used external doping. The concept is proved on thiophene-phenylene co-oligomers (TPCO) consisting of four (host) and six (dopant) conjugated rings. We show that <1% self-doping doubles the photoluminescence in the TPCO single crystals, while not affecting much their charge transport properties. The Monte-Carlo modelling of photoluminescence dynamics revealed that host-dopant energy transfer is controlled by both excitonic transport in the host and host-dopant Förster resonant energy transfer. The self-doping concept is further broadened to a variety of conjugated oligomers synthesized via Suzuki, Kumada, and Stille cross-coupling reactions. We conclude that self-doping combined with improved excitonic transport and host-dopant energy transfer is a promising route to highly luminescent semiconducting organic single crystals for optoelectronics.

3.1. Introduction

Emerging organic light-emitting devices, e.g., organic light-emitting transistors (OLETs) and electrically-pumped lasers, need materials combining high luminescence and efficient charge transport.[1-4] The latter requires tight molecular packing, which usually results in luminescence quenching. One of the effective ways to control and enhance the light-emitting properties of organic semiconducting materials is their doping by highly luminescent molecules as commonly used in organic light emitting diodes. For example, if the dopant absorption spectrum overlaps with the fluorescence spectrum of the host material, the host-dopant Förster resonant energy transfer (FRET) can be used to control the luminescence efficiency and spectra of the doped host material.[5-8]

The most attractive materials for OLET and organic injection lasers are organic semiconducting single crystals,[4, 9-16] which can also be doped by highly luminescent molecules to improve their luminescence properties via host-dopant energy transfer.[17-19] Despite the FRET effect is well understood in various donor-acceptor systems,[20] its detailed study in organic crystals (donor) doped by luminescent molecular acceptors has not been done yet. Although color tuning via donor-acceptor energy transfer was demonstrated in molecularly doped single crystals,[21] such important issues as doping level optimization and exciton diffusion, which can be harnessed to enhance the host-dopant energy transfer efficiency and hence the device performance, have not been addressed.

Vapor-grown organic semiconducting single crystals with dopant-controlled and dopant-enhanced fluorescence have already been demonstrated where the host and dopant molecules were synthesized separately, their powders were milled and mixed, and finally the crystals were grown from the mixture of the two.[18, 21] On the other hand, during the host material synthesis small amounts of various byproducts are usually produced. If one of them is highly luminescent and has a lower optical energy gap than the host, it could serve as a dopant controlling the luminescence of the material via exciton transport in the host material and consecutive FRET to the dopant. As a result, molecular self-doping of the host by the energy acceptor is realized thereby removing the necessity to synthesize the dopant separately. Moreover, in this manner one avoids complicated purification of the host organic semiconductor from the dopant; accordingly, the overall cost of the material could be substantially reduced. This approach radically differs from both physical self-doping used earlier to dope the amorphous phase of polyfluourene by its β-phase,[22]

and self-doping by charges recently demonstrated within one molecule (perylene diimide) by amine substituents.[23]

In this work, we introduce the concept of molecular self-doping as a novel approach to control the luminescence of nominally chemically pure (>99%) conjugated organic materials. For this purpose, we used thiophene-phenylene co-oligomer (TPCO) single crystals that combine pronounced luminescence and efficient charge transport.[24-26] As the host material, we synthesized TPCO with the molecular structure 5,5′-*bis*[4-(trimethylsilyl)phenyl]-2,2′-bithiophene (TMS-P2TP-TMS),[24] where P and T stand for 1,4-phynelene and 2,5-thiophene, respectively; TMS is trimethylsilyl group. We found that a longer TPCO, 5,5‴-*bis*[4-(trimethylsilyl)phenyl]-2,2′:5′,2″:5″,2‴-quaterthiophene (TMS-P4TP-TMS) that emerges in minute amounts (<1%) as a byproduct during the host synthesis acts as an efficient energy acceptor of the host excitation energy in the crystal. To identify and quantify such a minute amount of dopant that is chemically very similar to the host, we applied a photoluminescent (PL) method with sensitivity to dopant down to 100 ppm level at the presence of the host of a very similar molecular structure. The optimal doping doubles the PL quantum yield (QY) of the solution-grown TPCO single crystals while retaining the efficient charge transport properties. Monte-Carlo modelling of the PL time-resolved spectra recorded in variously doped crystals was used to reveal the interplay between exciton diffusion in the host material and FRET to the dopant. We further broadened the scope of the self-doping concept onto other molecular crystals, which were grown from various conjugated oligomers synthesized via different chemical routes. Our findings clearly demonstrate that molecular self-doping combined with enhanced excitonic transport and host-dopant energy transfer paves the way to highly luminescent semiconducting organic crystals for optoelectronics applications.

3.2. Materials and Methods

TMS-P2TP-TMS and TMS-P4TP-TMS characterization, sublimation methods, doping and crystal growth, and organic field-effect transistors performances are presented in Ref. 27.

Photoluminescence: PL spectra and QY of the TMS-P2TP-TMS and TMS-P4TP-TMS solutions and solid samples are presented in Ref. 27.

Time-resolved PL under 100-fs, 400-nm excitation was measured by a streak camera (C5680, Hamamatsu) combined with a polychromator (for the details of

polarization-resolved, room and low temperature measurements see Sections 3.5.1-3.5.5).

Monte-Carlo simulations: Monte-Carlo (MC) simulations were performed as a random walk of excitons in a 3D cubic crystal grid with a subsequent FRET to the dopants (Section 3.5.6).

3.3. Results and Discussion

The detailed syntheses routes of self-doped TMS-P2TP-TMS material (host) and their self-dopant, i.e. a longer TPCO, 5,5′′′-*bis*[4-(trimethylsilyl)phenyl]-2,2′:5′,2′′:5′′,2′′′-quaterthiophene (TMS-P4TP-TMS) are presented in Ref. 27.

Figure 3.1 shows host and dopant optical spectra, which demonstrate a noticeable overlap between the two (marked as gray area) thereby promising efficient energy transfer of the host excitation via, e.g., FRET to the dopant. The dopant PL QY in solution was measured in Ref. 27 as 44±2%, which is a factor of two higher than that of the host (20±2%). This makes it feasible to tune the luminescence spectrum and enhance QY in the doped host crystal utilizing host-dopant energy transfer via exciton diffusion in the host matrix with consecutive host-dopant FRET.
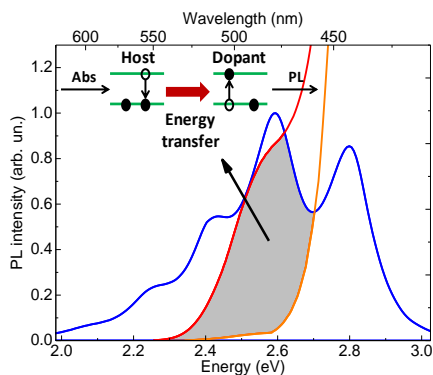
Figure 3.1. Implementation of the self-doping concept. Illustration of the feasibility of Förster resonant energy transfer (FRET) in TMS-P2TP-TMS crystals self-doped by TMS-P4TP-TMS. As the PL spectrum of the donor (host), PL of the grinded 0.01% doped crystal is shown by the blue line; grinding was used to decrease the PL reabsorption. The red and orange lines demonstrate PL excitation spectra of 1% and 0.01% doped crystals, respectively (for details, see SI of Ref. 27), where the band at ~2.55 eV is attributed to donor (dopant) absorption. The inset illustrates FRET in the doped host. The gray area indicates the spectral overlap between host PL and dopant absorption required for FRET.

Figure 3.2a shows PL spectra of the self-doped crystals at three representative doping levels together with the reference host and dopant spectra (marked as the shaded areas). Upon increase of the doping level, the PL spectra shift to the red from one reference spectrum to another, which is attributed to the increased share of the red-shifted dopant PL (for the complete set of host and dopant PL spectra, see Ref. 27). As direct dopant excitation at 400 nm is negligible due to low dopant concentration, the observed PL features are assigned to host-dopant energy transfer. Host and dopant PL exhibit identical polarization properties (Section 3.5.2), which suggests that the dopant molecules substitute the host sites in the doped crystals as was earlier reported for other doped TPCO crystals.[18] Although the dopant molecule has a similar shape but a longer length as compared to the host ones, it could substitute the host one with some deformations of dopant and adjacent host molecules, which is illustrated by molecular dynamics simulation (Section 3.5.2). As it has been demonstrated in Ref. 27, we were unable to attain the purity of the host material from the dopant molecules better than 99.99%, which also suggests that the dopant molecules are firmly embedded in the host matrix.

To prove the energy transfer between the host and dopants, we recorded PL transients at the blue and red flanks of PL spectra (Figure 3.2a), which correspond mainly to host and dopant PL, respectively (Figure 3.2b-c). Decay of the host PL (Figure 3.2b) accelerates from ~0.4 to ~0.1 ns with increasing the doping level. Correspondingly, dopant PL (Figure 3.2c) acquires a raising component with the time that is similar to the blue-flank decay (0.07–0.2 ns; Section 3.5.4). Shortening of decay times of the blue-flank transients with doping and the corresponding rise in the red-flank transients are fully consistent with host-dopant energy transfer. Finally, PL at the red flank decays considerable longer as compared to the blue flank (0.7–0.8 *vs.* 0.07– 0.4 ns) again confirming its origin from the dopant.

Another convenient way to characterize the energy transport process in the crystals is to analyze the dynamical red shift of the mean PL energy (Figure 3.2d and Section 3.5.5). For the lowest doping level, PL originates mostly from the host excitons (mean energy of ~2.55 eV), with a weak PL shift to the red due to energy transfer to the dopants. At the doping level of 0.2% and higher, the majority of excitons in the crystal are transferred to the lower energy levels with the red-shifted PL energy of ~2.3 eV, which corresponds to the dopant PL (the red line in Figure S3.6a). The low-temperature transient PL data demonstrate that the host-dopant energy transfer is weakly temperature-dependent (Section 3.5.5), which is consistent with FRET domination over exciton diffusion.
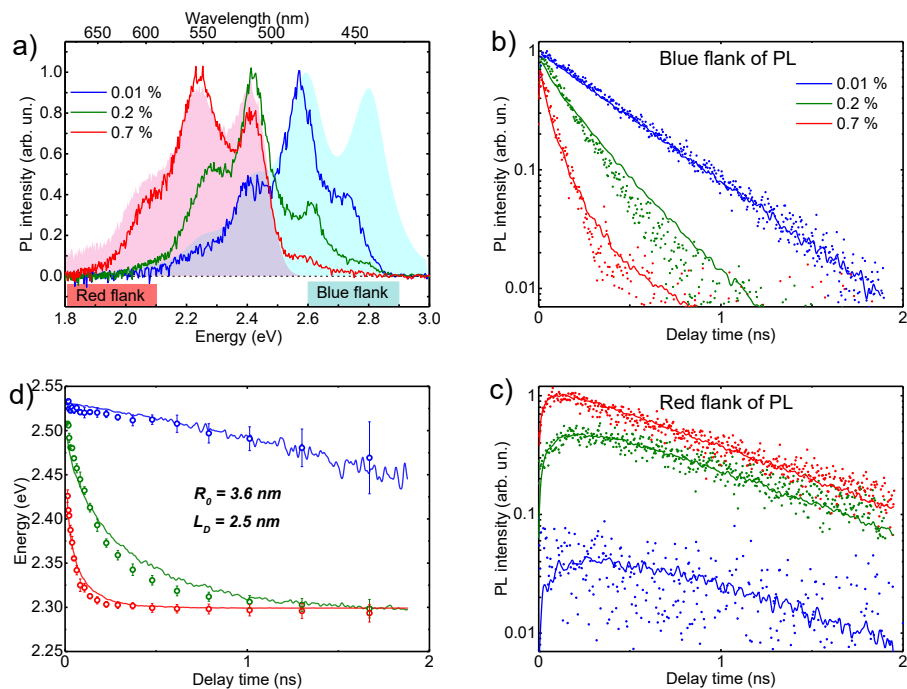
Figure 3.2. PL data of the doped crystals. (a) PL spectra in a few self-doped crystals after 400-nm excitation (lines), obtained from the streak-camera PL maps integrated over the 0–2 ns time window, in the microscopic configuration (for the PL maps, see Figure S3.9). The cyan and red shaded spectra represent, respectively, the reference spectra of the grinded 0.01% doped crystal (the host PL spectrum) at 405-nm excitation and the 0.7% doped crystal at 465-nm excitation, where mostly the dopant is excited. (b, c) PL transients extracted from the PL maps at the blue and red PL spectral flanks (indicated in (a) by the blue and red rectangles) originated mostly from host and dopant PL, respectively. Dots are the experimental data; the lines are the outcome of the MC simulations. Scaling between the experimentally obtained and simulated PL intensities is preserved. For the 0.7% doped crystal, dopant PL begins to dominate at long times, which leads to the bi-exponential decay of the transient. (d) Experimental (circles) and MC simulated (solid lines) dynamical red shifts of the mean PL energy. Solid lines depict the MC simulated mean energy values with the following output parameters: the Förster radius of 3.6 nm and the exciton diffusion length of 2.5 nm (Section 3.5.7).

The strong PL reabsorption affects not only the PL spectra in as-grown crystals (Figure 3.2c) but also results in underestimation of the PL QY values. To correct the PL QY of as-grown crystals for PL reabsorption, two methods were applied in Ref. 27. Parker's one[28] is based on deconvolution of the experimental PL spectrum into a

linear combination of the reabsorption-free PL spectra of the host crystal and the dopant in host crystal, which are represented by cyan and red shaded spectra in Figure 3.2a, respectively. The second PL reabsorption correction method is based on comparison of the PL spectra of the as-grown and mechanical grinded crystals.[25, 29-30]

Both methods gave very close values of the reabsorption PL QY.[27] Reabsorption-corrected PL QYs calculated by Parker's method are shown in Figure 3.3 as a function of the doping level. In the 0.7% doped (referred further on as an optimally doped) crystal, PL QY climaxes at almost 40%, which is close to that of the dopant in solution (the red line in Figure 3.2d). In the lowest doped crystal (0.01%), PL QY of ~20% is equal to that of the host molecule in solution (the violet line in Figure 3.2d). This fully corroborates the time-resolved data where the optimally doped crystals show the fastest host PL decay time (Figure S3.7a). In the crystals doped at >1%, PL QY decreases, and the host-dopant energy transfer becomes less efficient (Figure S3.7a and S3.9b). This is explained by aggregation of dopant molecules, which also results in the visible defects in the highly doped samples (demonstrated in Ref. 27). According to Ref. 27 the PL QY data as well as PL spectral data are virtually identical for the self- and externally doped samples; therefore, the two doping techniques result in the optically indistinguishable crystals.

To support the FRET mechanism of host-dopant energy transfer and unravel the balance between exciton diffusion and FRET in host-dopant energy transfer, we performed MC simulations of the energy transport in the host matrix with randomly distributed dopants (Sections 3.5.6). The simulated data describe well the experimental PL transients and red shifts (Figure 3.2b-d) and the experimental PL QY (Figure 3.3) at the doping levels up to the optimal one. At the higher doping levels, the obvious discrepancy between simulated and experimental PL QYs is explained by the fact that the dopant aggregation was not included in the MC simulations.

From the MC simulation (see Sections 3.5.6-8), the Förster radius R_0 was obtained as 3.6 ± 0.2 nm, which corroborates the value of 4.0 nm calculated directly from the Förster equation (for details see Section 3.5.10). The exciton diffusion length amounts to $L_d = 2.5\pm0.4$ nm, which is at the short side of the known exciton diffusion lengths of ~5–10 nm in amorphous organic films.[31] This is ascribed to weak intermolecular interaction in the host crystal as the coupling between the transition dipole moments of the nearest molecules corresponds to weak J-aggregation (see Figure S3 in Ref. 25). Weak J-aggregate-type coupling also

explains why the host crystal PL QY equals to that of diluted host molecules. In the optimally doped crystal, about 90% of the initial host excitons transfer their energy to the dopants mostly via FRET, i.e., the majority of the host excitons are already generated within the Förster radius from the dopant (for the interplay between FRET and exciton diffusion, see Section 3.5.8).
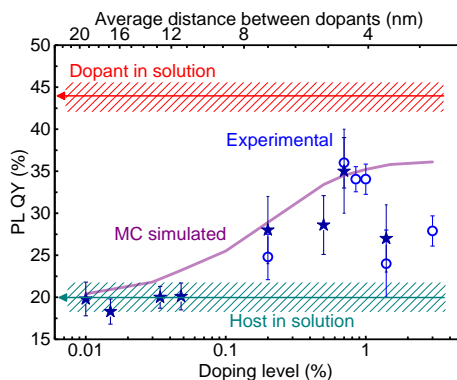
Figure 3.3. Experimental (symbols) and MC simulated (the purple line) PL QY values as functions of the doping level. The blue open dots and navy stars show the data for externally and self-doped crystals, respectively. The experimental PL QYs are corrected for PL reabsorption.[27] The horizontal lines demonstrate the host and dopant PL QYs in solution, the experimental accuracy is depicted by hatching. The upper axis in (d) shows an average distance between the dopants in the host crystals (Section 3.5.1).

Here we have harnessed the byproduct of Suzuki reactions to synthesize a doped organic semiconductor with enhanced luminescence. However, formation of byproducts due to ligand exchange within the organometallic catalytic cycle is known not only for Suzuki but also for other Pd-catalyzed cross-coupling reactions used for synthesis of conjugated materials.[32] To demonstrate that the molecular self-doping is not limited to a single aforementioned case, we studied different conjugated oligoarylenes synthesized via Suzuki, Kumada, and Stille cross-coupling reactions: TPCOs (Chapters 3 and 5 of this Thesis), oligophenylene and furan/phenylene co-oligomer (Chapter 4 of this Thesis) with various conjugated lengths and terminal substituents (see Ref. 27). All these reactions produce self-dopants with longer conjugation lengths as minor byproducts. The time-resolved PL data on crystals of these oligomers clearly indicate prominent energy transfer from the host to the self-dopants (see Ref. 27) which broadens the scope of the self-doping approach.

As the accuracy of standard techniques used to prove the purity of organic materials (NMR, HPLC, GPC, elemental analysis and mass-spectroscopy) might miss such minor byproducts, we believe that the effect of these tiny-amount molecular self-dopants on the luminescent properties of the nominally chemically pure materials has been largely overlooked in the past. In our view, the self-dopant molecules are embedded in host crystal matrix substituting the host sites as was demonstrated above for TMS-P2TP-TMS/TMS-P4TP-TMS, i.e., the host and dopant form co-crystals[33]. Despite much less solubility of the self-dopants in organic solvents as compared to the host, the self-dopant does not precipitate during self-doping, but it is incorporated in the host crystal. This can be explained by complex formation between the dopant and host molecules already in solution as both have the similar rod-like molecular structures so that they stick together with their molecular axes having nearly the same orientation. These complexes survive in the course of further processing including co-crystallization so that the dopant substitutes the host sites in the host crystal lattice. As a result, complete purification of the host from the dopant is a complicated task.

It might well be possible that unintentional doping by longer oligomers also occurred in numerous earlier luminescent studies in nominally chemically pure (>99%) solid samples of conjugated oligomers synthesized via metal-catalyzed cross-coupling reactions. As shown herein, the luminescent dopant even at low content (<1%) in the host material could strongly affect its luminescent properties. This may be one of the reasons for poor understanding of the luminescent properties of conjugated materials as a very minute amount of dopants can be sufficient to drastically change the luminescence in host-guest systems based on conjugated oligomers.[34] For example, if the self-dopant is low-emissive, it may quench luminescence of the material via host-dopant energy transfer limiting the exciton diffusion length and resulting in non-radiative losses of excitation energy. Accordingly, molecular self-doping can be detrimental in materials for organic photovoltaics, where long exciton diffusion length is a prerequisite for high performance of organic solar cells.[35-36] On the other hand, by finding an appropriate route for the host material synthesis, molecular self-doping could be applied to a vast variety of conjugated oligomers as a means to control their luminescence by a minute amount of dopant. Agreeably, the control of the self-doping level is an important issue for applications. In the TMS-P2TP-TMS/TMS-P4TP-TMS host-dopant system, the synthesized crude powder had a reproducible doping level of about 1%, which accidently was very close to the optimal doping level needed for applications.

Nonetheless, in the TMS-P2TP-TMS/TMS-P4TP-TMS system the self-doping level is readily controlled via vacuum sublimations; in other materials (see Ref. 27), the self-doping level can be also controlled during solution processing, which is more promising for practical applications. Basically, solution processing in the course of chemical synthesis grants a plenty of opportunities to control the self-doping level as the host and the self-dopant have similar but different molecular structures and, therefore, much or less different physical and chemical properties. For example, using the strong difference in solubility of the self-dopant and host molecules, one could control the self-doping level during the chemical synthesis by using appropriate solvents and temperature.

3.4. Conclusion

To summarize, we have introduced the molecular self-doping concept as a novel approach to controlling the luminescence in single crystals prepared from nominally chemically pure conjugated oligomers via excitonic transport and host-dopant energy transfer. We have demonstrated that molecular self-doping operates in various conjugated oligomers synthesized via different Pd-catalyzed cross-coupling reactions so that their luminescence in solid-state is strongly affected by the self-dopants. Self-doping offers a number of attractive benefits as compared to more conventional external molecular doping. First, the byproducts produced during the host synthesis could be shorter or longer than the host oligomers. The former are easily removed by standard purification, while the latter remain due to their lower solubility, ensuring the red-shifted dopant absorption spectrum, which is necessary for efficient host-dopant FRET. Second, molecular self-doping provides suitable dopant oligomers in tiny amount immediately in the host powder; therefore, there is no need to synthesize and process the dopant separately which lowers the costs of the chemical synthesis and purification. Finally, the longer dopant is typically less soluble that rises the solubility issues for external doping but not so critical for self-doping, where the host molecules probably impede dopant aggregation. The moderate but still detrimental effect of doping on the charge transport (shown for the crystal in Ref. 27) can be reduced by exciton transport optimization, which would lead to even lower doping levels to facilitate highly efficient host-dopant energy transfer. In a broader context, the molecular self-doping concept is deemed as a promising route for designing the perspective organic optoelectronic materials compatible with solution-based technologies of organic electronics.

Author Contributions

SAP developed the synthetic routes, and OVB synthesized the materials. ODP and VGK grew the crystals and measured their steady-state PL. NMS measured the steady-state PL in solutions. DID assembled the OFET samples and measured their characteristics. AAM performed the time-resolved PL measurements and Monte-Carlo simulations; these were designed and supervised by MSP. DYuP conceived the project which was further developed with MSP. AAM and ODP contributed equally to this work.

3.5. Supplementary Information

3.5.1. Average Distance between the Dopant Molecules in the Crystal

Assuming that dopant molecules are uniformly distributed in the doped crystal, the average distance, d, between dopant molecules in crystals with the molar doping level, n_d, was calculated as:

$$d = \sqrt[3]{\frac{M}{\rho \, N_A \, n_d}},$$

(3.1)

where $M = 462$ g·mol^{-1} is the host (TMS-P2TP-TMS) molar mass, $\rho = 1.18$ g·cm^{-3} is the host crystal density,[24] N_A is the Avogadro number.

3.5.2. Polarization-Resolved PL Data and Molecular Dynamics Simulations of the Dopant in the Host Matrix

To estimate the mutual orientations of the dopant and host molecules in the crystal, the polarization-resolved PL data were collected. The excitation beam polarization was set parallel to one of the crystal sides (i.e. oriented along the crystallographic axis a or b), and the polarization of PL was analyzed with a polarizer placed before the polychromator. Figure S3.1 shows the polarization-resolved PL data at the 450 nm and 550 nm PL bands, which belong to the host crystal and the dopants in the host crystal, respectively (Figure 3.2a). PL from both the host crystal (the blue line in Figure S3.1) and the dopants (the red line in Figure S3.1) is weakly polarized, with the similar polarization extinction coefficient of $\rho = 0.8 \pm 0.1$. This suggests

that the dopant molecules (having a similar shape but a longer length as compared to the host one) substitute the host sites in the doped crystals.
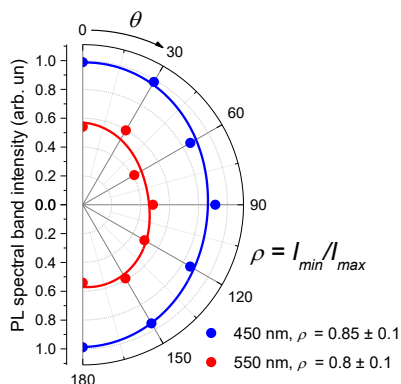
Figure S3.1. Angular polarization dependences of intensities of two PL spectral band for the 0.05% doped crystal (450 nm, blue dots; 550 nm, red dots). The solid lines are fits by the function $A \cdot cos^2(\theta - \theta_0) + B$, where θ is the angle between polarizations of PL and the excitation beam, with the fitting parameters A =0.14±0.05 and 0.13±0.05, B =0.86±0.05 and 0.44±0.05, θ_0=5±10° and 10±15°, for 450 and 550 nm, respectively. The PL intensity of the 450-nm band is normalized to unity at $\theta - \theta_0 = 0$. The polarization extinction coefficients for each PL band, ρ, were calculated as $\rho = B/(A + B)$. The excitation wavelength was set at 400 nm.

Figure S3.2 illustrates possible dopant substitution of a host molecule in the TMS-P2TP-TMS crystal structure, where the pristine host crystal molecular packing is taken from the x-ray diffraction data,[24] and the atoms rearrangements are simulated using molecular dynamics by Avogadro: an open-source molecular builder and visualization tool[37] The substitution results mainly in bending of the nearest TMS groups (Figure S3.2) and small torsional/bending deformations of the dopant and adjacent host conjugated cores.
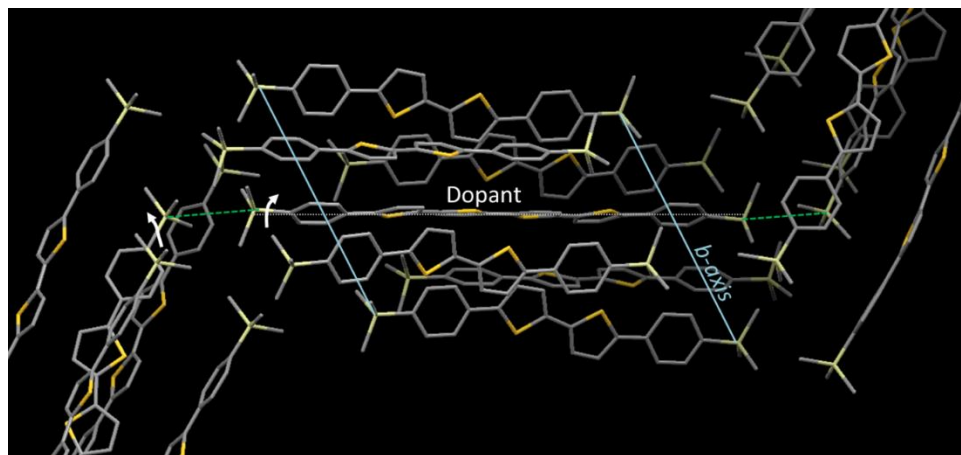
Figure S3.2. Model of doped TMS-P2TP-TMS crystalline aggregate simulated for 21 molecules (7 for each layer), where the central host molecule is substituted by a dopant one. The green dash lines show the distance between the Si atoms of the TMS groups of the host and the dopant, which are maximally displaced as compared to their initial positions. The white arrows show their rearrangement directions. For clarity, the methyl groups are omitted, and only 18 molecules are shown.

3.5.3. Time-Resolved PL Maps for the Doped Crystals

Time-resolved PL data were collected by the streak-camera (C5680, Hamamatsu) equipped with a polychromator. The excitation pulses (400 nm, 100 fs) were produced by the doubled output of a Ti:sapphire laser (Coherent Mira). The laser repetition rate was reduced to 1.9 MHz by an external pulse picker (Coherent) to exclude excited-state population accumulation. The time-resolved PL spectra of the crystals at the room temperature were collected by an inverted microscope (Zeiss Axiovert 100) with a 10x, NA=0.25 objective; the excitation spot size was ~5 µm in diameter. The apparatus response function was ~10 ps in duration.
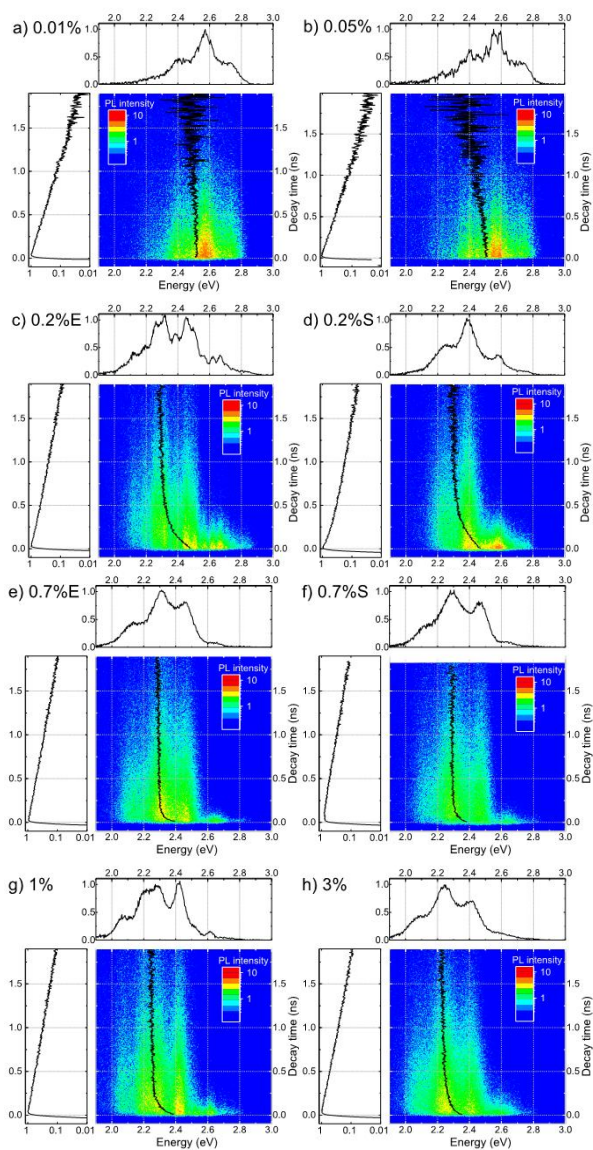
Figure S3.3. Each panel shows the PL maps (center), time-integrated PL spectra (top) and frequency-integrated time-resolved PL transients (left) collected in the microscopic configuration for variously doped crystals (the doping level is shown in the panels). The mean energy value at each time is shown by black lines in the maps. The PL mean energy does not coincide with the PL maximum due to asymmetry of the PL spectra. For the S/E indices, refer to self-/external self-doping (for details see Ref. 27). The excitation wavelength was set at 400 nm.

Figure S3.3 plots PL maps, time-integrated spectra, transients integrated over the whole spectral region, and mean energy values at each time (the dynamical red shift of the mean PL energy)[38] of the crystals doped in the range of 0.01–3%. Brief inspection of the PL maps shows that, with increase of the doping level, PL shifts more to the red, and the dynamical red shift accelerates. This is assigned to FRET from the host (blue-shifted spectrum) to the dopant (red-shifted spectrum), most probably, preceded by the exciton diffusion in the host material.

3.5.4. Analysis of PL Maps

Signal-to-noise ratio and dynamical range. Figure S3.4 plots the PL transients in a 10-ns time window for the 0.01% (lowest) and the 1.4% doped crystals. Panel (a) shows that in the blue flank (2.6 – 2.9 eV) the signals are overwhelmed by the CCD readout noise after 2 ns. Panel (b) demonstrates that in the red flank (1.8 – 2.1 eV) the readout noise becomes dominant after ~5 ns; before this time the decaying part of the transients is clearly monoexponential. Therefore, as a compromise between the signal-to-noise ratio and time resolution (a longer time base of the streak camera decreases the time resolution), we choose the 2-ns time window for all transients.
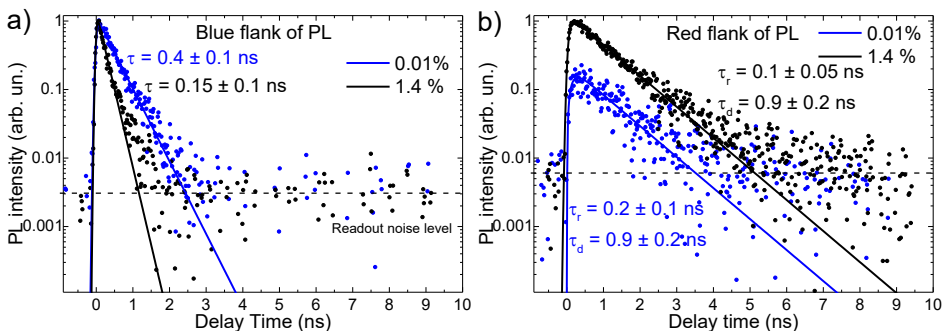
Figure S3.4. PL transients of the 0.01% and 1.4% doped crystals (dots) recorded in 10-ns time window. The solid lines are the mono- (in a) and bi- (in b) exponential fits with their time constants shown next to the fits. The dash lines show the CCD noise level calculated as a root mean square value of the data in the negative (-0.5 – 0) time window. The scaling between the experimental PL intensities is preserved. The excitation wavelength was set at 400 nm.

A closer inspection of the blue flank PL transients reveals a small but noticeable deviation of the transient in the 1.4% doped crystal from a single exponential decay at ~1 ns. This effect will be discussed later in this Section.

Spectrally-resolved transients and transient spectra. Figure S3.5a,b shows PL transients from Figure 3.2b,c and the corresponding exponential fits (lines) with the fit parameters summarized in Figure S3.5c. In the 0.01% doped crystal, the blue-flank decay time (blue, Figure S3.5a) is only slightly faster than the lifetime of host excitons, τ_h (0.4±0.1 ns vs 0.45±0.05 ns shown as cyan line in Figure S3.6b), indicating quite inefficient host-dopant energy transfer . This also warrants the usage of the 0.01% doped crystal as a representative for the spectroscopic properties of the pristine host crystal. In the 0.7% doped crystal, the red-flank PL decay time (red, Figure S3.5b) is similar to the lifetime of dopant excitations, τ_d, (shown as orange line in Figure S3.6b), indicating dominant contribution of dopant PL.
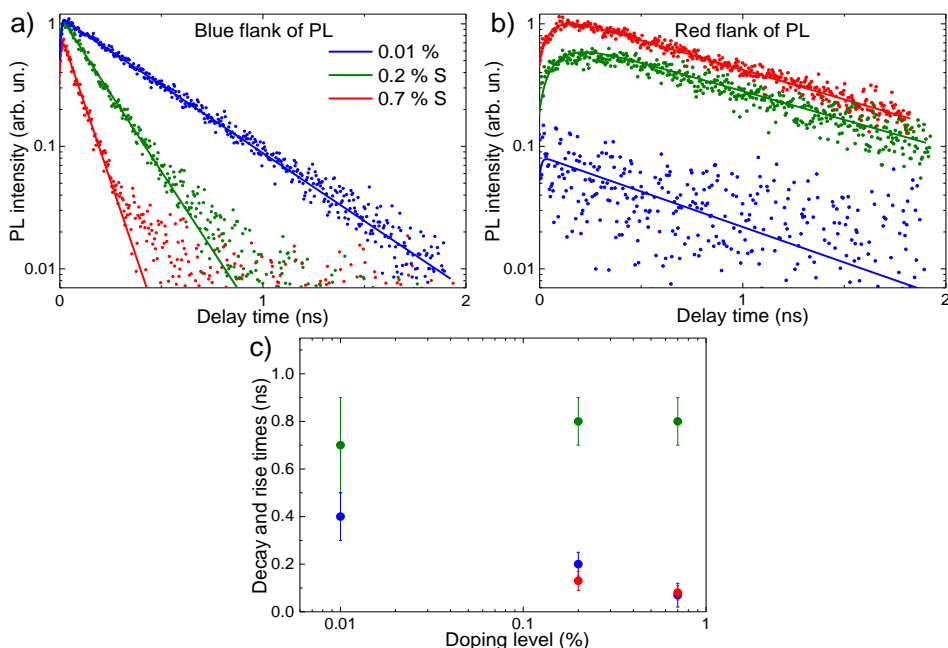
Figure S3.5. PL transients from Figure 3.2b,c (dots). The lines are the monoexponential fits in panel (a) and mono- and bi-exponential fits in panel (b). Scaling in (a) and (b) between the experimental PL intensities is preserved. The corresponding decay times from panel (a) are shown in panel (c) as the blue dots, while the decay and rise times (for 0.2% and 0.7% doping levels) from panel (b) are shown as the green and red dots, respectively. The vertical bars in (c) indicate the error margins of the fits. The excitation wavelength was set at 400 nm.

Figure S3.6a plots the PL spectra in such a way, which highlights the PL features of the pristine host crystal and dopant molecules in the crystals. The PL map of the

lowest doped 0.01% crystal was integrated over the short 0–0.1 ns time window where the host contribution is the most pronounced (Figure S3.3a). This reproduces the PL spectrum of the pristine host crystal (blue line, Figure S3.6a). The PL spectrum of the 0.7% E doped crystal was time-integrated over the long 1.5–2.0 ns time window; this reproduces the PL spectrum of the dopant (red line, Figure S3.6a). From these two spectra, the mean energy E_0 of the dopant PL and the host-dopant energy gap ΔE (defined as the difference between the host and dopant PL mean energies) were obtained as $E_0 = 2.3 \pm 0.02$ eV and $\Delta E = 0.25 \pm 0.02$ eV. Note that the PL spectra of crystals collected with the streak camera in the microscopic configuration are slightly affected by reabsorption of host PL as follows from the decreased intensities of the band at ~2.8 eV as compared to PL spectra of the grinded host crystals (shown in Ref. 27).
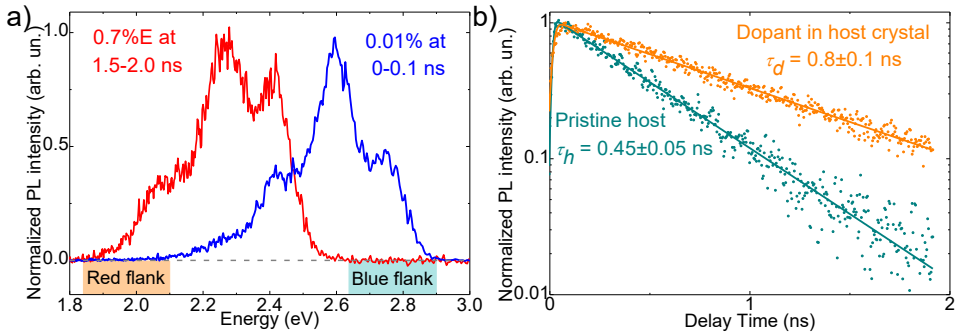
Figure S3.6. Time-resolved PL spectra and transients corresponding to the pristine host and the dopant in host crystal. (a) PL spectra of the 0.01% (blue line) and 0.7%E (red line) doped crystals resulted from time-integrating the PL maps over the short (0–0.1 ns) and long (1.5–2.0 ns) time windows, respectively. (b) The transients were obtained by integrating over 2.65–2.9 eV (cyan dots) and 1.85–2.1 eV (orange dots) PL spectral regions (shown in panel (a) by the color bars) of the lowest (0.01%) and the 0.7% E-doped crystals, respectively. The orange and cyan solid lines are monoexponential fits convoluted with the apparatus response of ~10 ps. The corresponding PL decay times are shown next to the fits. The excitation wavelength was set at 400 nm.

Figure S3.6b shows PL transients assigned to the pristine host and the dopant in the host crystal. To obtain the pristine host PL transients, PL integration over the 2.65–2.9 eV spectral region of the map for the lowest doped 0.01% crystal (Figure S3.3a) was used (the cyan bar in Figure S3.6a), because this region is not contaminated by the dopant PL (red line in Figure S3.6a). Similarly, to obtain the PL transients of the dopant in the host crystal, the 1.85–2.1 eV spectral region of the PL map for the 0.7% E doped crystal (Figure S3.3e) was used (the orange bar in Figure

S3.6a). Fitting these transients with a monoexponential function resulted in the lifetimes of the host excitons ($\tau_h = 0.45 \pm 0.05$ ns) and dopant excitations ($\tau_d = 0.8 \pm 0.1$ ns). The four parameters, i.e. E_0, ΔE, τ_h and τ_d, will be used as the input for the Monte-Carlo (MC) simulations (Section 3.5.6).

To evaluate how fast the host-dopant energy transfer occurs in the variously doped crystals, Figure S3.7 depicts the blue flank and red flank PL transients for PL maps of all samples. Figure S3.9b summarizes the short-time decay and rise times obtained from the monoexponential fits of the blue flank PL transients and biexponential fits of the red flank PL transients in Figure S3.7a,b, respectively.
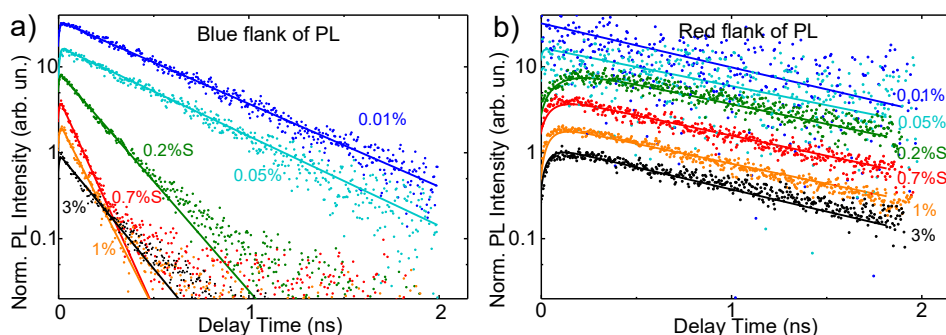
Figure S3.7. Spectrally integrated PL transients for PL maps of all samples (the doping levels are shown next to the transients). The PL transients in panels (a) and (b) were obtained by integrating PL maps over the 2.6–2.9 eV (PL blue flank) and the 1.8–2.1 eV (PL red flank) spectral regions, respectively. The solid lines in (a) and (b) are mono and bi-exponential fits, respectively, convoluted with an apparatus response of 10 ps. The corresponding decay times obtained from the fits in panels (a) and (b) and rise times obtained from the fits in panel (b) are shown in Figure S3.9b by blue, olive and red dots, respectively. All transients are vertically-shifted (normalized) for clarity. The excitation wavelength was set at 400 nm.

Here we would like to comment on an apparent deviation from the monoexponential behavior of the blue flank transients for the 0.7% (Figure S3.5a) and 1.4% (Figure S3.4a) doped crystals at long times. The blue flank of PL also contains a contribution from the dopant PL, which is unobservably weak for the low dopant concentrations but becomes visible at 0.2–0.7% doping levels. Dopant PL has a longer lifetime as compared to the host PL, which explains the longer tail of PL in the 0.7% and 1.4% doped crystal (i.e., when the dopant PL becomes dominant). This effect is readily captured by MC simulations (see Section 3.5.6).

To demonstrate that solvent molecules that potentially might be incorporated in our solution-grown crystals do not affect the PL transients, we recorded the PL

transients for host crystals grown by PVT technique, which should completely remove the solvent molecules. Figure S3.8 shows that there is no difference between the transients for the solution and vapor-grown crystals (the doping level for both 0.01%). As a result, we suggest that the solvent molecules do not affect the crystal structure or do not get embedded into it.
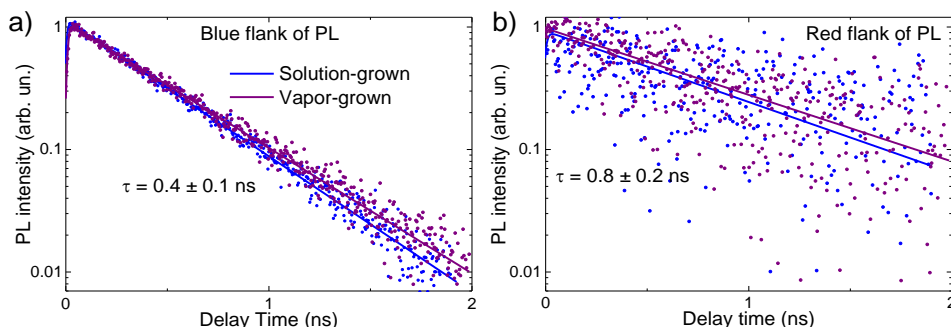
Figure S3.8. PL transients of the 0.01% doped solution and vapor-grown crystals. The solid lines are the monoexponential fits. The experimental PL intensities is normalized to the unity. The corresponding decay times are shown next to the fit lines. The excitation wavelength was set at 400 nm.

Dynamical red shift. Another convenient way to characterize the energy transport process in the crystals is to analyze the dynamical red shift of the mean PL energy (Figure S3.9a). For the lowest doping level, PL originates mostly from the host excitons (mean energy of ~2.55 eV), with a weak PL shift to the red due to energy transfer to the dopants. At the doping level of 0.2% and higher, the majority of excitons in the crystal are transferred to the lower energy levels with the red-shifted PL energy of ~2.3 eV, which corresponds to the dopant PL (the red line in Figure S3.6a).

Figure S3.9b summarizes the characteristic times of the dynamical red shifts obtained from the exponential fits plotted in Figure S3.9a. In the lowest doped crystal, the characteristic time of the dynamical red-shifts is much longer than the host excitons lifetime (6 ns *vs.* 0.45 ns) indicating low probability of the host-dopant energy transfer. With the doping level increase, substantial acceleration of the dynamical red shift is observed, which is quantitatively similar to the delay/raise times of the transients at the blue- and red flanks of PL (Figure S3.9b).
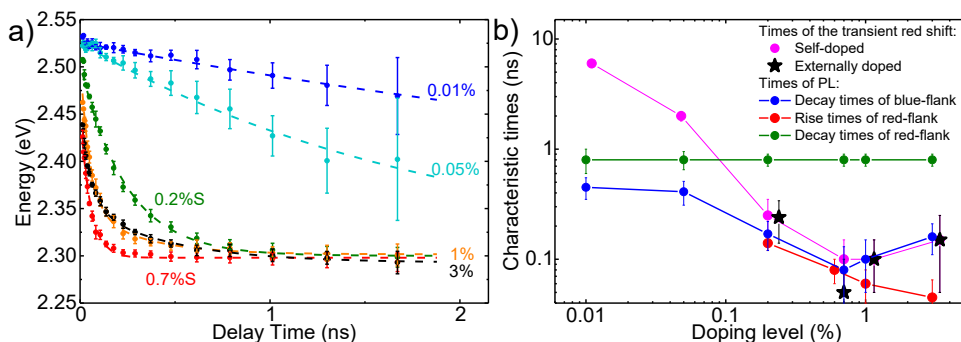
Figure S3.9. Dynamical red shifts (a) of the mean PL energy for the PL maps of all samples (the doping levels are shown next to the transients), and the characteristic times (b) extracted from exponential fits in panel (a) and Figure S3.7. The dash lines in (a) are monoexponential fits by the function $E = E_0 + \Delta E \cdot exp(-t/\tau)$, with the mean energy of the dopant PL $E_0 = 2.3 \pm 0.02$ eV and the host-dopant energy gap $\Delta E = 0.25 \pm 0.02$ eV obtained earlier in this Section. The times of the dynamical red shifts, τ, obtained from the fits are shown in panel (b) by the black line (magenta dots and black stars for self- and externally doped crystals, respectively). The blue, olive and red dots in panel (b) show the decay times of the blue-flank and red-flank and the rise times of red-flank PL (the PL transients are plotted in Figure S3.7), respectively. The overlapping data points in (b) were slightly shifted horizontally for presentation purposes. The vertical bars in (b) show the error margins of the fits. The excitation wavelength was set at 400 nm.

In the 1% and 3% doped crystals, the characteristic times of dynamical red shifts as well as the blue-flank PL decay times become longer than the ones at the 0.7% doping level, which could be explained by aggregation of dopant molecules in host matrix resulting also in defects observed in the highly doped samples. Therefore, the 0.7% doping level appears as optimal as, on the one hand, this dopant concentration allows efficient host-dopant energy transfer, and, on the other hand, the low-defect structure of the doped crystals is still maintained.

3.5.5. Time-Resolved PL Spectroscopy at Low Temperatures

Both exciton diffusion in the host material and host-dopant FRET explain host-dopant energy transfer. The dynamics of FRET are weakly dependent on temperature, in sharp contrast with exciton diffusion.[20] To reveal the contributions of the two, we analyzed the time-resolved PL data in the lowest (0.01%) and optimally (0.7%S) doped crystals at 77 and 293 K (Figure S3.10).
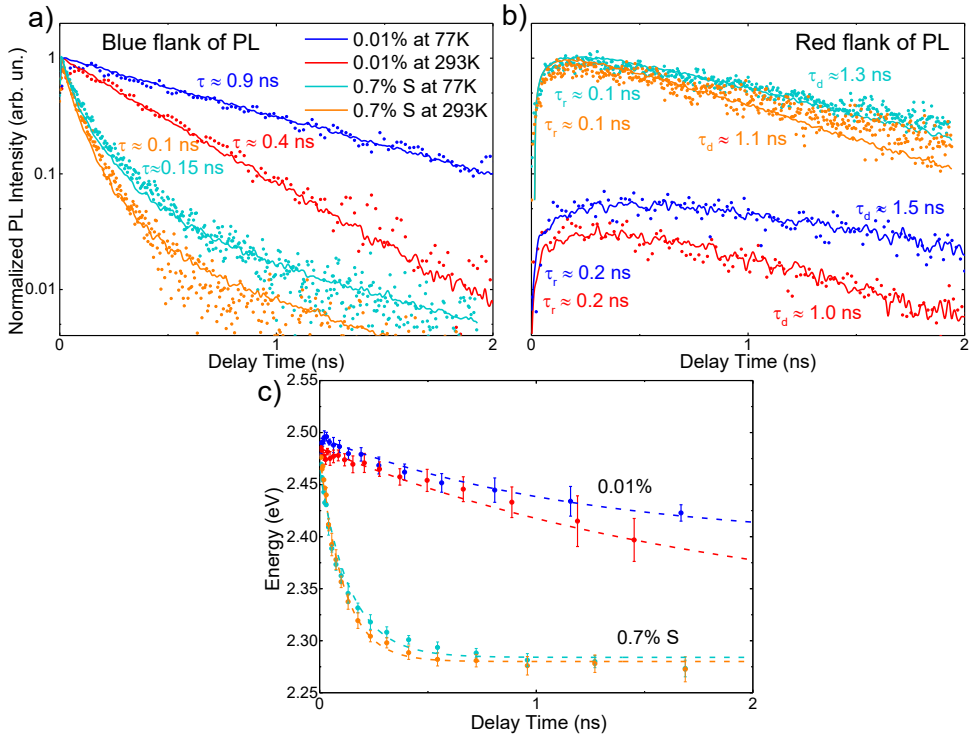
Figure S3.10. Experimental (dots) and MC simulated (lines; see Section 3.5.7 for the detailed description) PL transients at 77 K and 293 K for 0.01% and 0.7% S doped crystals. (a, b) PL transients extracted from the PL maps at the blue and red PL spectral flanks (i.e., 2.6–2.9 eV and 1.8–2.1 eV spectral regions indicated in Figure S3.6a), which originate mostly from host and dopant PL, respectively. Scaling between the experimental PL intensities is preserved. The corresponding decay times attributed to short-time blue flank PL transients in (a), the rise and decay times attributed to red flank PL transients in (b) obtained from the monoexponential and bi-exponential fits, respectively, are shown next to the transients. (c) The dynamical red shifts of the mean PL energy are shown by red and orange dots for 293 K, and by blue and cyan dots for 77 K. The solid lines are monoexponential fits to the function $E = E_0 + \Delta E^* \cdot exp(-t/\tau)$, with the mean energy of the dopant PL $E_0 = 2.3 \pm 0.02$ eV and host-dopant energy gap $\Delta E^* = 0.2 \pm 0.05$ eV. The latter value is slightly lower than the one obtained in the microscopic configuration (Figure S3.6a) due to increased reabsorption in the 90° PL collection geometry. From the fits, the times of the dynamical red shifts, τ, in the 0.01% doped crystal at 77 K and 293 K were obtained as 1.5±0.1 and 1.3±0.1 ns, respectively; for the 0.7% S doped crystal, they are 0.1±0.05 ns at both temperatures. The excitation wavelength was set at 400 nm.

For the temperature-dependent time-resolved PL data measurements, the samples were placed in a liquid nitrogen cryostat (Oxford), and the time-resolved PL were collected in a 90° geometry with respect to the excitation pulse. In this case, the

excitation spot size was ~50 µm because of a long (5 cm) focal distance lens outside the cryostat. The apparatus response function was ~10 ps in duration.

Figure S3.10a,b shows that PL decays are slower at 77 K (blue and cyan) than at 293 K (red and orange), which we take as an indication of suppressed non-radiative pathways (which most probably are thermally-activated) for the host crystal and the dopant. Suppression of the non-radiative pathways is more pronounced for the blue-flank PL (Figure S3.10a), i.e., for the host crystal PL. In contrast, the rise times of the red-flank PL transients, which are the most sensitive to host-dopant energy transfer, are similar at 77 and 293 K (Figure S3.10b). This indicates that the host-dopant energy transfer weakly depends on the temperature.

Figure S3.10c shows the dynamical red shifts of the mean PL energy. In the 0.01% doped crystal, the PL dynamical red-shift is slightly slower at 77 K than at 293 K, which is assigned to the slowed exciton diffusion. In the 0.7% doped crystal, the dynamical red shifts are similar for both temperatures, which suggests that exciton diffusion is of limited importance for the host-dopant energy transfer. Therefore, we conclude that exciton diffusion contributes to the host-dopant energy transfer mainly in the weakly-doped crystals, while in the optimally-doped ones the FRET process takes over.

To perform MC simulations for the low temperature conditions, we need to know the non-radiative lifetimes of the host excitons τ_{hn}^{77K} and the dopant excitation τ_{dn}^{77K} at 77 K. These can be calculated from PL QY at 77 K, which in turn can be directly related to PL QY at 293 K by integrating the relevant PL maps. For the host PL QY, we integrated PL maps of the 0.01% doped crystal at the two temperatures over the 0–2 ns time window and 2.65–2.9 eV spectral region, i.e., where the dopant does not produce PL (the red line in Figure S3.6a). This resulted in the ratio of QYs at 77 K and 293 K as $QY_h^{77K}/QY_h^{293K} \approx 2$. For the dopant QY, we integrated PL maps of the 0.7% doped crystal over the 0–2 ns time window and 1.85–2.1 eV spectral range, i.e., where the host almost does not produce PL (the blue line in Figure S3.6a), to obtain $QY_d^{77K}/QY_d^{293K} \approx 1.1$. Finally, assuming that the radiative lifetime does not change with temperature, the non-radiative lifetimes of the host excitons and the dopant excitation were calculated as $\tau_{hn}^{77K} = 1.6 \pm 0.4$ ns and $\tau_{dn}^{77K} = 1.8 \pm 0.4$ ns, respectively.

3.5.6. MC Simulation

Host-dopant energy transfer in the crystals was modelled as exciton hopping in the host matrix followed by Förster resonance energy transfer to dopant molecules (Figure S3.11).[39] 3D cubic crystal grid was generated with the cell volume that equals to the average volume per host molecule in the host crystals lattice (Figure S3.11). The dopants were randomly placed into grid cells with concentration n_d (red dots in Figure S3.11). The host excitons were randomly placed into the grid cells in such a way that they avoided the grid cells occupied by the dopants (navy dots in Figure S3.11). The exciton density was maintained low enough (one exciton per 200 unit cells) to avoid exciton-exciton annihilation.
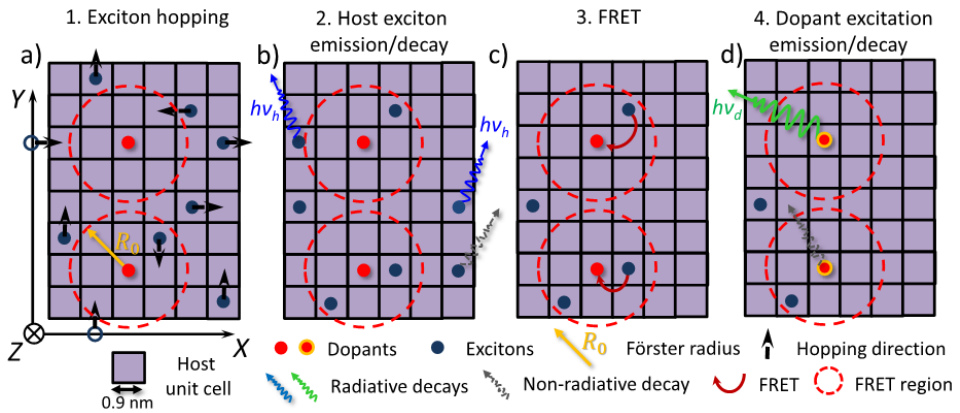
Figure S3.11. Schematics of one time step in the MC simulations. Each purple matrix represents a 2D projection of the 3D host grid at one time step of the MC simulation, where one of the four possibilities for the generated exciton is realized. The notations of all symbols are shown below the matrixes.

At each time step, one of the following three possibilities for the generated exciton is realized (Figure S3.11a-c):

1) Exciton hopping (Figure S3.11a): the exciton hops between the neighboring cells with the hopping time τ_{hop}. The periodic boundary conditions are applied, i.e., if the exciton crosses the border it emerges at the other side. The exciton hopping time, τ_{hop}, was considered as a global parameter (i.e., identical for all samples).

2) Exciton emission/decay (Figure S3.11b): the host exciton decays either radiatively with the lifetime τ_{hr} or non-radiatively with the lifetime τ_{hn}. In the former case, the exciton emits a photon (Figure 1.7b, blue curved arrow) with the mean energy of $E_0 + \Delta E$ (calculated before in Section 3.5.4b). The lifetimes τ_{hr} and

τ_{hn} were calculated from the following equations: $1/\tau_h = 1/\tau_{hr} + 1/\tau_{hn}$; $QY_h = \tau_{hn} / (\tau_{hr} + \tau_{hn})$, where the exciton lifetime of the host, τ_h, was extracted from the time-resolved PL measurements (Section 3.5.4b), and QY_h is the measured host PL QY in dilute solution.[27]

3) FRET (Figure S3.11c): Isotropic FRET (Figure 1.7b, gray dash arrows) occurs to one of the dopants with the Förster rate:[20]

$$K = 1/\tau_h \cdot (R_0/r)^6 \tag{3.2}$$

where r is the distance between the exciton and the dopant, and R_0 is the Förster radius, which is considered as a global parameter.

For the dopant, the following only possibility is available:

4) Dopant excitation emission/decay (Figure S3.11d): the dopant excitation decays either radiatively with the lifetime τ_{dr} or non-radiatively with the lifetime τ_{dn}. In the first case, the emitted photon (Figure 1.7b, red curved arrow) has the mean energy of E_0. The lifetimes τ_{dr} and τ_{dn} were calculated from the following equations: $1/\tau_d = 1/\tau_{dr} + 1/\tau_{dn}$; $QY_d = \tau_{dn} / (\tau_{dr} + \tau_{dn})$, where the exciton lifetime of the dopant in the host matrix, τ_d, was extracted from the time-resolved PL measurements (Section 3.5.4b), and QY_d is the measured dopant PL QY in diluted solution.[27]

The exciton diffusion length L_d was calculated as $L_d = (\tau_h \cdot l^2 /\tau_{hop})^{1/2}$, where $l = (a \cdot b \cdot c/Z)^{1/3}$ is the unit cell size in the simulated 3-D crystal grid (~0.9 nm; the unit cell parameters a, b, c and Z for the host crystal were taken from Ref. 24). The host and dopant PL transients were plotted as $N_h(t)/(N_d(t) + N_h(t))$ and $N_d(t)/(N_d(t) + N_h(t))$ functions, respectively, where $N_d(t)$ and $N_h(t)$ are the number of photons emitted by the dopant and the host, respectively. To account for imperfect filtering-off dopant PL at the blue flank of the integration spectral range a small amount of dopant PL was added to the host transients (1% for the 0.7% doped crystal, which was scaled proportionally to the dopant concentration for the other crystals). The simulated PL QY was calculated by integrating $N_d(t) + N_h(t)$ over time and dividing by the initial number of excitons. The average energy of the emitted photons $E(t)$ was calculated for each time step t as $E(t) = E_0 + \Delta E \cdot N_h(t) / (N_d(t) + N_h(t))$.

Each MC simulation consisted of 100 runs. Each run starts with a new set of 5000 randomly-placed excitons, and after each 10 runs the dopants are randomly redistributed over the grid.

3.5.7. Parameters of Monte-Carlo Simulations

Table S3.1. Global parameters (input, free, and output) of the Monte-Carlo simulation for the four crystals (0.01%, 0.05%, 0.2%, 0.7% doping levels) at 293 K, and for the two crystals cooled to 77 K (0.01% and 0.7% doping levels). The error margins for the input parameters are given according to the accuracy of the measured data. The error margins for the free parameters were obtained according to their χ^2 minimization procedure (Section 3.5.9).

Parameter (units)	Value at 293K	Value at 77K	Type (Source)
Mean host photon energy, $E_0 + \Delta E$ (eV)	2.55 ± 0.02		Input (Section 3.5.4b)
Mean dopant photon energy, E_0 (eV)	2.3 ± 0.02		Input (Section 3.5.4b)
Host-dopant energy gap, ΔE (eV)	0.25 ± 0.02		Input (Section 3.5.4b)
Host radiative lifetime, τ_{hr} (ns)	2.0 ± 0.2		Input (Section 3.5.4b)
Dopant radiative lifetime, τ_{dr} (ns)	1.9 ± 0.2		Input (Section 3.5.4b)
Host non-radiative lifetime, τ_{hn} (ns)	0.5 ± 0.1	1.6 ± 0.4	Input (Section 3.5.4b/3.5.5)
Dopant non-radiative lifetime, τ_{dn} (ns)	1.45 ± 0.2	1.8 ± 0.4	Input (Section 3.5.4b/3.5.5)
Exciton lifetime in host matrix, τ_h (ns)	0.45 ± 0.05	0.9 ± 0.2	Input (Section 3.5.4b/3.5.5)
Excitation lifetime of dopants, τ_d (ns)	0.8 ± 0.1	0.9 ± 0.2	Input (Section 3.5.4b/3.5.5)
PL QY of host matrix, QY_h (%)	20 ± 2	44 ± 2	Input (Figure 3.2d/ Section 3.5.5)
PL QY of dopants, QY_d (%)	44 ± 2	48 ± 5	Input (Section 3.5.5)
Förster radius, R_0 (nm)	3.6 ± 0.2	4.0 ± 0.2[a]	Free at 293K/ Output at 77K
Hopping time, τ_{hop} (ns)	0.05 ± 0.02	0.25 ± 0.1	Free
Diffusion length, L_d (nm)	2.5 ± 0.4	1.7 ± 0.6	Output

[a] the scaling factor of $[QY_h^{77K}/QY_h^{293K}]^{1/6}$ is ~*1.12*. (see Equation 3.4)

All parameters in the MC simulation, excluding the doping level, n_d, were the global parameters, i.e., identical for all crystals (Table S3.1). Most of these parameters were directly extracted from the experimental data (marked as "input" in Table S3.1). The only free parameters are the Förster radius R_0 and the hopping time τ_{hop} (marked as "free" in Table S3.1); these were obtained for the best approximation of the experimental data for the four crystals with the following doping levels: 0.01%, 0.05%, 0.2%, 0.7%. The data for the highest-doped crystals were not included in the global fit as in these crystals the host-energy transfer becomes less efficient due to defects in the crystals. Note that the FRET probability is conserved upon cooling to

77 K (see Section 3.5.5), because the increase in the $R_0{}^6$ value is compensated by the host exciton lifetime increase (Equation 3.2), i.e. $R_0{}^6/\tau_h \sim 1$. The τ_{hop} was kept as a free parameter for both temperatures (Table S3.1).

3.5.8. Distributions of the Energy Transport Length
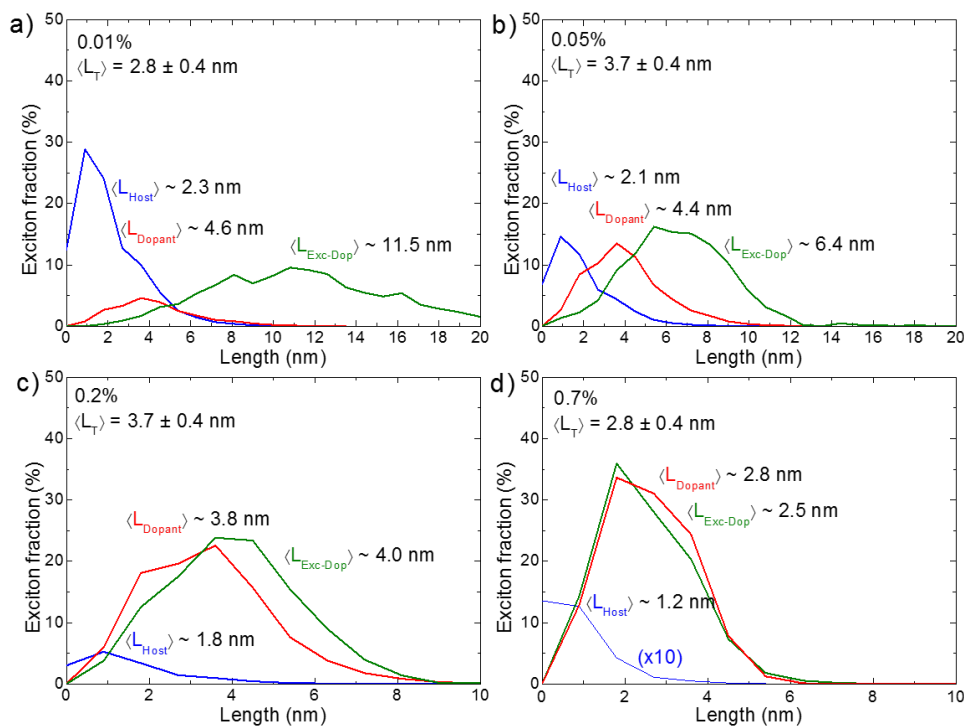
Figure S3.12. Energy transport length distributions in variously doped crystals, for the excitons in the host matrix without FRET, L_{Host} (blue), and for the excitons transferred to dopants, L_{Dopant} (red). The distribution of the shortest exciton-dopant distances, $L_{Exc-Dop}$ (olive), is also shown for comparison. The doping levels and respective averaged energy transport lengths are shown next to the histograms.

In the MC simulations, the energy transport is realized via exciton diffusion in the host matrix and subsequent host-dopant FRET. Figure S3.12a-d shows the calculated length (i.e., the distance between the initial and final positions) distributions for two types of excitons: the excitons that do not leave the host matrix L_{Host} (blue), and the excitons that are eventually transferred to the dopants L_{Dopant} (red). For comparison,

distributions of the shortest distance between the exciton and the (nearest) dopant $L_{Exc-Dop}$ is also shown (olive). At the lowest doping level (Figure S3.12a), L_{Host} is close to the exciton diffusing length of 2.5 nm in the neat crystal. L_{Dopant} of ~4.6 nm is longer than the Förster radius of 3.6 nm, which makes FRET realized only for a small fraction of the initial excitons that were lucky to have a dopant molecule in their close proximity. In contrast, for the optimal dopant level of 0.7% (Figure S3.12d), L_{Host} diminishes to ~1.2 nm with a very few excitons diffused over this distance because it becomes more energetically profitable for an exciton to be FRET-transferred to the dopant. Of course, this is due to the fact that the $L_{Exc-Dop}$ histogram peaks well below the Förster radius.

Figure S3.13 plots the averaged energy transport length, L_T, defined as a distance between the initial and final exciton positions (be it in the host or in the dopant). Apparently, the longest L_T is reached with competitive contributions from exciton diffusion and FRET. However, this does not necessarily warrant the highest PL QY because it appears more advantageous for an exciton to end up at the dopant with its higher PL QY as soon as possible. In the optimally doped crystal, the averaged shortest exciton-dopant distance (~2.5 nm, Figure S3.12d) is shorter than the Forster radius, which ensures most excitons be transferred to the dopants.
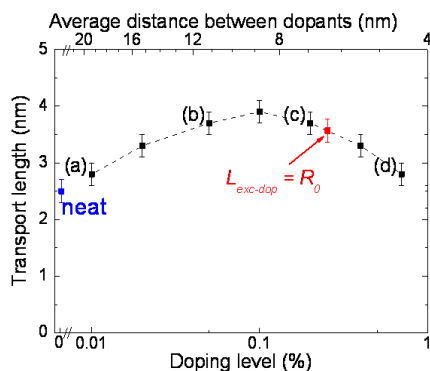
Figure S3.13. Averaged energy transport lengths, L_T, as a function of the doping level. The top axis shows the average distance between the dopants in host crystal (Section 3.5.2), the vertical bars stand the error margins of MC simulations, and the Figure S3.12 data labels indicate the data points extracted from the corresponding panels.

Figure S3.14 depicts the quantum efficiency of energy transfer defined as the ratio of the excitons transferred to dopants number to the initial number of excitons in the crystals. The energy transfer efficiency increases with the doping level to reach impressive ~90% in the optimally doped crystal (0.7%). This value could further be

increased by optimizing the exciton diffusion to provide a pathway towards more sparse dopants.
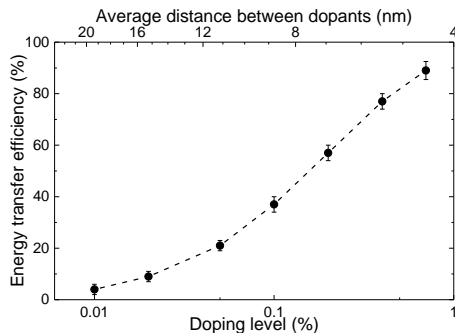
Figure S3.14. Energy transfer efficiency in variously doped crystals. Vertical bars demonstrate the error margins of MC simulations. The upper axis shows the average distance between the dopants in host crystal (Section 3.5.2).

3.5.9. Stability of the MC Simulations with respect to the Förster Radius and the Exciton Hopping Time

The Förster radius is one of the two global MC parameters, which were chosen for the best agreements with the experimental data. Figure S3.15 shows the results of MC simulations with different Förster radius R_0, where the second free global parameter (hopping time τ_{hop}) was adjusted until the best agreement with the experimental data is obtained. For $R_0 = 3$ nm, the MC simulation do not reproduce the transients at high doping levels (0.2% S and 0.7% S doped crystals, Figure S3.15a). For $R_0 = 4$ nm, the MC simulation miss the low (0.05%) doped crystals (Figure S15b). The obtained Förster radius $R_0 = 3.6$ nm provides the best reproduction of all the experimental data.
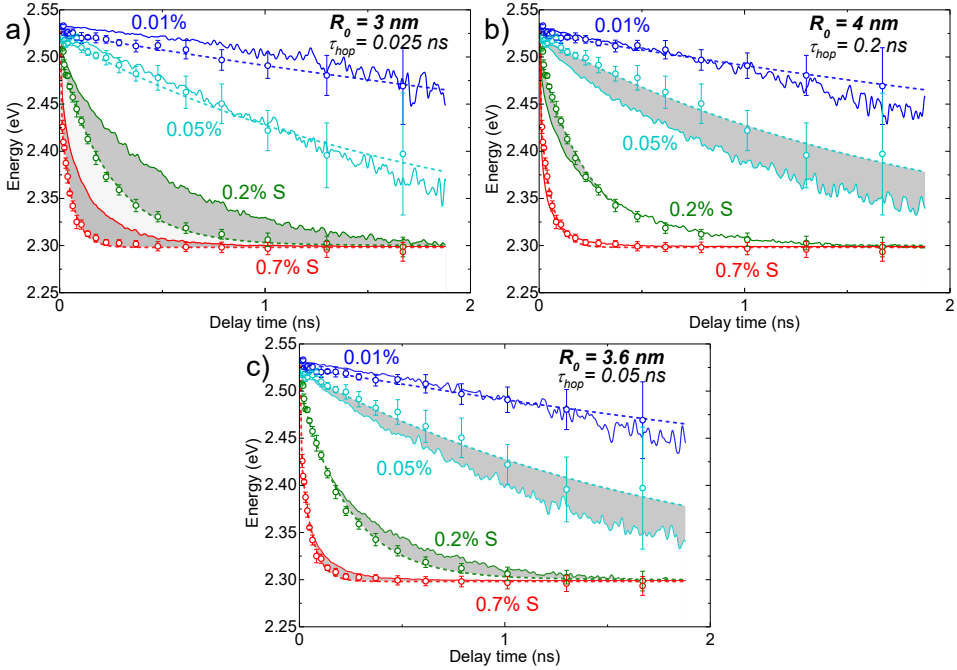
Figure S3.15. Experimental (circles) and MC simulated (solid lines) dynamical red shifts of the mean PL energy for the representative doping levels: 0.01% (blue), 0.05% (cyan), 0.2% (olive), 0.7% (red), for the self-doped crystals at 293 K. Solid lines depict the MC simulated mean energy values with the Förster radius taken as 3 nm (a), 4 nm (b), and 3.6 nm (c). The dash lines are monoexponential fits from Figure S3.9a; the disagreements are shown by the gray regions.

To highlight stability of the MC results, we tested fairness of the fit by the least squared deviation as a criterion:

$$\chi^2 \equiv C \cdot \sum_i \sum_m \left(E_{data}(t) - E_{MC}(t) \right)^2 \tag{3.3}$$

where $E_{data}(t)$ is the experimental value of the mean PL energy at the time moment t, $E_{MC}(t)$ is the corresponded MC value, m is number of data points, i is the crystal index (1, 2, 3, 4 stand for the 0.01%, 0.05%, 0.2%, and 0.7% doping levels, respectively), and C is the normalization coefficient ($\sim 1/eV^2$). Figure S3.16 shows that the MC simulations are stable with respect to simultaneous variations in the Förster radius and the hopping time, and therefore provide unique values for the both.
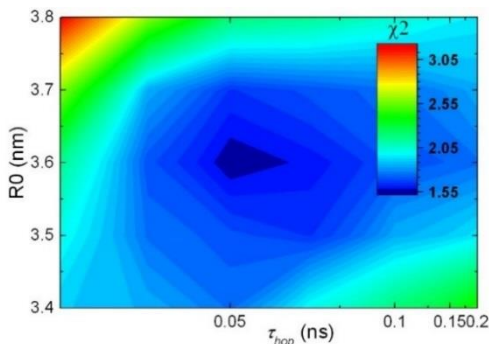
Figure S3.16. χ2 map of the least squared deviations between the MC calculations and experimental data for the self-doped crystals as a function of the Förster radius. R_0, (at the vertical axis) and hopping time, τ_{hop}, (at the horizontal axis) at 293 K. The global minimum value of χ2 and its width determine the values and uncertainties, respectively, of the global parameters as $R_0 = 3.6 \pm 0.2$ nm and $\tau_{hop} = 0.05 \pm 0.02$ ns.

3.5.10. Förster Radius Calculations

As the dopant extinction coefficient cannot be directly measured in the crystal phase, we calculated the Förster radius for the donor (host, TMS-P2TP-TMS) and acceptor (dopant, TMS-P4TP-TMS) molecules dissolved in a medium with the refractive index *n* = 2 according to the Förster formula:[20]

$$R_0{}^6 = \frac{9000 \cdot ln10 \cdot \gamma^2 \cdot QY_h}{128 \cdot \pi^6 \cdot n^4 \cdot N_A} \int_{\tilde{v}} \frac{\varepsilon_A(\tilde{v}) \cdot F_D(\tilde{v}) \cdot d(\tilde{v})}{\tilde{v}^4} \tag{3.4}$$

where $QY_h = 20\%$ is the donor PL QY in the absence of the acceptor (dopant); $\varepsilon_A(\tilde{v})$ is the extinction spectrum of dopant in solution red-shifted by ~0.04 eV to coincide with the low-energy edge of PL excitation spectrum of the strongly doped crystal, and $F_D(\tilde{v})$ is the PL spectrum of the donor (for which the PL spectrum of the lowest doped crystal was used from Ref. 27; $\gamma^2 = [\cos \beta_{DA} - 3 \cdot \cos \beta_A \cdot \cos \beta_D]^2$, where β_{DA} is the angle between the direction of the transition dipole moments of the donor and acceptor molecules, β_A and β_D are the angles between the vector connecting the centers of the acceptor and donor molecules and their transition dipole moments. The coefficient γ^2 was taken as 2/3 assuming the orientationally-scrambled transition dipole moments.

There are a number of approximations and uncertainties built into Equation 3.4. First, this equation is valid for a diluted solution but not for a crystal thereby neglecting dense packing of the donor. Second, the overlap integral in Equation 3.4 contains inaccuracies due to the unknown dopant absorption spectrum in crystal.

Third, the point dipole approximation is questionable for the dopant (TMS-P4TP-TMS) in the host crystal (TMS-P2TP-TMS) as both are rod-like conjugated molecules. Nevertheless, the calculated Förster radius of 4.0 nm is in reasonable agreement with the one obtained from the MC simulations (3.6 ± 0.2 nm).

3.5.11. Other Self-Doped Crystals
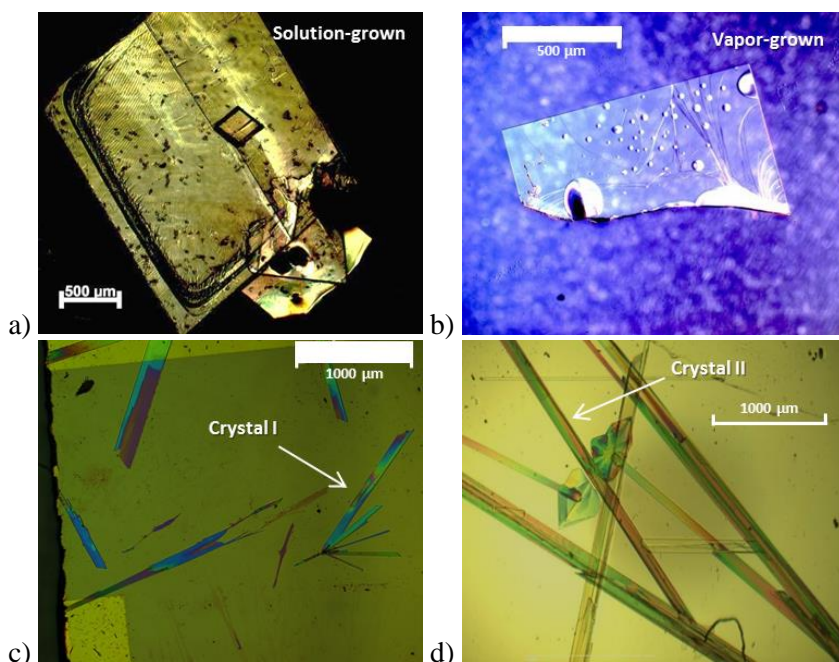
Figure S3.17. Microscope images of TMS-4P-TMS (a-b) and Hex-TTPTT-Hex (c, d) crystals. The crystals shown in panel b were grown from vapor, others were grown from solution. The Hex-TTPTT-Hex crystals were grown from different batches of the same synthetic protocols, and labeled by I and II.

To demonstrate that the proposed self-doped concept holds true for other luminescent organic semiconducting materials, we chose four different conjugated oligoarenes synthesized through widely used Pd-catalyzed cross-coupling reactions — Suzuki, Kumada, and Stille:[32, 40] 4,4‴-*bis*(trimethylsilyl)-1,1′:4′,1″:4″,1‴-quaterphenyl (TMS-4P-TMS), 1,4-*bis*{5-[4-(trimethylsilyl)phenyl]thiophen-2-yl}benzene, i.e. AC5-TMS (source material for the crystals in Chapter 5 of this Thesis),[41] 1,4-*bis*(5′-hexyl-2,2′-bithiene-5-yl)benzene (Hex-TTPTT-Hex)[42] and 1,4-*bis*(5-phenylfuran-2-yl)benzene, FP5.[30](source material for the crystals in Chapter 4 of this Thesis) These oligomers include 4 or 5 conjugated rings (phenylenes,

thiophenes, furans) and have various terminal substituents (TMS, hexyl, H). The corresponding synthetic routes and possible ways of formation of self-dopants with longer conjugated length during the cross-coupling reactions are presented in Ref. 27.

Crystal images. Crystals based on the materials with different self-doping levels were grown as shown in Ref. 27 The crystals of TMS-4P-TMS, TMS-PTPTP-TMS (detailed PL data are shown in Chapter 5 of this Thesis), and FP5 (detailed PL data are shown in Chapter 4 of this Thesis) images are shown in Figure S3.17.
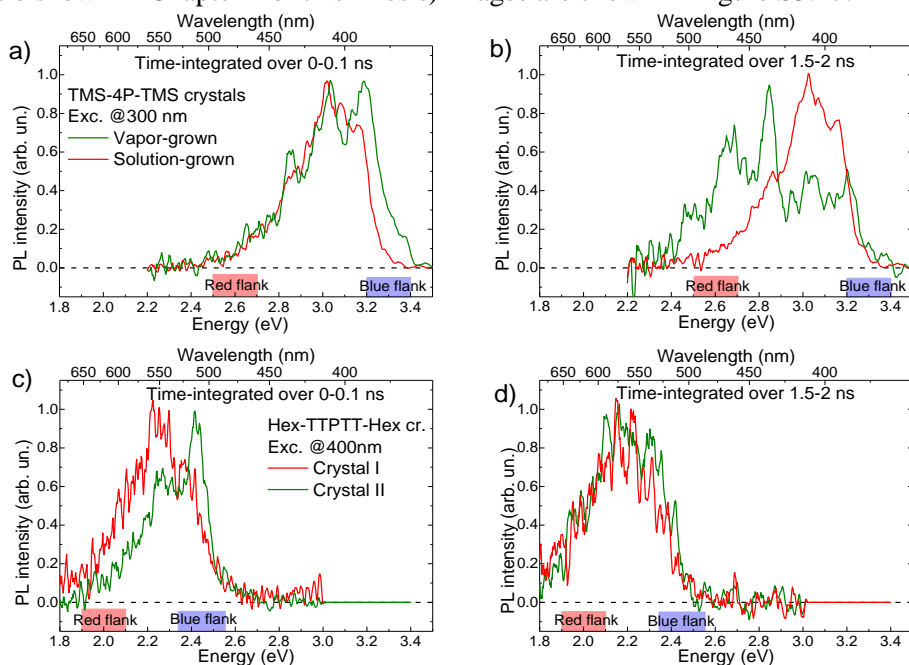
Figure S3.18. Time-resolved PL spectra of TMS-4P-TMS and Hex-TTPTT-Hex crystals integrated over 0–0.1 ns (left column) and 1.5–2 ns (right column) time windows. The experimental PL intensities are normalized to unity. The excitation wavelength for each crystal is shown in the panels.

Time-resolved PL data. Figure S3.18 compares PL spectra integrated over 0–0.1 ns (left column) and 1.5–2 ns (right column) time windows for pairs of crystals of each oligomer (TMS-4P-TMS and Hex-TTPTT-Hex), which were grown from vapor (green) and solution (red), except a pair of solution-grown Hex-TTPTT-HEX crystals (panels c, d). The spectra within each pair are different in the short or/and long-time windows, which is assigned to host-dopant energy transfer of different efficiency (see below).
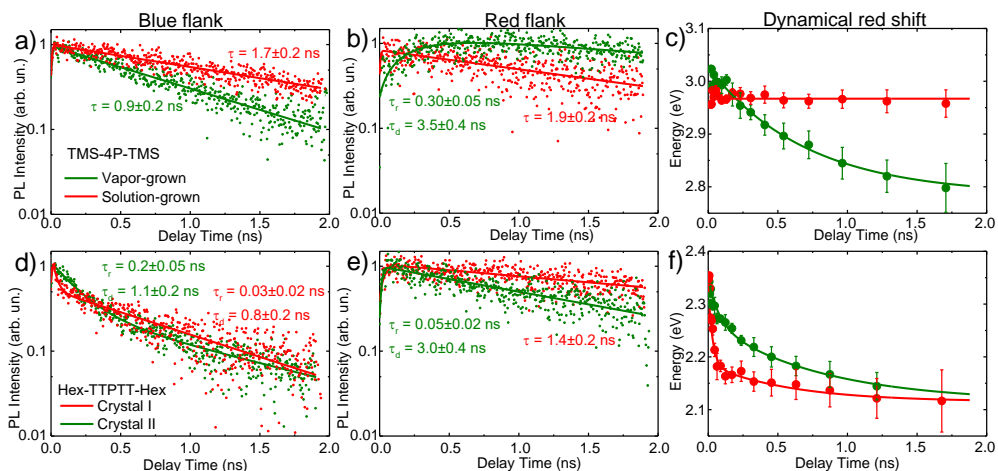
Figure S3.19. Spectrally-integrated PL transients (left and middle column) and dynamical red shifts of the mean PL energy (right column) of the vapor (olive) and solution grown (red) TMS-4P-TMS crystals and crystal I (red) and II (olive) of Hex-TTPTT-Hex. The PL transients in the left and middle columns were obtained by integrating PL over the blue and the red flanks of PL, respectively, as indicated in Figure S3.18. The solid lines are mono and bi-exponential fits convoluted with an apparatus response of 10 ps. The corresponding decay and rise times obtained from the fits are shown next to the transients. Scaling between the experimental PL intensities is preserved. The solid lines in the right column are monoexponential fits by the function $E = E_0 + \Delta E \cdot exp(-t/\tau)$, with the fit parameters given in Table S3.2. The excitation wavelength was set at 300 nm for the TMS-4P-TMS crystals and 400 nm for the Hex-TTPTT-Hex crystals.

Within each vapor/solution-grown crystal pairs, one crystal showed a faster PL decay at the blue spectral flank and a pronounced PL rise at the red flank. These PL features are characteristic for the host-dopant energy transfer as was described in detail for the TMS-P2TP-TMS crystals. For instance, Figure S3.19a,b compares the PL transients at the blue (a) and red flank (b) for the vapor and solution-grown TMS-4P-TMS crystals. The blue-flank PL decay time for the vapor-grown crystal is shorter than that of the solution-grown one (a). On the other hand, the red-flank PL of the vapor-grown crystal raises with a time constant close to that of the blue-flank decay (b). In contrast, the solution-grown crystal shows the same dynamics at the red and blue flanks. Finally, the TMS-4P-TMS vapor-grown crystal demonstrates the pronounced dynamical red shift of the mean PL energy (Figure S3.19c), while there is not such shift for the vapor-grown counterpart. Therefore, the vapor-grown TMS-4P-TMS crystal demonstrates efficient host-dopant energy transfer, whereas the solution-grown one does not. Thus, we conclude that the vapor-grown TMS-4P-

TMS crystals are self-doped, while the solution-grown ones are not, which we assign to extremely low solubility of the dopant (TMS-6P-TMS) in toluene.

Similar behavior of the time-resolved PL was also observed for the Hex-TTPTT-Hex crystals (Figure S3.19d-f), which is attributed to energy transfer from the host to the self-dopant (the self-dopants are described in Section 3.5.11a). The vapor-grown crystals demonstrate less pronounced dynamical red shift as compared to the solution-grown ones (Table S3.2). We assign this difference to less efficient host-dopant energy transfer, which results mainly from the lower self-doping level in the crystals.

Table S3.2. Fitting parameters for the function $E = E_0 + \Delta E \cdot exp(-t/\tau)$ of the dynamical red shift of the mean PL energy, where E_0 is the mean energy of the dopant PL and ΔE is the host-dopant energy gap estimated from the time-resolved PL spectra (Figure S3.18).

Crystals	E_0, eV	ΔE, eV	Solution-grown (crystal I) τ, ns	Vapor-grown (crystal II) τ, ns
TMS-4P-TMS	2.79 ± 0.04	0.2 ± 0.04	~0.7	>>10
Hex-TTPTT-Hex	2.12 ± 0.02	0.25 ± 0.02	~0.05	~0.4

Amongst all the crystals studied, the shortest time of the dynamical red shift in observed in the Hex-TTPTT-Hex crystal I (~50 ps, Table S3.2), which indicates the most efficient host-dopant energy transfer. The different behavior of the time-resolved PL in the Hex-TTPTT-Hex crystals (both solution-grown, Figure S3.19d-f) is explained by different self-doping levels of samples I and II, presumably due to uncontrollable factors during the synthesis. More detailed account on the PL properties of this and other self-doped crystals will be reported elsewhere.

3.6. References

1.   Jabbour, G. E., *et al.*, High T$_g$ Hole Transport Polymers for the Fabrication of Bright and Efficient Organic Light-Emitting Devices with an Air-Stable Cathode. *IEEE J. Quantum Electron.* **2000**, *36*, 12-17.

2.   Capelli, R.; Toffanin, S.; Generali, G.; Usta, H.; Facchetti, A.; Muccini, M., Organic Light-Emitting Transistors with an Efficiency That Outperforms the Equivalent Light-Emitting Diodes. *Nat. Mater.* **2010**, *9*, 496(8).

3.   Usta, H.; Sheets, W. C.; Denti, M.; Generali, G.; Capelli, R.; Lu, S.; Yu, X.; Muccini, M.; Facchetti, A., Perfluoroalkyl-Functionalized Thiazole–Thiophene Oligomers as N-Channel

Semiconductors in Organic Field-Effect and Light-Emitting Transistors. *Chem. Mater.* **2014**, *26*, 6542-6556.

4. Hotta, S.; Yamao, T.; Bisri, S. Z.; Takenobu, T.; Iwasa, Y., Organic Single-Crystal Light-Emitting Field-Effect Transistors. *J. Mater. Chem. C* **2014**, *2*, 965-980.

5. Schwartz, G.; Pfeiffer, M.; Reineke, S.; Walzer, K.; Leo, K., Harvesting Triplet Excitons from Fluorescent Blue Emitters in White Organic Light-Emitting Diodes. *Adv. Mater.* **2007**, *19*, 3672-3676.

6. Zheng, T.; Choy, W. C. H., High Efficiency Blue Organic Leds Achieved by an Integrated Fluorescence–Interlayer–Phosphorescence Emission Architecture. *Adv. Funct. Mater.* **2010**, *20*, 648-655.

7. Lei, Y.-L.; Jin, Y.; Zhou, D.-Y.; Gu, W.; Shi, X.-B.; Liao, L.-S.; Lee, S.-T., White-Light Emitting Microtubes of Mixed Organic Charge-Transfer Complexes. *Adv. Mater.* **2012**, *24*, 5345-5351.

8. McDonald, T. O.; Martin, P.; Patterson, J. P.; Smith, D.; Giardiello, M.; Marcello, M.; See, V.; O'Reilly, R. K.; Owen, A.; Rannard, S., Multicomponent Organic Nanoparticles for Fluorescence Studies in Biological Systems. *Adv. Funct. Mater.* **2012**, *22*, 2469-2478.

9. Bisri, S. Z.; Takenobu, T.; Yomogida, Y.; Shimotani, H.; Yamao, T.; Hotta, S.; Iwasa, Y., High Mobility and Luminescent Efficiency in Organic Single-Crystal Light-Emitting Transistors. *Adv. Funct. Mater.* **2009**, *19*, 1728-1735.

10. Yamao, T.; Sakurai, Y.; Terasaki, K.; Shimizu, Y.; Jinnai, H.; Hotta, S., Current-Injected Spectrally-Narrowed Emissions from an Organic Transistor. *Adv. Mater.* **2010**, *22*, 3708-3712.

11. Bisri, S. Z.; Takenobu, T.; Sawabe, K.; Tsuda, S.; Yomogida, Y.; Yamao, T.; Hotta, S.; Adachi, C.; Iwasa, Y., P-I-N Homojunction in Organic Light-Emitting Transistors. *Adv. Mater.* **2011**, *23*, 2753-2758.

12. Bisri, S. Z.; Sawabe, K.; Imakawa, M.; Maruyama, K.; Yamao, T.; Hotta, S.; Iwasa, Y.; Takenobu, T., Organic Single-Crystal Light-Emitting Transistor Coupling with Optical Feedback Resonators. *Sci. Rep.* **2012**, *2*, 985(8).

13. Fang, H.-H.; Ding, R.; Lu, S.-Y.; Yang, J.; Zhang, X.-L.; Yang, R.; Feng, J.; Chen, Q.-D.; Song, J.-F.; Sun, H.-B., Distributed Feedback Lasers Based on Thiophene/Phenylene Co-Oligomer Single Crystals. *Adv. Funct. Mater.* **2012**, *22*, 33-38.

14. Shang, H., *et al.*, Comparative Study of Single and Dual Gain-Narrowed Emission in Thiophene/Furan/Phenylene Co-Oligomer Single Crystals. *J. Phys. Chem. C* **2017**.

15. Gierschner, J.; Park, S. Y., Luminescent Distyrylbenzenes: Tailoring Molecular Structure and Crystalline Morphology. *J. Mater. Chem. C* **2013**, *1*, 5818-5832.

16. Park, S. K., *et al.*, Highly Luminescent 2d-Type Slab Crystals Based on a Molecular Charge-Transfer Complex as Promising Organic Light-Emitting Transistor Materials. *Adv. Mater.* **2017**, *29*, 1701346.

17. Wang, H., *et al.*, Doped Organic Crystals with High Efficiency, Color-Tunable Emission toward Laser Application. *Cryst. Growth Des.* **2009**, *9*, 4945-4950.

18. Nakanotani, H.; Adachi, C., Amplified Spontaneous Emission and Electroluminescence from Thiophene/Phenylene Co-Oligomer-Doped p-bis(p-Styrylstyryl)Benzene Crystals. *Adv. Opt. Mater.* **2013**, *1*, 422-427.

19. Ding, R., *et al.*, Highly Efficient Three Primary Color Organic Single-Crystal Light-Emitting Devices with Balanced Carrier Injection and Transport. *Adv. Funct. Mater.* **2017**, 1604659(9).

20. Lakowicz, J. R., Energy Transfer. In *Principles of Fluorescence Spectroscopy*, Lakowicz, J. R., Ed. Springer US: Boston, MA, 2006; pp 443-475.

21. Fang, H.-H.; Lu, S.-Y.; Wang, L.; Ding, R.; Wang, H.-Y.; Feng, J.; Chen, Q.-D.; Sun, H.-B., Preparation and Time-Resolved Fluorescence Study of Rgb Organic Crystals. *Org. Electron.* **2013**, *14*, 389-395.

22. Lu, H. H.; Liu, C. Y.; Chang, C. H.; Chen, S. A., Self-Dopant Formation in Poly(9,9-Di-N-Octylfluorene) Via a Dipping Method for Efficient and Stable Pure-Blue Electroluminescence. *Adv. Mater.* **2007**, *19*, 2574-2579.

23. Russ, B., *et al.*, Power Factor Enhancement in Solution-Processed Organic N-Type Thermoelectrics through Molecular Design. *Adv. Mater.* **2014**, *26*, 3473-3477.

24. Postnikov, V. A., *et al.*, Molecularly Smooth Single-Crystalline Films of Thiophene–Phenylene Co-Oligomers Grown at the Gas–Liquid Interface. *Cryst. Growth Des.* **2014**, *14*, 1726-1737.

25. Kudryashova, L. G.; Kazantsev, M. S.; Postnikov, V. A.; Bruevich, V. V.; Luponosov, Y. N.; Surin, N. M.; Borshchev, O. V.; Ponomarenko, S. A.; Pshenichnikov, M. S.; Paraschuk, D. Y., Highly Luminescent Solution-Grown Thiophene-Phenylene Co-Oligomer Single Crystals. *ACS Appl. Mater. Interfaces* **2016**, *8*, 10088-10092.

26. Inada, Y.; Yamao, T.; Inada, M.; Itami, T.; Hotta, S., Giant Organic Single-Crystals of a Thiophene/Phenylene Co-Oligomer toward Device Applications. *Synth. Met.* **2011**, *161*, 1869-1877.

27. Parashchuk, O. D.; Mannanov, A. A.; Konstantinov, V. G.; Dominskiy, D. I.; Surin, N. M.; Borshchev, O. V.; Ponomarenko, S. A.; Pshenichnikov, M. S.; Paraschuk, D. Y., Molecular Self-Doping Controls Luminescence of Pure Organic Single Crystals. *Adv. Funct. Mater.* **2018**, *28*, 1800116.

28. Parker, C. A., *Photoluminescence of Solutions*; Elsevier, Amsterdam-London-New York, 1968.

29. Ahn, T.-S.; Al-Kaysi, R. O.; Müller, A. M.; Wentz, K. M.; Bardeen, C. J., Self-Absorption Correction for Solid-State Photoluminescence Quantum Yields Obtained from Integrating Sphere Measurements. *Rev. Sci. Instrum.* **2007**, *78*, 086105.

30. Kazantsev, M. S., *et al.*, Highly-Emissive Solution-Grown Furan/Phenylene Co-Oligomer Single Crystals. *RSC Adv.* **2016**, *6*, 92325-92329.

31. Köhler, A.; Bässler, H., The Electronic Structure of Organic Semiconductors. In *Electronic Processes in Organic Semiconductors*, Wiley-VCH Verlag GmbH & Co. KGaA: 2015; pp 1-86.

32. Ananikov, V. P., *et al.*, Development of New Methods in Modern Selective Organic Synthesis: Preparation of Functionalized Molecules with Atomic Precision. *Russ. Chem. Rev.* **2014**, *83*, 885.

33. Aakeroy, C. B.; Salmon, D. J., Building Co-Crystals with Molecular Sense and Supramolecular Sensibility. *CrystEngComm* **2005**, *7*, 439-448.

34. Egelhaaf, H. J.; Gierschner, J.; Oelkrug, D., Polarizability Effects and Energy Transfer in Quinquethiophene Doped Bithiophene and OPV Films. *Synth. Met.* **2002**, *127*, 221-227.

35. Serbenta, A.; Kozlov, O. V.; Portale, G.; van Loosdrecht, P. H. M.; Pshenichnikov, M. S., Bulk Heterojunction Morphology of Polymer:Fullerene Blends Revealed by Ultrafast Spectroscopy. **2016**, *6*, 36236.

36. Kozlov, O.; de Haan, F.; Kerner, R.; Rand, B.; Cheyns, D.; S. Pshenichnikov, M., *Real-Time Tracking of Singlet Exciton Diffusion in Organic Semiconductors*, 2016; Vol. 116.

37. Hanwell, M. D.; Curtis, D. E.; Lonie, D. C.; Vandermeersch, T.; Zurek, E.; Hutchison, G. R., Avogadro: An Advanced Semantic Chemical Editor, Visualization, and Analysis Platform. *J. Cheminf.* **2012**, *4*, 17.

38. Akselrod, G. M.; Prins, F.; Poulikakos, L. V.; Lee, E. M. Y.; Weidman, M. C.; Mork, A. J.; Willard, A. P.; Bulović, V.; Tisdale, W. A., Subdiffusive Exciton Transport in Quantum Dot Solids. *Nano Lett.* **2014**, *14*, 3556-3562.

39. Mikhnenko, O. V.; Blom, P. W. M.; Nguyen, T.-Q., Exciton Diffusion in Organic Semiconductors. *Energy Environ. Sci.* **2015**, *8*, 1867-1888.

40. Cordovilla, C.; Bartolomé, C.; Martínez-Ilarduya, J. M.; Espinet, P., The Stille Reaction, 38 Years Later. *ACS Catalysis* **2015**, *5*, 3040-3053.

41. Starikova, T. Y.; Surin, N. M.; Borshchev, O. V.; Pisarev, S. A.; Svidchenko, E. A.; Fedorov, Y. V.; Ponomarenko, S. A., A Novel Highly Efficient Nanostructured Organosilicon Luminophore with Unusually Fast Photoluminescence. *J. Mater. Chem. C* **2016**, *4*, 4699-4708.

42. Kazantsev, M. S.; Beloborodova, A. A.; Frantseva, E. S.; Rybalova, T. V.; Konstantinov, V. G.; Shundrina, I. K.; Paraschuk, D. Y.; Mostovich, E. A., Methyl Substituent Effect on Structure, Luminescence and Semiconducting Properties of Furan/Phenylene Co-Oligomer Single Crystals. *CrystEngComm* **2017**, *19*, 1809-1815.

Chapter 4. Long-Range Exciton Transport in Brightly Fluorescent Furan/Phenylene Co-oligomer Crystals
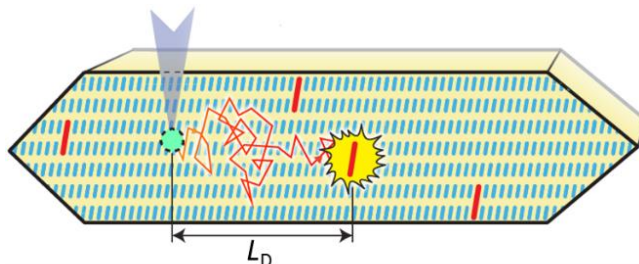
Design of bright-emitting crystalline organic semiconductors for optoelectronic applications requires thorough understanding of the singlet exciton transport process. In this work we show that singlet exciton diffusion length in a promising semiconductor crystal based on furan/phenylene co-oligomers, amounts to 24 nm. To do so, we employed the photoluminescence quenching technique with a specially synthesized quencher, a longer furan/phenylene co-oligomer, which was smoothly implanted into the host crystal lattice. Extensive Monte-Carlo simulations, exciton-exciton annihilation experiments and numerical modelling fully supported our findings. We further demonstrated high potential of the furan/phenylene co-oligomer crystals for light-emitting applications by fabricating solution-processed organic light emitting transistors.

4.1. Introduction

Organic highly-luminescent semiconductor materials stand as the basis for modern organic electroluminescent devices such as light-emitting diodes and, in a longer term, light-emitting transistors and injection lasers.[1-7] The most attractive organic optoelectronic materials combine high luminescence with efficient charge transport.[8-12] Along with the charge transport, exciton diffusion is an important fundamental process controlling the performance of organic light-emitting and photovoltaic devices. For instance, in bulk heterojunction photovoltaic devices, photogenerated excitons diffuse to a heterojunction interface in order to dissociate into a free charge carriers, electrons and holes.[13-15]

An efficient approach to control and enhance luminescence in modern organic light-emitting devices — material doping by highly fluorescent molecules[16-18] — relies on exciton diffusion to provide energy transport from the host crystal to the dopant molecule. Higher dopant concentrations generally lead to enhancement of host-dopant energy transfer,[19-21] while low doping levels are required for retaining high charge carriers mobility.[21-24] Long-range exciton diffusion in minimally doped organic semiconductors materials paves the way to resolving these mutually exclusive requirements to achieve widely tunable fluorescent properties.[17]

Heteroaryl-containing co-oligomers[8-9, 25] have demonstrated high potential for organic optoelectronics due to unique combination of efficient charge transport and high fluorescence efficiency. Particularly, a furan/phenylene co-oligomer 1,4-bis(5-phenylfuran-2-yl)benzene (hereafter FP5) was recently demonstrated to possess higher solubility, charge carrier mobility and fluorescence efficiency as compared to its thiophene analogue.[26] Furthermore, organic light-emitted transistors (OLETs) based on single crystals vapor-grown from a furan-incorporated thiophene/phenylene oligomers have recently been demonstrated.[9] All these put the exciton transport in FP5 single crystals in the research spotlight as a decisive player between the photons absorbed by the host crystal and emitted by the implanted dopants.

In this work, we study exciton diffusion length in furan/phenylene co-oligomer FP5 single crystals by time-resolved photoluminescence (PL) volume quenching technique. For the quencher, we synthesized a new highly fluorescent molecule 5,5'-bis(4-(5-phenylfuran-2-yl)phenyl)-2,2'-bifuran (FP8), which smoothly embeds into the host crystal lattice and provides efficient host-quencher Förster energy transfer. Experimental PL transients and the spectral red shift at different quencher

concentrations were successfully modelled by Monte Carlo (MC) simulations from which the exciton diffusion length of 24±4 nm was obtained. This value agrees well with the results of exciton-exciton annihilation experiments. A high potential of doped FP5 crystals for optoelectronics is demonstrated by their efficient charge transport and functionality in solution-processed OLETs.

4.2. Materials and Methods

FP5 synthesis and purification, steady-state optical spectroscopy, crystal growth and OLET devices are represented in corresponded Ref. (A.A. Mannanov, et al., *J. Mater. Chem. C.*, **2019**; *DOI: 10.1039/C8TC04151B*).

Time-resolved photoluminescence. Time-resolved PL was recorded by a streak camera (C5680, Hamamatsu) combined with a polychromator. The excitation pulses were generated by the doubled output of a Ti:sapphire laser (Coherent Mira); their central wavelength was set at 375 nm. Time-resolved PL spectra of the crystals at the room temperature were collected in an inverted microscope (Zeiss Axiovert 100) with a 10x, NA=0.25 objective. The laser beam was defocused to a diameter of ∼15 μm at the crystal surface to avoid possible photon bleaching and exciton annihilation in the samples (for details, see Section 4.5.12). In all cases, the apparatus response was ~20 ps (Gaussian sd width).

Monte-Carlo simulations. Monte-Carlo (MC) simulations were performed as a random walk of excitons in a 3D cubic crystal grid with a subsequent Förster resonant energy transfer (FRET) to the quenchers; the details are reported in Ref. 21 The exciton-exciton annihilation was modelled as follows: if the distance between two excitons becomes shorter than the exciton annihilation radius, one of them immediately disappears (annihilates).

4.3. Results and Discussion

4.3.1. Choice of Quenching Technique and Quencher Molecule

PL quenching-based techniques are among the most common spectroscopic methods for obtaining exciton diffusion length.[15, 27-28] Here molecular quenchers are added to the initial material at different concentrations; the resulted dependence of either time-resolved PL or PL QY (or both) on the average inter-quencher distance allows retrieval of the diffusion length. For the volume PL quenching, a prospective

quencher should: (i) be readily embedded into the host crystal with minimal distortions of its structure, and (ii) provide efficient quenching of the host excitons via e.g. FRET. Efficient PL from the quencher is a convenient extra as it allows matching the accelerating decay of host PL with the delayed quencher PL.[20-21] Earlier we speculated[21] that such a prosperous quencher, FP8 (Figure 4.1a), would be a self-dopant of FP5, i.e. a by-product emerging in minute amount at the last step of the FP5 synthesis (see Ref. 21). FP8 — a longer than FP5 linear π-conjugated molecule — should have a red-shifted absorption spectrum, which is beneficial for efficient FRET from FP5 to FP8. Moreover, as FP8 and FP5 have similar molecular structures with alternating furan and phenylene rings, FP8 might co-crystallize with FP5 resulting in homogeneously doped FP5 crystals so that the quencher is dispersed in the host crystal at the molecular level. For these reasons, we decided to focus our attention at FP8 as a promising quencher of FP5 PL.

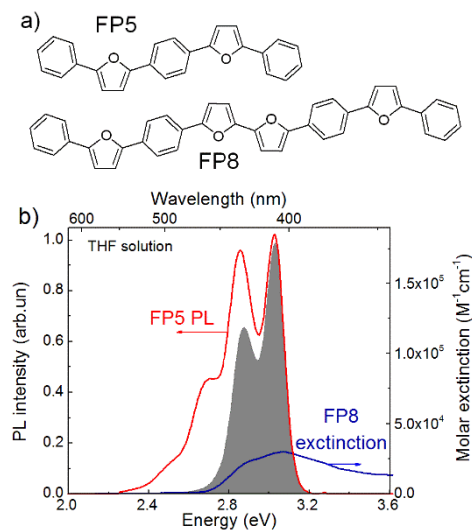### 4.3.2. Optical Properties of Host and Quencher Molecules

Figure 4.1. a) Molecular structure of FP5 and FP8. b) FP5 (host) PL spectrum (red) and FP8 (quencher) extinction spectrum (blue) in THF solutions. The gray area represents the product of the PL spectrum of the host (FP5) and absorption spectrum of the quencher (FP8) required for FRET estimations (Section 4.5.1).

FP8 was synthesized in a separate experiment by a combination of oxidative homocoupling reaction followed by the borylation and Suzuki cross-coupling reactions (the synthesis has been performed by Evgeny A. Mostovich).

To reveal the potential of FP8 as a suitable quencher, we recorded optical absorption of FP8 and PL spectra of FP5 in diluted solutions (Figure 4.1b). Substantial spectral overlap of the two spectra provides a good indication that FRET might potentially occur between the host excitons in FP5 crystal and FP8 quenchers. From the spectral overlap of FP5 and FP8 in diluted solution, the Förster radius in crystal was estimated as 4.9±0.5 nm (Section 4.5.1).

4.3.3. Doping of the Host Single Crystals

Raw FP5 material was self-doped with FP8 at concentration of ~0.2% as measured by PL spectroscopy, which has been done by Anatoly D. Kuimov. To obtain this value, the raw FP5 powder was dissolved in CH_2Cl_2 (10^{-3} M), and the PL spectrum of the solution was recorded under excitation at 460 nm; the concentration of FP8 was then straightforwardly obtained from its molar extinction, UV and PL spectra measured in CH_2Cl_2 (10^{-6} M). The residual FP8 concentration in the purified FP5 powder (Section 4.5.3) was estimated as lower than 0.002% (i.e. 20 ppm). This value was obtained from the minimum intensity of the FP8 PL that could still be clearly distinguished at the background FP5 PL.

We used the purified FP5 powder to grow doped FP5 single crystals by adding FP8 with the prescribed molar ratio; the microscope images of the FP5 crystals are shown in Section 4.5.2. As the lowest controlled quencher concentration was dictated by the presence of minute (<0.002%) self-dopant content (presumably FP8), the lowest concentration of intentional doping with FP8 was set as 0.01%.

Time-resolved PL spectroscopy combined with MC simulations (Section 4.5.3) revealed that the purified crystals are self-doped with concentration of ~0.002% (assuming only FP8 as the self-dopant), in accord with the PL data.

For accurate determination of the exciton diffusion length in FP5 single crystal we needed a reference crystal that is even purer than the purified crystals. This was achieved by growing FP5 single crystals from the purified FP5 powder by the PVT method (referred below as PVT crystal). An estimate based on time-resolved PL data and MC simulations yielded the self-doping level of <10 ppm (Section 4.5.3).

To demonstrate smooth embedding of FP8 molecules into the FP5 host matrix, x-ray measurements were performed on the single crystals solution-grown from the

purified and 0.1% doped FP5. Their crystal lattice parameters appeared to be identical; they also corroborate the previously published data on FP5 crystal structure.[26] Moreover, molecular dynamics simulations (Section 4.5.4) demonstrated that two head-to-tail host molecules in the FP5 crystal structure can be substituted by one FP8 molecule. This substitution results mainly in small torsional/bending deformations and adjustments of FP8, whereas the adjacent host conjugated cores maintain their original positions. The time- and polarization-resolved PL data (Section 4.5.5) are fully consistent with these conclusions. All these data support our idea that the FP8 molecules are molecularly dispersed in the FP5 crystal matrix without noticeable distortion of the FP5 crystal structure.
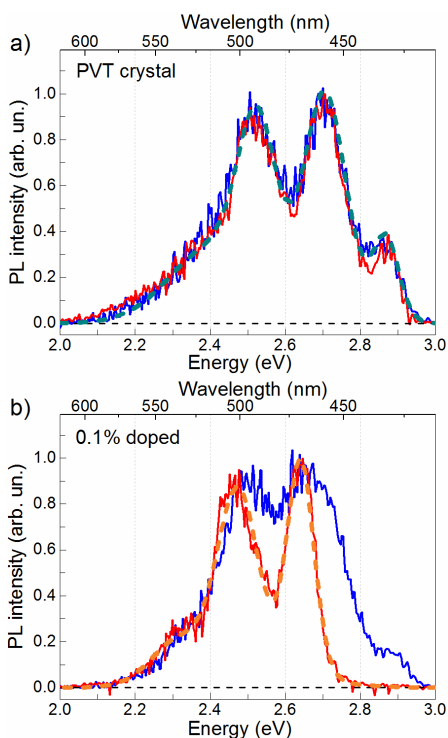
Figure 4.2. PL spectra of the PVT (a) and 0.1% doped (b) FP5 crystals obtained from time-integrating PL data over the 0–0.05 ns (blue line) and 2–10 ns (red line) time windows. Cyan and orange dashed lines in panels (a) and (b) represent a four- and three-Gaussians fit, respectively, to the experimental spectra.

Figure 4.2 shows time-resolved PL spectra of the PVT and 0.1%-doped FP5 crystals at short and long times. The PVT-crystal spectrum almost does not change with time (Figure 4.2a). In contrast, PL of the 0.1%-doped crystals experiences a

considerable spectral shift (Figure 4.2b), from a spectrum similar to the one of the PVT crystal at short times, to an entirely different spectrum at long times. Our working hypothesis is that the excitation energy is transferred from the host lattice to the quenchers via FRET. Therefore, we assign the short-time PVT PL spectrum to the host and the long-time 0.1%-doped crystal PL spectrum to the quencher.

4.3.4. Host PL Quenching

Figure 4.2 shows that the host and quenchers spectra strongly overlap (especially at the red flank), which indicates that the PL transients bear both host and quencher contributions. To factorize their shares, we performed decomposition of the PL maps for each doped crystal into a linear combination of the PVT and quencher spectra at each delay time (Section 4.5.8). The reconstructed maps (Figure S4.7) fully reproduce the experimental ones which corroborates our hypothesis of the host-dopant energy transfer.
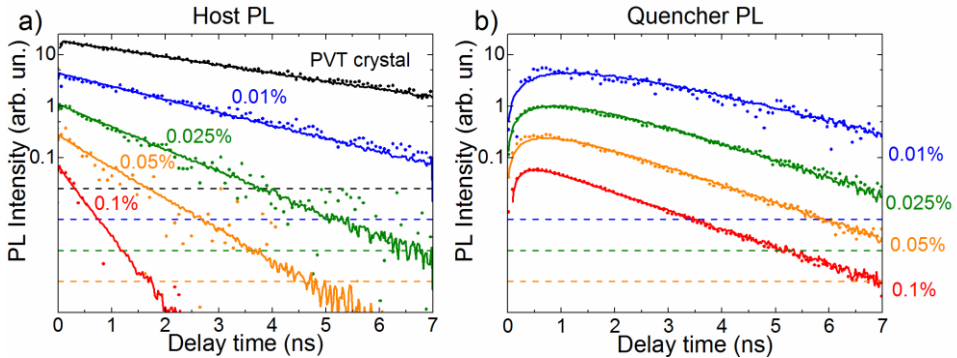
Figure 4.3. Experimental (dots) and MC simulated (lines) PL transients for the variously doped FP5 crystals. The experimental PL transients were extracted from decomposition of the PL maps into the host (a) and quencher (b) PL reference spectra (cyan and orange dashed lines in Figure 4.2a, b, respectively). Each PL transient is re-scaled by a factor of 4 with respect to the previous one. Dashed lines indicate the $5 \cdot 10^{-3}$ level with respect to the corresponding maximum of the PL transient. Quencher concentrations are shown next the respected transients.

Figure 4.3 shows the shares of the host (a) and quencher (b) PL obtained from the PL maps decomposition, as functions of time delay for variously doped FP5 single crystals. Decay of the host PL accelerates from ~2.9 to ~0.25 ns with the doping increase (Figure 4.4); respectively, the quencher PL acquires a raising

component, whose rise time shortens from 0.45 to 0.25 ns. Shortening of the decay times of the blue-flank transients and the corresponding rise in the red-flank transients with doping are fully consistent with the donor-acceptor energy transfer from the host to quenchers in the crystals. Furthermore, the crystals doped higher than 0.01% demonstrate similar red-flank PL decay times of 1.4±0.2 ns, which are considerably shorter than that of the PVT crystal (2.9±0.2 ns), and, therefore, are attributed to the PL lifetime of the quencher. This is also in line with the transient red-shifts of PL mean energy, i.e. energy transfer dynamics from the host to the quenchers (Section 4.5.3).
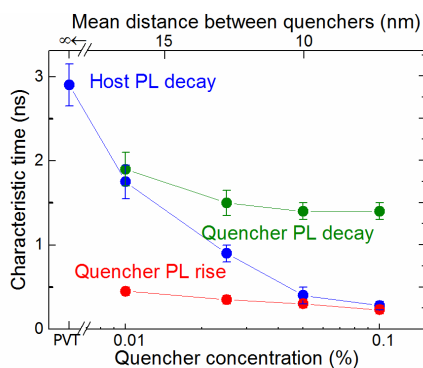
Figure 4.4. Characteristic PL times for variously doped FP5 crystals. The decay times (the fastest times in the case of the biexponential behavior, i.e. for the blue flank PL transient of the 0.1% crystal) of exponential fits from Figure 4.3a are depicted as the blue dots, while the decay and rise times of bi-exponential fits from Figure 4.3b are shown as the green and red dots, respectively. The vertical bars indicate the uncertainty margins of the exponential fits. The upper axis shows the mean distance between quenchers in the host crystal (for details see Section 4.5.7).

The characteristic times obtained from mono- or bi-exponential fits of the experimental transients are summarized in Figure 4.4. The blue-flank decay time (blue dots) shortens with the increase of quencher concentration, which is consistent with the cross-over regime from unquenched (lifetime of 2.9±0.2 ns) to strongly quenched host PL. At high doping levels, the blue-flank decay time (blue dots) approaches to the red-flank rise times (red dots) because PL quenching begins to fully determine the host excitation lifetime. The red-flank decay (green dots) levels off with the doping increase, which reflects dominance of the quencher PL.

4.3.5. Exciton Diffusion Length

The host and quencher PL transients obtained from Monte Carlo (MC) simulations are shown in Figure 4.3 as solid lines; the simulated and experimental PL transients are in excellent agreement (for MC parameters, see Section 4.5.9). The exciton diffusion length amounts to $L_D = 24\pm4$ nm as directly calculated from the distributions of exciton diffusion lengths (Section 4.5.10); this value corresponds to the exciton diffusion coefficient of $D = L_D^2 / \tau = 2.5\cdot10^{-3}$ cm²/s (where $\tau = 2.9$ ns is the exciton lifetime). Note that a commonly-used relation $L_D = l_0\sqrt{\tau/\tau_{\mathrm{hop}}}$[15, 27-28] (where $l_0 = 0.77$ nm is the unit cell size in the model, $\tau_{\mathrm{hop}} = 1.5$ ps is the exciton hopping time) yields the exciton diffusion length of ~40 nm, i.e. it overestimates the diffusion length by a factor 1.5.[29] Diffusion lengths for the doped crystals calculated from the host exciton lifetime (Figure 4.4) are also systematically overestimated (Section 4.5.10). To mitigate this problem, the exciton lifetimes should be taken at the ~0.62 level rather than at the conventional e^{-1}=0.37 level.

Singlet exciton diffusion amongst molecules or polymer conjugated segments is controlled by either dipole–dipole or Dexter energy transfers.[27-28] Typically, L_D is longer for systems with well-ordered, tight molecular packing with low energetic disorder.[30-31] For single crystals, a large spread of L_D ranging from 2.5 to 60 nm for singlet excitons were reported,[19, 31-33] with the maximum for anthracene.[34] (for the list of the singlet exciton diffusion lengths in organic crystals see Section 4.5.11). Note that ultrafast singlet-to-triplet conversion in anthracene[19, 35-36] challenges the latter value as attributed solely to singlet exciton diffusion. Therefore, the exciton diffusion length in the FP5 crystal lies at the longest side of the distribution of exciton diffusion lengths for organic semiconductor single crystals, and successfully competes with that in such well-studied single crystals as naphthalene, anthracene, and tetracene. One particular argument for explaining the long exciton diffusion length in a FP5 crystal is its intrinsically high torsional rigidity, which results is much lower reorganization energy for exciton transfer as compared to its thiophene analogue.[37-38]

4.3.6. Exciton-Exciton Annihilation

A complimentary method to study exciton diffusion is exciton-exciton annihilation.[14, 39-40] This technique is based on creating such high exciton density so that the probability of two diffusing excitons to meet after some time is not negligible.

If such an event occurs, a double-excited electronic state is formed that quickly relaxes back to the single-exciton state. As a result, one exciton is lost for PL (typically, via non-radiative channel), and therefore PL decay accelerates. The exciton annihilation approach does not require any PL quenchers; however, it necessitates the exact knowledge of the exciton density (i.e. the light power, excitation profile, and material absorption), which becomes the main source of (systematic) uncertainty in such experiments.

Experimental PL transients in FP5 crystals for the excitation flux varied in the range of $0.5 - 50$ µJ/cm^2 (for the excitation flux estimation see Section 4.5.12) are shown in Figure 4.5a. With the increase of excitation flux, the transient decay times increase, which is ascribed to exciton-exciton annihilation. The share of annihilated excitons is shown in Figure 4.5b as a function of initial mean exciton-exciton distance. The share is calculated as a maximal PL yield (i.e. the time integral over the transient) without annihilation (i.e. at 0.5 µJ/cm^2 flux) minus the PL yield at a given intensity, with the difference normalized to the maximal PL yield. At the strongest excitation flux, the share of annihilated excitons becomes as high as ~20%.
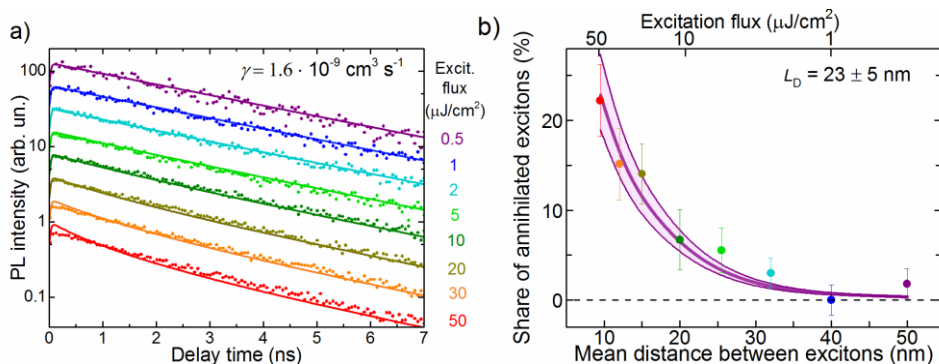
Figure 4.5. Experimental PL transients (a) and the share of annihilated excitons (b) under various excitation fluxes in the PVT crystal. The lines in panel (a) resulted from a global fit to Equation 4.1. The details of calculation of the exciton density and the mean distance between the excitons are given in Section 4.5.13. The thin lines in panel (b) show the results of the Monte-Carlo simulations. The shaded area in (b) shows the L_D uncertainty region.

It is not straightforward to calculate the exciton diffusion length directly from Figure 4.5b as exciton-exciton annihilation, being a bimolecular process, depends nonlinearly on the exciton population. Therefore, the experimental PL transients at different excitation intensities in Figure 4.5a were globally fitted to the solution of the kinetic rate equation:[19, 41]

$$n(t) = e^{-t/\tau}/(1 + n_0 \cdot \gamma \cdot \tau(1 - e^{-t/\tau})), \tag{4.1}$$

where $n(t)$ is the time-dependent exciton concentration, n_0 is the initial exciton concentration (Section 4.5.13), $\gamma = 4\pi \cdot R_a \cdot L_D{}^2/\tau$ is the singlet annihilation rate, and R_a is the annihilation radius. The annihilation rate was found to be, which is a factor of three lower than the singlet annihilation rate in tetracene crystals ($5 \cdot 10^{-9}$ $cm^3 s^{-1}$)[42], and a factor of six lower than in anthracene crystals (10^{-8} cm^3 s^{-1})[43]. For the value of the annihilation radius we followed Ref. 42 where the singlet annihilation radius was taken as an average exciton hopping distance, i.e. $R_a = 0.77$ nm for the FP5 single crystal. Thus, the exciton diffusion length is calculated as 23 ± 5 nm, which matches very well the value derived from the volume PL quenching technique.

Alternatively, the diffusion length can be readily obtained from MC simulations in which the exciton-exciton annihilation was incorporated (see Section 4.5.14). From the diffusion lengths distribution (Figure S4.13), the average diffusion length was obtained as $L_D = 23 \pm 5$ nm, which is fully consistent with the value obtained from the analytical approach.

4.4. Conclusions

In conclusion, we have measured singlet exciton diffusion length in 1,4-bis(5-phenylfuran-2-yl)benzene (FP5) single crystals and demonstrated their light-emitting applications. We identified a suitable quencher molecule, furan-phenylene 5,5'-bis(4-(5-phenylfuran-2-yl)phenyl)-2,2'-bifuran (FP8), synthesized it separately and demonstrated its smooth embedding into the FP5 structure. High-quality FP5 single crystals doped by FP8 up to 0.1% were grown. Using ultrafast PL spectroscopy combined with Monte Carlo simulations, we obtained the singlet exciton diffusion length in FP5 single crystal as long as 24±4 nm, which is among the top values for organic semiconductor crystals. This result was independently verified in the exciton-exciton annihilation experiments. Remarkably, long exciton diffusion length allowed us to harvest the majority excitons on dopants at 10's of ppm doping levels and thereby to minimize the determinant effect of the dopants on charge transport. Finally, we fabricated solution-processed organic light-emitting transistors based on FP5 crystals molecularly doped by FP8. All these findings clearly demonstrate high potential of molecular crystals based on furan-containing oligomers for organic photonics and optoelectronics.

Author Contributions

MSK, DYuP and MSP conceived, developed and supervised the project. AAM performed the time- and polarization-resolved PL measurements, exciton annihilation experiments, Monte-Carlo and molecular dynamics simulations. MSK, ADK grew the crystals from solution, fabricated, and measured the OFETs. ADK performed the purification of materials by PVT and measurements of their optical properties and doping with the use of optical spectroscopy in solutions. VGK obtained the PL spectra and QYs in the crystals. DID grew the PVT crystals. VAT and DSA assembled and studied the OLET devices. NVG and VVB performed photothermal absorption spectroscopy. IPK performed quantum chemical calculations. AAS and TVR performed the x-ray diffraction experiments. IKS performed thermal analysis. EAM synthesized and characterized the materials.

4.5. Supporting Information

4.5.1. Förster Radius Calculations

The FP8 (quencher) extinction coefficient could not have been accurately measured in the doped FP5 crystals due to their high background absorption (this has been relatively shown by Nikita V. Gultikov with photothermal deflection spectroscopy; the absolute optical extinction spectrum of the FP5 crystal is shown in Figure S9 of Ref. 44). Therefore, the Förster radius for the donor (FP5, host) and acceptor (FP8, quencher) was estimated for two isolated molecules, i.e. their optical spectra and PL QY were taken from diluted solutions.

The donor PL spectrum, $F_D(\tilde{v})$, and the acceptor extinction spectrum, $\varepsilon_A(\tilde{v})$, measured in THF solutions are shown in Figure 4.1b. The former was normalized in such a way that the integral of PL spectrum equals to unity considering wavelengths in centimeters to enable its usage for Förster radius formula[45] (as it was demonstrated above in Section 3.5.10), where $QY_h = 91\%$ is PL QY of the donor molecule diluted in acetonitrile solvent[26]; N_A is Avogadro's constant; $\gamma^2 \approx 1.5$ is the orientational factor (see Section 4.5.10); n is the refractive index of a medium was taken as 2. The resulted Förster radius amounts to 4.9±0.5 nm.

4.5.2. Microscope Images of FP5 Crystals
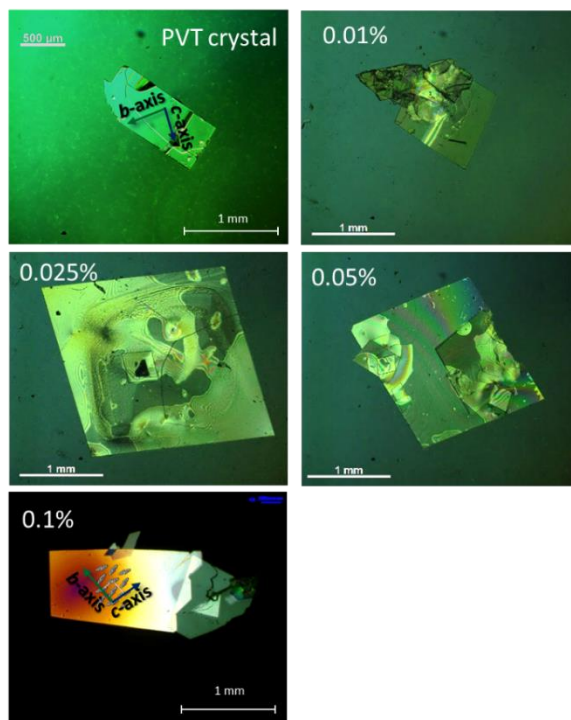
Figure S4.1. Microscopy images of the vapor-grown (PVT) and variously doped solution-grown FP5 crystals. The prescribed doping levels for solution-grown crystal are indicated in the images. The crystallographic axes (*b-,c-*) orientations with respect to the crystal orientation are shown as green and blue arrows for the PVT and 0.1% doped crystals, respectively, according to the XRD data.[26]

4.5.3. Transient Red-Shift of Mean PL Energy

A convenient way to characterize energy transport (as compared to spectrally-resolved transients, Figure 4.3) is to analyze the transient red shift of the mean PL energy;[46-47] the respective data are shown in Figure S4.2. For the PVT crystal, the excitons largely retain their initial energy around 2.59 eV. Nevertheless, a small red shift of 0.02 eV indicates residual contamination of the FP5 host with small amounts of FP8 (or possibly with other side products of the chemical synthesis). At the doping level of 0.025% and higher, the majority of excitons are transferred to the quencher

(FP8) within the first nanosecond as evident from the long-time red-shifted PL, which is mostly attributed to the quencher PL spectral region (see Section 4.3.3).
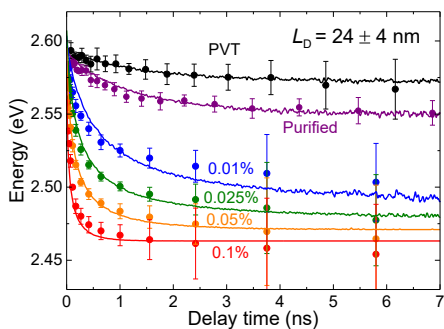
Figure S4.2. Experimental (circles) and MC simulated (lines) transient red-shifts of the mean PL energy for the representative doping levels: PVT (black), purified (purple), 0.01% (blue), 0.025% (olive), 0.05% (orange) and 0.1% (red) crystals. For the PVT (black) and purified crystal (purple) the quencher concentrations were retrieved by MC simulations as $8.5 \cdot 10^{-4}$% and 0.002%, respectively.

To retrieve the unknown quencher concentrations in the PVT and purified crystals (see discussion in Section 4.3.3), we simulated their transient red shifts with concentrations as fit parameters (Figure S4.2, black and purple, respectively). The best agreement with the experimental data was achieved for 0.00085 % (PVT crystal) and 0.002% (purified crystal) concentrations of FP8. Note that these values should be taken with caution as they rely on the model used.

4.5.4. Molecular Dynamics Simulations of FP8 in FP5 Crystal Structure

Figure S4.3 illustrates how one FP8 molecule substitutes two (head-to-tail) host molecules in the FP5 crystal structure. The pristine host (FP5) crystal molecular packing was taken from the x-ray diffraction data,[26] and the atoms rearrangements were simulated using molecular dynamics (MD) by "Avogadro: an open-source molecular builder and visualization tool".[48] The substitution results mainly in small torsional/bending deformations and adjustments of FP8, whereas the adjacent the FP5 conjugated cores maintain their initial positions (Figure S4.3).

Figure S4.3. Model of an FP5 crystalline aggregate simulated for 28 molecules (7 for each layer), where the two central (head-to-tail) host molecule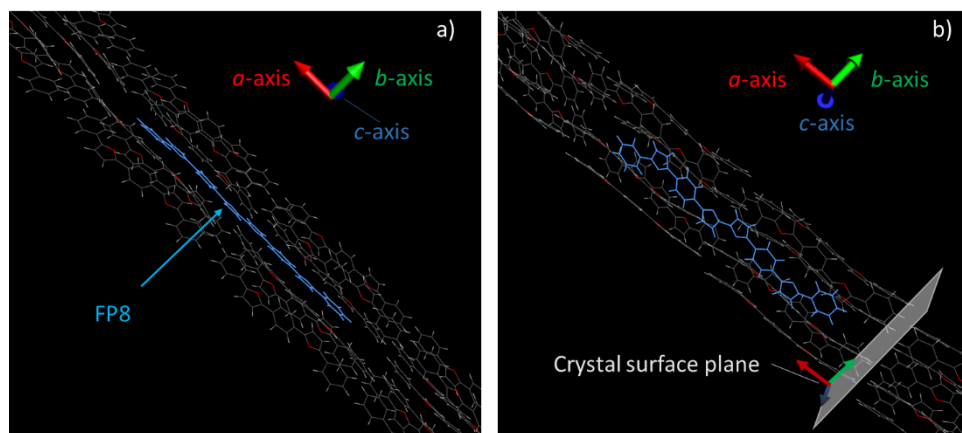s are substituted by FP8. Red, green and blue arrows are the crystallographic *a*-, *b*- and *c*- axes, respectively, of the FP5 crystal. [26] For better visibility, the orientation in panel (b) is turned by 45° around the crystallographic *a*-axis with respect to panel (a). Gray plane in (b) shows the orientation of the FP5 crystal surface plane (100).

4.5.5. Polarization-Resolved PL Data

The results of the MD simulations were verified by polarization-sensitive time-resolved measurements in the following way. According to Ref. 26, the FP5(host) and FP8 (quencher) transition dipole moments are directed from the meta position carbon atom of an outer phenylene to the opposite one (Figure S4.4a). The projection of these dipole moments onto the 100 plane of FP5 crystal structure (this plane coincides with the surfaces of the crystal plates) to which the excitation beam is orthogonal and from which PL is collected, are shown in Figure S4.4b by yellow arrows. The projections of the FP5 transition dipole moment to the crystallographic *b*- and *c*- axes are almost equal (their ratio is ~0.93) while the projection of the FP8 transition dipole moment onto the crystallographic *c*-axis is approximately three times longer than its projection to *b*-axis (~2.9). This brings us to the following conclusion: PL originated from the FP5 (host) should be weakly polarized with the polarization ratio (similar to the corresponding parameter introduced in Ref. 49) of $\rho_h = (0.93)^2 \approx 0.86$, while FP8 (quenchers) PL should be polarized along the crystallographic *c*-axis with $\rho_q = (0.35)^2 \approx 0.12$.
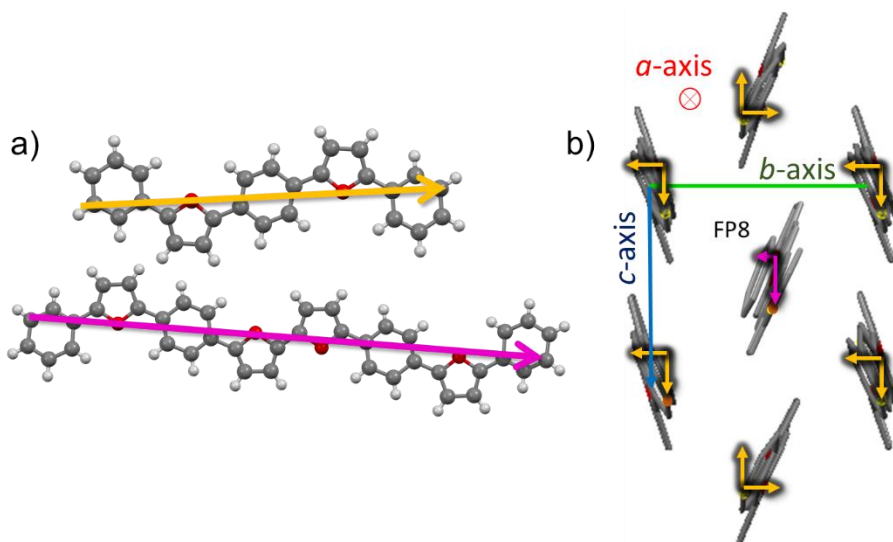
Figure S4.4. Transition dipole moments of FP5 and FP8 (yellow and pink arrows, respectively)[26] (a) and the view of the FP8-doped FP5 crystal structure (Figure S4.3) along a-axis (b). The yellow and pink arrows in (b) show the projections of the FP5 and FP8 transition dipole moments on the b and c axes, respectively. The FP8 molecule in the center is surrounded by 14 FP5 molecules in the herringbone arrangement; for the ease of presentation only 6 of them are shown.

The results of polarization- and time-resolved PL measurements on the PVT and 0.1% doped crystals are shown in Figure S4.5; the figure orientation is identical to Figure S4.4b. First, we established that PL polarization for the PVT crystal does not depend on the polarization of the excitation radiation in agreement with the herringbone packing of FP5 molecules in the crystal structure.[26] Therefore, for practical reasons (ease of alignment) the excitation beam polarization was set parallel to one of the crystal edges (at 30° in Figure S4.5). To improve the contrast of PL anisotropic properties of the host crystal and the quenchers in the host crystal, we followed the logics of Figure 4.2 and discussion around it. Namely, PL of the PVT and 0.1% doped crystals were obtained in the time windows of 0–1 ns and 1–5 ns, respectively. The short time (0–1 ns) PL decay is due to (yet) non-quenched host PL of the PVT crystal, and the long time (1–5 ns) window corresponds to the quencher PL in the 0.1% doped crystal (Figure S4.2, red).
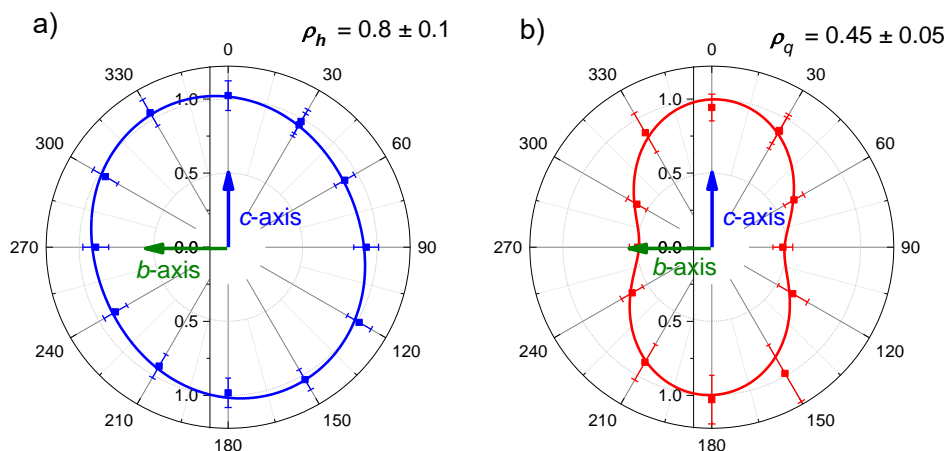
Figure S4.5. Polarization-resolved PL for the PVT crystal in the 0–1 ns (a) and 0.1% doped crystal in the 1–5 ns time window (b). The crystallographic axes *b*- and *c*- (olive and blue arrows, respectively) correspond to those in Figure S4.4b. The maximum PL intensity is normalized to unity. The solid lines are fits by the function $A \cdot cos^2(\theta - \theta_0) + B$, where θ is the angle between polarizations of PL and the crystallographic *c*-axis, while A, B and θ_0 are the fitting parameters. The polarization ratio ρ for host and quencher PL bands were calculated as $\rho = B/(A + B)$.[49] The excitation wavelength was set at 375 nm.

Host PL (Figure S4.5a) is nearly non-polarized ($\rho_h = 0.8 \pm 0.1$), which is in line with the results of MD simulations (Figure S4.4b). FP8 quenchers PL in the doped crystals (Figure S4.5b) shows a notable anisotropy with the preferential direction along the *c*-axis and the polarization ratio of $\rho_q = 0.45 \pm 0.05$. Again, this result is consistent with the MD simulations albeit the experimental anisotropy is somewhat higher than theoretically-predicted, which might be due to polarization scrambling in the microscope objective. All in all, the polarization-resolved measurements confirm the model in Figure S4.3 thereby giving credit to the supposition of smooth embedding of the FP8 quencher into the FP5 host lattice.

4.5.6. Calculations of the orientation factor in Förster radius

With MD simulations of the molecular structure in the doped crystals (Section 4.5.4) at hand, we are in a position to evaluate the orientation factor γ^2 in Förster radius equation (Section 4.5.1). For this, we calculated the dipole-dipole interaction energy

between the quencher and two nearest shells of host molecules (14 and 24 molecules are in the first and second shells, respectively):[45]

$$E_{dip-dip} \sim \gamma \cdot r^{-3} = [\cos \beta_{DA} - 3 \cdot \cos \beta_A \cdot \cos \beta_D] \cdot r^{-3}, \quad (4.1)$$

where β_{DA} is the angle between the direction of the transition dipole moments of the donor and acceptor molecules located at the distance r, β_A and β_D are the angles between the line connecting the centers of the acceptor and donor molecules, respectively, and their transition dipole moments. Figure S4.6 shows the distribution of these interaction energies from which $<\gamma>^2$ was estimated as ~1.5.
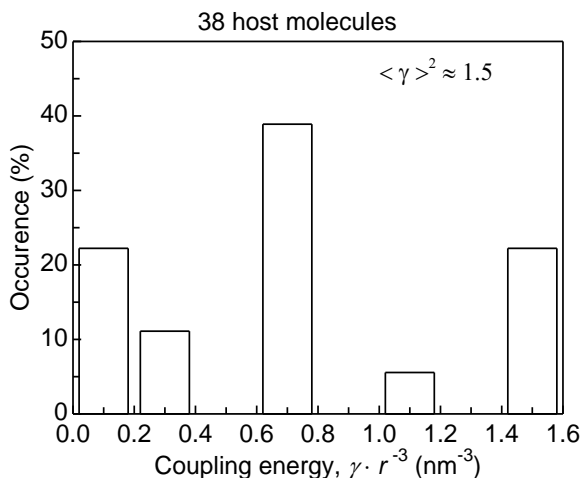
Figure S4.6. Distribution of the dipole-dipole interaction energies for a quencher (FP8) surrounded by 38 host (FP5) molecules.

4.5.7. Quencher-Quencher Mean Distance

Assuming that the quencher molecules are homogeneously distributed in the doped crystal, the mean distance d, between the nearest quenchers in the crystals with the molar doping level n_d was calculated as:

$$d = \sqrt[3]{\frac{M}{\rho N_A n_d}} = \sqrt[3]{\frac{1}{n_d}} \times 0.78 \text{ [nm]}, \quad (4.2)$$

where $M = 370$ g·mol^{-1} is the host (FP5) molar mass, $\rho = 1.316$ g·cm^{-3} is the host crystal density.[26]

4.5.8. Photoluminescence maps
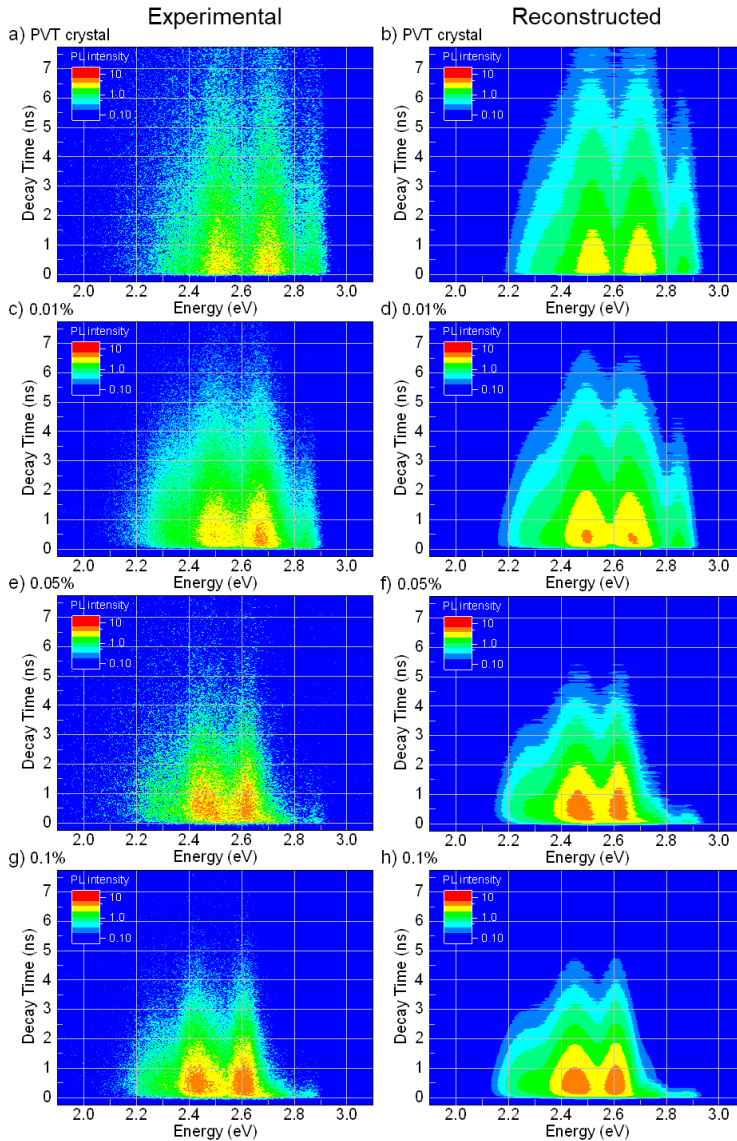
Figure S4.7. Experimental (left column) and reconstructed (right column) PL maps of variously doped FP5 single crystals (the quencher concentration is shown in the panels). The reconstructed PL maps are obtained as the weighted sum of the reference host and quencher spectra (shown in Figure 4.2) for each time step of 1 ps. Note the logarithmic scale of the color-coding. The excitation wavelength was set at 375 nm. The resulted shares of both spectra are depicted in Figure 4.3.

4.5.9. MC Simulations Parameters

Table S4.1. Global parameters (input, free, and output) of the Monte-Carlo simulation for the four crystals (0.01%, 0.025%, 0.05%, 0.1% doping levels). The uncertainty margins for the input parameters are given according to the accuracy of the measured data. The error margins for the free parameters were obtained according to the χ^2 minimization procedure.

Parameter (units)	Value at 293 K	Type (Source)
Mean host photon energy, $E_0 + \Delta E$ (eV)	2.6 ± 0.02	Input (Figure 4.2)
Mean quencher photon energy, E_0 (eV)	2.46 ± 0.02	Input (Figure 4.2)
Donor-acceptor energy gap, ΔE (eV)	0.14 ± 0.02	Input (Figure 4.2)
Exciton lifetime in host matrix, τ (ns)	2.9 ± 0.2	Input (Figure 4.4a)
Excitation lifetime of quenchers, τ_q (ns)	1.4 ± 0.1	Input (Figure 4.4a)
PL QY of host matrix, QY_h (%)	50 ± 5	Input (V.Konstantinov's integrating sphere measurements at Lomonosov Moscow State University)
PL QY of quenchers, QY_q (%)	70 ± 5	
Host radiative lifetime, τ_r (ns)	5.8 ± 0.2	Obtained from τ and QY_h
Quencher radiative lifetime, τ_{qr} (ns)	1.5 ± 0.2	Obtained from τ_q and QY_q
Host non-radiative lifetime, τ_n (ns)	5.6 ± 0.5	Obtained from τ and QY_h
Quencher non-radiative lifetime, τ_{qn} (ns)	4.5 ± 0.4	Obtained from τ_q and QY_q
Förster radius, R_0 (nm)	4.9 ± 0.5	Input (Section 4.5.1)
Hopping time, τ_{hop} (ps)	1.5 ± 0.5	Free
Diffusion length, L_D (nm)	24 ± 4	Output

Table S4.1 lists the parameters used in MC simulations; most of them are directly extracted from the prior experimental data (marked as "Input" in Table S4.1). The only free parameter (marked as "free" in Table S1), is the hopping time τ_{hop} which was obtained from the best approximation of the experimental data for the full set of doped crystals.

To evaluate the stability of MC results, we tested the goodness of the fit by the least squared deviation as a criterion:

$$\chi^2 \equiv C \cdot \sum_i \sum_m \left(E_{data}(t) - E_{MC}(t) \right)^2 \qquad (4.3)$$

where $E_{data}(t)$ is the experimental value of the mean PL energy at the time moment t, $E_{MC}(t)$ is the corresponded MC value, m is number of data points, i is the crystal index ($i = 1, 2, 3, 4$ stand for the 0.01%, 0.025%, 0.05%, 0.1% doping levels,

respectively), and C is the normalization coefficient ($\sim 1/\mathrm{eV}^2$) chosen in such a way to normalize the minimal χ^2 value to unity. Figure S4.8 shows that the MC simulations are stable with respect to variations in the exciton diffusion length (the output parameter of the MC simulations) and the host PL QY. We fixed the ratio of QYs of the host and quencher to the experimental value of 0.7 because the measurements of the relative QYs are much more accurate than their absolute values. As evident from Figure S4.8, the χ2 value is very weakly dependent on PL QYs but is sharply dependent on the exciton diffusion length thereby demonstrating good convergence finesse of the MC simulations.
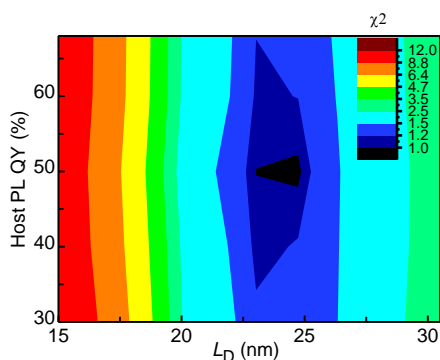
Figure S4.8. χ^2 map of the least squared deviations between the MC calculations and experimental data for the FP5 crystals as a function of the host PL QY and exciton diffusion length, L_D. The $QY_h/QY_q=0.7$ ratio was fixed. The global minimum value of χ^2 and its width determine the values and uncertainties, respectively, of the global parameter as $L_D = 24 \pm 4$ nm

4.5.10. Distributions of the Exciton Propagation Distances for the Quenching Volume Method

Figure S4.9 shows the exciton displacement (i.e. the distance between the initial and final positions) distributions for all excitons in the host matrix. Initially, the excitons (one exciton per $1.3 \cdot 10^5$ FP5 molecules; for details, see Section 4.5.12 are randomly distributed over the crystal matrix in such a way that an exciton is never placed on the cell which is already occupied by another exciton (or a quencher). The final exciton position is the one where the exciton ceases to exist (i.e. it either decays radiatively or non-radiatively, or is transferred to the quencher). The exciton diffusion lengths are directly calculated from the distributions as their mean values.
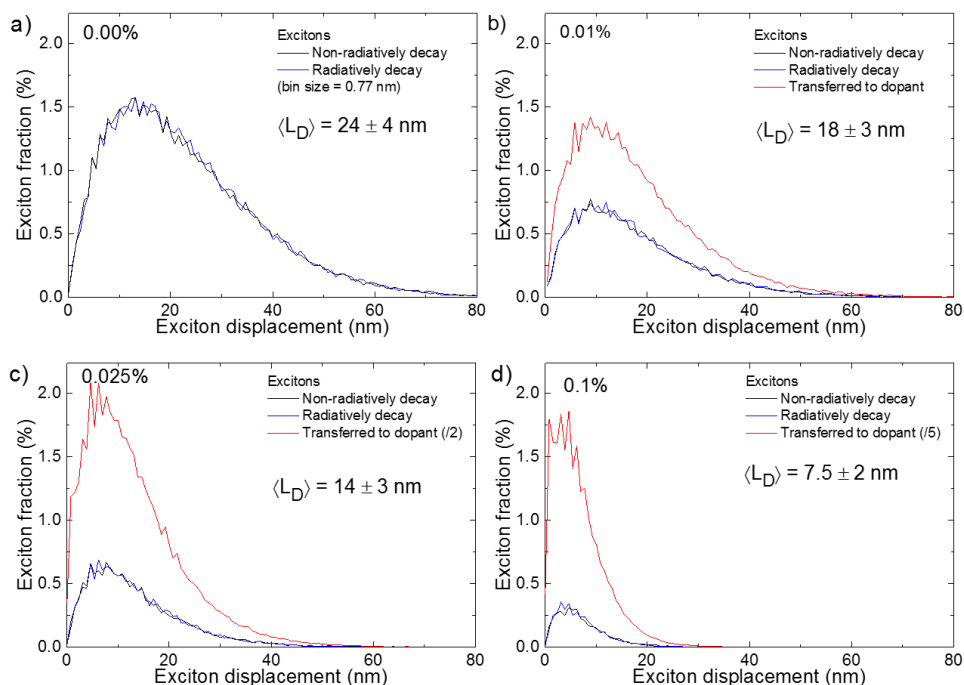
Figure S4.9. Distributions of exciton diffusion lengths in variously doped crystals in the quenching volume method. The quencher concentrations and mean exciton diffusion lengths L_D are shown in the respected panels. Red curves: excitons transferred to the quenchers via FRET (the final FRET step is not included); blue curves: radiatively decaying excitons; black curves: non-radiatively decaying excitons.
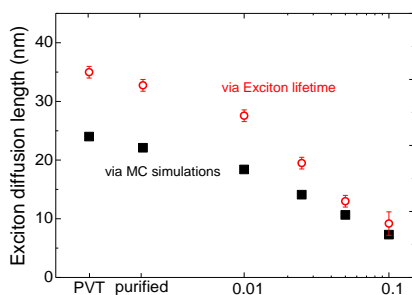
Figure S4.10. Exciton diffusion length as derived from MC simulations (black) and from host exciton lifetime (blue-flank decay) for variously doped FP5 single crystals.

4.5.11. Singlet exciton diffusion length in various organic single crystals

Table S4.2. Singlet exciton diffusion length in various organic single crystals measured via PL methods

Crystalline structure	L_D, nm	Reference	Technique
Naphthalene	50[a]	Gallus *et al.* [50]	Surface PL quenching
Anthracene	60[a]	Mulder[34]	Surface PL quenching
Phenanthrene	8	Gillus *et al.* [51]	Surface PL quenching
Tetracene	12	Vaubel *et al.* [32]	Exciton-exciton annihilation and surface PL quenching
PTCDA	25[b]	Lunt *et al.* [31]	Volume PL quenching with QY measurements
TMS-P2TP-TMS	2.5	Parashchuk *et al.* [21]	Time-resolved volume PL quenching

[a] There might be a contribution from triplet excitons due to the ultrafast singlet-to-triplet conversion and subsequent delayed triplet-to-singlet conversion.[19, 35-36]

[b] The data were measured for polycrystalline films and extrapolated for single crystals.

4.5.12. Excitation Intensity

For long exciton diffusion lengths, exciton-exciton annihilation[40] presents a serious challenge as the excitation intensity should be attenuated to the values where the probability of two excitons to meet becomes negligibly low. Therefore, we carefully investigated PL decays in the PVT crystal (where the exciton diffusion is the longest) in a broad range of excitation fluxes of 0.5–50 μJ/cm^2 (i.e. peak power was ranged in 0.625 – 62.5 W). To achieve such fluxes, we placed the microscope objective focus (~4 μm in diameter; ~12.5 μm^2 in area) right onto the crystal surface. The excitation spot size was measured by imaging the laser beam focused on a silicon wafer placed in the objective focus.
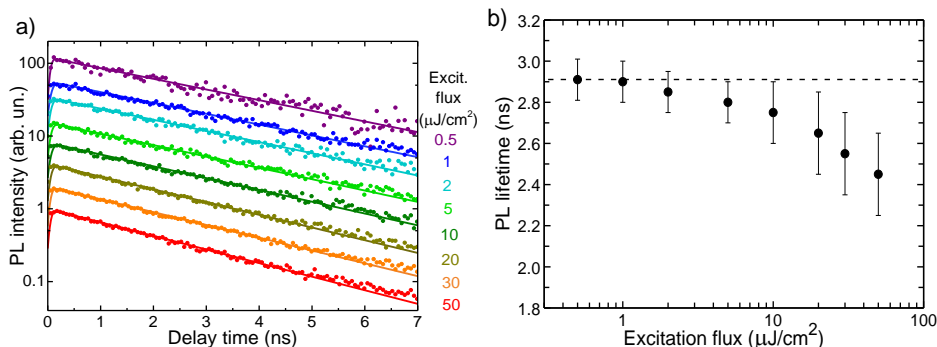
Figure S4.11. Experimental (dots) PL transients (a) and PL lifetimes (b) under various excitation flux in the PVT crystal. The solid lines in panel (a) are the monoexponential fit of the PL transients. PL lifetimes shown in panel (b) are extracted from the fits. The dash line represents the PL lifetime of the host (2.9 ns). The excitation wavelength was set at 375 nm.

The respective transients with exponential fits (Figure S4.11a) show clear evidence of exciton-exciton annihilation (in a separate experiment we established that this is not caused by sample photodegradation). The decay times obtained from the monoexponential fits are summarized in Figure S4.11b as a function of excitation intensity. With the decrease of excitation flux, PL lifetime increases indicating the reduction of exciton annihilation. At the excitation flux below ~5 µJ/cm^2 the decay time converges to ~2.9 ns, which is the host exciton lifetime, where the exciton annihilation becomes negligible. Accordingly, all other experiments were performed at the excitation intensity of 1 µJ/cm^2.

4.5.13. Calculations of the Mean Distance between the Excitons in the Annihilation Experiments

The density of excitations for the excitation flux of 1 µJ/cm^2, is estimated as ~$1.5 \cdot 10^{16}$ cm^{-3} (the crystal thickness of ~1 µm and the sample absorbance of OD~0.5 at the excitation wavelength 375 nm). Thus, at the excitation flux of 1 µJ/cm^2 one exciton exists in the ~40x40x40 nm^3 volume, i.e. the mean distance between the excitons is d_{e-e}=40 nm.

For MC simulations on annihilation, we need to know the number of excitons per one unit cell. The density of molecules in the FP5 crystal[26] is ~$2 \cdot 10^{21}$ cm^{-3} which results in the averaged crystal unit cell size of ~0.77 nm, or one exciton per $1.3 \cdot 10^5$ FP5 molecules for the excitation flux of 1 µJ/cm^2.

4.5.14. Monte-Carlo simulation for the exciton-exciton annihilation technique
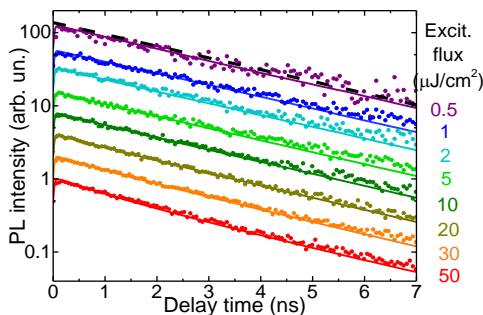
Figure S4.12. Experimental (dots) and Monte-Carlo simulated (lines) PL transients under various excitation fluxes in the PVT crystal. In the MC simulations, the annihilation radius, Ra, was set as the average unit cell size (0.77 nm).
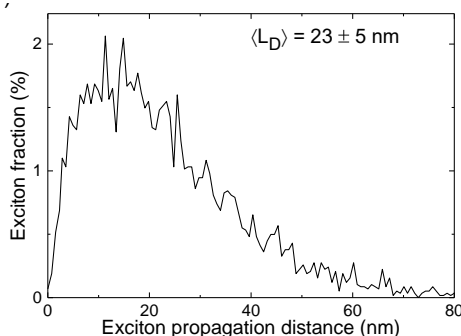
Figure S4.13. MC simulated distribution of exciton displacements in the PVT FP5 single crystal for the lowest excitation flux (i.e. in the absence of exciton-exciton annihilation). The bin size in the horizontal axis is 0.77 nm.

4.5.15. Energy Transfer Efficiency

Figure S4.14 shows quantum efficiency of energy transfer defined as a ratio of the number of excitons transferred to the quenchers to the number of initial excitons in the crystals. With the increase of quencher concentration, the energy transfer efficiency reaches ~90% in the 0.1% doped crystal.
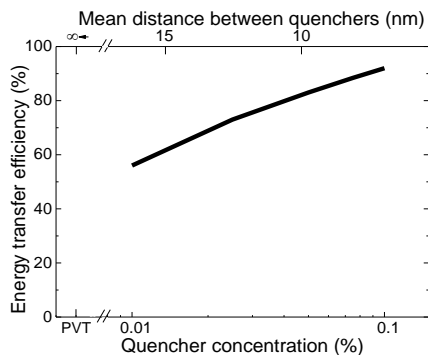
Figure S4.14. Monte-Carlo simulated energy transfer efficiency from the host excitons to the quenchers. The upper axis shows a mean distance between quenchers in the host crystals (for details see Section 4.5.13)

4.5.16. Photoluminescence Transients of FP5 Samples

For spectroscopy on liquid FP5 solution, FP5 molecules were dissolved in acetonitrile (CH_3CN) at concentration of 1 mg/L. The solution was stirred on a magnetic stirrer for ~5 hours at 50°C, cooled down to the room temperature and placed in a 1 mm thickness quartz cuvette.

The FP5 drop-cast sample was prepared by drop-casting from a FP5 solution in $CHCl_3$ (0.5 mg/L) on a glass substrate with subsequent drying for at least 30 minutes.

Solid solution: for FP5 solid solution sample preparation, poly(methyl methacrylate) (PMMA) was dissolved in acetonitrile (CH_3CN) at concentration of 15 g/L. The solution was stirred on a magnetic stirrer for ~5 hours at 50°C. Then the solution was mixed with 0.01 g/L FP5/CH_3CN solution at 1:1 volume ratio. The resulted FP5 concentration in PMMA matrix amounted to 85 mg/L, i.e. one FP5 molecule per 5000 PMMA monomers which excluded FP5 intermolecular interactions. The solid matrix (solid solution) was prepared by drop-casting from the solution on a glass substrate with subsequent drying for ~2 hours.

Optical properties of FP5 were studied in dilute liquid/solid solutions, a drop-cast sample, and single crystal (presumably ~0.01% FP8-doped). A liquid solution absorption spectrum in Figure S4.15a shows a fine structure that is characteristic for furan-containing molecules[52-53] as compared to other linear conjugated molecules such as oligothiophenes, oligo(phenylenevinylenes), oligo(thiophene-phenylenes etc., which typically do not show the fine structure in solution. This fine structure could be assigned to higher rigidity of furan-containing conjugated oligomers.[52-53] Another possible reason could be the molecule planarization through the

intramolecular H–O interaction similarly to earlier reported for EDOT-type materials.[54] The PL spectrum of FP5 demonstrates two maxima at 407 and 431 nm in liquid (Figure S4.15a) and solid solutions (Figure S4.16).

The PL QY of FP5 in liquid solution is high, reaching 91±3%.[26] The FP5 PL QY is consistent with the high PL QY in 2,5-diarylfurans[55] indicating that the phenyl-furan moiety favours efficient luminescence. One can speculate that the high PL QY is an important prerequisite for a highly luminescent crystalline phase. Indeed, the PL QY measured for FP5 single crystals is as high as 60% (as it has been shown in Ref. 26). The PL spectra of FP5 single crystals are red-shifted by ~0.45 eV (80 nm) as compared to that in solution (Figure S4.15a). This shift can be assigned to PL reabsorption because of considerable overlap between the absorption and PL spectra (Figure S4.15a) and to the solid state shift, i.e. to the higher polarizability of the molecular environment in the crystal as compared to solution. The latter can explain a ~0.2 eV (30 nm) red-shift (the difference in the PL onset in solution and crystal) as follows from the PL data collected using a microscope, which were free of strong PL reabsorption as the PL passed in the crystal a path shorter than 10 µm.
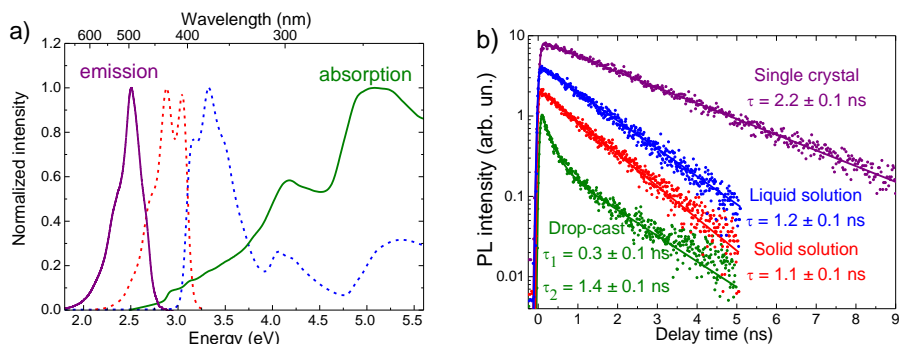
Figure S4.15. Optical properties of FP5. a) Absorption (dashed blue) and photoluminescence (dashed red) spectra measured in diluted CH_3CN solution, absorption of drop-cast sample (olive), PL spectra of single (purple) and grinded (black) crystal measured using the integrating sphere (the latter is superimposed at the long-wavelength range of the former); b) PL kinetics in CH_3CN diluted solution (red), solid solution (blue), drop-cast sample (olive) and single crystal (purple). The transients were integrated over the 2.7–3.1 eV (400–460 nm) region for solutions and over 2.35–2.75 eV (450–530 nm) region for the drop-cast sample and the single crystal, respectively. The solid lines are exponential fits convoluted with an apparatus response of 50 ps; the corresponding decay times are shown next to the transients. All transients are arbitrarily normalized for the ease of representation.

To further investigate the luminescent properties of FP5, we measured the PL kinetics in the same samples, i.e. single crystals, dilute solid/liquid solutions, and drop-cast sample (Figure S4.15b). As the kinetics in both liquid and solid solutions show similar lifetimes, we conclude that restriction of molecular motions in the solid solution does not have any influence the PL lifetime and spectra. However, the close packing of FP5 molecules in a single crystal results in a two-times longer PL lifetime. Note that PL in the solutions and crystal decays monoexponentially indicating the only luminophore type. On the other hand, PL in the drop-cast sample decays much faster and is not monoexponential (Figure S4.15b) that can be assigned to disorder. From this we conclude that the structural order in the single crystal facilitates longer exciton lifetime.
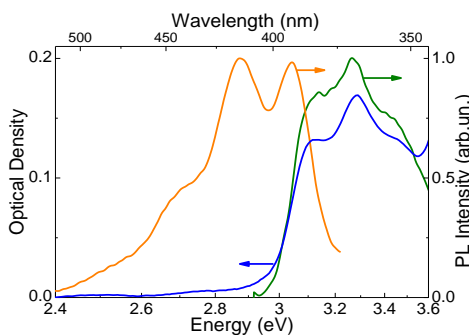
Figure S4.16. FP5/PMMA solid-solution. (a) Excitation (olive, 435 nm detection wavelength) and PL (orange, 370 nm excitation wavelength) spectra of 85 mg/L FP5/PMMA solid solution drop-casted on a glass substrate and absorption spectrum (blue) of a FP5 solid solution with concentration increased by a factor of 5 (425 mg/L). The excitation and PL spectra are normalized to their maxima.

The non-radiative recombination rate in organic crystals usually decreases upon cooling that is assigned to either less efficient exciton migration[56] or slower non-radiative transitions,[57] or both. We recorded the PL kinetic in the FP5 single crystal at 77 K (Figure S4.17b) and found that the PL lifetime is similar to the room temperature value. This indicates that the non-radiative recombination in FP5 single crystal is temperature independent. In contrast, at 77 K the time-resolved PL in the drop-cast sample becomes much longer than at room temperature (Figure S4.17e). This hints at a lower non-radiative recombination rate, which could be assigned to less mobile excitons. We speculate that the temperature-independent non-radiative recombination in FP5 single crystal is not due to exciton migration but mainly due to intersystem crossing, i.e., conversion of singlet excitons to triplet ones, which are

about 1 eV lower in energy according to our gas-phase calculations (shown in Ref. 26).

Table 4.2 summarizes the photophysics data and shows that the radiative rate constant (k_r) is more than two times lower in single crystal as compared to the solutions. At the same time, the PL QY decreases in the single-crystal only by 27% as compared to isolated FP5 molecules, i.e. in solution. As a result, the non-radiative rate constant (k_{nr}) increases in single crystal twice. The lower k_r in crystal means that the transition dipole moment for closely packed FP5 molecules decreases that could be assigned to H-aggregation,[58] which is indicative from the nearly collinear transition dipole moments oriented almost normally to the bc basal plane (shown in Ref. 26). The optical evidence of H-aggregation (i.e. a weak oscillator strength of the lowest energy optical transition) follows from weak absorption near the absorption edge in the absorption spectrum of the drop-cast sample (shown in Ref. 26). However, despite the lower transition dipole moment in FP5 aggregates, the well-ordered structure of single crystals still provides high PL QY (the very similar conclusion was reported for distyrylbenzene[56]), which is to the best of our knowledge the highest among furan co-oligomers and solution-grown semiconducting single crystals containing heteroaryls.

Table 4.3. Photoluminescence properties of FP5 at room temperature. η_0 is the internal PL QY, $k_r = \eta_0/\tau$ is the radiative decay rate, $k_{nr} = (1-\eta_0)/\tau$ is the non-radiative decay rate.

	η_0 [%]	τ [ns]	k_r [ns^{-1}]	k_{nr} [ns^{-1}]
Liquid Solution	91±3	1.2±0.1	0.76±0.07	0.08±0.03
Single Crystal (~0.01% FP8-doped)	66±2[a]	2.2±0.1	0.30±0.02	0.16±0.01

[a]averaged and reabsorption corrected (see below).

The low-defect structure of the FP5 single crystals was also confirmed by a much weaker PL spectral diffusion (i.e. temporal changes in the PL spectrum) in the single crystal as compared to the drop-cast sample (Figure S4.17c, f). Thus, all PL data suggest that the high luminescent properties of FP5 single crystals stem from their highly ordered structure.

We stress that no signatures of PL degradation were observed in FP5 single crystals after many repeated measurements of PL QY and kinetics on the very same samples neither during the measurements nor after a few weeks storing under ambient conditions. In contrast, PL in liquid and solid solutions degraded even after

short exposure to light. These observations suggest that closely packed FP5 crystalline structure enhances the photostability and shelf lifetime.

In summary, furan-phenylene co-oligomer FP5 demonstrates the unique combination of high luminescence efficiency and efficient charge transport in a solution-processed single crystal. Considering suitable solubility and high thermal stability of FP5, this combination opens the way for mass production of optoelectronic materials and devices using printing technologies.

Figure S4.17 summarizes PL spectra, time-resolved kinetics, and spectral diffusion data in different FP5 samples (single crystal, drop-cast, solutions) recorded using the streak-camera at 77 and 293 K. The monoexponential room-temperature PL decay time of 2.2±0.1 ns in the single crystal does not change upon cooling to 77 K (Figure S4.17b). Weak spectral diffusion (i.e. the temporal shift of the transient PL spectrum) in the single crystal (Figure S4.17c) is temperature independent that can be ascribed to ordered molecular packing in the crystal.

The PL spectrum of the drop-cast sample is noticeably broader than that of the single crystal, presumably due to larger heterogeneities (Figure S4.17d). The PL decay in the drop-cast sample at room temperature becomes bi-exponential with two characteristic times of 0.3±0.1 ns (75%) and 1.4±0.1 ns (25%), and strongly temperature dependent (Figure S4.17e). Finally, the spectral diffusion at 293 K in the drop-cast sample (Figure S4.17f) is considerable stronger as compared to that in the single crystal (170±5 meV *vs.* 40±5 meV) and shows prominent temperature dependence. Thus, the PL of the drop-cast sample is consistent with thermally-activated exciton migration in the strongly disordered energy landscape[28] due to high concentration of exciton traps or/and quenching sites. This is in sharp contrast with the single crystal where thermally activated hopping appears to be substantially reduced. Finally, the diluted liquid and solid solutions, where intermolecular interactions are switched off, show similar PL properties (Figure S4.17g, h, i). The PL spectrum is substantially shifted to the blue as compared to the single-crystal and drop-cast samples as expected for non-interacting molecules in a weakly polarizable matrix. No spectral diffusion is observed in the solutions (Figure S4.17i) as the molecular excitation resides at the same site.
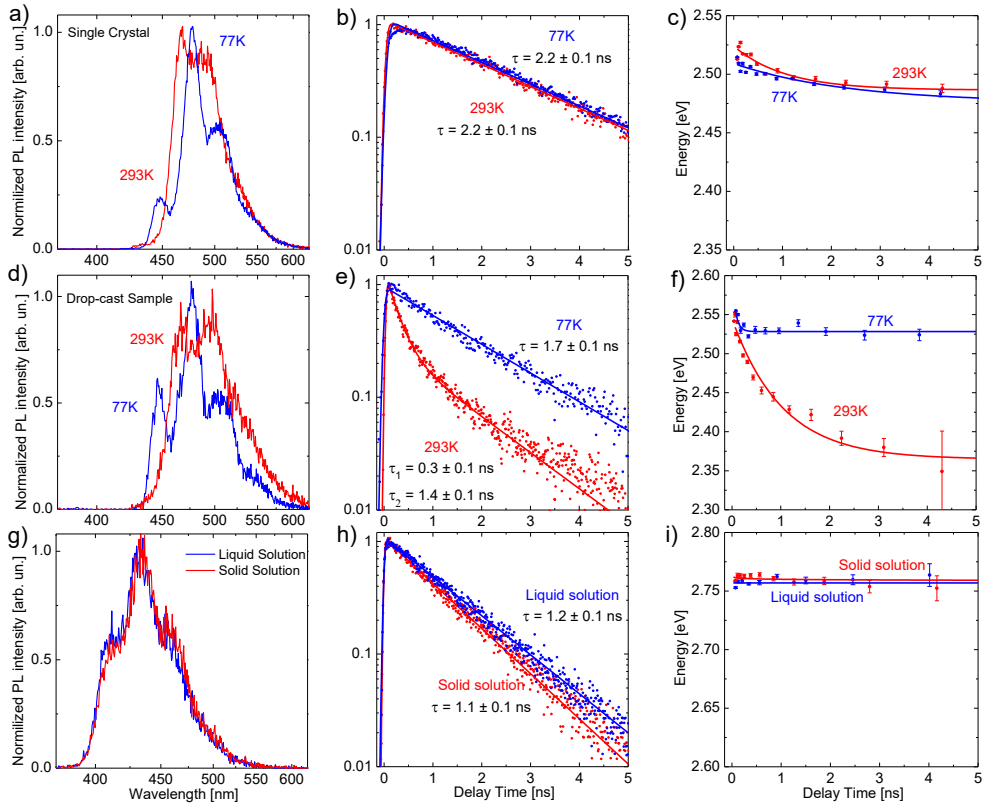
Figure S4.17. PL spectra (left), time-resolved kinetics (middle) and spectral diffusion (right) in FP5 single crystal (first row), drop-cast sample (second row), solutions (third row) recorded at 77 and 293 K. The PL excitation wavelength was 400 nm for the single-crystal/drop-cast sample (a-f) and 385 nm for the solutions (g-i). The kinetics were integrated over 425–550 nm (b, e) and 400–525 nm (h). The lines in (b, e, h) and (e) are mono- and bi-exponential fits, respectively convoluted with an apparatus response. The time-dependent mean energy values of the PL spectrum are shown in (c, f, i). The solid lines are exponential fits which amplitude ΔE provides an estimate for the energetic disorder as the following: in the crystal (c), $\Delta E_{77K} = 25\pm5$ meV, $\Delta E_{293K} = 40\pm5$ meV; in the drop-cast sample (f), $\Delta E_{77K} = 25\pm5$ meV, $\Delta E_{293K} = 170\pm5$ meV; in the solution (i), $\Delta E_{293K} = 0$ meV.

Figure S4.18 compares PL spectra of FP5 samples in the 90° and 180°-geometries of PL collection. In the latter, the PL was collected in the microscopic arrangement mainly from the excitation spot of ~5 μm resulting in a minimal PL reabsorption effect. Here, the PL high-frequency onset at 435 nm is clearly observed, whereas in the 90°-geometry with the excitation spot of ~100 μm, the PL blue part is reabsorbed following in a very weak PL signal at 435 nm.
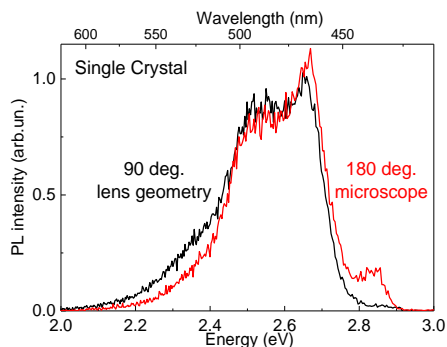
Figure S4.18. PL spectra of a FP5 single crystal at room temperature recorded by the streak camera at two different configurations of PL collection: 90°-geometry with a converging lens (focal length of 7.5 cm, excitation spot of ~100 μm) and 180°-geometry with a microscope objective (10x, NA=0.25) focusing the excitation beam into a spot size of ~5 μm. The excitation wavelength was 400 nm. The spectra are arbitrarily normalized. The 0-0 transition at 440 nm is suppressed in the 90°-geometry because of PL reabsorption.

4.6. References

1.   Kido, J.; Kimura, M.; Nagai, K., Multilayer White Light-Emitting Organic Electroluminescent Device. *Science* **1995**, *267*, 1332-1334.

2.   Friend, R. H., et al., Electroluminescence in Conjugated Polymers. *Nature* **1999**, *397*, 121-128.

3.   Forrest, S. R., The Path to Ubiquitous and Low-Cost Organic Electronic Appliances on Plastic. *Nature* **2004**, *428*, 911-918.

4.   Muccini, M., A Bright Future for Organic Field-Effect Transistors. *Nat. Mater.* **2006**, *5*, 605-613.

5.   Capelli, R.; Toffanin, S.; Generali, G.; Usta, H.; Facchetti, A.; Muccini, M., Organic Light-Emitting Transistors with an Efficiency that Outperforms the Equivalent Light-Emitting Diodes. *Nat. Mater.* **2010**, *9*, 496-503.

6.   Hotta, S.; Yamao, T.; Bisri, S. Z.; Takenobu, T.; Iwasa, Y., Organic Single-Crystal Light-Emitting Field-Effect Transistors. *J. Mater. Chem. C* **2014**, *2*, 965-980.

7.   Kuehne, A. J. C.; Gather, M. C., Organic Lasers: Recent Developments on Materials, Device Geometries, and Fabrication Techniques. *Chem. Rev.* **2016**, *116*, 12823-12864.

8.   Hotta, S.; Yamao, T., The Thiophene/Phenylene Co-Oligomers: Exotic Molecular Semiconductors Integrating High-Performance Electronic and Optical Functionalities. *J. Mater. Chem.* **2011**, *21*, 1295-1304.

9.   Oniwa, K., et al., Single Crystal Biphenyl End-Capped Furan-Incorporated Oligomers: Influence of Unusual Packing Structure on Carrier Mobility and Luminescence. *J. Mater. Chem. C* **2013**, *1*, 4163-4170.

10. Komori, T.; Nakanotani, H.; Yasuda, T.; Adachi, C., Light-Emitting Organic Field-Effect Transistors Based on Highly Luminescent Single Crystals of Thiophene/Phenylene Co-Oligomers. *J. Mater. Chem. C* **2014**, *2*, 4918-4921.

11. Gierschner, J.; Varghese, S.; Park, S. Y., Organic Single Crystal Lasers: A Materials View. *Adv. Opt. Mater.* **2016**, *4*, 348-364.

12. Park, S. K., et al., Highly Luminescent 2d-Type Slab Crystals Based on a Molecular Charge-Transfer Complex as Promising Organic Light-Emitting Transistor Materials. *Adv. Mater.* **2017**, *29*, 1701346.

13. Brabec, C.; Scherf, U.; Dyakonov, V., *Organic Photovoltaics: Materials, Device Physics, and Manufacturing Technologies*; Wiley-VCH Verlag GmbH & Co. KGaA: Weinheim, Germany, 2011.

14. Lanzani, G., *The Photophysics Behind Photovoltaics and Photonics*; Wiley-VCH: Weinheim, Germany, 2012.

15. Hedley, G. J.; Ruseckas, A.; Samuel, I. D. W., Light Harvesting for Organic Photovoltaics. *Chem. Rev.* **2017**, *117*, 796-837.

16. Ho, C. L.; Wong, W. Y.; Wang, Q.; Ma, D.; Wang, L.; Lin, Z., A Multifunctional Iridium‐Carbazolyl Orange Phosphor for High‐Performance Two‐Element Woled Exploiting Exciton‐Managed Fluorescence/Phosphorescence. *Adv. Funct. Mater.* **2008**, *18*, 928-937.

17. Kamtekar Kiran, T.; Monkman Andrew, P.; Bryce Martin, R., Recent Advances in White Organic Light‐Emitting Materials and Devices (WOLEDs). *Adv. Mater.* **2009**, *22*, 572-582.

18. Nakanotani, H.; Saito, M.; Nakamura, H.; Adachi, C., Emission Color Tuning in Ambipolar Organic Single‐Crystal Field‐Effect Transistors by Dye‐Doping. *Adv. Funct. Mater.* **2010**, *20*, 1610-1615.

19. Powell, R. C.; Soos, Z. G., Singlet Exciton Energy Transfer in Organic Solids. *J. Lumin.* **1975**, *11*, 1-45.

20. Wang, H., et al., Doped Organic Crystals with High Efficiency, Color-Tunable Emission toward Laser Application. *Cryst. Growth Des.* **2009**, *9*, 4945-4950.

21. Parashchuk, O. D.; Mannanov, A. A.; Konstantinov, V. G.; Dominskiy, D. I.; Surin, N. M.; Borshchev, O. V.; Ponomarenko, S. A.; Pshenichnikov, M. S.; Paraschuk, D. Y., Molecular Self-Doping Controls Luminescence of Pure Organic Single Crystals. *Adv. Funct. Mater.* **2018**, *28*, 1800116.

22. Bisri, S. Z.; Takenobu, T.; Takahashi, T.; Iwasa, Y., Electron Transport in Rubrene Single-Crystal Transistors. *Appl. Phys. Lett.* **2010**, *96*, 183304.

23. Podzorov, V., Organic Single Crystals: Addressing the Fundamentals of Organic Electronics. *MRS Bull.* **2013**, *38*, 15-24.

24. Nakanotani, H.; Adachi, C., Amplified Spontaneous Emission and Electroluminescence from Thiophene/Phenylene Co-Oligomer-Doped P-Bis(P-Styrylstyryl)Benzene Crystals. *Adv. Opt. Mater.* **2013**, *1*, 422-427.

25. Kazantsev, M. S.; Beloborodova, A. A.; Kuimov, A. D.; Koskin, I. P.; Frantseva, E. S.; Rybalova, T. V.; Shundrina, I. K.; Becker, C. S.; Mostovich, E. A., Synthesis, Luminescence and Charge Transport Properties of Furan/Phenylene Co-Oligomers: The Study of Conjugation Length Effect. *Org. Electron.* **2018**, *56*, 208-215.

26. Kazantsev, M. S., et al., Highly-Emissive Solution-Grown Furan/Phenylene Co-Oligomer Single Crystals. *RSC Adv.* **2016**, *6*, 92325-92329.

27. Menke, S. M.; Holmes, R. J., Exciton Diffusion in Organic Photovoltaic Cells. *Energy Environ. Sci.* **2014**, *7*, 499-512.

28. Mikhnenko, O. V.; Blom, P. W. M.; Nguyen, T.-Q., Exciton Diffusion in Organic Semiconductors. *Energy Environ. Sci.* **2015**, *8*, 1867-1888.

29.   de Sousa, L. E.; da Silva Filho, D. A.; de Sousa, R. T.; de Oliveira Neto, P. H., Exciton Diffusion in Organic Nanofibers: A Monte Carlo Study on the Effects of Temperature and Dimensionality. *Sci. Rep.* **2018**, *8*, 14066.

30.   Bässler, H., Charge Transport in Disordered Organic Photoconductors a Monte Carlo Simulation Study. *Phys. Status Solidi (b)* **1993**, *175*, 15-56.

31.   Lunt Richard, R.; Benziger Jay, B.; Forrest Stephen, R., Relationship between Crystalline Order and Exciton Diffusion Length in Molecular Organic Semiconductors. *Adv. Mater.* **2009**, *22*, 1233-1236.

32.   Vaubel, G.; Baessler, H., Diffusion of Singlet Excitons in Tetracene Crystals. *Mol. Cryst. Liq. Cryst.* **1970**, *12*, 47-56.

33.   Meth, J. S.; Marshall, C. D.; Fayer, M. D., An Examination of Radiative and Nonradiative Excitation Transport in Thin Anthracene Crystals: Transient Grating Experiments. *Solid State Commun.* **1990**, *74*, 281-284.

34.   Mulder, B. J., Anisotropy of Light Absorption and Exciton Diffusion in Anthracene Crystals Determined from Externally Sensitized Fluorescence. *Philips Res. Rep.* **1967**, *22*, 142.

35.   Michel–Beyerle, M. E.; Haberkorn, R.; Kinder, J.; Seidlitz, H., Direct Evidence for the Singlet–Triplet Exciton Annihilation in Anthracene Crystals. *Phys. Status Solidi (b)* **1978**, *85*, 45-49.

36.   Kalinowski, J.; Stampor, W.; Di Marco, P.; Garnier, F., Photogeneration of Charge in Solid Films of A-Sexithiophene. *Chem. Phys.* **1998**, *237*, 233-243.

37.   Koskin, I. P.; Mostovich, E. A.; Benassi, E.; Kazantsev, M. S., Way to Highly Emissive Materials: Increase of Rigidity by Introduction of a Furan Moiety in Co-Oligomers. *J. Phys. Chem. C* **2017**, *121*, 23359-23369.

38.   Stehr, V.; Fink, R. F.; Tafipolski, M.; Deibel, C.; Engels, B., Comparison of Different Rate Constant Expressions for the Prediction of Charge and Energy Transport in Oligoacenes. *Wiley Interdiscip. Rev.: Comput. Mol. Sci.* **2016**, *6*, 694-720.

39.   Suna, A., Kinematics of Exciton-Exciton Annihilation in Molecular Crystals. *Phys. Rev. B* **1970**, *1*, 1716-1739.

40.   Lewis, A. J.; Ruseckas, A.; Gaudin, O. P. M.; Webster, G. R.; Burn, P. L.; Samuel, I. D. W., Singlet Exciton Diffusion in Meh-PPV Films Studied by Exciton–Exciton Annihilation. *Org. Electron.* **2006**, *7*, 452-456.

41.   Shaw, P. E.; Ruseckas, A.; Samuel, I. D. W., Exciton Diffusion Measurements in Poly(3-Hexylthiophene). *Adv. Mater.* **2008**, *20*, 3516-3520.

42.   Fleming, G. R.; Millar, D. P.; Morris, G. C.; Morris, J. M.; Robinson, G. W., Exciton Fission and Annihilation in Crystalline Tetracene. *Aust. J. Chem.* **1977**, *30*, 2353-2359.

43.   Babenko, S. D.; Benderskii, V. A.; Goldanskii, V. I.; Lavrushko, A. G.; Tychinskii, V. P., Singlet Exciton Annihilation in Anthracene Crystals. *Phys. Status Solidi (b)* **1971**, *45*, 91-97.

44.   Kazantsev, M. S.; Beloborodova, A. A.; Frantseva, E. S.; Rybalova, T. V.; Konstantinov, V. G.; Shundrina, I. K.; Paraschuk, D. Y.; Mostovich, E. A., Methyl Substituent Effect on Structure, Luminescence and Semiconducting Properties of Furan/Phenylene Co-Oligomer Single Crystals. *CrystEngComm* **2017**, *19*, 1809-1815.

45.   Lakowicz, J. R., Energy Transfer. In *Principles of Fluorescence Spectroscopy*, Lakowicz, J. R., Ed. Springer US: Boston, MA, 2006; pp 443-475.

46.   Madigan, C.; Bulović, V., Modeling of Exciton Diffusion in Amorphous Organic Thin Films. *Phys. Rev. Lett.* **2006**, *96*, 046404.

47.   Akselrod, G. M.; Prins, F.; Poulikakos, L. V.; Lee, E. M. Y.; Weidman, M. C.; Mork, A. J.; Willard, A. P.; Bulović, V.; Tisdale, W. A., Subdiffusive Exciton Transport in Quantum Dot Solids. *Nano Lett.* **2014**, *14*, 3556-3562.

48.   Hanwell, M. D.; Curtis, D. E.; Lonie, D. C.; Vandermeersch, T.; Zurek, E.; Hutchison, G. R., Avogadro: An Advanced Semantic Chemical Editor, Visualization, and Analysis Platform. *J. Cheminf.* **2012**, *4*, 17.

49.   Prutskij, T.; Percino, M. J.; Perova, T. S., Polarization Anisotropy of Photoluminescence from Triphenylamine-Based Molecular Single Crystals. *Cryst. Res. Technol.* **2013**, *48*, 1039-1043.

50.   Gallus, G.; Wolf, H. C., Excitonendiffusion in Naphthalin-Aufdampfschichten. *Zeitschrift für Naturforschung A* **1968**, *23*, 1333.

51.   Gillus, G.; Wolf, H. C., Direct Measurement of the Diffusion Length of Singulet Excitons in Solid Phenanthrene. *Phys. Status Solidi (b)* **1966**, *16*, 277-280.

52.   Gidron, O.; Varsano, N.; Shimon, L. J. W.; Leitus, G.; Bendikov, M., Study of a Bifuran Vs. Bithiophene Unit for the Rational Design of Π-Conjugated Systems. What Have We Learned? *Chem. Commun.* **2013**, *49*, 6256-6258.

53.   Gidron, O.; Bendikov, M., A-Oligofurans: An Emerging Class of Conjugated Oligomers for Organic Electronics. *Angew. Chem. Int. Ed.* **2014**, *53*, 2546-2555.

54.   Milián Medina, B.; Wasserberg, D.; Meskers, S. C. J.; Mena-Osteritz, E.; Bäuerle, P.; Gierschner, J., Edot-Type Materials: Planar but Not Rigid. *J. Phys. Chem. A* **2008**, *112*, 13282-13286.

55.   Klukas, F.; Grunwald, A.; Menschel, F.; Müller, T. J. J., Rapid Pseudo Five-Component Synthesis of Intensively Blue Luminescent 2,5-di(Hetero)Arylfurans via a Sonogashira–Glaser Cyclization Sequence. *Beilstein J. Org. Chem.* **2014**, *10*, 672-679.

56.   Gierschner, J.; Park, S. Y., Luminescent Distyrylbenzenes: Tailoring Molecular Structure and Crystalline Morphology. *J. Mater. Chem. C* **2013**, *1*, 5818-5832.

57.   Kanazawa, S.; Ichikawa, M.; Koyama, T.; Taniguchi, Y., Self-Waveguided Photoemission and Lasing of Organic Crystalline Wires Obtained by an Improved Expitaxial Growth Method. *Chemphyschem* **2006**, *7*, 1881-1884.

58.   McRae, E. G.; Kasha, M., Enhancement of Phosphorescence Ability Upon Aggregation of Dye Molecules. *J. Chem. Phys.* **1958**, *28*, 721-722.

Chapter 5. Photoluminescence Polarization Anisotropy in Organic Semiconductor Crystals
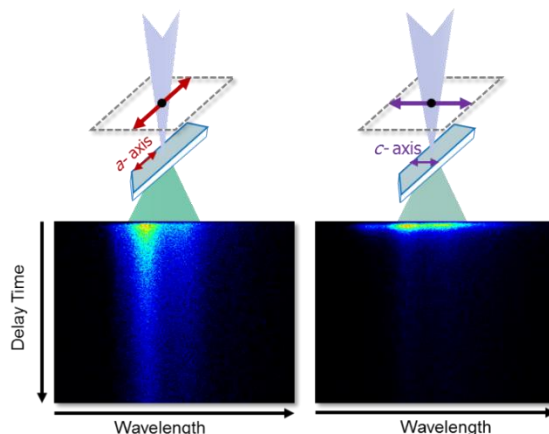
Modern organic electroluminescent devices such as light-emitting diodes and light-emitting transistors are based on highly ordered organic semiconductors. In single crystals based on a thiophene-phenylene co-oligomer (TPCO) with bulky terminal substituents (TMS - trimethylsilyl group), the face-on orientation of the molecules with respect to the crystal plate promises highly anisotropic photoluminescent (PL) properties. In this Chapter, we analyse time-resolved PL polarization response in TPCO crystals based on the 1,4-bis{5-[4-(trimethylsilyl)phenyl]thiophen-2-yl}benzene. PL was excited at the normal incidence and collected in the backward direction. Regardless of the excitation polarization, PL in these crystals is mainly polarized along the transition dipole moments of the molecules, which are almost co-directional with the crystallographic **c**-axis. The PL efficiency strongly depends on the excitation polarization, with the highest efficiency observed for the excitation polarized along the crystallographic **a**-axis, i.e. almost *orthogonal to the transition dipole moments of the molecules*. This highly surprising feature is explained via the presence of weakly- or even non-radiative states which are responsible for PL quenching. We further propose surface defect states and molecular seld-dopants as possible candidates for such states. Finally, the molecular self-dopants are shown to considerably contribute to PL of solution-grown AC5-TMS single crystals.

5.1. Introduction

Current organic electroluminescent devices such as light-emitting diodes (OLEDs) and light-emitting transistors (OLETs) are based on organic highly-luminescent semiconductor materials. Despite their high internal quantum efficiencies, OLEDs typically suffer from limited light-outcoupling efficiencies because of light capturing in their layered structure.[1-2] Specifically, the random orientation of molecular transition dipole moments in the OLED emissive layer critically limits the light-outcoupling efficiency of OLEDs.[3-4] In-plane oriented transition dipole moments of molecules improve the out-coupling efficiency up to 30%, which was observed by characterization of the emissive layer via angular dependent photoluminescence (PL) collected from the emissive layer.[5]

Single crystals of thiophene-phenylene co-oligomers (TPCO) have demonstrated high potential for OLETs due to a unique combination of high charge mobility and excellent luminescence efficiency.[6-7] The attractive feature of organic single crystals is the perfect alignment of the molecules and hence their transition dipole moments, which might cause PL to be strongly polarized.[8-11] The effects of PL anisotropy in TPCO single crystals due to the dipole moments alignment and Davydov's splitting might be used to perform the color selected outcoupling from an individual OLET using a light polarizer.[9] Despite these interesting optical features, only a handful of studies have been published on the effective application of TPCO crystal PL anisotropy.

Typically, TPCOs are rod-like and crystallized in platy crystals, with their long molecular axis and hence the transition dipole moments oriented almost orthogonally to the crystal plate (the so-called edge-on orientation).[12] This leads in a strong light waveguiding effect so that nearly all luminescence is emitted from the crystals edges and defects.[12] However, if the molecules in the single-crystal plate are packed in the nearly face-on orientation, light-outcoupling could be strongly improved.[11] Such an inclination can be realized by using strongly polar [13] or bulky[14] terminal substituents attached to TPCOs. Specifically, bulky trimethylsilyl terminal groups resulted in a strong inclination of molecules in crystals with the 5,5′-diphyenyl-2,2′-bithiophene core.[14] The molecules in this crystal are inclined from the normal to the crystal plate by about 50°. As the result, stronger luminescence from such TPCO single crystal is expected to originate normally to the crystal plane, and this luminescence could be strongly polarized.

In this chapter, we analyze time-resolved polarization PL anisotropy in TPCO crystals based on 1,4-bis{5-[4-(trimethylsilyl)phenyl]thiophen-2-yl}benzene (AC5-TMS). Single crystals of AC5-TMS were grown using the physical vapor transport technique and from solution by the solvent-antisolvent crystallization. X-ray diffraction experiments indicated the nearly face-on orientation of the molecules to the largest crystal face, which corresponds to the basal crystal plane. PL was excited at the normal incidence and collected in the backward geometry in an inverted microscope. Regardless of the excitation polarization, PL is strongly polarized along the molecular backbone. However, quite surprisingly, PL induced by the excitation which is orthogonally polarized with respect to the molecular backbone exhibits much higher intensity as compared to the parallel one. Such an unexpected anisotropic feature is assigned to anisotropic PL quenching by dark states. We hypothesize that such dark states might originate from the near-surface defects and/or weakly luminescent molecular self-dopants; further analysis is clearly required to establish its exact origin.

5.2. Materials and Methods

Materials. Synthesis, sublimation and basic characterization of AC5-TMS (Figure 5.1)[15] with the batch codes[**] 396.019, 244.011 and 396.030 were performed at the Functional Materials for Organic Electronics and Photonics Lab at the Enikolopov Institute of Synthetic Polymer Materials (headed by Prof. S.A. Ponomarenko).
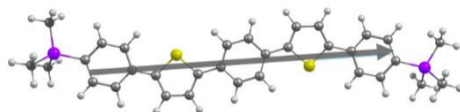
Figure 5.1. Molecular structure of AC5-TMS and its calculated transition dipole moment.

The transition dipole moment of an isolated AC5-TMS (Figure 5.1) was obtained from time-dependent density functional theory (TD-DFT) calculations at B3LYP/6-31g(d,p) level using the GAMESS package[16-17] (performed by A.Yu. Sosorev at the Lomonosov Moscow State University). The calculated transition dipole moment of

---

[**] The internal-use batch codes are provided here as a reference for the further generation of PhD students.

AC5-TMS molecule is directed from the near meta position of the carbon atom of the outer phenylene to the opposite one (Figure 5.1, gray arrow).

Crystals. AC5-TMS crystals growth was performed by D. Dominskiy and V. Konstantinov at the Organic Electronics Lab (headed by Prof. D.Yu. Paraschuk, the Lomonosov Moscow State University). AC5-TMS crystals were molecular self-doped by longer TPCOs during the chemical synthesis (see SI of Ref.18 for more details). AC5-TMS crystals with different self-doping levels were grown using solution growth by the solvent-antisolvent crystallization (similar to Ref.14) from the 396.030 batch of the material, and using vapor growth by the physical vapor transport (PVT) technique (similar as in Ref.18) from the 396.019 and 244.011 batches. Analisys of the self-doping level was performed by N. Surin at the Enikolopov Institute of Synthetic Polymeric Materials; the details can be found in Ref.18.

Optical imaging of the AC5-TMS crystals was implemented with a microscope (Zeiss AxioImager A2m) in the episcopic circular-polarized differential interference contrast (C-DIC) mode. Figure 5.2 shows images of two variously doped AC5-TMS single crystals with molar doping levels of 0.015±0.005% (a) and 0.2±0.02% (b). As discussed in Chapters 3 and 4, the PVT-grown crystals prepared from the purest source material are considered as the crystals with the lowest self-dopant concentration.
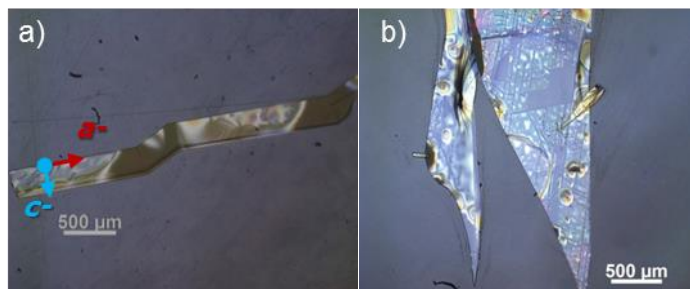
Figure 5.2. Micrographs of the PVT (a) and solution (b) grown AC5-TMS crystals prepared from the following batches: 396.019 (a) and 396.030 (b). In panel (a), the crystallographic c- and a-axes are superimposed to the image.

XRD characterization. X-ray diffraction experiments and the data analysis of the single crystal of AC5-TMS were performed by V.A. Tafeenko (Moscow State University) and T.V. Rybalova (Novosibirsk State University). According to the X-ray data, the crystal class is triclinic, and the space group is P1. The cell parameters

are as follows: a = 6.2686(2), b = 13.5181(5), c = 18.7693(6) Å, α = 103.156(3), β = 95.384(3), γ = 102.875°; V = 1492.21(9) Å^3, d_{calc}=1.199 g/cm^{-1}. There are two symmetrically independent molecules (Z=2) in the unit cell, designated as M1 and M2 (Figure 5.3a). The thiophene-phenylene 5-rings fragments of both molecules are planar. Figure 5.3b shows the herringbone packing motif (the angle between the planes of M1 and M2 is 52.5°), which is similar to that reported for other thiophene-phenylene co-oligomers.[12, 19] The Si atoms of trimethylsilyl groups belong to the (01-1) plane parallel to the largest crystal face (Figure 5.3c). The molecules are packed in layers, which thickness is about 12 Å. The crystallographic *a*-axis corresponds to the longest crystal edge.
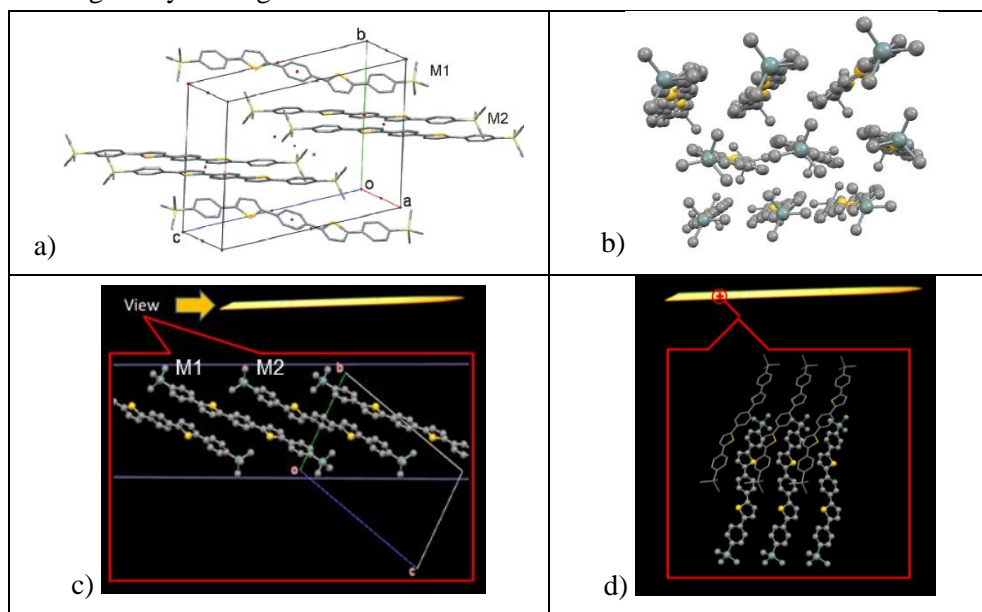
Figure 5.3. Molecular packing of AC5-TMS crystals. (a) the crystal unit cell (circumvented by the thin straight lines); six surrounding molecules are shown for illustration; (b) the herringbone arrangement of the molecules as viewed along the [001] direction; (c-d), top: an image of the crystal plate (top view); (c) as viewed along the longest crystal edge; one molecular layer marked by two horizontal blue lines is shown. Molecules are oriented face-on; they are inclined to the largest crystal face (01-1) with angles of 25° (M1) and 30°(M2); (d) as viewed normally to the largest crystal face (i.e., view along [01-1]). The figure is courtesy of M.S.Kazantsev (Novosibirsk State University).

Crystal surface characterization. The crystal surface was studied with an atomic-force microscopy (AFM, NTEGRA Spectra, NT-MDT) in the tapping mode (HQ Line Series HQ:XSC 11 cantilevers on chip, MicroMasch); the molecular steps are clearly observed (Figure 5.4). The height of each step is ~1.4 nm, which perfectly

corresponds to the thickness of one molecular layer calculated from the X-ray data (Figure 5.3c).
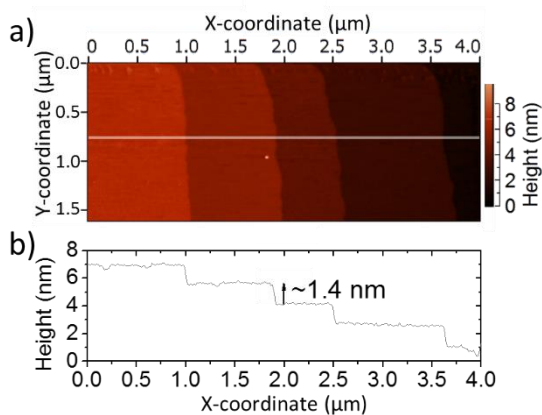
Figure 5.4. (a) AFM image of a PVT-grown AC5-TMS crystal (batch code 396.019) and the profile along the white line (b).

Photoluminescence measurements. PL quantum yield (QY) measurements were performed by V. Konstantinov (Organic Electronics Lab, Lomonosov Moscow State University). PL QY of the AC5-TMS PVT crystal (the batch code 396.019) was $26\pm5\%$.

Time-resolved PL was recorded by a streak camera (C5680, Hamamatsu) combined with a polychromator (250is, Chromex). The excitation pulses were generated by the doubled output of a Ti:sapphire laser (Coherent Mira) with the central wavelength of 400 nm (in several experiments 450 nm, Section 5.3.4). Time-resolved PL spectra of the crystals were collected at room temperature in an inverted microscope (Zeiss Axiovert 100) with a 10x, NA=0.25 objective. Figure 5.5 shows a typical microscope white field image of AC5-TMS crystal. The laser beam was focused on a sample surface to a diameter of ~4 μm (for details see Section 5.3.3). In all cases, the apparatus response was ~20 ps (Gaussian sd width).
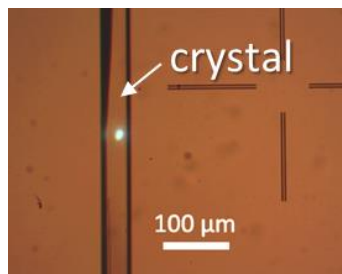
Figure 5.5. Micrograph of the PVT AC5-TMS crystal (looks like a stripe limited by vertical black shades) prepared from the 244.011 batch (molar doping levels of 0.04±0.03%) in the wide field. The blue spot represents PL produced by 400 nm laser excitation focused onto the crystal surface.

For polarization-resolved measurements, a quarter-wave plate (AQWP05M, Thorlabs) and a film polarizer were placed into the laser excitation beam (before the microscope) to control its polarization orientation (the excitation flux was adjusted as described below in Section 5.2), and another film polarizer was placed before the polychromator to control the PL polarization. To check the polarization sensitivity of the experimental setup, an amorphous conjugated polymer film was used. It is known that energy migration effectively randomizes the PL polarization in MEH-PPV spin-cast films within a few picoseconds[20] so that any memory of the excitation polarization orientation is lost within the apparatus response of the streak-camera. According to Figure 5d and 6d in Ref.20, PL of the MEH-PPV films does not depend on the excitation polarization and is isotropic in the spectral region of 2.0 – 3.0 eV. Instead of MEH-PPV, we used an even more disordered polymer, MDMO-PPV (with a longer and more branched alkyl side chain). Figure 5.6a demonstrates that energy migration and associated with its polarization scrambling in the MDMO-PPV spin-cast film occur within <50 ps (for the details of the experimental arrangement, see Chapter 3), i.e. much faster than the PL lifetime of 0.65 ns. Figure 5.6b-c shows angular polarization dependences of PL. The PL response of the MDMO-PPV spin-cast film is fully isotropic (b), and the PL intensity does not depend on the polarization of the excitation beam (c). Thus, the polarization response of the experimental setup is nearly isotropic, i.e. it is insensitive to the polarization orientation of the excitation beam nor to the PL polarization orientation.
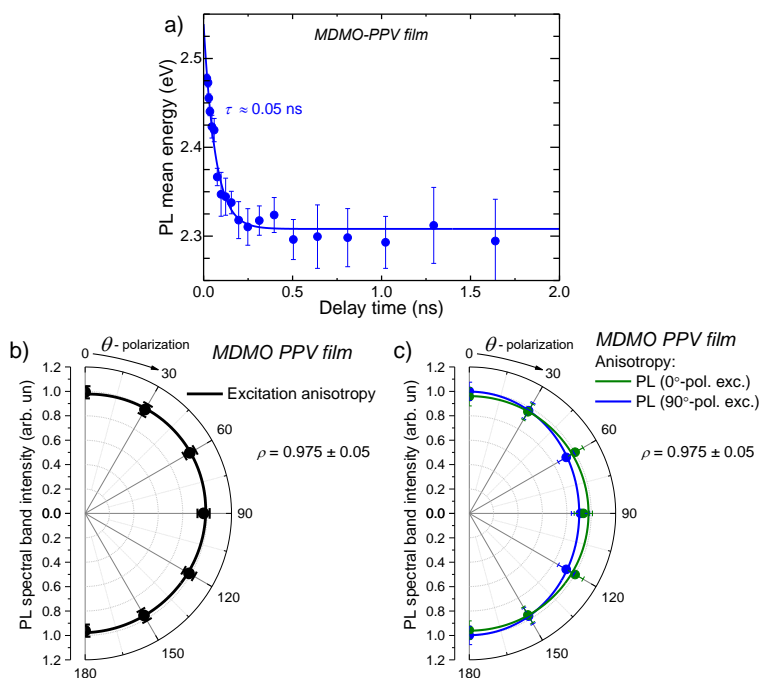
Figure 5.6. (a) Transients red shifts of the mean PL energy of a MDMO-PPV spin-cast film. The solid line is the monoexponential fit by a function $E = E_0 + \Delta E \cdot exp(-t/\tau)$. (b-c) Angular polarization dependences of PL intensities: non-polarized PL (dots) *vs.* the excitation polarization direction (b), PL intensities induced by two orthogonally polarized excitations (c). In each case, the PL intensities are normalized to unity. The lines are fits to the data by Equation 5.1 (see Section 5.3.1). The parameters of the fits are shown in the graphs. The incident excitation flux was set at 8 μJ/cm^2. The excitation wavelength was set at 400 nm.

Optical absorption and steady-state PL of AC5-TMS. Figure 5.7a shows absorption and PL spectra of AC5-TMS molecules dissolved in tetrahydrofuran (THF). The measurements were performed by N. Surin at the Enikolopov Institute of Synthetic Polymeric Materials as described in Ref.15 The excitation and PL spectra of the PVT crystal were measured with non-polarized light and without polarizing filters using a Perkin Elmer LS50B Luminescence Spectrometer (Figure 5.7b). Taking into account that the PL reabsorption might suppress the first high-frequency vibrational sub-band in the crystal, the PL spectra of the solution and the crystal have very similar shapes. The PL spectrum of the crystal is red-shifted by ~0.15 eV with respect to the solution, which is assigned to the higher polarizability

of the crystal matrix as compared to solution (the solid-state spectral shift). Further in this Chapter the excitation wavelength was set at 400 nm (except Section 5.3.4) to achieve efficient PL excitation in single crystals (Figure 5.7b).
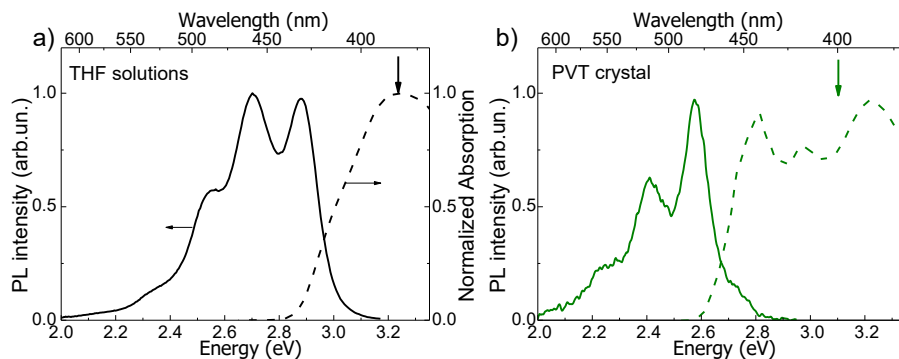
Figure 5.7. Optical properties of AC5-TMS in THF solution at a concentration of ~10^{-6} M (a) and in the PVT crystal prepared from the material with the batch code 396.019 (b); (a) absorption (dashed line) and PL (solid line) spectra, for which the excitation wavelength was set at 380 nm (the black downward arrow); (b) excitation (dashed line) and PL (solid line) spectra. For the excitation spectrum the detection wavelength was set at 550 nm, and for the PL spectrum the excitation wavelength was set at 400 nm (the green downward arrow). Note that the excitation spectrum is in the saturated regime due to strong absorbance of the crystal.

The PL lifetime of AC5-TMS in diluted THF solution (i.e. without interchromophore interactions) was measured as 1.0±0.1 ns (Figure 5.8).
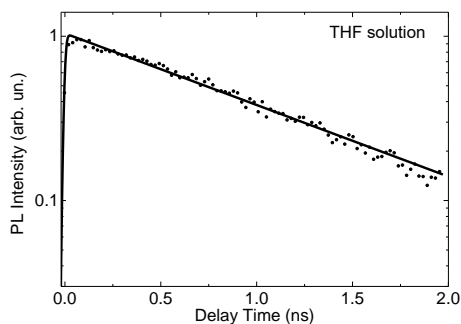
Figure 5.8. Normalized PL transient of AC5-TMS diluted solution in THF (concentration ~10^{-6} M). The PL transient was integrated over the spectral region of 2.0–3.2 eV. The line is a monoexponential fit convoluted with an apparatus response of 20 ps. The incident excitation flux was set at 8 µJ/cm^2. The excitation wavelength was set at 400 nm.

Refractive indices. In the solid state, resonant absorption of the molecules adds up to macroscopic polarization, which may have a significant effect on the optical

properties of the material such as high and anisotropic reflectivity.[21] In the 1970's, the reflectance spectroscopy revealed a wide band (>1 eV in width) of extremely high reflectivity in some molecular crystals.[22-24] The Kramers–Kronig analysis indicated that this reflectivity is due to a strong excitonic absorption band. Therefore, the possibility of such a scenario in AC5-TMS crystals should be considered as the transition dipole moments of the rod-like AC5-TMS molecules (Figure 5.1) have a nearly face-on orientation, i.e. form a small angle with the largest crystal face (Figure 5.3).

The reflectivities of a PVT crystal were measured in the microscope configuration at resonance (400 nm) and off-resonance (550 nm) excitation conditions for two polarizations (Table 5.1). The reflectivities at 550 nm were obtained with a broadband light generated by launching the Ti:sapphire output into a photonic crystal optical fiber (Newport, SCG-800) and selecting a part of the white-light continuum with a 20-nm bandwidth interference filter; the flux was set at 50 μJ/cm^2. Such an arrangement minimizes possible interference effects caused by reflections from both crystal surfaces [23]. For the off-resonance excitation, the corrections were also applied to account for multiple surface reflections[23] and the substrate reflection; these corrections are not needed for the resonant excitation because of high crystal absorption (for details, see below).

The off-resonance reflectivities of AC5-TMS crystal can be compared with the known refraction indices of other 5-ring TPCOs. For the AC5 crystal, the refractive index for light polarized normally to the molecular axis is 1.62 measured in the range of 500-600 nm,[24] and the refractive index for light polarized along to the molecular axis is 2.5 as calculated from the Sellmeier equation at 500 nm from Ref.25. This results in the corresponding reflectivity values of 6% and 18%. Analogously, from the spectroscopic ellipsometry data for another 5-ring TPCO with TTPTT conjugated core,[26] the calculated reflectivities at 500 nm for polarizations across and along the molecular axis amounted to 5% and 11%, correspondingly. These calculated reflectivities are in reasonable agreement with the data in Table 5.1.

Therefore, the single-surface optical transmissions of the excitation beam at 400 nm for the polarizations along the **c-** and **a-** axes are 70±5% and 92±5%, respectively, whereas the difference in transmission of the two PL polarizations (500-550 nm) is expected to be no more than 15%. Therefore, the excitation intensities and PL polarized along and across the projection of the transition dipole moment on the largest crystal face (plate) should be corrected for their reflectivities while the

correction of PL emerging at different polarization for the surface reflection is not necessary.

Table 5.1. Resonance and off-resonance reflectivity for the AC5-TMS crystal for the excitation polarizations oriented along *c-* and *a-* crystallographic axes.

Polarization direction	Resonance reflectivity (at 400 nm), %	Off-resonance reflectivity (at 550 nm), %
c- cryst. axis	30 ± 5	12 ± 5 [a)]
a- cryst. axis	8 ± 5	10 ± 5 [a)]

[a)] *Corrected for multiple reflection of the crystal and glass substrate reflection*

Absorption depth. To estimate the excitation density (i.e. the number of excitations per one molecule), we need to know the optical density (OD) of the AC5-TMS crystals. The OD is unavailable from direct transmission spectroscopy because the crystals are too optically thick. Therefore, we estimated the OD from the X-ray data and the extinction coefficient of AC5-TMS molecules in solution: $\varepsilon = 7 \cdot 10^4$ M^{-1}cm^{-1} at 400 nm[15] (neglecting intermolecular interactions). From the X-ray data, the density of molecules in crystal is $\sim 1.3 \cdot 10^{21}$ cm^{-3}, which corresponds to a cubic cell of ~ 0.91-nm size per molecule. As the molecules in AC5-TMS crystals are nearly aligned along *c-*crystallographic axis, the orientational factor[22] of 3 should be taken into account. In addition, the dipole moments of the molecules M1 and M2 in AC5-TMS unit cell (Figure 5.1 and 5.3) are inclined to the largest crystal face (01-1) with angles of 25° and 30° (i.e., a projection factor is $cos^2(25 \div 30°) \approx 0.75$). Thus, for the light normally incidental to the largest crystal face (01-1) with the polarization oriented nearly along the molecular backbones (*c-*polarized excitation, see Section 5.3.1), OD of AC5-TMS crystal of 1 µm thickness at 400 nm is estimated to be ~ 25, i.e. the absorption depth is ~ 20 nm (at a e^{-1} level).

The dipole moments of M1 and M2 molecules (Figure 5.1 and 5.3) are inclined to *a-* crystallographic axis with angles of 89° and 72° and to *c-*crystallographic axis with angles of 25° and 30° (flat angles). Therefore, for the light normally incident to the largest crystal face (01-1) with the polarization oriented along crystallographic *a-*axis (*a-*polarized excitation, see Section 5.3.1), optical absorption will be dominated by M2 molecule. As a result, the corresponding OD of AC5-TMS crystal is estimated to be at least by a factor of $cos^2(72°)/cos^2(30°) \approx 0.13$ lower than that for *c-*polarized excitation. As the estimated absorption depth for *c-*polarized

excitation (light) is ~20 nm at 400 nm, the absorption depth for *a*-polarized excitation is estimated to be ~150 nm.

Excitation intensity. To study PL polarization anisotropy in the AC5-TMS crystals, the excitation flux incident to a crystal surface was set at 8 μJ/cm^2, which is low enough to avoid non-linear effects; for details, see Section 5.3.3. Before any measurement, the excitation flux was carefully adjusted to 8 μJ/cm^2 to ensure direct comparison of the results. Considering the optical reflection losses, the *c*-polarized excitation flux of 8 μJ/cm^2 corresponds to the excitation density of ~5.0·10^{18} cm^{-3} in the AC5-TMS crystal, i.e. one excitation per ~6x6x6 nm^3 volume; the mean distance between the excitations is $d_{e-e} \approx 6$ nm. The same flux of the *a*-polarized excitation corresponds to the excitation density of ~6.5·10^{17} cm^{-3}, i.e. one excitation per ~11x11x11 nm^3 volume; the mean distance between the excitations is $d_{e-e} \approx 11$ nm.

5.3. Results and Discussion

5.3.1. Polarization-Resolved PL Data

The X-ray diffraction experiments (see Material and Methods, Section 5.2) on AC5-TMS crystal revealed the face-on orientation of the molecules relative to the crystal largest face which is illustrated in Figure 5.9a. Such molecular alignment is expected to result in strongly polarized PL with the polarization parallel to the transition dipole moments of the molecules.[8-10, 27] More precisely, according to the projections of the molecular transition dipole moments (Figure 5.9a) onto the largest crystal face, the PL polarization direction is expected to be oriented mostly along crystallographic *c*-axis.

The polarization-sensitive PL measurements were performed in such a way that the largest crystal face was always oriented orthogonally to the focused excitation beam, and PL was collected in the opposite direction (Figure 5.9b). In the experimental geometry, the 0°-orientations of the polarizer in the excitation beam path and the analyzer of the PL were assigned to the crystallographic *a*-axis (Figure 5.9), which lies in the largest crystal face; the polarization angle θ is counted clockwise. The projection of the crystallographic *c*-axis on the largest crystal face forms an angle of ~95° with the *a*-axis (Figure 5.9a). For the ease of discussion, we refer to the 0° and 90°-orientations of the polarizer (analyzer) as *a*- and *c*-polarized excitations (PL), respectively.

150
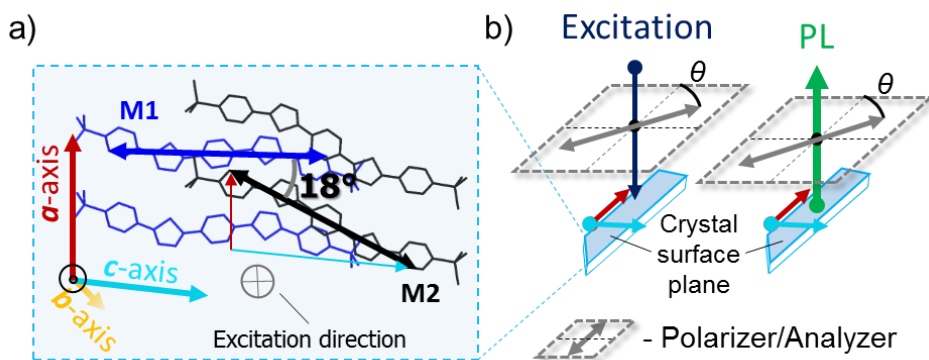
Figure 5.9. (a) Top view of the AC5-TMS molecular packing (for details, see Materials and Methods, Section 5.2). The plane of panel (a) corresponds to the largest crystal face (light blue shading). Symmetrically non-equivalent molecules M1 and M2 are depicted in blue and gray, respectively. The projections of the transition dipole moments of the M1 and M2 molecules (Materials and Methods, Section 5.2) onto the largest crystal face are shown as blue and black arrows. The red and cyan thin arrows in show the projections of the transition dipole moments of M2 onto the *a*- and *c*- crystallographic axes. The excitation beam is directed normally to the largest crystal surface face; (b) the polarization-resolved experimental geometry with respect to the crystallographic axes for the excitation (left) and PL detection (right). θ is the angle between the polarizations of the excitation beam or PL and the *a*-axis (red arrow), the cyan arrow in the figure is a projection of the crystallographic *c*-axis on the largest crystal face.

Angular polarization dependencies were obtained for a PVT crystal grown from the material with the batch code 244.011 (Section 5.3.1 and 5.3.7), and for a solution-grown crystal from the material with the batch code 396.030 (Section 5.3.7). PL spectra, transients and transient red-shifts of the PL mean energy presented in Results and Discussion were obtained for a PVT crystal grown from the material with batch code 396.019 (Sections 5.3.2 – 5.3.7), and for a solution-grown crystal from the material with the batch code 396.030 (Section 5.3.7).
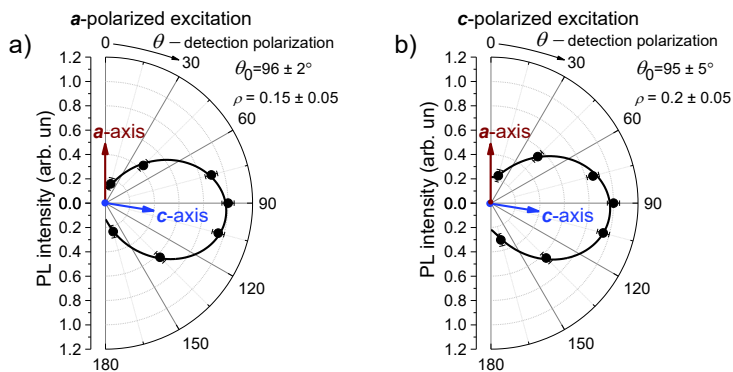
Figure 5.10. Angular polarization dependences of PL intensities (dots) induced by **a**- and **c**-polarized excitations in the PVT AC5-TMS crystal (batch code 244.011). In each case, the maximum PL intensity is normalized to unity. The solid lines are fits to the data by Equation 5.1; the parameters of the fits are shown in the graphs. The incident excitation flux was set at 8 µJ/cm^2. The excitation wavelength was set at 400 nm.

Figure 5.10 shows anisotropic PL properties of the PVT crystal where the PL data were collected for the **a**-polarized (panel a) and **c**-polarized (panel b) excitations. To obtain the polarization direction resulting in the maximal PL, the angular dependences were fitted by the following function:[10, 28]

$$F(\theta) = A \cdot cos^2(\theta - \theta_0) + B, \tag{5.1}$$

where θ is the polarization angle, A, B and θ_0 are the fitting parameters (θ_0 is the polarization angle where PL is maximal). From the fit of Equation 5.1, the PL polarization is mainly oriented along the crystallographic **c**-axis ($\theta_0 = 95 \pm 5°$) regardless of the excitation polarization. This result is perfectly in line with the expectations based on the molecular packing.

The polarization ratio was calculated as the following: [10, 28]

$$\rho = B / (A + B), \tag{5.2}$$

which quantifies the PL anisotropy and allows us to estimate the ratio of the transition dipole moment projections on the mutually ortogonal axes in the largest crystal plane (as mentioned earlier, these axes are close to the **a**- and **c**-crystallographic axes). From Figure 5.10, the ρ value is in the range of 0.15–0.2, which could be assigned to the nearly parallel orientation of the M1 and M2 in the AC5-TMS crystal (Figure 5.8a). This ratio is higher than $tan^2(18°/2) \approx 0.03$, which was calculated from the angle (18°) between the projections of the transition dipole moments of molecules M1 and M2 on the largest crystal face and assuming that the the ρ value corresponds to the sum of the corresponding PL intenisties

(Figure 5.9). This difference between the calculated and measrued ρ values could be attributed to a contrubution to PL from other species with different orientations of the transiton dipole moments (for details see Section 5.3.4 and Section 5.3.6).

Figure 5.11 shows the PL excitation anisotropy in the AC5-TMS PVT crystal. According to the molecular packing (Figure 5.9) and PL polarization data (Figure 5.10), the maximal PL is expected to be achieved at *c*-polarized excitation. Contrarily to this expectation, the PL intensity is *by a factor of 3 higher for the **a**-polarized excitation* as compared to the *c*-polarized excitation (Figure 5.11). Using the fit with Equation 5.1, we find that the excitation polarization direction of the highest PL is inclined by $\theta_0 = 2 \pm 5°$ to the *a*-axis, which significantly diverges from the direction of the transition dipole moments of M1 and M2 molecules ($\theta_{M1} \approx 91°$ and $\theta_{M2} \approx 109°$; Figure 5.9). Thus, the excitation polarization producing the maximum PL in the AC5-TMS crystal, is tilted by $90 \pm 10°$ with respect to the expected direction.
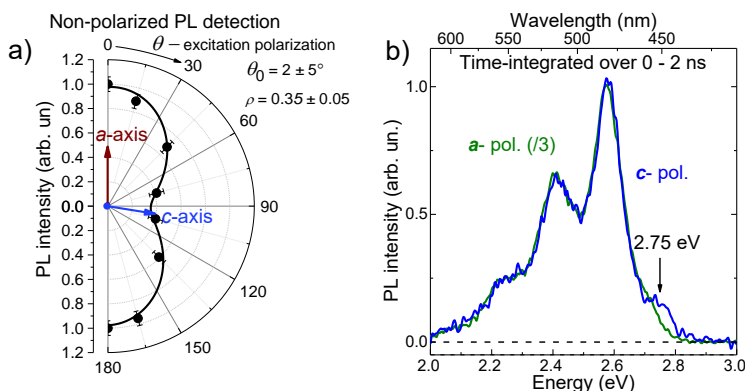
Figure 5.11. Nonpolarized PL anisotropy as a function of excitation polarization in the PVT AC5-TMS crystal (batch code 244.011). (a) Dependence of the non-polarized PL on the excitation polarization direction. The solid line in (a) is the fit to the data by Equation 5.1. The parameters of the fits are shown in the graph; (b) non-polarized PL spectra integrated over 0–2 ns time windows at *a*- (olive) and *c*-polarized (blue) excitations. The incident excitation flux was set at 8 $\mu J/cm^2$. The excitation wavelength was set at 400 nm.

5.3.2. PL Transients

To reveal the photophysics behind the surprising PL excitation anisotropy, we studied PL transients at *a*- and *c*-polarized excitations (Figure 5.12). Both PL transients demonstrate a bi-exponential behavior with the fast and slow exponential decays of 0.05–0.15 ns and 0.75–0.9 ns, respectively. The latter timescale is similar to the PL lifetime in diluted solution (1.0±0.1ns), while the former is attributed to PL quenching due to the presence of additional nonradiative relaxation channel. For the PL transient at the *c*-polarized excitation, the initial decay (i) is faster than the one at *a*-polarized excitation (0.05±0.02 *vs.* 0.15±0.01 ns) and (ii) has a larger share (0.85 *vs.* 0.5). This explains the unusual PL excitation anisotropy observed in the previous section: the *c*-polarized excitation with a higher absorption loses its energy much faster and more efficiently than the *a*-polarized excitation with a lower absorption (Section 5.2).
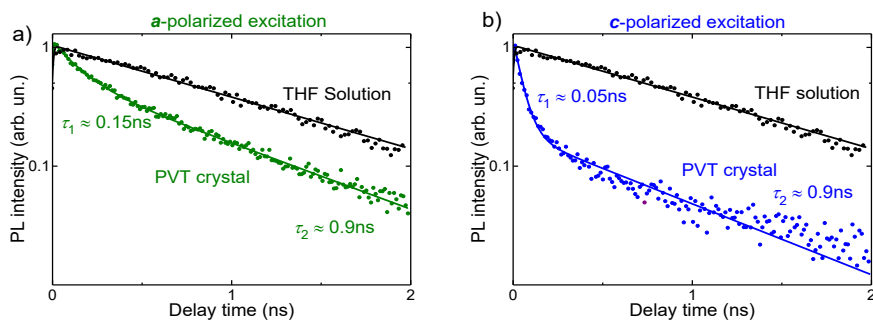
Figure 5.12. PL transients (dots) at *a*- (a) and *c*-polarized (b) excitations for the PVT AC5-TMS crystal (batch code 396.019). Olive and blue lines in are bi-exponential fits to the PL transients. The PL transient of AC5-TMS in diluted THF solution and the corresponding monoexponential fit are reproduced from Figure 5.8 for comparison. All spectra and transients are normalized to unity. PL detection was non-polarized. The incident excitation flux is 8 $\mu J/cm^2$; the excitation wavelength was set at 400 nm.

5.3.3. PL at Various Excitation Flux

Before building up a model that could account for our observations, we should verify experimentally if they originated (or not) from too high excitation power. Therefore, we studied time- and polarization-resolved PL data for a broad range of excitation fluxes of 4–200 $\mu J/cm^2$. To achieve such a flux range, the excitation peak power was tuned in the range 5–250 W by changing attenuation filters with various ODs, the

focal point of the microscope objective (~4 µm in diameter; ~12.5 µm^2 in area) was placed right onto the crystal surface. The excitation spot size was measured by imaging the laser beam focused on a silicon wafer placed in the objective focus.

We began our consideration from the short- (0–30 ps) and long-time (300–1000 ps) PL intensities as functions of excitation flux at the *a*- and *c*- polarized excitations (Figure 5.13). These time windows were selected according to bi-modal population relaxation (Figure 5.12a-b). For the excitation flux <20 µJ/cm^2, the short-time PL increases linearly with the excitation flux, while at higher excitation fluxes it begins to saturate. The saturation could be explained by a substantial share of the molecules being excited. However, the long-time PL intensity dependence is linear for all excitation fluxes.

The observed non-linear dependences of the PL intensities are well-described by a standard expression:[29]

$$I_{PL}(I_{exc}) = \frac{C \cdot I_{exc}}{1 + I_{exc} / I_{sat}}, \tag{5.3}$$

where I_{PL} is the PL intensity, I_{exc} and I_{sat} are excitation and excitation saturation fluxes, respectively, and C is a normalization coefficient. Fitting the data in Figure 5.13 by Equation 5.3 shows that, at *a*-polarized excitation, the saturation is achieved at almost twice higher excitation flux than that at *c*-polarized excitation (650 *vs.* 350 µJ/cm^2). This finding is qualitatively consistent with a shorter absorption depth for the *c*-polarized excitation (~20 nm) than for the *a*-polarized one (~150 nm; Section 5.2). The difference could be assigned to the inaccuracy in deriving the saturation intensities and the approximations used. In particular, it is possible that the saturation intensities defined by Equation 5.3 for a two-level system, are affected by depopulation of the excited state. Using the calculated I_{sat} at the *c*-polarized excitation, the excitation density is estimated as ~2.1·10^{20} cm^{-3} (i.e. the distance between the excitations is 1.7 nm), i.e. ~15% of molecules in the crystal are excited at 350 µJ/cm^2 flux. For the *a*-polarized excitation, the excitation density is estimated as ~0.8·10^{20} cm^{-3} (i.e. the distance between the excitations is 2.4 nm), i.e. ~5% of molecules in the crystal are excited at 650 µJ/cm^2 flux.
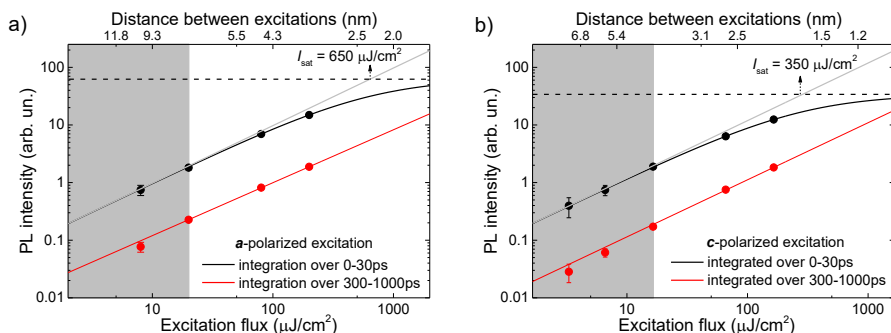
Figure 5.13. PL intensity (dots) averaged over the $0 - 30$ ps (black) and $300 - 1000$ ps (red) time windows at various excitation fluxes for a- (a) and c-polarized (b) excitations in the PVT AC5-TMS crystal (batch code 396.019). Vertical scaling between the panels is preserved. The black and red lines are fits with Equation 5.3. Gray lines represent low-flux asymptotes to highlight deviations from the linear regime. The dash lines show the PL intensity under the saturation flux. The top axes show the averaged distances between the excited molecules right after the excitation (for details see Section 5.2) considering different absorption depths for a- and c-polarized excitations (Section 5.2). The difference between the panels originates from the different absorption depths (extinction anisotropy) for the excitation beam polarized along the a- and c-axes. The shaded areas represent the range of the excitation fluxes at which the PL intensity depends linearly on the flux. The excitation wavelength was set at 400 nm.

Figure 5.14a-b shows PL transients for different excitation fluxes. The transients were fitted by bi-exponential functions; the resulted lifetimes and the shares of fast- and slow-exponent contributions are shown in panels (c,d) and (e,f), respectively. For the a-polarized excitation (Figure 5.14, left column) with increase of the excitation flux, the shares do not change (Figure 5.14e). The lifetime corresponding to the fast exponent slightly increases from 0.15 ± 0.02 to 0.23 ± 0.02 ns (Figure 5.14c), whereas the lifetime corresponding to the slow exponent remains at 0.85 ns within an experimental uncertainty of ±0.05 ns (Figure 5.14c). For the c-polarized excitation (Figure 5.14, right column), the lifetimes do not change with the excitation flux, similarly to the a-polarized excitation (Figure 5.14d), but the fast-time share decreases from 0.85 ± 0.05 to 0.7 ± 0.05 (Figure 5.14f). Thus, the increase in the c-polarized excitation flux leads to reduced PL quenching, whereas the increase in the flux of the a-polarized excitation affects the PL transients noticeably weaker.
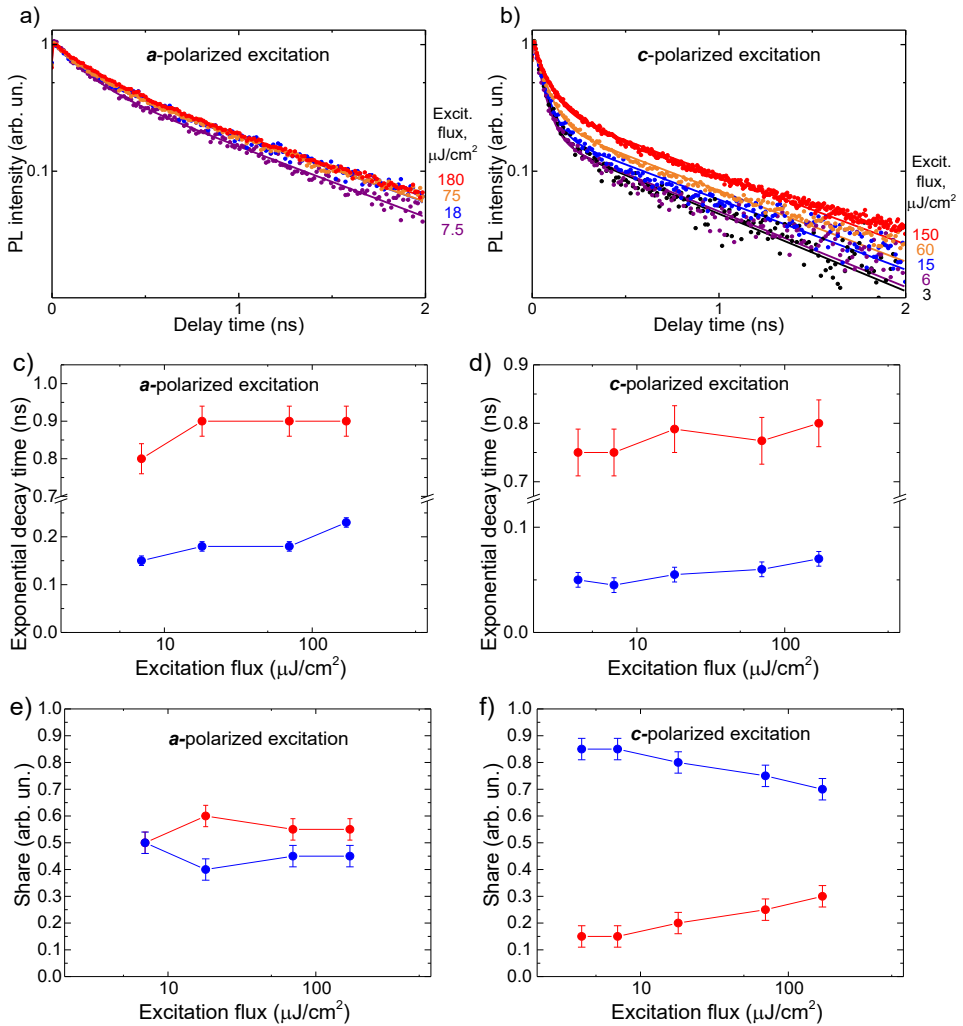
Figure 5.14. PL data for **a**- (left column) and **c**-polarized (right column) under various excitation fluxes in the PVT AC5-TMS crystal (batch code 396.019). PL detection was non-polarized. The PL transients (dots; normalized to unity) obtained by integrating over the full spectral region (2.0 – 3.0 eV) are shown in panel (a-b), the solid lines are bi-exponential fits. The short- (blue) and long- (red) PL lifetimes are plotted in panels (c-d), the shares of the short- and long- components obtained from the bi-exponential fits are shown in panels (e-f). The vertical bars indicate the uncertainty margins of the fits. The excitation wavelength was set at 400 nm.

5.3.4. Spectral Dynamics

To understand the energy landscape and probabilities of non-radiative transitions in AC5-TMS crystal, we performed the detailed analyses of the PL spectra and dynamics for the different excitation polarizations. Figure 5.15a-b show that the PL spectra originated from the *a-* and *c-*polarized excitation are slightly different. The difference comes from the band at 2.78 eV that is quite prominent at short times for PL originated from the *c-*polarized excitation and is almost absent for PL originated from the *a-*polarized excitation. Apart from this feature, the spectra are quite similar and their shapes do not substantially change with time. Therefore, we focus on the temporal behavior of the 2.78 eV band.

Figure 5.15c-d show the transients which reveal the dynamics of the aforementioned band as compared to the dynamics at the red flank of the spectra. The latter shows a bi-exponential decay similar to the one depicted in Figure 5.14a-b. However, the 2.78 eV band decays much faster, especially for the *c-*polarized excitation. This strongly suggests that for *the c-polarized excitation the long-time spectrum originates from a different species than the short-time spectrum*. All said is also applicable to the *a-*polarized excitation but to a lesser extent as follows from comparison of the transients in Figure 5.15c-d.

An insightful way of looking at the energy transition from one spectral species to others is to follow the mean PL energy in time (Figure 5.15e-f). Initially, PL originated from *c-*polarized excitation is blue-shifted as compared to its counterpart from the *a-*polarized excitation. However, as the time progresses, PL of the *c-*polarized excitation experiences a red shift of ~65 meV, while the PL produced by the *a-*polarized excitation exhibits the red shift of only ~30 meV. This is consistent with disappearance of the 2.78 eV band which has a lower amplitude for the *a-*polarized excitation.
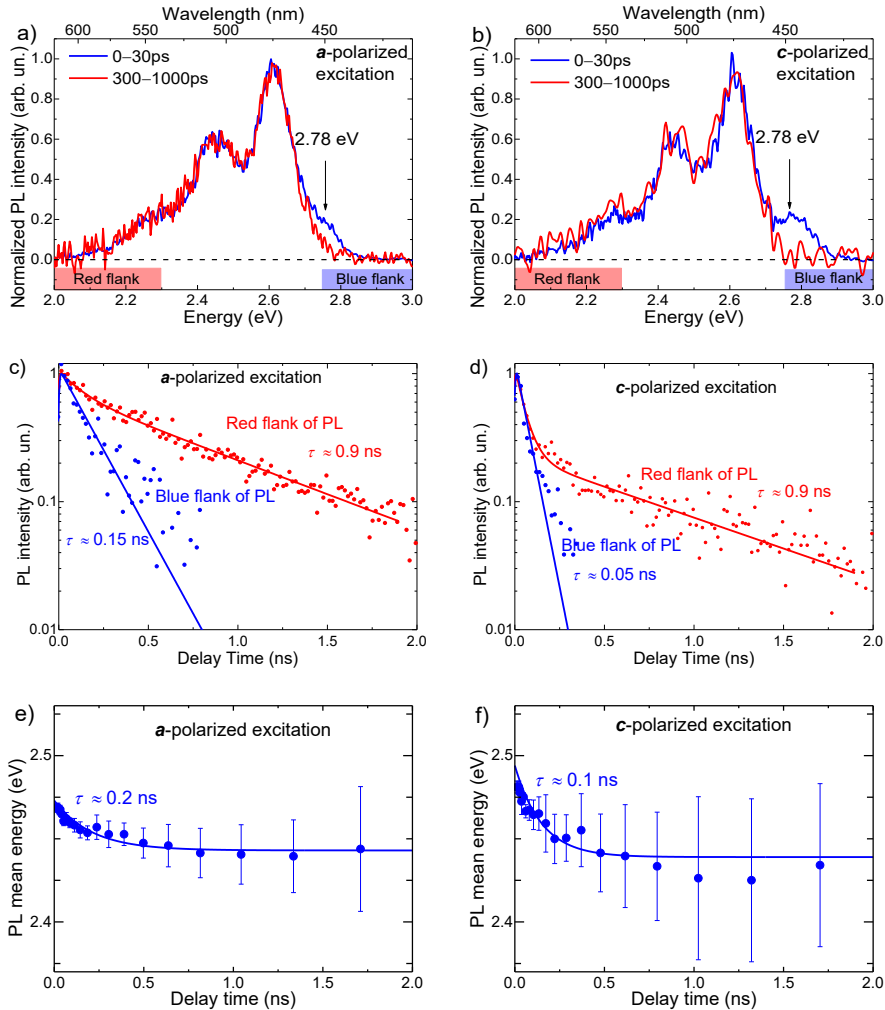
Figure 5.15. Time-resolved PL for the *a*- (left column) and *c*-polarized (right column) excitations in the PVT AC5-TMS crystal (batch code 396.019). (a-b) Time-resolved PL spectra integrated over 0–30 ps (blue) and 300–1000 ps (red) time windows. The detected PL is *c*-polarized, its intensities are normalized to unity. (c-d) The PL transients obtained by integrating over the blue flank (2.75–3.0 eV, the blue bar in panels (a, b) and over the red flank (2.0–2.3 eV, the red bar in panels a, b). The PL intensities are normalized to unity. The solid lines in panels (c-d) are mono- (blue) and bi- (red) exponential fits to the PL transients. (e-f) Transients red shifts of the mean PL energy. The solid lines in panel (e-f) are monoexponential fits by the function $E = E_0 + \Delta E \cdot exp(-t/\tau)$ with $\Delta E = 0.03 \pm 0.01$ eV (e) and $\Delta E = 0.065 \pm 0.02$ eV (f), for E_0 and τ values see the plots. The incident excitation flux is 8 µJ/cm^2; the excitation wavelength was set at 400 nm.

Finally, Figure 5.16 shows time-resolved PL induced by the excitation at 450 nm (2.76 eV) corresponding to the highest energy PL band (at 2.78 eV) of the AC5-TMS crystal. The intensity of PL originated from the 450 nm excitation is slightly higher for the c-polarized excitation as compared to the a-polarized one (Figure 5.16b). The stronger PL for the c-polarized excitation is expected from the molecular packing of AC5-TMS molecules in crystal (Section 5.3.1). This is in sharp contrast with the 400 nm excitation, where PL induced by the a-polarized excitation is by a factor of 3 higher than for that induced by the c-polarized excitation (Figure 5.11b).
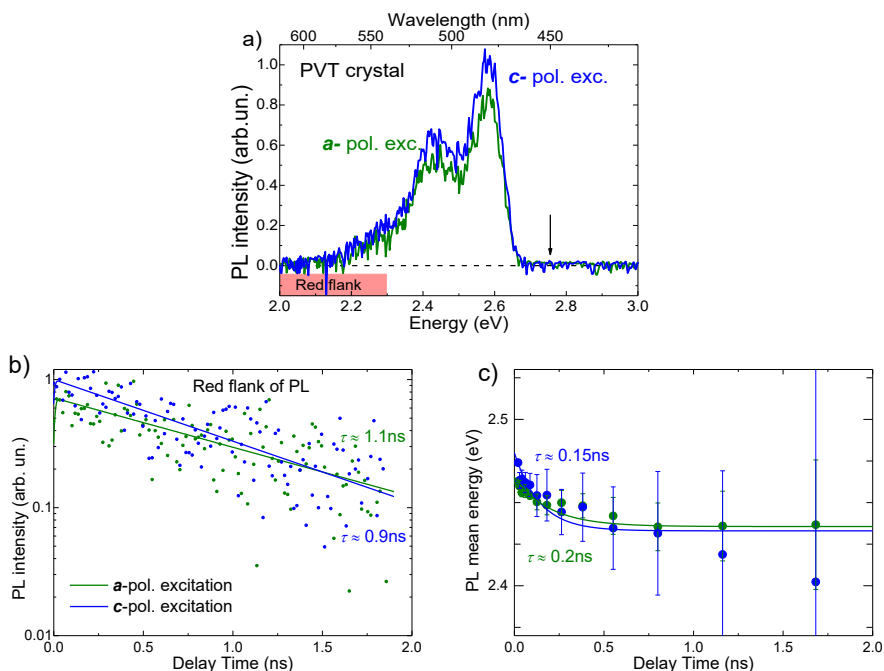
Figure 5.16. PL data for the PVT AC5-TMS crystal (batch code 396.019) recorded at the excitation wavelength of 450 nm. PL spectra (c-polarized) for the a-polarized (olive) and c-polarized (blue) excitations are shown in panel (a), where the black arrow demonstrates the excitation wavelength. The PL transients (dots) are plotted in panel (b), they are obtained by integrating over the red-flank as shown in panel (a). Scaling in panels (a, b) between the PL intensities is preserved. The solid lines in panel (b) are monoexponential fits to the transients. In panel (c), the corresponding transient red shifts of the mean PL energy are shown. The incident excitation flux was set at 2 μJ/cm^2 (because the laser source is not efficient at this wavelength). The solid lines in panel (b) are monoexponential fits by the function $E = E_0 + \Delta E \cdot exp(-t/\tau)$ with $\Delta E = 0.025 \pm 0.01$ eV (olive line) and $\Delta E = 0.045 \pm 0.02$ eV (blue line), for E_0 and τ values see the plots.

From comparison of PL transients recorded at the two excitation wavelengths (Figure 5.15c-f and Figure 5.16), it follows that there is no fast-decaying PL component at 450-nm-excitation, which is in line with the direct excitation of the yet unknown species corresponding to the long-time spectrum (Figure 5.15). From that we conclude that the PL lifetime of the long-living species is ~0.9 ns.

5.3.5. Model of Energy Relaxation

To develop a spectroscopic model which accounts for the results observed, we first summarize the most important findings:

1. PL is mainly *c*-polarized regardless of the excitation polarization (Figure 5.10).
2. The *a*-polarized excitation results in the PL intensity by a factor of 3 higher as compared to the *c*-polarized excitation (Figure 5.11).
3. The long-time PL spectra decay with a lifetime of ~0.85±0.15 ns regardless of the excitation polarization (Figure 5.12, Figure 5.14c-d and Figure 5.15c-d).
4. At the *c*-polarized excitation, 85% of PL decays with 0.05±0.02 ns time (Figure 5.14f at the excitation flux of 8 µJ/cm^2). In contrast, the decay at the *a*-polarized excitation is much longer (0.15±0.02 ns) and accounts for approximately 50% of initial PL (Figure 5.14e at the excitation flux of 8 µJ/cm^2).
5. PL depends on the excitation flux so that the more pronounced changes are observed for the *c*-polarized excitation. With increase of the excitation flux, the PL intensity begins to saturate at the short time scale (<30 ps), whereas the PL lifetime slightly increases at long times (>300 ps).
6. The mean PL energy shows a red-shift of 0.03±0.01 and 0.065±0.02 eV with time for *a*- and *c*-polarized excitation, respectively.
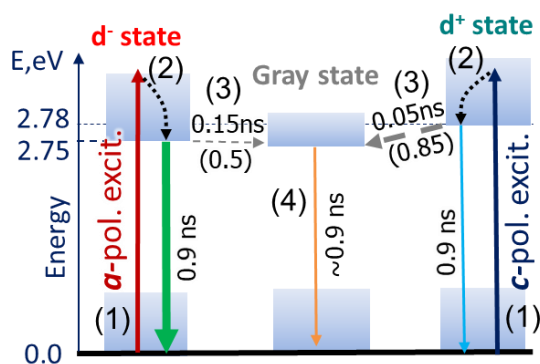
Figure 5.17. The energy level diagram. Energy levels of the ground, d-, d+ and gray states are shown as the gradient cyan bars, where the lower edge is assigned to be the bottom of a state. The following processes in the panel are shown: (1) a- and c-polarized excitations are depicted as the straight red and navy arrows, respectively; (2) dashed black arrows are non-radiative vibrational transitions to the bottom of the excited state. PL (the green and cyan arrows) originated from differently (a- and c-, respectively) polarized excitations with the corresponding PL lifetimes; (3) non-radiative transitions to the gray state are shown by the gray dashed arrows, their characteristic times and probabilities are depicted next to the arrows; (4) the gray state PL (the orange dashed arrow) with the experimentally determined lifetime (the calculated radiative lifetime is given in Table 5.2).

The points 4-6 clearly indicate that the photophysics in the AC5-TMS crystals involves more than one excited state species participating in the energy relaxation. Otherwise, we would observe monoexponential PL decays regardless the excitation wavelength, polarization, and intensity.[30, 31]

Figure 5.17 summarized energy levels in AC5-TMS crystal. This model is derived from the PL data: it includes d^- and d^+ states that populated by a- and c-polarized excitations, respectively, and the gray state. The model involves the following photophysical processes:

1.   The a- and c-polarized laser beam with the photon energy of 3.1 eV excites the d^- and d^+ states, respectively.

2.   The excitation follows non-radiative vibrational relaxation within the 100´s fs timescale to the bottom of the corresponding excited state.

3.   The d^- and d^+ states decay with lifetimes of ~0.15 ns and ~0.05 ns, respectively, mainly into the gray state, which produces the dominant contribution to PL. The d^- state lies ~0.035 eV lower than the d^+ state according to the PL mean energy just after a- and c-polarized excitations (Figure 5.15e-f); this value is also consistent with the Davydov splitting (Equation 5.4). The gray state lies slightly (by

162

~0.03 eV) lower than the d^- state according to the observed transient red-shifts of PL mean energy (Figure 5.15e). The transition dipole moment of the gray state is oriented almost collinearly with the transition dipole moment of the d^+ state which insures efficient energy transfer from it.

4. The radiative decay of the gray state results in the **c**-polarized PL with the excitation lifetime of ~0.9 ns.

5.3.6. Discussion

What exactly are the $d+$, $d-$ and gray states? We do not know exactly as yet. At this moment, we could only put forward a few hypotheses of their origin.
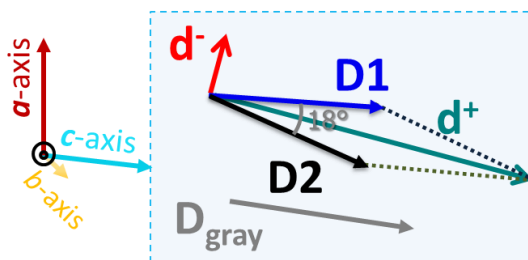
Figure 5.18. Orientations of transition dipole moments. **D1** and **D2** are projections of the transition dipole moments of M1 and M2 molecules (Section 5.2) onto the largest crystal face (01-1), respectively. Projections of the crystallographic axes onto the largest crystal face are depicted in the left. **D**$_{gray}$ is the transition dipole moment of an assumed *gray* state.

$d+$ and $d-$ states.

Figure 5.18 presents a model of orientations of transition dipole moments and energy levels in AC5-TMS crystal. The unit cell of AC5-TMS crystal contains two independent molecules with the transition dipole moments **D1** and **D2**. Their coupling generally forms two excited states[32-33] with transition dipole moments d^+ and d:[31-32] $d^+ = \frac{1}{\sqrt{2}}(D2 + D1)$ and $d^- = \frac{1}{\sqrt{2}}(D1 - D2)$. As $|D1| = |D2|$, the transition dipole moments d^+ and d^- are mutually orthogonal. d^+ is closely oriented to **c**- crystallographic axis, while the d^- dipole moment is closely oriented to **a**-axis as shown in Figure 5.18. Thus, due to better coupling of the co-oriented transition dipole moment and excitation polarization, the **a**-polarized excitation largely excites the d^- state, and the **c**-polarized excitation excites the d^+ state.

The excited states d^+ and d^- are shown in the energy diagram presented in Figure 5.17. The important parameter here is the Davydov splitting, i.e., the energy between the d^- and d^+ states, which can be estimated as [30, 34]

$$\hbar\Delta\omega = \frac{\mu_0{}^2 \cdot \gamma}{4\pi\epsilon_0 r^3} \approx 40 \text{ meV}, \tag{5.4}$$

where μ_0 is the transition dipole moment (~6 D), extracted from the DFT calculations of AC5-TMS, r is the distance between M1 and M2 molecules in AC5-TMS crystal, γ is the square root of orientation factor (~1.28, for details see Section 4.5.6). This theoretical result is similar to the experimental finding (40 vs 35 meV).

The Davydov splitting *per se*, however, does not explain the lower intensity of PL excited by the c-polarized light. Because of this, we need to assume an additional channel of non-radiative energy relaxation mostly operating at the c-polarized excitation. We assume that the PL red-shifts occurred to the same energy level regardless of excitation polarization (Figure 5.15e,f), are caused by energy transfer from the host AC5-TMS matrix to an energetically lower-lying emissive *gray* state with the transition dipole moment **D**~gray~ ("gray" here refers to its unknown origin, which is discussed in Section 5.3.6). Thus, the c-polarized excitation we assign the long-time spectrum to PL of the gray state, to which the energy is transferred from the host AC5-TMS matrix in 50 ps (Figure 5.15).

Molecular self-dopants (gray states). Chemical synthesis of TPCOs via cross-coupling reactions results in side products, amongst which there exist the so-called self-dopants[18] (Chapter 3) with a similar or longer conjugated length than the parent TPCO molecule. During the AC5-TMS synthetic route, a self-dopant with the chemical structure TPTTPT is likely to be formed.[15] The molecular lengths of TPTTPT and AC5-TMS are similar (Figure 5.19a), their molar mass are close (482 vs. 538 g/mol). As the result, TPTTPT could still be present in the source AC5-TMS material even after elaborate purification. Because of the longer conjugated length of the presumed self-dopant (TPTTPT, Figure 5.19) and hence its narrower optical gap (Table 5.2), the energy transfer from the host (AC5-TMS) to the self-dopant could occur via, e.g., the Förster resonant energy transfer, similarly to the one described in Chapter 3. Thus, is this scenario the weakly luminescent "gray" state results from a molecular self-dopant.

Table 5.2. Results of DFT calculations of AC5-TMS and TPTTPT molecules. E_{HOMO} and E_{LUMO} are energies of HOMO and LUMO (calculated via $E_{LUMO} = E_{HOMO} + E_g$, where E_g is the optical gap estimated from the intersection point of absorption and PL spectra), E_{S1} is an energy of excited S_1-state and t_r is the radiative lifetime of the molecule excitation. The calculations were performed at B3LYP/6-31g(d,p) level using GAMESS package [16-17] by M.K. Nuraliev and A.Yu. Sosorev at the Lomonosov Moscow State University.

	E_{HOMO}, eV	E_{LUMO}, eV	E_g, eV	E_{S1}, eV	t_r, ns
AC5-TMS	-4.95	-1.80	3.15	2.49	1.6
TPTTPT	-4.92	-1.84	3.08	2.29	2.0
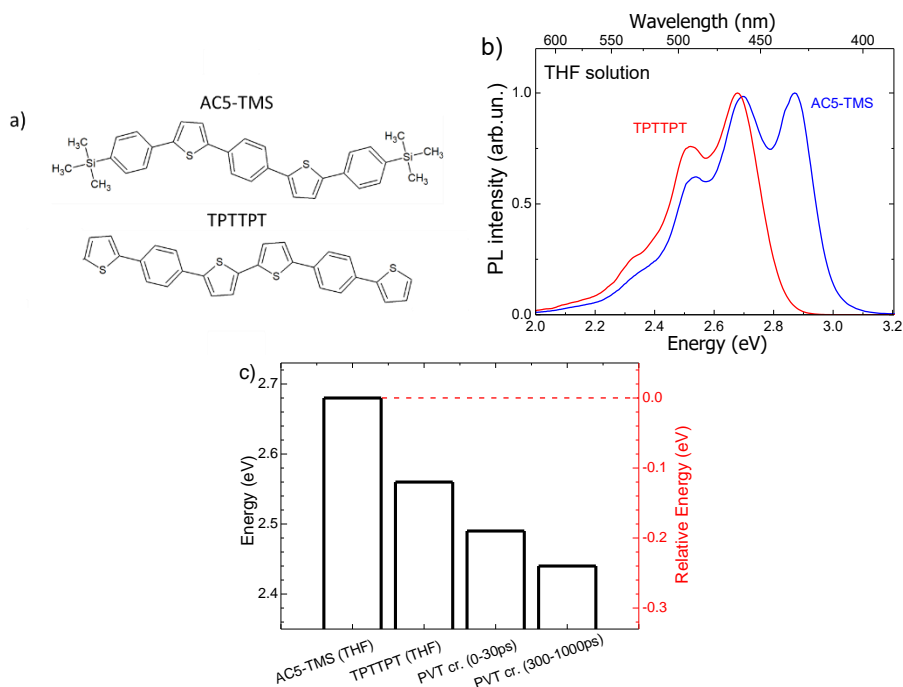
Figure 5.19. AC5-TMS and TPTTPT: (a) chemical structure, (b) the PL spectrum of AC5-TMS in diluted (10^{-5} M, blue) THF solution and the reconstructed PL spectrum of a molecular self-dopant (presumably, TPTTPT). The spectra are normalized to unity. The measurements and the reconstruction were performed by N. Surin (Enikolopov Institute of Synthetic Polymeric Materials) as described in Ref.15 The corresponding PL mean energies (c), those of the PVT crystal (batch code 396.019) are reproduced from Figure 5.15f. The right axis demonstrates PL mean energies of the samples with respect to that of the AC5-TMS solution.

The idea of self-doping is supported by the following arguments.

First, the optical gap of the self-dopant is narrower than that of AC5-TMS by 0.2 eV (E_{S1} in Table 5.2) which is consistent with the red shifted PL of the self-dopant (Figure 5.19b). Note that the absorption spectrum of the self-dopant is not available.

Second, the PL data are in line with the assumption of self-doping. The PL spectra of AC5-TMS and self-dopant in solution essentially differ from each other only in the blue spectral range, where PL of the self-dopant is much weaker than that of AC5-TMS (Figure 5.19b). This is fully consistent with the observation that the highest energy band– and only this sub-band – vanishes from PL of the AC5-TMS crystal in ~50 ps (Figure 5.15b). This sub-band is at 2.78 eV, which perfectly corresponds to the highest-energy PL band of AC5-TMS in solution at 2.84 eV, the energy difference of 0.06 eV should be assigned to the solid-state shift. The value of transient red shift of the PL mean energy (0.03–0.065 eV, Figure 5.15e,f) is in a reasonable correspondence with the difference of the PL mean energy between AC5-TMS and self-dopant in solution (0.12 eV, Figure 5.19c). Importantly, the PL transients excited at 450 nm show the monoexponential behavior (Figure 5.16b) which is in line with the direct self-dopant excitation (Figure 5.16).

Third, the MD modelling shows that the transition dipole moment of TPTTPT molecules embedded into the AC5-TMS crystal lattice is aligned nearly along the transition dipole moment of the host molecules (Figure 5.20). This should facilitate the energy transfer from the host (AC5-TMS crystal) to the self-dopant (TPTTPT). Furthermore, the energy transfer to the self-dopant affects the PL polarization ratio, i.e., ρ, expected from the X-ray diffraction results of the AC5-TMS crystal (Figure 5.3) to be ~0.03 (Section 5.2). The increase ρ up to 0.2 observed in Section 5.3.1 could be assigned to the contribution of PL originated from self-dopants inclined to the *c-* crystallographic axis (Figure 5.20).

Additional experiments are still needed to check this hypothesis. First of all, one needs a purer source material. Using much deeper purification of the source material by high-vacuum sublimation (which has not been done yet) and further crystal growth from the material by PVT are expected to result in much lower concentration of self-dopants. To support our assignment of the gray state to a molecular self-dopant, in the next section we present the results on solution-grown crystals, in which the effect of molecular self-doping is much more evident albeit the fact that the dopant molecules might be different.
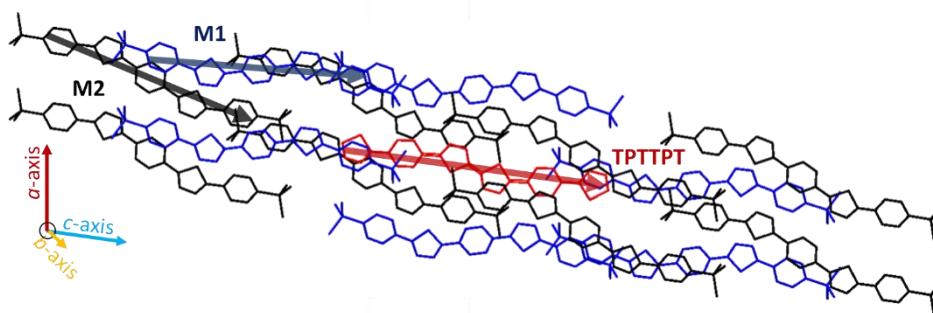
Figure 5.20. Modelling of an AC5-TMS crystalline aggregate simulated for 28 molecules, i.e. 7 for each layer (from the X-ray diffraction data, Section 5.2), where the TPTTPT molecule substitutes one central AC5-TMS molecule (M1 or M2). The atoms rearrangements were simulated using molecular dynamics in the "Avogadro: an open-source molecular builder and visualization tool" package.[35] The crystallographic *a-*, *b-* and *c-* axes of the AC5-TMS crystal are depicted on the left side. For better visibility, only 14 AC5-TMS molecules (our of 28 in the simulation box) are shown. The figure plane corresponds to the largest face of AC5-TMS crystal. Semitransparent arrows represent the transition dipole moments of the selected M1, M2 and TPTTPT molecules. For clarity, the methyl groups are omitted in both panels.

Near-surface PL quenchers (dark states). Due to possible degradation of the near-crystal surface layer, e.g. under light, oxygen and/or moisture, defects are formed that could quench PL. Such defects — PL quenchers forming a dark state — could result from lifetime or/and photo degradation, which can be enhanced by ambient environment where the atmospheric oxygen diffuses in the near surface layer. Then the photoexcitation could activate its photooxidation. We faced similar issue of the photoinduced defects in Chapter 2, where we had to scan the excitation spot over the organic thin film to avoid fast photodegradation. Such PL quenchers could extend to a few or even tens of nm beneath the surface, making this depth comparable with the penetration (absorption) depth of *c-*polarized excitation (~20 nm).

This hypothesis is based on the following findings: i) the energy relaxation from the d^+ state (*c-*polarized excitation) is more efficient for than that from the d^- state (*a-*polarized excitation); however, the faster energy transfer from d^+ state does not result in higher *c-*polarized PL. Therefore, this might be considered as different PL quenching efficiency caused by different excitation distribution beneath the crystal surface due to different penetration depths of *a-* and *c-* polarized excitations (Section 5.2); ii) the increase of the excitation flux decreases PL quenching for *c-*polarized

excitation (Figure 5.14) because the major part of PL quenchers in the near-surface layer have been already excited due to energy transfer from the d^+ state.

To verify this hypothesis, an additional experimental set of measurements in the oxygen free environment is needed. Moreover, one needs to minimize the contact of freshly grown PVT crystals with air and light. Repeating PL measurement with the same crystal after its deliberate exposure to the air environment would allow verification of this hypothesis.

5.3.7. Solution-grown Crystal

As shown in Chapter 4, energy transfer from the excitations originated in the host material to self-dopants modifies PL anisotropic properties of organic crystals. Time-resolved PL spectroscopy was shown to be sensitive to the 10's of ppm levels of self-doping in organic semiconductor crystals (Chapter 4). To evaluate the molecular self-doping effect on the PL properties, a solution-grown AC5-TMS crystal which underwent lower purification than the PVT crystal (see Section 5.2), was studied with the polarization-resolved PL measurements. According to the PL spectral reconstruction in THF solution (Figure 5.21), molecular self-dopant are present: the longer TPCO molecules (most probably AC8-TMS molecule as was suggested in Ref.18; see Figure S27) to which energy transfer might occur in the solution-grown crystal.
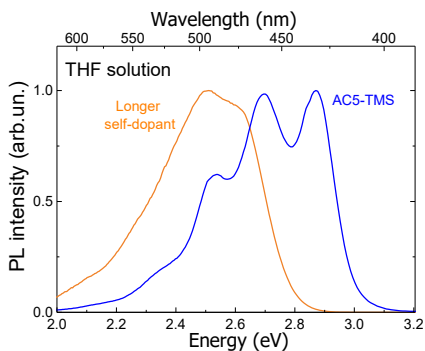
Figure 5.21. The PL spectrum of AC5-TMS (the batch code 396.030) recorded in diluted (10^{-5} M) solution (blue) and the reconstructed PL spectrum of a (presumably) AC8-TMS molecular self-dopant (orange). The spectra are normalized to unity. The concentration and PL QY of the AC8-TMS molecular self-dopant is estimated as $0.2\pm0.02\%$ and ~58%, respectively. The measurements and the reconstruction were performed by N. Surin (Enikolopov Institute of Synthetic Polymeric Materials) as described in Ref.15.

Figure 5.22 compares PL spectra integrated over 0–30 ps (a) and 300–1000 ps (b) time windows for the pair of the AC5-TMS crystals: the PVT (the batch code 396.019) and solution-grown (the batch code 396.030, with the highest self-doping level of 0.2±0.02% in the source material; for details see Section 5.2) crystal. Although spectral shapes are somewhat different for all time windows, the short-time spectra of the two crystals bear more resemblance that the long-time ones. For the latter, the total disappearance of the blue flank is quite obvious which should result in a larger temporal red shift.
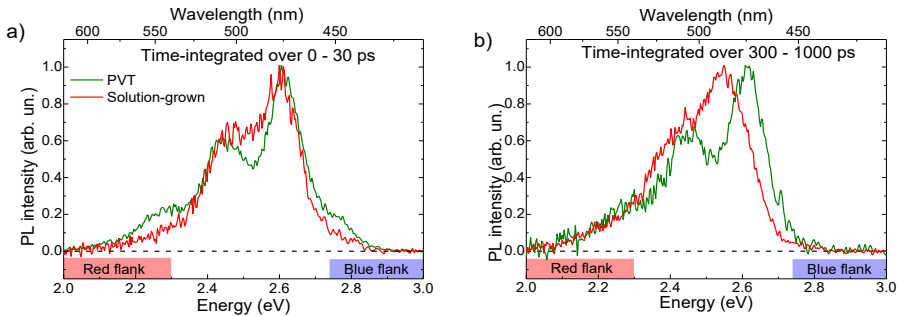
Figure 5.22. Time-resolved non-polarized PL spectra of the PVT (batch code 396.019) and solution grown (batch code 396.030) AC5-TMS crystals integrated over 0–30 ps (a) and 300–1000 ps (b) time windows. The PL intensities are normalized to unity. The incident excitation flux was set at 8 µJ/cm². The excitation wavelength was set at 400 nm.

For a deeper understanding of the energy transfer mechanism in AC5-TMS solution-grown crystal, we analyzed the PL features at the blue and red spectral flanks which were previously attributed to the host molecule and the long molecular self-dopant, respectively (Chapter 3). Figure 5.23 shows PL transients obtained by integrating over the blue-flank and red-flank PL spectral regions for the solution-grown crystal PL induced by the *a*- and *c*- polarized excitations. The solution-grown crystal showed a slower PL decay at the blue spectral flank with respect to the PVT one (Figure 5.15c-d) indicating a slower host-dopant energy transfer. In the framework of the self-dopant hypothesis (see Section 5.3.6), this might be explained by a lower concentration of the short self-dopant (TPTTPT) in the solution-grown crystal as compared to the PVT-grown crystal. The TMS terminal groups increase the solubility so that the TPTTPT self-dopants are far less soluble and hence weakly embed in the structure of solution-grown crystals.[14]

The analysis of PL properties in the solution-grown crystal at the *a*- and *c*-polarized excitations brings us to the same conclusion as described for the PVT

crystal with one important difference: the PL at long times is stronger red-shifted with respect to PL in the PVT crystal (Figure 5.15e-f). This indicates energy transfer to the longer self-dopants (i.e. having a shorter energy band gap).
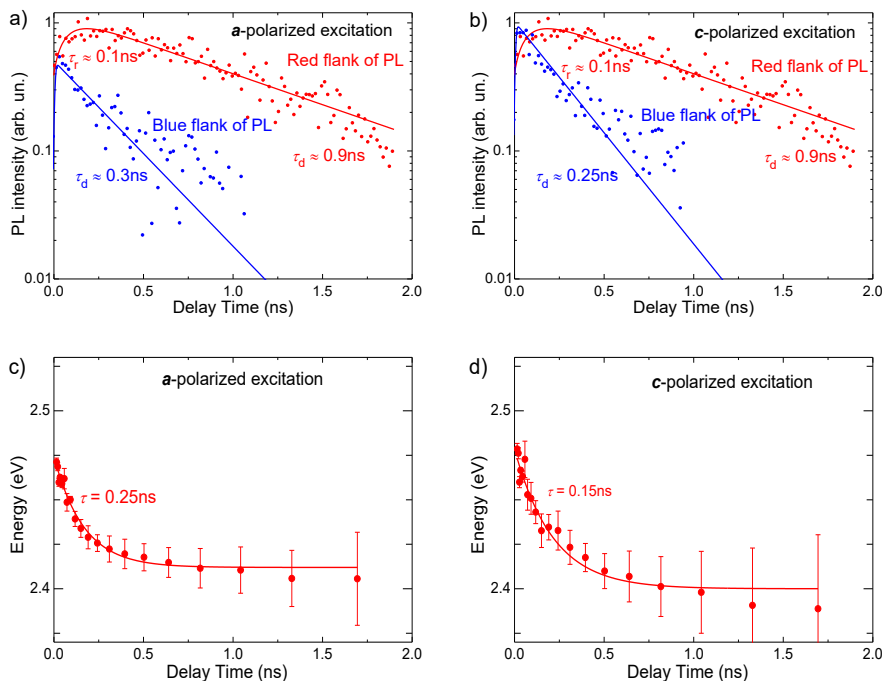
Figure 5.23. Transients of *c*-polarized PL of the solution-grown AC5-TMS crystal (batch code 396.030) at *a*- (left column) and *c*-polarized (right column) excitations. The PL transients are obtained by integrating over the blue flank (2.75–3.0 eV) and over the red flank (2.0–2.3 eV). Scaling between the PL intensities in panels (a) and (b) is preserved. The solid lines in panels (a-b) are mono- (blue) and bi- (red) exponential fits to the PL transients. In panel (c-d), the corresponding transient red shifts of the PL mean energy are shown. The solid lines in panel (c-d) are monoexponential fits by the function $E = E_0 + \Delta E \cdot exp(-t/\tau)$ with $\Delta E = 0.05 \pm 0.02$ eV (c) and $\Delta E = 0.08 \pm 0.02$ eV (d). The incident excitation flux was set at 8 μJ/cm^2. The excitation wavelength was set at 400 nm.
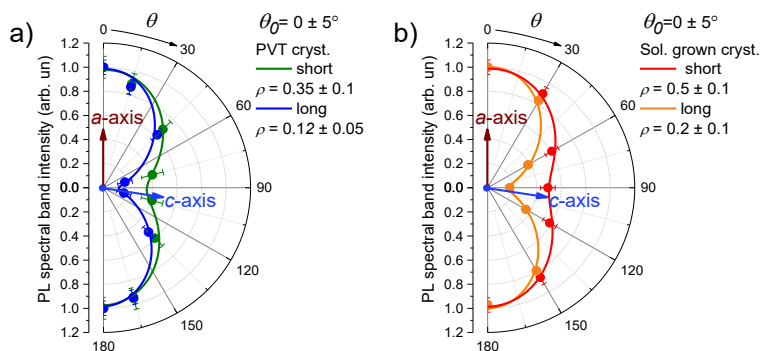
Figure 5.24. Non-polarized PL intensity as a function of the excitation polarization angle recorded at the short (0–30 ps) and long (300–1000 ps) time windows in the PVT (a; batch code 244.011) and solution grown (b; batch code 396.030) crystals. The solid lines are fits to the data by Equation 5.1. The parameters of the fits are shown in the graphs. The incident excitation flux was set at 8 $\mu J/cm^2$ at the wavelength of 400 nm.

Figure 5.24c-d demonstrate dependencies of non-polarized PL on the orientation of the excitation polarization at the short- and long-time windows for the PVT and solution grown crystals; the dependencies are quite similar for both crystals. The polarization ratio, ρ, increases with the time delay. Figure 5.25a-d shows angular polarization dependences of PL time-integrated over the short- and long-time windows for both crystals at *a-* and *c-*polarized excitations. For both crystals, the anisotropic PL properties are very similar.

The results discussed for the solution-grown crystal are quite similar to those described for the PVT crystal, with one difference: the solution-grown crystal is molecularly doped with presumably AC8-TMS molecules that seem to substitute the shorter dopant (presumably, TPTTPT) because of their different solubilities.
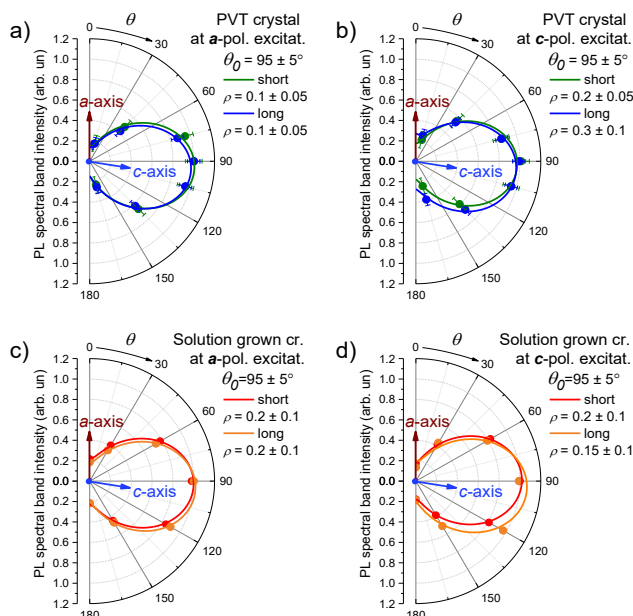
Figure 5.25. Angular polarization dependences of PL intensities induced by a-polarized (a,c) and c-polarized (b,d) excitations at the different time windows: 0–30 ps ("short", olive/red), and 300–1000 ps ("long", blue/orange), for the PVT (a-b; batch code 244.011) and solution grown (c-d; batch code 396.030) crystals. PL intensities are normalized to unity. The solid lines are fits by Equation 5.1. The incident excitation flux was set at 8 µJ/cm2. The excitation wavelength was set at 400 nm.

5.4. Conclusions

In this chapter, anisotropic PL polarization properties in TPCO crystal with the face-on orientation of the molecules with respect to the to the largest crystal face have been studied. In AC5-TMS crystals grown by the PVT method (from vapor), we have found that PL is polarized along the molecular backbones. However, PL induced by the excitation orthogonally polarized with respect to the molecular backbones unexpectedly exhibits much higher efficiency as compared to the parallel one. Blue and red flanks of time-resolved PL clearly show the biexponential behavior, which is characteristic for excitation energy transfer. We assigned this unexpected PL behavior to the presence of additional spices that results in the gray and dark states in the optical bandgap of the AC5-TMS crystal. We put forward the following hypotheses of their origin: molecular self-dopants (gray states) and crystal

surface PL quenchers (dark states). Both hypotheses have their pros and cons so that a number of experiments were proposed to verify them. The additional analyses on the AC5-TMS solution-grown crystals brought us to the similar conclusions as found for the PVT crystal, with one difference: the gray state PL is further red-shifted with respect to the one in the PVT crystal. This result seems to support the assignment of the gray state to the self-dopants. However, more detailed experiments and further analyses on PL polarization anisotropy of AC5-TMS crystals are still needed.

5.5. References

1. Koh, T.-W.; Spechler, J. A.; Lee, K. M.; Arnold, C. B.; Rand, B. P., Enhanced Outcoupling in Organic Light-Emitting Diodes via a High-Index Contrast Scattering Layer. *ACS Photonics* **2015**, *2*, 1366-1372.
2. Jou, J.-H.; Kumar, S.; Agrawal, A.; Li, T.-H.; Sahoo, S., Approaches for Fabricating High Efficiency Organic Light Emitting Diodes. *J. Mater. Chem. C* **2015**, *3*, 2974-3002.
3. Kim, J.-S.; Ho, P. K. H.; Greenham, N. C.; Friend, R. H., Electroluminescence Emission Pattern of Organic Light-Emitting Diodes: Implications for Device Efficiency Calculations. *J. Appl. Phys.* **2000**, *88*, 1073-1081.
4. Gu, G.; Garbuzov, D. Z.; Burrows, P. E.; Venkatesh, S.; Forrest, S. R.; Thompson, M. E., High-External-Quantum-Efficiency Organic Light-Emitting Devices. *Opt. Lett.* **1997**, *22*, 396-398.
5. Mayr, C.; Schmidt, T. D.; Brütting, W., High-Efficiency Fluorescent Organic Light-Emitting Diodes Enabled by Triplet-Triplet Annihilation and Horizontal Emitter Orientation. *Appl. Phys. Lett.* **2014**, *105*, 183304(4).
6. Muccini, M., A Bright Future for Organic Field-Effect Transistors. *Nat. Mater.* **2006**, *5*, 605-613.
7. Hotta, S.; Yamao, T.; Bisri, S. Z.; Takenobu, T.; Iwasa, Y., Organic Single-Crystal Light-Emitting Field-Effect Transistors. *J. Mater. Chem. C* **2014**, *2*, 965-980.
8. Qu, S.; Lu, Q.; Wu, S.; Wang, L.; Liu, X., Two Dimensional Directed Π–Π Interactions in a Linear Shaped Bi-1,3,4-Oxadiazole Derivative to Achieve Organic Single Crystal with Highly Polarized Fluorescence and Amplified Spontaneous Emissions. *J. Mater. Chem.* **2012**, *22*, 24605-24609.
9. Yomogida, Y.; Sakai, H.; Sawabe, K.; Gocho, S.; Bisri, S. Z.; Nakanotani, H.; Adachi, C.; Hasobe, T.; Iwasa, Y.; Takenobu, T., Multi-Color Light-Emitting Transistors Composed of Organic Single Crystals. *Org. Electron.* **2013**, *14*, 2737-2742.
10. Wang, M.; Gong, Y.; Alzina, F.; Sotomayor Torres, C. M.; Li, H.; Zhang, Z.; He, J., Angle-Dependent Photoluminescence Spectroscopy of Solution-Processed Organic Semiconducting Nanobelts. *J. Phys. Chem. C* **2017**, *121*, 12441-12446.
11. Goto, K.; Yamashita, K.; Yanagi, H.; Yamao, T.; Hotta, S., Strong Exciton-Photon Coupling in Organic Single Crystal Microcavity with High Molecular Orientation. *Appl. Phys. Lett.* **2016**, *109*, 061101(5).

12.   Hotta, S.; Yamao, T., The Thiophene/Phenylene Co-Oligomers: Exotic Molecular Semiconductors Integrating High-Performance Electronic and Optical Functionalities. *J. Mater. Chem.* **2011**, *21*, 1295-1304.

13.   Mizuno, H., et al., Optically Pumped Lasing from Single Crystals of a Cyano-Substituted Thiophene/Phenylene Co-Oligomer. *Adv. Opt. Mater.* **2014**, *2*, 529-534.

14.   Postnikov, V. A., et al., Molecularly Smooth Single-Crystalline Films of Thiophene–Phenylene Co-Oligomers Grown at the Gas–Liquid Interface. *Cryst. Growth Des.* **2014**, *14*, 1726-1737.

15.   Starikova, T. Y.; Surin, N. M.; Borshchev, O. V.; Pisarev, S. A.; Svidchenko, E. A.; Fedorov, Y. V.; Ponomarenko, S. A., A Novel Highly Efficient Nanostructured Organosilicon Luminophore with Unusually Fast Photoluminescence. *J. Mater. Chem. C* **2016**, *4*, 4699-4708.

16.   Schmidt, M. W., et al., General Atomic and Molecular Electronic Structure System. *J. Comput. Chem.* **1993**, *14*, 1347-1363.

17.   Gordon, M. S.; Schmidt, M. W., Chapter 41 - Advances in Electronic Structure Theory: Gamess a Decade Later A2 - Dykstra, Clifford E. In *Theory and Applications of Computational Chemistry*, Frenking, G.; Kim, K. S.; Scuseria, G. E., Eds. Elsevier: Amsterdam, 2005; pp 1167-1189.

18.   Parashchuk, O. D.; Mannanov, A. A.; Konstantinov, V. G.; Dominskiy, D. I.; Surin, N. M.; Borshchev, O. V.; Ponomarenko, S. A.; Pshenichnikov, M. S.; Paraschuk, D. Y., Molecular Self-Doping Controls Luminescence of Pure Organic Single Crystals. *Adv. Funct. Mater.* **2018**, *28*, 1800116.

19.   Yamao, T.; Miki, T.; Akagami, H.; Nishimoto, Y.; Ota, S.; Hotta, S., Direct Formation of Thin Single Crystals of Organic Semiconductors onto a Substrate. *Chem. Mater.* **2007**, *19*, 3748-3753.

20.   Camposeo, A.; Pensack, R. D.; Moffa, M.; Fasano, V.; Altamura, D.; Giannini, C.; Pisignano, D.; Scholes, G. D., Anisotropic Conjugated Polymer Chain Conformation Tailors the Energy Migration in Nanofibers. *J. Am. Chem. Soc.* **2016**, *138*, 15497-15505.

21.   Weiser, G., Strong Exciton Polaritons in Anisotropic Crystals: Macroscopic Polarization and Exciton Properties. In *Photophysics of Molecular Materials*, Lanzani, G., Ed. Wiley-VCH Verlag GmbH & Co.: 2006; pp 429-496.

22.   Corry, B.; Jayatilaka, D.; Martinac, B.; Rigby, P., Determination of the Orientational Distribution and Orientation Factor for Transfer between Membrane-Bound Fluorophores Using a Confocal Microscope. *Biophys. J.* **2006**, *91*, 1032-1045.

23.   Jenkins, F. A.; White, H. E., *Fundamentals of Optics*; McGraw-Hill, 1976.

24.   Yamao, T.; Taniguchi, Y.; Yamamoto, K.; Miki, T.; Ota, S.; Hotta, S.; Goto, M.; Azumi, R., Anisotropic Refractive Indices of Organic Crystals of Thiophene/Phenylene Co-Oligomers Determined by Microspectroscopic Measurements. *Jpn. J. Appl. Phys.* **2007**, *46*, 7478-7482.

25.   Yamao, T.; Okuda, Y.; Makino, Y.; Hotta, S., Dispersion of the Refractive Indices of Thiophene/Phenylene Co-Oligomer Single Crystals. *J. Appl. Phys.* **2011**, *110*, 053113(7).

26.   Bruevich, V. V., et al., Large-Size Single-Crystal Oligothiophene-Based Monolayers for Field-Effect Transistors. *ACS Appl. Mater. Interfaces* **2019**, *11*, 6315-6324.

27.   Varghese, S., et al., Stimulated Resonance Raman Scattering and Laser Oscillation in Highly Emissive Distyrylbenzene-Based Molecular Crystals. *Adv. Mater.* **2012**, *24*, 6473-6478.

28.   Prutskij, T.; Percino, M. J.; Perova, T. S., Polarization Anisotropy of Photoluminescence from Triphenylamine-Based Molecular Single Crystals. *Cryst. Res. Technol.* **2013**, *48*, 1039-1043.

29.   Dorrington, A. A.; Jones, T. W.; Danehy, P. M., Photophysics of Laser Dye-Doped Polymer Membranes for Laser-Induced Fluorescence Photogrammetry. *Appl. Opt.* **2004**, *43*, 6629-6638.

30.   Lakowicz, J. R., Energy Transfer. In *Principles of Fluorescence Spectroscopy*, Lakowicz, J. R., Ed. Springer US: Boston, MA, 2006; pp 443-475.

31.   Lanzani, G., *The Photophysics Behind Photovoltaics and Photonics*; Wiley-VCH: Weinheim, Germany, 2012.

32.   Davydov, A. S., The Theory of Molecular Excitons. *Soviet Physics Uspekhi* **1964**, *7*, 145-178.

33.   Gierschner, J.; Park, S. Y., Luminescent Distyrylbenzenes: Tailoring Molecular Structure and Crystalline Morphology. *J. Mater. Chem. C* **2013**, *1*, 5818-5832.

34.   Delport, G.; Vialla, F.; Roquelet, C.; Campidelli, S.; Voisin, C.; Lauret, J.-S., Davydov Splitting and Self-Organization in a Porphyrin Layer Noncovalently Attached to Single Wall Carbon Nanotubes. *Nano Lett.* **2017**, *17*, 6778-6782.

35.   Hanwell, M. D.; Curtis, D. E.; Lonie, D. C.; Vandermeersch, T.; Zurek, E.; Hutchison, G. R., Avogadro: An Advanced Semantic Chemical Editor, Visualization, and Analysis Platform. *J. Cheminf.* **2012**, *4*, 17.

Chapter 6. Luminescent Organic Semiconducting Langmuir Monolayers
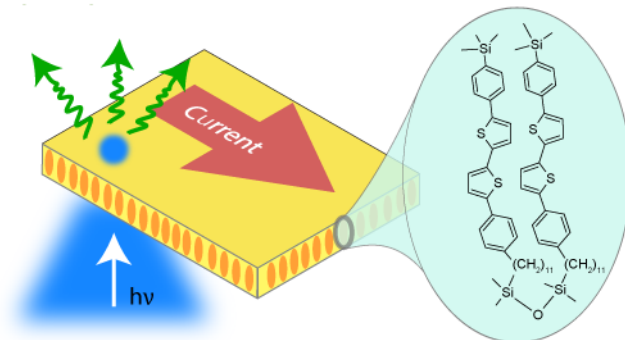
In recent years, monolayer organic field-effect devices such as transistors and sensors have demonstrated their high potential. In contrast, monolayer electroluminescent organic field-effect devices are still in their infancy. One of the key challenges here is to create such organic material that self-organizes in a monolayer and combines efficient charge transport with luminescence. Herein, we report a novel organosilicon derivative of oligothiophene-phenylene dimer D2-Und-P2TP-TMS (D2: tetramethyldisiloxane, Und: undecylenic spacer, P: 1,4-phenylene, T: 2,5-thiophene, TMS: trimethylsilyl) that meets these requirements. The self-assembled Langmuir monolayers of the dimer were investigated by steady-state and time-resolved photoluminescence spectroscopy, atomic force microscopy, X-ray reflectometry, grazing incidence X-ray diffraction, and their semiconducting properties were evaluated in organic field-effect transistors. We found that the best uniform, fully covered, highly ordered monolayers were semiconducting. Thus, the ordered 2D packing of conjugated organic molecules in the semiconducting Langmuir monolayer is compatible with its high-yield luminescence so that molecular 2D aggregation per se does not preclude highly luminescent properties. Our findings pave the way to rational design of functional materials for monolayer organic light-emitting transistors and other optoelectronic devices.

6.1. Introduction

Organic field-effect transistors form a general platform for the new generation of lightweight, flexible, and cheap electronics such as various sensors,[1-5] logic circuits,[6-8] photodetectors[9-11] etc. For light-emitting organic electronic devices, the planar OFET architecture is the most promising because it enables higher electroluminescent quantum efficiency of organic light-emitting transistors as compared to the already commercialized OLEDs.[12-14] This promise is still, however, to be fulfilled.

The electrical current in organic field-effect devices, such as OFETs and OLETs, flows within a few-nm thick surface layer of the active material adjacent to the dielectric; this fact drives the progress in monolayer organic electronics.[15-21] Ultrathin films are very beneficial for light-emitting field-effect devices as they are free of waveguiding effects that reduce the light output from thick light-emitting devices (OLEDs and OLETs). However, realization of electroluminescence in a monolayer device presents a formidable challenge.

One of the problems is molecular aggregation, which commonly results in luminescence quenching. Recently, Gholamrezaie *et al.* have shown that photoluminescence (PL) of a self-assembled oligothiophene monolayer dramatically decreases with the increase of the monolayer coverage (growth time).[22] Therefore, selection of appropriate organic molecules for efficient luminescent semiconducting monolayers is of the utmost importance. From the materials point of view, thiophene/phenylene co-oligomers (TPCO) based materials look attractive due to their success in single-crystal OLETs.[23-25]

As for monolayer device fabrication, Langmuir techniques are advantageous because they allow fast and robust self-assembly of organic semiconducting monolayers as a technological alternative to many hours long self-assembly from solution.[26] Organosilicon derivatives of oligothiophenes or benzothieno[3,2-b][1]-benzothiophene (BTBT) have demonstrated the best performance in Langmuir monolayer OFETs.[27-28] However, neither oligothiophenes nor BTBT show significant luminescence in films.

It should be noted that various Langmuir films with semiconducting or luminescent properties have been reported up to now. Typical luminescent Langmuir films can be prepared from the transition metal complexes[29], which, however, do not show any semiconducting properties. Albeit Langmuir technique was used earlier for preparation of thin films of quinquethiophene or poly(3-hexylthiophene) mixed

with arachidic acid at molar ratio of 60%/40% (because in pure form these materials do not form any Langmuir films) for organic light emitting diodes (i.e., for semiconducting and luminescent films), those films were not individual monolayers (contained from 3 to 45 monolayers) and showed extremely weak (<0.01%) electroluminescence quantum yield.[30-31]

Herein, we demonstrate that ordered 2D packing of organic conjugated molecules in a semiconducting Langmuir monolayer is compatible with its pronounced luminescence. Using a novel organosilicon derivative of a TPCO, we demonstrate that strong 2D molecular aggregation is not an obstacle for highly luminescent semiconducting monolayers, and the PL quantum yield in the ordered 2D monolayer is considerably higher than that in a polycrystalline inhomogeneously 3D ordered spin-cast film.

6.2. Materials and Methods

The oligothiophene-phenylene dimer, 1,3-*bis*[11-(4-{5'-[4-(trimethylsilyl)phenyl]-2,2'-bithien-5-yl}phenyl)undecyl]-1,1,3,3-tetramethyldisiloxane, D2-Und-P2TP-TMS (Figure 6.1) was designed and synthesized as described in Ref. 32 Figure 6.2 shows D2-Und-P2TP-TMS absorption and PL spectra in diluted in THF solution (these spectra have been obtained in Ref. 32).
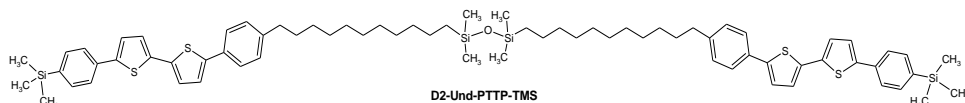

Figure 6.1. Chemical structure of the oligothiophene-phenylene dimer D2-Und-P2TP-TMS.
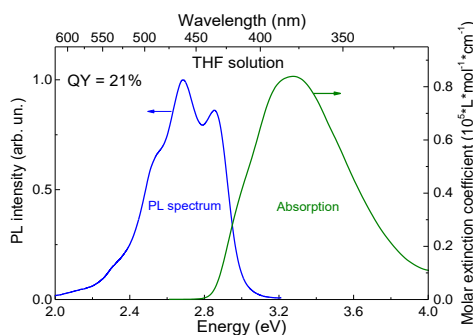

Figure 6.2. Absorption (green), and PL (blue, excitation at 3.3 eV) spectra of D2-Und-P2TP-TMS. The PL quantum yield was estimated to be 21±3%.[32]

The D2-Und-P2TP-TMS Langmuir-Blodgett (LB) and Langmuir-Schaefer (LS) films and monolayer LS OFET were prepared and characterized as it has been shown in Ref. 32. Note, the dielectric passivation of substrates with octyldimethylchlorosilane (ODMS) was applied to reduce the impact of surface traps. The semiconducting properties were found only in the LS monolayers deposited on the ODMS-treated substrate surface. LB deposition on ODMS-treated substrates was impossible due to their high surface hydrophobicity.

Spin-cast sample. For preparation D2-Und-P2TP-TMS spin-cast sample, D2-Und-P2TP-TMS material was dissolved in toluene with concentration of 1 g/L. The solution was spin-cast on a glass coverslip substrate at 400 rpm for 120 s.

Thin film characterization. The examination of films thickness and morphology was implemented with an atomic-force microscopy (NTEGRA Spectra, NT-MDT) in the tapping mode (HQ Line Series HQ:XSC 11 cantilevers on chip, MicroMasch). The spin-cast film thickness was measured with a surface profilometer (Dektak 6; stylus type with a radius of 12.5 μm and the force 3 mg).

Time-resolved photoluminescence. Time-resolved PL kinetics were measured by a streak camera (C5680, Hamamatsu) combined with a polychromator. The samples were excited at a wavelength of 375 nm (3.3 eV) for the diluted solution and 400 nm (3.1 eV) for the LS films and the spin-cast sample by 100 fs pulses produced by the doubled output of a Ti:sapphire laser combined with a 1.9 MHz pulse picker (Coherent Mira). For the diluted solution, the time-resolved PL collected in the 90°-geometry using a 360 nm longpass filter (SCHOTT WG360). For the LS films and the spin-cast sample, their time-resolved PL were collected by the inverted microscope (Zeiss Axiovert 100) with a 10x, NA=0.25 objective, and a 425-nm longpass dichroic beamsplitter (Chroma T425lpxr); the excitation spot size was ~5 μm in diameter. In all cases, the apparatus response function was ~7 ps. To avoid degradation under illumination, the solid samples were purged with nitrogen. All experiments were performed at room temperature.

6.3. Results and Discussion

To evaluate the PL efficiency in D2-Und-P2TP-TMS films, we recorded their PL spectra in the integrating sphere and calculated their PL quantum yield (QY). As a reference, we used a polycrystalline spin-cast D2-Und-P2TP-TMS sample, its optical microphotograph in cross-polarizers is shown in Figure 6.3a. The PL QY in the spin-cast sample was ~1.5% that is much lower than that in diluted THF solution

$(21\pm3\%)^{32}$. Supposedly, inhomogeneous 3D packing of D2-Und-P2TP-TMS in the spin-cast sample results in considerable PL quenching. In contrast, PL QY in LS films absorbing only 1.6±0.3% of light at 405 nm, was evaluated as 7±2%; therefore, the 2D LS film is much more luminescent than the 3D spin-cast film (the spin-cast sample height estimation is shown in Figure 6.3b). Thus, we conclude that strong 2D molecular aggregation does not prevent efficient luminescence in the semiconducting monolayers.
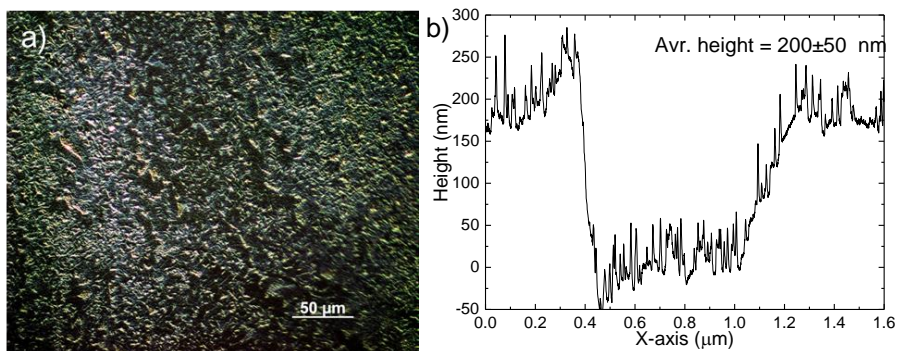
Figure 6.3. Optical microphotograph in cross-polarizers (a) and spin-cast sample depth profile (b) of a scratch on the surface (e.g. the scratch is located between 0.4 and 1.2 μm).

To highlight the effect of different packing of D2-Und-P2TP-TMS on its luminescent properties, we compared the PL time-resolved spectra in the annealed LS film, spin-cast sample, and diluted solution (Figure 6.4). The PL spectrum of the LS film is ~0.15 eV red-shifted as compared to that in solution (Figure 6.4a). The red shift indicates considerable intermolecular interactions in the LS film. PL of the LS film decayed biexponentially with two characteristic times of ~50 and ~420 ps (Figure 6.4b and Table 6.1). The former is attributed to PL self-quenching due to densely packed molecules in the film. The longer decay was close to that observed in diluted solution and hence is attributed to the excited state lifetime (Table 6.1). These results were independent of the substrate treatment by ODMS (Figure S6.1).
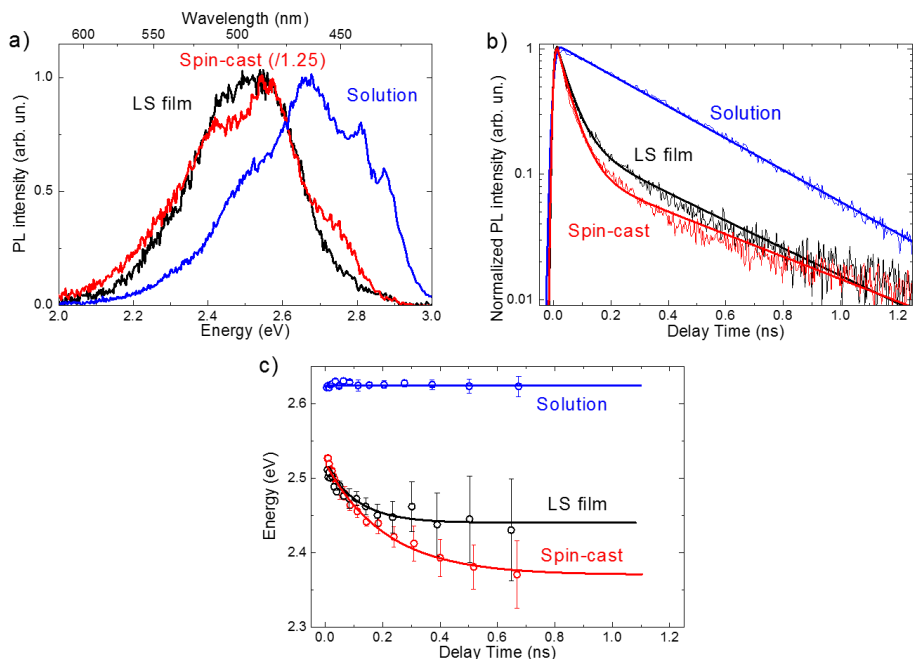
Figure 6.4. PL data on D2-Und-P2TP-TMS. PL spectra (a), time-resolved kinetics (b) and spectral diffusions (c) of the LS film (black), 5-g/L toluene solution (blue) and spin-cast sample (red). Scaling between the spectra of the LS film and the spin-cast sample is preserved; the spectrum of D2-Und-P2TP-TMS in toluene is arbitrarily normalized. The transients in (b) are obtained by integrating the PL time-resolved maps in the 2.0–3.0 eV spectral region, and normalized to their maxima. The solid lines are mono- or bi-exponential fits convoluted with the apparatus response ~7 ps; the corresponding fit parameters are given in Table 6.1. In (c), the time-dependent mean energy of the PL spectrum is shown together with monoexponential fits of $E = E_0 + \Delta E \cdot exp(-t/\tau)$ (for the solution: $E_0 = 2.62$ eV and no spectral shift is observed; for the LS film: $E_0 = 2.44$ eV, $\Delta E = 80\pm20$ meV, $\tau = 110\pm50$ ps; for the spin-cast film: $E_0 = 2.37$ eV, $\Delta E = 150\pm20$ meV, $\tau = 210\pm50$ ps).

The PL spectra of the LS film and the spin-cast sample (Figure 6.4a) are similar. The latter was slightly broader, which we assign to heterogeneous 3D packing as compared to the ordered 2D packing in the LS film. PL in the spin-cast sample decays with times similar to those of the LS film; however, the 45-ps component has a higher share. Spectral diffusion in the LS and spin-cast films is much stronger than in solution which is consistent with the model of thermally activated exciton hopping towards the low energy sites.[36,37] The magnitude of spectral diffusion in the LS film is noticeably lower as compared to the spin-cast sample (Figure 6.4c; 80±20 meV *vs.* 150±20 meV, respectively) in line with improved structural ordering of the LS film.

All these data strongly suggest that reduced PL self-quenching due to structural 2D ordering is the major factor enhancing PL in the LS film.

Table 6.1. Fitting parameters for the bi-exponential [$H_1 \cdot exp(-t/\tau_1) + H_2 \cdot exp(-t/\tau_2)$] function of the PL transients in Figures 6.2b, S6.4b and 6.7b. The sum of H_1 and H_2 is normalized to unity. The deviation margins are derived as uncertainty of the mean calculated over all individual transients.

D2-Und-P2TP-TMS samples	H_1	τ_1, ps	H_2	τ_2, ps
Diluted sample	-	-	1	350 ± 10
Spin-cast sample	0.90 ± 0.10	45 ± 10	0.10 ± 0.05	480 ± 20
LS film	0.80 ± 0.10	50 ± 10	0.20 ± 0.05	420 ± 20
LS ODMS film	0.80 ± 0.10	55 ± 10	0.20 ± 0.05	450 ± 20
LB film	0.75 ± 0.10	60 ± 10	0.25 ± 0.05	470 ± 20

Interestingly, the PL intensities in the LS film and the spin-cast sample are similar (refer to Figure 6.5 for statistics) despite the latter is a factor of ~50 thicker (the spin-cast sample profile in shown in Figure 6.3b). This is consistent with a considerably higher PL QY in the LS film as compared to the spin-cast sample. Therefore, our PL data clearly indicate that highly ordered 2D molecular packing of D2-Und-P2TP-TMS molecules is more beneficial for efficient PL than heterogeneous polycrystalline 3D packing in the spin-cast sample.
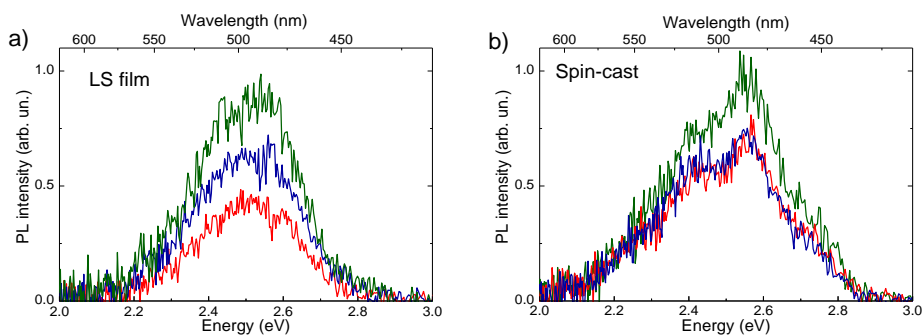
Figure 6.5. Statistics of measured PL spectra for LS (a) and spin-cast (b) samples. The PL spectra were measured from three different spots of each sample.

6.4. Conclusions

To sum up, we have synthesized and characterized novel tetramethyldisiloxane dimer D2-Und-P2TP-TMS, containing semiconducting oligothiophene-phenylene (P2TP) fragments, as it has been demonstrated in Ref. 32. The material was well-soluble in widely used organic solvents due to short P2TP core and terminal trimethylsilyl groups, and was highly stable allowing deposition of Langmuir monolayers at ambient laboratory conditions. We found that 2D packing influences the structure and luminescent properties of the monolayers deposited either vertically (LB) or horizontally (LS), the comparison of two types of films are demonstrated in Section 6.5.2. The better 2D ordered LS monolayers are both semiconducting and exhibiting prominent PL, which is significantly more efficient than the PL in the reference polycrystalline inhomogeneously 3D ordered spin-cast sample. The PL time-resolved spectra strongly suggest that reduced PL self-quenching due to 2D structural ordering is the major factor enhancing PL in the LS film.

Overall, we have demonstrated that Langmuir monolayers prepared from conjugated organic molecules can combine semiconducting properties and pronounced PL. These findings pave the way to the rational design of functional materials for monolayer organic light-emitting transistors and other optoelectronic devices.

Author Contributions

E.V.A. prepared and characterized Langmuir films, A.A.M. and O.V.K. performed time-resolved PL experiments, A.S.S. made AFM and electrical characterizations of the monolayer films, O.V. and O.V.B. synthesized the materials, A.V.B. and M.A.S. made XRD experiments, S.N.C. analyzed the XRD data, V.G.K. and V.V.D. measured the PL QY, O.V.K. prepared and analyzed spin-cast samples, M.S.P. planned and supervised the time-resolved PL experiments, D.Y.P. and S.A.P. supervised the project.

6.5. Supplementary Information

6.5.1. LS monolayer on ODMS-treated and standard silicon substrates
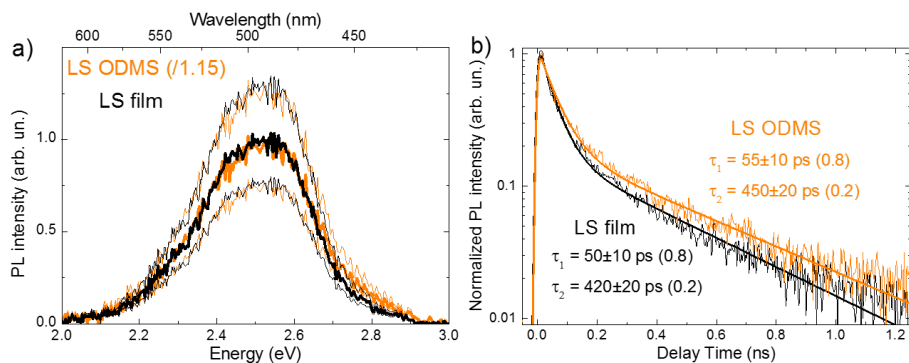
Figure S6.1. PL spectra (a), time-resolved kinetics (b) for LS films of D2-Und-P2TP-TMS prepared on bare (black, LS) and ODMS-treated (orange, LS ODMS) silicon substrates. In (a), scaling between the spectra of the LS film and the LS ODMS film is preserved. Thick lines in (a) indicate mean values resulted from averaging of several measurements; thin lines border the region within one standard deviation from the mean. The PL transients were obtained by integrating the PL time-resolved maps in the 2.0–3.0 eV spectral region, and normalized to their maxima. The solid lines in (b) are biexponential fits convoluted with an apparatus response ~7 ps; the corresponding decay times are shown next to the transients.
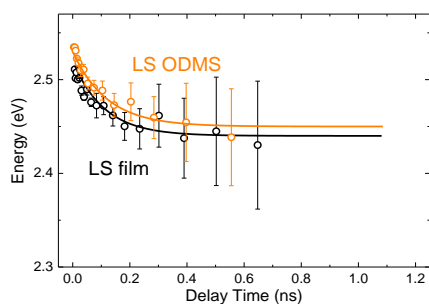
Figure S6.2. Thransient red-shifts of PL mean energy D2-Und-P2TP-TMS LS films prepared on bare (black, LS film) and ODMS-treated (orange, LS ODMS) silicon substrates. The time-dependent mean energy of the PL spectrum is shown together with monoexponential fits $E = E_0 + \Delta E \cdot exp(-t/\tau)$, where E_0 value was fixed (for LS film: $E_0 = 2.44$eV, $\Delta E = 90\pm20$ meV, $\tau = 110\pm50$ ps; for LS ODMS film: $E_0 = 2.45$eV, $\Delta E = 80\pm20$ meV, $\tau = 110\pm50$ ps).

6.5.2. LS *vs.* LB Films

D2-Und-P2TP-TMS monolayer films morphologies significantly dependent on deposition methods presumably affecting to their PL properties. To compare Langmuir-Blodgett (LB) and Langmuir-Schaefer (LS) monolayer deposition techniques, we investigated LB and LS films properties with AFM and ultrafast PL spectroscopy.
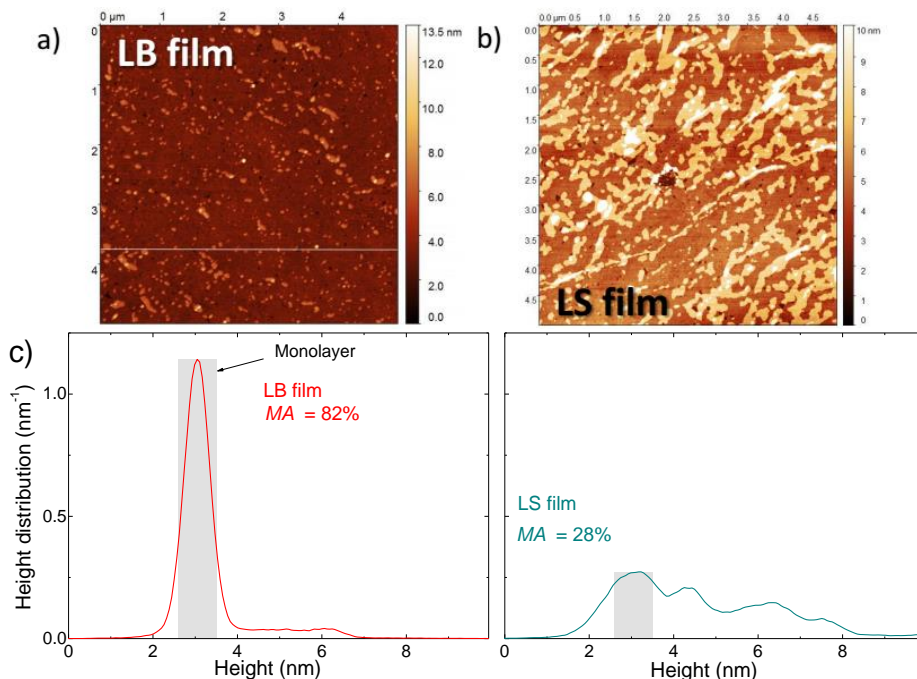
Figure S6.3. AFM data of the LB and LS films. AFM images of LB (a) and LS (b) D2-Und-P2TP-TMS films, and their height distribution (c, red and cyan lines, respectively); the estimated share *MA* (introduced below) of films are shown next to the height distribution.

The atomic force microscopy (AFM) data (Figure S6.3a-b) for LB and LS films confirmed that morphology of all these films is uniform and domainless with a fully covered bottom monolayer having thickness of 3.0-3.2 nm (Figure S6.3c). This value is in a good agreement with the theoretically calculated length of D2-Und-P2TP-TMS molecule in its closed conformation (35 Å), that corresponds to a vertical orientation of the P2TP units in the monolayer.[32] The film transfer at the surface pressure higher than the collapse pressure (33–35 mN/m) resulted in the appearance of multilayer areas that are not present in the films transferred before the monolayer

collapse. Solvent vapor annealing resulted in disappearance of the multilayers and increased the percentage of monolayer areas.[32] By "monolayer areas" (*MA*) we understand the areas with only monolayer coverage compared to the areas with bi- or polylayers. We assign this morphology change to molecular repacking that result in better ordering of the layer.
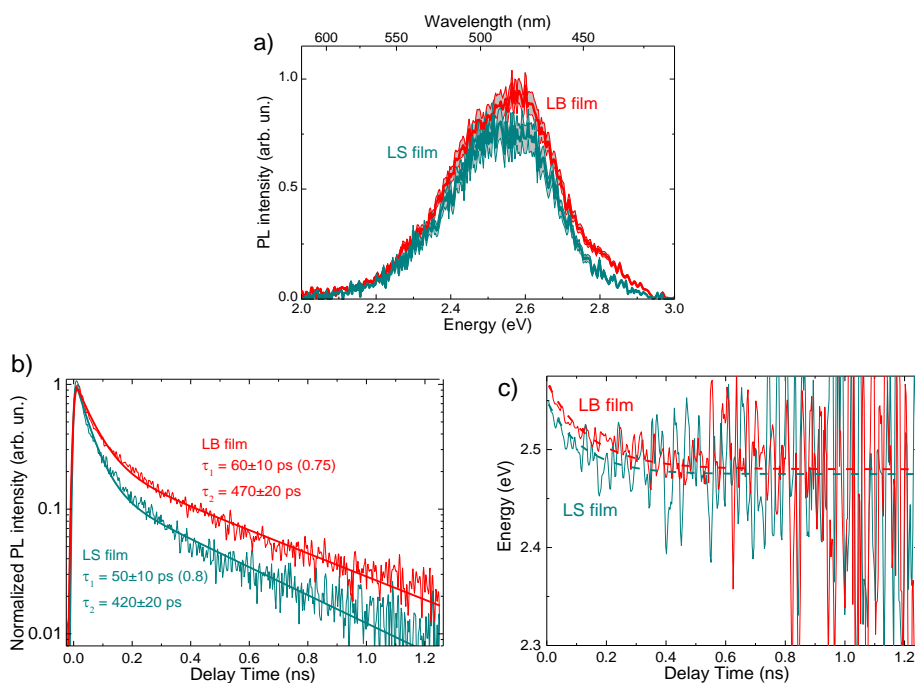
Figure S6.4. PL data of the LB and LS films. (a) The PL spectra are normalized to the maximum of the annealed LB film spectrum. Thick lines indicate the mean values resulted from averaging of several measurements, while thin lines show the region within one standard deviation (SD) from the mean. The transients in (b) were integrated over the $2.0 - 3.0$ eV spectral region and normalized to their maxima. The solid lines are bi-exponential fits convoluted with an apparatus response of ~7 ps; the corresponding decay times are shown next to the transients. The PL mean energy values of the D2-Und-P2TP-TMS films in (c) were smoothed by Sovitzky-Golay method with 7 point of window; the dash lines are monoexponential fits $E = E_0 + \Delta E * \exp(-T/t)$, where E_0 value was fixed (for LB film: $E_0 = 2.48$eV, $\Delta E = 90 \pm 20$meV, $t = 200 \pm 50$ ps; for LS film: $E_0 = 2.47$eV, $\Delta E = 80 \pm 20$ meV, $t = 110 \pm 50$ ps).

Despite their similarity in PL spectral shape (Figure S6.4a), the PL of LS film decays faster as compared to the annealed LB film (Figure S6.4a) resulting in lesser PL intensity. The counter-intuitive fact is that the thinner LB monolayer film produces stronger PL by a factor of 1.25 than the LS thicker film (figure S6.3c). Here

we speculate that the quenching process is enhanced by the presence of the second (or third) layer which provides additional subways to an exciton quenching (Figure S6.5).
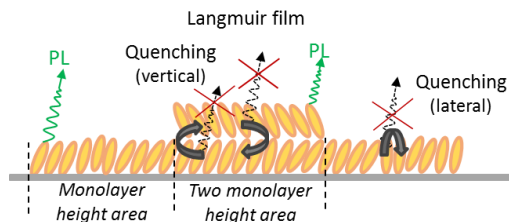
Figure S6.5. Proposed model of PL quenching in monolayer films. The molecules in the LB film on the substrate (gray) are shown by the orange ovals. Green and black thin arrows with red crosses demonstrate high and low probability to PL, respectively. Thick black lines are assigned to the PL quenching process originated in the lateral and the vertical directions as it mentioned on the panel.

In the crystalline monolayer, PL quenching mainly occurs in the lateral direction while the second layer opens the vertical direction, too (Figure S6.5). To characterize the probability of PL quenching in vertical direction, we calculated *MA* as the ratio of the area with the one monolayer height in the film to the whole sample area including areas with the Langmuir film absence, i.e., fully covered sample of one monolayer height film has $MA = 100\%$. The Langmuir film *MA* values (shown in Figure S6.3c) calculated from the film height distribution functions by taking an integral value under the corresponding distribution over the width (the full width at half maximum for monolayer in non-annealed LB film, e.g. ~1.0 nm range) around the monolayer peak position at ~3.1 nm. Thus, we suggested that higher integral PL intensity of LB films might be explained by higher *MA* with respect to LS film. Moreover, the faster transient red-shifts of PL mean energy for LS film with respect to LB film (110±50 ps *vs.* 200±50 ps) prove higher energy transfer efficiency increasing PL quenching probability. However, further PL investigations of Langmuir films with various *MA* are needed to reveal the unique exciton dynamic in 2-D crystalline system excluding three dimensional factors.

6.6. References

1.   Andringa, A. M.; Spijkman, M. J.; Smits, E. C. P.; Mathijssen, S. G. J.; van Hal, P. A.; Setayesh, S.; Willard, N. P.; Borshchev, O. V.; Ponomarenko, S. A.; Blom, P. W. M.; de Leeuw, D. M.

Gas Sensing with Self-Assembled Monolayer Field-Effect Transistors. *Org. Electron.* **2010**, *11*, 895-898.

2. Mulla, M. Y.; Tuccori, E.; Magliulo, M.; Lattanzi, G.; Palazzo, G.; Persaud, K.; Torsi, L. Capacitance-Modulated Transistor Detects Odorant Binding Protein Chiral Interactions. *Nat. Commun.* **2015**, *6*, 6010(9).

3. Dumitru, L. M.; Manoli, K.; Magliulo, M.; Palazzo, G.; Torsi, L. Low-Voltage Solid Electrolyte-Gated OFETs for Gas Sensing Applications. *Microelectronics Journal* **2014**, *45*, 1679-1683.

4. Casalini, S.; Leonardi, F.; Cramer, T.; Biscarini, F. Organic Field-Effect Transistor for Label-Free Dopamine Sensing. *Org. Electron.* **2013**, 14, 156-163.

5. Casalini, S.; Dumitru, A. C.; Leonardi, F.; Bortolotti, C. A.; Herruzo, E. T.; Campana, A.; de Oliveira, R. F.; Cramer, T.; Garcia, R.; Biscarini, F. Multiscale Sensing of Antibody-Antigen Interactions by Organic Transistors and Single-Molecule Force Spectroscopy. *ACS Nano* **2015**, *9*, 5051-5062.

6. Klauk, H.; Zschieschang, U.; Pflaum, J.; Halik, M. Ultralow-Power Organic Complementary Circuits. *Nature* **2007**, 445, 745-748.

7. Baeg, K. J.; Jung, S. W.; Khim, D.; Kim, J.; Kim, D. Y.; Koo, J. B.; Quinn, J. R.; Facchetti, A.; You, I. K.; Noh, Y. Y. Low-Voltage, High Speed Inkjet-Printed Flexible Complementary Polymer Electronic Circuits. *Org. Electron.* **2013**, *14*, 1407-1418.

8. Mandal, S.; Dell'Erba, G.; Luzio, A.; Bucella, S. G.; Perinot, A.; Calloni, A.; Berti, G.; Bussetti, G.; Duò, L.; Facchetti, A.; Noh, Y.-Y.; Caironi, M. Fully-Printed, All-Polymer, Bendable and Highly Transparent Complementary Logic Circuits. *Org. Electron.* **2015**, *20*, 132-141.

9. Yu, H.; Bao, Z.; Oh, J. H. High-Performance Phototransistors Based on Single-Crystalline n-Channel Organic Nanowires and Photogenerated Charge-Carrier Behaviors. *Adv. Funct. Mater.* **2013**, *23*, 629-639.

10. Smithson, C. S.; Wu, Y.; Wigglesworth, T.; Zhu, S. A More Than Six Orders of Magnitude UV-Responsive Organic Field-Effect Transistor Utilizing a Benzothiophene Semiconductor and Disperse Red 1 For Enhanced Charge Separation. *Adv. Mater.* **2015**, *27*, 228-233.

11. Smithson, C. S.; Ljubic, D.; Wu, Y.; Zhu, S. Rapid UV-A Photo Detection Using a BTBT Organic Thin-Film Transistor Enhanced by a 1,5-Dichloro-9,10-Dintiro-Anthracene Acceptor. *Org. Electron.* **2016**, *37*, 42-46.

12. Capelli, R.; Toffanin, S.; Generali, G.; Usta, H.; Facchetti, A.; Muccini, M. Organic Light-Emitting Transistors with an Efficiency That Outperforms the Equivalent Light-Emitting Diodes. *Nat. Mater.* **2010**, *9*, 496-503.

13. Muccini, M.; Koopman, W.; Toffanin, S. The Photonic Perspective of Organic Light-Emitting Transistors. *Laser & Photonics Reviews* **2012**, *6*, 258-275.

14. Zhang, C.; Chen, P.; Hu, W. Organic Light-Emitting Transistors: Materials, Device Configurations, and Operations. *Small* **2016**, *12*, 1252-1294.

15. Borshchev, O. V.; Ponomarenko, S. A. Self-Assembled Organic Semiconductors for Monolayer Field-Effect Transistors. *Polymer Science, Series C* **2014**, *56*, 32-46.

16. Mottaghi, M.; Lang, P.; Rodriguez, F.; Rumyantseva, A.; Yassar, A.; Horowitz, G.; Lenfant, S.; Tondelier, D.; Vuillaume, D. Low-Operating-Voltage Organic Transistors Made of Bifunctional Self-Assembled Monolayers. *Adv. Funct. Mater.* **2007**, *17*, 597-604.

17.	Smits, E. C. P.; Mathijssen, S. G. J.; van Hal, P. A.; Setayesh, S.; Geuns, T. C. T.; Mutsaers, K. A. H. A.; Cantatore, E.; Wondergem, H. J.; Werzer, O.; Resel, R. *et. al.* Bottom-Up Organic Integrated Circuits. *Nature* **2008**, *455*, 956-959.

18.	Mathijssen, S. G. J.; Smits, E. C. P.; van Hal, P. A.; Wondergem, H. J.; Ponomarenko, S. A.; Moser, A.; Resel, R.; Bobbert, P. A.; Kemerink, M.; Janssen, R. A. J.; de Leeuw, D. M. Monolayer Coverage and Channel Length Set the Mobility in Self-Assembled Monolayer Field-Effect Transistors. *Nat. Nanotechnol.* **2009**, *4*, 674-680.

19.	Ponomarenko, S. A.; Borshchev, O. V.; Meyer-Friedrichsen, T.; Pleshkova, A. P.; Setayesh, S.; Smits, E. C. P.; Mathijssen, S. G. J.; de Leeuw, D. M.; Kirchmeyer, S.; Muzafarov, A. M. Synthesis of Monochlorosilyl Derivatives of Dialkyloligothiophenes for Self-Assembling Monolayer Field-Effect Transistors. *Organometallics* **2010**, *29*, 4213-4226.

20.	Lenz, T.; Schmaltz, T.; Novak, M.; Halik, M. Self-Assembled Monolayer Exchange Reactions as a Tool for Channel Interface Engineering in Low-Voltage Organic Thin-Film Transistors. *Langmuir* **2012**, *28*, 13900-13904.

21.	Schmaltz, T.; Amin, A. Y.; Khassanov, A.; Meyer-Friedrichsen, T.; Steinruck, H. G.; Magerl, A.; Segura, J. J.; Voitchovsky, K.; Stellacci, F.; Halik, M. Low-Voltage Self-Assembled Monolayer Field-Effect Transistors on Flexible Substrates. *Adv. Mater.* **2013**, *25*, 4511-4514.

22.	Gholamrezaie, F.; Kirkus, M.; Mathijssen, S. G. J.; de Leeuw, D. M.; Meskers, S. C. J. Photophysics of Self-Assembled Monolayers of a pi-Conjugated Quinquethiophene Derivative. *J. Phys. Chem. A* **2012**, *116*, 7645-7650.

23.	Yamao, T.; Shimizu, Y.; Terasaki, K.; Hotta, S. Organic Light-Emitting Field-Effect Transistors Operated by Alternating-Current Gate Voltages. *Adv. Mater.* **2008**, *20*, 4109-4112.

24.	Bisri, S. Z.; Takenobu, T.; Yomogida, Y.; Shimotani, H.; Yamao, T.; Hotta, S.; Iwasa, Y. High Mobility and Luminescent Efficiency in Organic Single-Crystal Light-Emitting Transistors. *Adv. Funct. Mater.* **2009**, *19*, 1728-1735.

25.	Hotta, S.; Yamao, T. The Thiophene/Phenylene Co-Oligomers: Exotic Molecular Semiconductors Integrating High-Performance Electronic and Optical Functionalities. *J. Mater. Chem.* **2011**, *21*, 1295-1304.

26.	Agina, E. V.; Usov, I. A.; Borshchev, O. V.; Wang, J.; Mourran, A.; Shcherbina, M. A.; Bakirov, A. V.; Grigorian, S.; Moller, M.; Chvalun, S. N.; Ponomarenko, S. A. Formation of Self-Assembled Organosilicon-Functionalized Quinquethiophene Monolayers by Fast Processing Techniques. *Langmuir* **2012**, *28*, 16186-16195.

27.	Sizov, A. S.; Anisimov, D. S.; Agina, E. V.; Borshchev, O. V.; Bakirov, A. V.; Shcherbina, M. A.; Grigorian, S.; Bruevich, V. V.; Chvalun, S. N.; Paraschuk, D. Y.; Ponomarenko, S. A. Easily Processable Highly Ordered Langmuir-Blodgett Films of Quaterthiophene Disiloxane Dimer for Monolayer Organic Field-Effect Transistors. *Langmuir* **2014**, *30*, 15327-15334.

28.	Sizov, A. S.; Agina, E. V.; Gholamrezaie, F.; Bruevich, V. V.; Borshchev, O. V.; Paraschuk, D. Y.; de Leeuw, D. M.; Ponomarenko, S. A. Oligothiophene-Based Monolayer Field-Effect Transistors Prepared by Langmuir-Blodgett Technique. *Appl. Phys. Lett.* **2013**, *103*, 043310.

29.	Agina, E. V.; Sizov, A. S.; Anisimov, D. S.; Trul, A. A.; Borshchev, O. V.; Paraschuk, D. Y.; Shcherbina, M. A.; Chvalun, S. N.; Ponomarenko, S. A. Thiophene-Based Monolayer Ofets Prepared by Langmuir Techniques. *Proc. SPIE* **2015**, *9568*, 95680Z.

30.	Borshchev, O. V.; Sizov, A. S.; Agina, E. V.; Bessonov, A. A.; Ponomarenko, S. A. Synthesis of Organosilicon Derivatives of [1]Benzothieno[3,2-B][1]-Benzothiophene Enabling Efficient

Monolayer Langmuir-Blodgett Organic Field Effect Transistors. *Chem. Commun.* **2017**, 53, 885-888.

31.   Janssen, P. G. A.; Pouderoijen, M.; van Breemen, A. J. J. M.; Herwig, P. T.; Koeckelberghs, G.; Popa-Merticaru, A. R.; Meskers, S. C. J.; Valeton, J. J. P.; Meijer, E. W.; Schenning, A. P. H. J. Synthesis and Properties of α,ω-Phenyl-Capped Bithiophene Derivatives. *J. Mater. Chem.* **2006,** *16*, 4335-4342.

32.   Huang, C. H.; McClenaghan, N. D.; Kuhn, A.; Hofstraat, J. W.; Bassani, D. M. Enhanced Photovoltaic Response in Hydrogen-Bonded All-Organic Devices. *Org Lett* **2005,** *7*, 3409-3412.

33.   Shumilkina, E. A.; Borshchev, O. V.; Ponomarenko, S. A.; Surin, N. M.; Pleshkova, A. P.; Muzafarov, A. M. Synthesis and Optical Properties of Linear and Branched Bithienylsilanes. *Mendeleev Commun* **2007,** *17*, 34-36.

34.   Brouwer, A. M. Standards for Photoluminescence Quantum Yield Measurements in Solution (IUPAC Technical Report). *Pure Appl. Chem.* **2011,** *83*, 2213-2228.

35.   Kazantsev, M. S., *et. al.*, Highly-Emissive Solution-Grown Furan/Phenylene Co-Oligomer Single Crystals. *RSC Adv.* **2016**, *6,* 92325-92329.

36.   Mikhnenko, O. V.; Blom, P. W. M.; Nguyen, T.-Q. Exciton Diffusion in Organic Semiconductors. *Energy Environ. Sci.* **2015**, *8*, 1867-1888.

37.   Kohler, A.; Bassler, H., *Electronic Processes in Organic Semiconductors: An Introduction*. Wiley-VCH: **2015**.

Summary

Organic optoelectronics is a rapidly growing field of fundamental and applied research promising cheap, light weighted, mechanically flexible, and – for some applications – even semitransparent devices. The state-of-the-art organic semiconductors stand as the basis for optoelectronics such as light-emitting diodes, photovoltaic cells, photodetectors and, in a longer term, light-emitting transistors and current-driven (injection) organic lasers. One of the main advantages of organic over inorganic semiconductors is their structural variability, which allows for creating semiconductor materials with specifically desired properties. Electrophysical and photophysical processes in organic semiconductors are governed by molecular packing, crystallinity, short- and long-range order, impurities, and doping. Design of advanced materials that combine the attractive electrophysical and photophysical properties is one of the strategic challenges in organic optoelectronics.

In general, organic semiconductors suffer from a low electrical conductivity as compared to their inorganic counterparts. This is one of the main reasons why most optoelectronic products available nowadays at the market still rely on inorganic semiconductors. Even though many organic optoelectronic semiconductors which have been studied for the last three decades are based on amorphous materials, well-ordered molecular packing provides an alternative way to gain the electrical conductivity and light emission – the key performance parameters of organic optoelectronics.

Enhancing the power conversion efficiency between optical (i.e., flux of photons) and electrical power (i.e., flow of free charge carriers) in both directions is one of the most discussed subjects in modern organic optoelectronics (**Chapter 1**). In this regard, the following topics are studied in this Thesis: molecular ordering in polycrystalline polymer-fullerene films controlled by thermal annealing (**Chapter 2**), doping of the host crystals with highly luminescent organic molecules (**Chapters 3-4**), probing photoluminescence anisotropy in organic single crystals (**Chapter 5**) and photoluminescence dynamics in organic semiconductor monolayers (**Chapter 6**). The results presented in this Thesis are obtained using in-situ Raman and ultrafast photoluminescence spectroscopies. Each chapter of the Thesis refers to a particular ordered organic semiconductor – semicrystalline polymer-fullerene blended films, single crystals, and crystalline monolayers.

To increase the power conversion efficiency of organic solar cells, post-deposition treatment of the semicrystalline polymer-fullerene blended films, such as

thermal or solvent vapor annealing, which directly affects molecular crystallinity, is widely applied. This calls for quick and noninvasive methods to control the molecular crystallinity during annealing of the already manufactured devices for every combination of perspective material. In **Chapter 2**, we present a novel spectroscopic technique, which allows for real-time tracking of the molecular crystallinity in films. The method is based on decomposition of the Raman spectrum of the sample film in the region of carbon-carbon stretching modes onto two reference components that correspond to the amorphous and quasi-crystalline phases of the polymer. A model for molecular crystallinity dynamics of the polymer phase was proposed for the polymer-fullerene blended films based on different fullerene derivatives. This model allowed us to better understand preparation conditions for the semicrystalline films and to optimize the post-deposition treatment protocols for manufacturing organic solar cells.

The high charge carrier mobility requires tight molecular packing readily achieved in organic semiconductor single crystals, but it usually results in inhibiting the light emission because of aggregation-induced luminescence quenching. This dichotomy can be resolved by doping the host crystals with highly luminescent organic molecules that requires their chemical synthesis and subsequent smooth embedding into the host matrix. In **Chapter 3**, we present an innovative concept of molecular self-doping, where a highly luminescent dopant emerges as a minute-amount byproduct during the host material synthesis, which circumvents the additional synthesis and eases the integration of the dopant into the host crystal lattice. In the promising thiophene-phenylene semiconducting crystals, ~1% self-doping doubled the light emission and still maintained solid the charge transport properties. The time-resolved experiments on photoluminescence dynamics backed by computer simulations revealed the efficient host-dopant energy transfer within organic single crystals on a sub-nanosecond scale. The self-doping concept opened an easy route to adopting other highly luminescent semiconductor organic crystals for optoelectronics applications.

In organic semiconductors, photon absorption leads to a formation of bound states between an electron and a hole, the so-called excitons. In organic materials, excitons diffuse via a random hopping between molecules or conjugated segments via their inter-/intramolecular interactions. Doping organic crystals with highly fluorescent molecules is used to enhance their luminescence, thereby making exciton diffusion a decisive player in the energy transfer process from the host crystal to the dopant. In **Chapter 4**, we show that the exciton diffusion length, in a promising

semiconductor crystal based on furan/phenylene co-oligomers, exceeds 25 nm, which is among the top values for organic semiconductor crystals. This key finding allowed us to harvest the majority of excitons on dopants at 10's of ppm molecular doping levels, which minimizes the determinant effect of the dopants on charge transport.

The attractive feature of organic semiconductor crystals is the perfect alignment of the molecules and hence their transition dipole moments, which might cause the luminescence to be strongly anisotropic. Understanding PL polarization properties is one of the key factors to achieve better performance of the molecular crystals in optoelectronic devices. Time-resolved, polarization-sensitive photoluminescence provides important insights for establishing the essential relationship between the molecular structure and optical properties in the systems. In **Chapter 5**, we reveal time-resolved photoluminescence anisotropy in single crystals of thiophene phenylene co-oligomers. According to the polarization-resolved photoluminescence measurements, photoluminescence was mainly polarized along the molecule backbones, regardless of the excitation polarization. However, the photoluminescence induced by the excitation orthogonally polarized with respect to the molecular backbones unexpectedly exhibited much higher efficiency as compared to the parallel one. This highly surprising result was explained via the presence of weakly- or even non-radiative states which are responsible for photoluminescence quenching. We proposed surface defect states and molecular self-dopants as possible candidates for such states.

In organic field-effect devices, the current flows in an ultrathin layer (one or a few molecular monolaters) in contact with the gate dielectric. As a result, ultrathin organic devices, e.g., transistors and sensors, become possible. Additionally, ultrathin semiconducting films are very beneficial for light-emitting field-effect devices as they are free of waveguiding effects that reduce the light output from the thicker films. These facts motivate fabrication of monolayer films of organic semiconductors using various self-assembly techniques. Amongst them, the Langmuir techniques are one of the most robust and fastest for producing monolayers with the well-controlled structure. In **Chapter 6**, we report photoluminescence properties of highly crystalline Langmuir films prepared from novel organosilicon derivative of thiophene-phenylene co-oligomers. Our photoluminescence time-resolved studies strongly suggested that the highly crystalline monolayers exhibit more efficient photoluminescence than thicker amorphous/polycrystalline films prepared from the same molecules. These findings

open the way to rational design of functional materials for monolayer organic light-emitting transistors and other optoelectronic devices.

Overall, this Thesis addresses the following questions: How could the polymer crystallinity be monitored during thermal annealing the polymer-fullerene organic photovoltaic devices? What are the fundamental dynamic processes that control the exciton dynamics, energy transfer efficiency, and luminescence polarization in organic single crystals? What are the differences in luminescence dynamics of the crystalline monolayers and bulk amorphous/polycrystalline structures? The current study on various highly ordered organic semiconductor structures provides essential connections between the photophysical and structural properties of the material used and develops new approaches for improving the performance of organic optoelectronic devices.

Samvatting

De organische opto-elektronica is een snelgroeiend fundamenteel en toegepast onderzoeksgebied, met een veelbelovend uitzicht op goedkope, lichte, mechanisch flexibele en – voor sommige toepassingen – zelfs semi-transparante 'devices'. De state-of-the-art organische halfgeleiders vormen de basis voor opto-electronica zoals lichtgevende diodes, foto-voltaïsche cellen, lichtdetectoren en, op langere termijn, lichtgevende transistoren en stroomgestuurde (injectie) organische lasers. Eén van de belangrijkste voordelen van organische boven anorganische halfgeleiders is hun mogelijke variatie in structuur, die het mogelijk maakt om halfgeleidermaterialen te maken met specifiek gewenste eigenschappen. Elektrofysische en fotofysische processen in organische halfgeleiders worden bepaald door moleculaire pakking, kristalliniteit, korte en lange afstandsordening, onzuiverheden en doping. Het ontwerpen van geavanceerde materialen die de aantrekkelijke elektrofysische en fotofysische eigenschappen combineren, is een van de strategische uitdagingen in de organische opto-elektronika.

In het algemeen hebben organische halfgeleiders een lagere elektrische geleidbaarheid vergeleken met hun anorganische tegenhangers. Dit is één van de belangrijkste redenen waarom de meeste opto-elektronische producten, die momenteel op de markt zijn, nog steeds anorganische halfgeleiders gebruiken. Hoewel veel van de organische halfgeleiders, die de afgelopen drie decades zijn bestudeerd, gebaseerd zijn op amorfe materialen, bied een goed geordende moleculaire pakking een alternatief om een betere elektrische geleidbaarheid en licht emissie te krijgen – de belangrijkste prestatieparameters van organische halfgeleiders.

Het verbeteren van de efficiëntie om energie om te zetten tussen optisch vermogen (een flux van fotonen) en elektrisch vermogen (een stroom van vrije ladingsdragers) in beide richtingen, is éen van de meest bediscussieerde onderwerpen in de moderne organische opto-elektronika (**Hoofdstuk 1**). In dit verband worden in dit proefschrift de volgende onderwerpen bestudeerd: moleculaire ordening in polykristallijne polymeer-fullereen films door thermische annealing (**Hoofdstuk 2**), doping van gast kristallen met zeer luminescerende organische moleculen (**Hoofdstuk 3-4**), het bekijken van fotoluminescentie anisotropie in organische éen-kristallen (**Hoofdstuk 5**) en de dynamica van de fotoluminescentie in organische halfgeleider monolagen (**Hoofdstuk 6**). De resultaten die in dit proefschrift worden gepresenteerd zijn verkregen met in-situ

Raman spectroscopie en ultrasnelle fotoluminescentie spectroscopie. In de diverse hoofdstukken worden verschillende ordeningen van de organische halfgeleiders gebruikt – semi-kristallijne polymeer-fullereen gemengde films, éen-kristallen en kristallijne monolagen.

Om de efficiëntie van de energie omzetting in organische zonnecellen te verhogen, wordt thermische en oplosmiddeldamp annealing (wat direct de moleculaire kristalliniteit beïnvloedt) veel gebruikt als nabehandeling van semi-kristallijne polymeer-fullereen films. Dit vraagt om snelle en niet-invasieve methoden, om de kristalliniteit te volgen tijdens het annealen van reeds gemaakte devices van diverse materialen. In **Hoofdstuk 2** presenteren we een nieuwe spectroscopische techniek die het mogelijk maakt om de moleculaire kristalliniteit in films in real-time te volgen. Deze methode is gebaseerd op het ontleden van het Raman spectrum, in het gebied van de C-C strek vibratie, in twee componenten die overeenkomen met de amorfe en de quasi-kristallijne fasen van het polymeer. Er is een model voorgesteld voor de dynamica van de moleculaire kristalliniteit van de polymeer fase, voor de polymeer-fullereen gemengde films, gebaseerd op verschillende fullereen derivaten. Met dit model konden we de preparatie condities van de semi-kristallijne films beter begrijpen. Ook konden we hiermee de nabehandeling van de gemaakte organische zonnecellen optimaliseren.

Een hoge mobiliteit van ladingsdragers vereist een dichte moleculaire pakking, die makkelijk bereikt wordt in organische halfgeleidende éen-kristallen, maar zorgt meestal ook voor minder licht emissie door de, door aggregatie geïnduceerde, luminescentie quenching. Deze dichotomie kan worden opgelost door de gast kristallen te dopen met zeer luminescente organische moleculen, die dan wel eerst gesynthetiseerd moeten worden en vervolgens moeten worden ingebed in de gast matrix. In **Hoofdstuk 3** presenteren we een innovatief concept van moleculaire zelf-doping, waar een hoog luminescente doping verschijnt als een zeer klein bijproduct gedurende de synthese van het gast materiaal. Dit omzeilt de extra synthese en vergemakkelijkt de inbedding van de doping moleculen in het gast kristalrooster. In de veelbelovende thiofeen-fenyleen halfgeleider kristallen werd met ~1% zelfdoping de licht emissie verdubbeld en bleven de ladingstransport eigenschappen behouden. De tijd opgeloste experimenten aan de fotoluminescentie dynamica, ondersteund door computersimulaties, lieten efficiënte doping-gast energie overdracht op een sub-nanoseconde tijdsschaal zien in deze organische éen-kristallen. Dit zelf-doping concept opent een makkelijke route om ook andere sterk luminescente organische halfgeleider kristallen te gebruiken voor opto-elektronische toepassingen.

In organische halfgeleiders leidt de absorptie van een foton tot de vorming van een gebonden toestand van een elektron en een gat, het zogenaamde exciton. In organische materialen diffunderen deze excitonen door willekeurig van molecuul naar molecuul of tussen geconjugeerde segmenten te springen, door middel van inter- en/of intra-moleculaire interacties. Het dopen van organische kristallen met sterk fluorescerende moleculen wordt gebruikt om de luminescentie te verhogen, waardoor exciton diffusie een beslissende speler wordt in het proces van de energieoverdracht van het gast kristal naar het doping molecuul. In **Hoofdstuk 4** laten we zien dat de exciton diffusie lengte, in een veelbelovend halfgeleider kristal gebaseerd op furaan-fenyleen co-oligomeer, groter is dan 25 nm, wat een van de topwaarden is voor organische halfgeleider kristallen. Deze belangrijke bevinding stelt ons in staat om de meeste excitonen te 'oogsten' op doping moleculen, met een doping niveau van enkele tientallen ppm's, wat het effect van de doping op het ladingtransport minimaliseert.

Een aantrekkelijk kenmerk van organische halfgeleider kristallen is de perfecte uitlijning van de moleculen en daarmee hun overgangsdipoolmomenten, waardoor de luminescentie sterk anisotroop kan zijn. Het begrijpen van de fotoluminescentie polarisatie eigenschappen is een van de sleutelfactoren om betere prestaties te bereiken van de moleculaire kristallen in opto-elektronische devices. Tijd opgeloste, polarisatie-gevoelige fotoluminescentie verschaft belangrijke inzichten in de essentiële relatie tussen de moleculaire structuur en de optische eigenschappen in deze systemen. In **Hoofdstuk 5** laten we tijd opgeloste anisotrope fotoluminescentie zien in één-kristallen van tiofeen-fenyleen co-oligomeren. Volgens de polarisatie-opgeloste fotoluminescentie metingen was deze luminescentie voornamelijk gepolariseerd langs de moleculaire as, ongeacht de excitatie polarisatie. De fotoluminescentie geïnduceerd door de excitatie die orthogonaal gepolariseerd was op de moleculaire as vertoonde echter onverwachts een veel hogere efficiëntie dan die vergeleken met parallelle polarisatie. Dit zeer verrassende resultaat werd verklaard door de aanwezigheid van zwak- of zelfs niet-stralende toestanden, die verantwoordelijk zijn voor de fotoluminescentie quenching. We stelden oppervlakte defect toestanden of moleculaire zelf-doping voor als mogelijke kandidaten voor zulke toestanden.

In organische veldeffect devices stroomt de stroom in een ultradunne laag (één of enkele moleculaire monolagen) in contact met de poort isolator. Daardoor worden ultradunne organische devices zoals transistors en sensoren mogelijk. Bovendien zijn ultradunne halfgeleidende films erg gunstig voor lichtgevende veldeffect

devices, omdat ze geen golfgeleider effecten hebben die de lichtopbrengst van dikkere films verminderen. Deze feiten zijn een motivatie voor de fabricage van monolaag films van organische halfgeleiders door middel van diverse zelf-assemblagetechnieken. Onder hen is de Langmuir-techniek éen van de meest robuuste en snelste voor het produceren van monolagen met een goed gecontroleerde structuur. In **Hoofdstuk 6** rapporteren we fotoluminescentie eigenschappen van zeer kristallijne Langmuir films, die zijn gemaakt zijn van een nieuw organisch-silicium derivaat van thiofeen-fenyleen co-oligomeren. Onze tijd opgeloste fotoluminescentie metingen suggereerden sterk dat de zeer kristallijne monolagen een efficiëntere fotoluminescentie vertonen dan de dikkere amorfe / polykristallijne films, gemaakt van dezelfde moleculen. Deze bevindingen openen de weg naar een rationeel ontwerp van functionele materialen voor monolaag organische lichtgevende transistoren en andere opto-elektronische devices.

Samenvattend behandelt dit proefschrift de volgende vragen: hoe kan de kristalliniteit van het polymeer worden gevolgd tijdens de thermische annealing van organische fotovoltaïsche devices gemaakt van polymeer-fullereen? Wat zijn de fundamentele dynamische processen die de exciton-dynamica, de efficiëntie van energie overdracht en de polarisatie van de luminescentie in organische éen-kristallen bepalen? Wat zijn de verschillen in de dynamica van de luminescentie in kristallijne monolagen en bulk amorfe/polykristallijne structuren? Dit onderzoek aan verschillende hoog geordende organische halfgeleider structuren legt essentiële verbindingen tussen de foto-fysica en de structurele eigenschappen van de bestudeerde materialen en verschaft nieuwe benaderingen voor het verbeteren van de prestaties van organische opto-elektronische devices.

Abstract

Organic optoelectronics is a rapidly growing field of fundamental and applied research promising cheap, light weighted, mechanically flexible, and – for some applications – even semitransparent devices. The state-of-the-art organic semiconductors stand as the basis for indispensable optoelectronic devices such as light-emitting diodes, photovoltaic devices and, in a longer term, light-emitting transistors and injection lasers. Apart from the chemical structure of the molecules, such characteristics of their solid phase as molecular packing, crystallinity, short- and long-range order, impurities, and doping govern electrophysical and photophysical processes in an organic semiconductor. Molecular packing is one of the key features that allows for fine-tuning the architecture of the organic semiconductor to gain new material properties.

This Thesis focuses on the understanding of photophysics and morphology in ordered organic semiconductor systems – semicrystalline polymer-fullerene blended films, various types of luminescent single crystals and monolayers. The Thesis aims to answer the following questions: How could the polymer crystallinity be monitored during thermal annealing the polymer-fullerene organic photovoltaic devices? What are the fundamental dynamic processes that control the exciton dynamics, energy transfer efficiency, and luminescence polarization in doped organic single crystals? What are the differences in luminescence dynamics of the crystalline monolayers and single crystals? Experimentally, the photophysics and morphology are probed by ultrafast photoluminescence and Raman spectroscopies. Such an extensive study in various highly ordered organic semiconducting structures provides the essential connections between the fast photophysics and the structural properties of the material, and aims to develop new approaches for improving the performance of organic optoelectronic devices.

De organische opto-electronika is een snelgroeiend fundamenteel en toegepast onderzoeksgebied, met een veelbelovend uitzicht op lichte, mechanisch flexibele en semitransparante 'devices'. De state-of-the-art organische halfgeleiders vormen de basis voor onmisbare opto-elektronische apparaten zoals lichtgevende diodes, fotovoltaïsche apparaten en, op langere termijn, lichtgevende transistoren en injectielasers. Naast de chemische structuur van de moleculen, zijn ook verschillende eigenschappen van de vaste fase van belang voor de electro-fysische en foto-fysische

processen in een organische halfgeleider, zoals moleculaire stapeling, kristalstructuur, korte en lange afstandsordening, onzuiverheden en doping. De moleculaire stapeling is een van de belangrijkste eigenschappen wat gebruikt kan worden om de architectuur van organische halfgeleiders te verfijnen en zo nieuwe materiaaleigenschappen te verkrijgen.

Dit proefschrift richt zich op het begrijpen van de foto-fysica en de morfologie van geordende organische halfgeleidersystemen: semi-kristallijne polymeer-fullereen gemengde films, verschillende soorten van luminescente één-kristallen en monolagen. Dit proefschrift probeert de volgende vragen te beantwoorden: Hoe kan de polymeer kristalliniteit worden gevolgd gedurende de thermische annealing van polymeer-fullereen organische fotovoltaïsche devices? Wat zijn de fundamentele dynamische processen die de exciton dynamica, de efficiëntie van energie overdracht en de luminescentie polarisatie bepalen in gedoopte organische één-kristallen? Wat zijn de verschillen in de dynamica van de luminescentie in kristallijne monolagen en één-kristallen? Experimenteel worden de foto-fysica en morfologie bestudeerd met ultrasnelle fotoluminescentie en Raman spectroscopie. Deze extensieve studie in verschillende hoog geordende organische halfgeleiderstructuren laat de essentiële verbindingen zien tussen de snelle foto-fysica en de structuur eigenschapen van het materiaal. Dit kan worden gebruikt om nieuwe benaderingen te ontwikkelen voor het verbeteren van de prestaties van organische opto-elektronische devices.

Acknowledgements

The story began at the Russian Academy of Sciences in 2013 at a scientific conference, where I met my future supervisors together for the first time. After I had an interview with them about a new opportunity - a 'Sandwich' Ph.D. program - that featured a close collaboration between Dutch and Russian scientific communities, I decided that I would love to pursue that intriguing challenge. I have never regretted my decision even for a second. I spent five wonderful and productive years working on the topics I enjoy that culminated in this thesis, and I would like to thank many people who supported and helped me on my way to become a Doctor of Science.

First of all, I would like to thank my promoters Kees Hummelen, Dmitry Paraschuk, and Maxim Pshenichnikov for providing me with an opportunity to be a key part of the joint research program between University of Groningen and Lomonosov Moscow State University.

Kees, I want to thank you for our fruitful discussions and for your positive attitude. You were always kind and welcoming during our scientific discussions and interviews.

I would like to express my sincere gratitude to my daily supervisors, Dmitry and Maxim, for the continuous support of my Ph.D. study and related research, for their patience, motivation, and for sharing their immense knowledge with me. Their guidance helped me during the writing of the Thesis and throughout the whole Ph.D. program. Thanks to them, I learned a lot of things not only about science, but also about life.

Dmitry, thank you for creating the friendly and lovely research environment in the Laboratory of Organic Electronics providing a wealth of opportunities for the professional development of young scientists. You have been a tremendous mentor for me. I would like to thank you for encouraging my research and for allowing me to grow as a research scientist.

Maxim, in all sincerity, I cannot find the right words to express my gratitude for your help and support during my Ph.D. studies. During the tough periods you were always on my side showing your highly professional approach to research, and I am grateful I had the opportunity to learn it from you. Your advice on both research, as well as on my career have been priceless.

Next, I wish to acknowledge the members of the reading committee: Jan Anton Koster, Koen Vandewal and Johannes Gierschner. Thank you for your advice, suggestions, and the time you spent to read and assess my thesis.

I will be forever thankful to my former research supervisor, Vladimir Bruevich. Vladimir has been helpful in giving me important advice during my graduate school career. He is and always has been my best football teammate with doctoral degree, as well as a great collaborator, exceptional mentor, and superb teacher. Vladimir was the reason why I decided to pursue a career in research, including this international program.

Each chapter of the thesis is a result of a different international collaboration. Therefore, I want to thank my collaborators from the research group of Organic Electronics at the Lomonosov Moscow State University - Vasiliy Trukhanov, Olga Parashchuk, Vlad Konstantinov, Dmitry Dominskiy, and Elizaveta Feldman. I am grateful that I had such intelligent and enthusiastic collaborators, who also became good friends. I am honored that I had the opportunity to work with them.

I also would like to acknowledge Sergei Ponomarenko and his group at the Institute of Synthetic Polymeric Materials in Moscow for the many batches? of molecules and monolayer samples which I was honored to study. I would like to express my special thanks to Elena Agina, Nikolay Surin, Oleg Borshchev, Alexey Sizov, and Daniil Anisimov. It was a pleasure to work with you, and I am really proud of the outcome of our joint projects.

My next acknowledge goes to the group of Maxim Kazantsev at the Vorozhtsov Novosibirsk Institute of Organic Chemistry for providing us with novel organic materials and samples, as well as for helpful scientific discussions. I enjoyed every single project I worked on together with you.

Life of a Ph.D. student can be difficult, and that I would like to thank the people who made it a lot simpler. Foppe de Haan, thank you very much for all your technical and daily support. Foppe, your software saved me tremendous amount of time when I was analyzing complex raw data. I am deeply grateful to Jeannette de Boer and Henriet van Mil-Boddeveld for their administrative support and all the paperwork they helped me with.

During Ph.D. I was a part of not one, but two research groups. I thank the group of Organic Electronics at the Lomonosov Moscow State University for our general life discussions, fun holiday celebrations, and perfect green tea. Additionally, it was always useful to hear their feedback, relevant comments, and remarks about my work during our weekly group meetings. Also, I acknowledge the Department of General Physics and Wave Processes at Lomonosov Moscow State University and especially the head of Department prof. Vladimir A. Makarov for huge administrative support and numerous edifying advice.

All time I spent in the Netherlands I associate with the Optical Condensed Matter Science (OCMP) group. It was a pleasure to work there and I thank all the group members who made my stay in Groningen unforgettable. Maxim, Ron, Foppe, Ben, Jeannette, Zhenya, Björn, Oleg, Julius, Chia-Lin, Nong, Benedito, Jan, Timen, Kevin, Keisuke, Anna, Nilesh, Qi, Sonya and all the others – it was great to have you around. I enjoyed our lunches and coffee breaks with all the discussions, and rare but still fun group activities. The daily work was enjoyable greatly thanks to the wonderful people who surrounded me. That friendly and kind atmosphere really made the basement of building 5117 like a second home to me.

There was not enough time for many social activities during my stay in the Netherlands, but everyone I met here are just amazing people. I would love to have every one of them as a teammate on a tough mountain hike! From the faculty of Science and Engineering I want to thank Régis, Laaya, Vova, Leonid, Misha, Jamo, Nataliia, and Dima for their support and all small talk inside and outside of the University. Additionally, I would like to thank my football party and especially Chen, Diego, Jose, and Shady for all energy and positivity I received playing with them every Sunday at Sportpark De Parrel - I still play from time to time (see you there!). Another energetic group of people I met in Groningen is Lindy hop dance community. Lineke, Arsalan, Jing, Carlijn, and Luna, there are not enough words to express my happiness from dancing and learning Lindy hop together. All master classes and social events were really exciting and breath-taking, and I wish to continue my jazz dance classes wherever I will be in the future. Also, I thank my roommate Alexei for his help, thoughtful discussions, smart suggestions, and fun small talk in our kitchen.

Besides the great colleagues, I also met several people OCMP who became my friends. Oleg, Zhenya, Björn, Julius and Chia-Lin, I loved spending time with you. Attractions, movie nights, watching football, pool games, barbeques, cooking, travelling, or just sitting at a bar – all activities we did together were really inspiring to me, and always made me happy.

I would like to express my special thanks to my dear friends and paranymphs – Zhenya and Björn. Throughout the last year we spent more and more enjoyable time together, and I wish I could continue that trend. Zhenya, you were always supportive and excited to try new activities. Thanks to your interesting ideas, I was never sad or lazy during breaks and holidays. Thank you for the idea to go to dance classes! I wish you all the best in your future career and personal life. Björn, you were the first person, with whom I could talk in English on many topics besides science, and

probably the only one, who could understand me at the beginning of my Ph.D. :). Intelligence and responsibility are the features I had always appreciated in you. I am confident that you will successfully finish your Ph.D. and I hope you will invite me for your defense.

Oleg, you showed me everything around the University campus and Groningen, including best bars. I wish I could repeat our long working days at the office 0017 with your post-rock atmosphere, weekend activities, tennis teaching, scientific conferences, and many small fun things we did together. Julius, sport had always connected us. On the first day, you impressed me by playing chess on such high level (you beat me without a single mistake!) Then I learnt climbing and belaying from you. And finally, I probably will never forget our tennis competitions. Chia-Lin, thank you very much for all your support with my job search. I am really happy that you made such a big step in your career.

I really appreciate the support from my Russian friends. Special thanks to my football team "Tasmanian Devils" of Lomonosov Moscow State University. Serega, Toshik, Lesha, Leshik plus Max - we did a great job together. We won 3 cups of the Department of Physics at MSU – I will remember all our games and other activities for years. I would like to thank my close friends all around the globe, with whom we studied together at Lyceum #31. Pasha, Varya, Sasha, Vage, Stas, Artem, Shurik, and others – lately I have seen you, probably, only couple of times a year but it was really important to me. Petr and Max, our friendship dates back to 2005, when we became classmates, and it never will fade. Max, I really appreciate your wise advice on career, job interviews, and your help with finalizing this Thesis. Petr, thank you for help with the Thesis-cover design and for your extraordinary and "ever seen-ever been" support that kept me going despite all the difficult situation I faced. You are the one who had turned every unpleasant situation I encountered into lots of laughs.

Finally, I want to thank my family. Мои дорогие родители и мой брат, спасибо вам большое за огромную поддержку и содействие, что вы оказывали мне на протяжении этого долгого пути. Вы всегда верили в меня и мягко, но настойчиво подталкивали меня в нужном направлении, когда это было необходимо. К сожалению, я не могу быть рядом, но всегда чувствую ваше тепло и поддержку и знаю: что бы ни случилось, есть место, где меня ждут и мне всегда будут рады. Спасибо вам за все.

<div align="right">

Artur Mannanov
Groningen
July 2019

</div>